Edited by Dieter M. Herlach

WILEY-VCH

Solidification and Crystallization

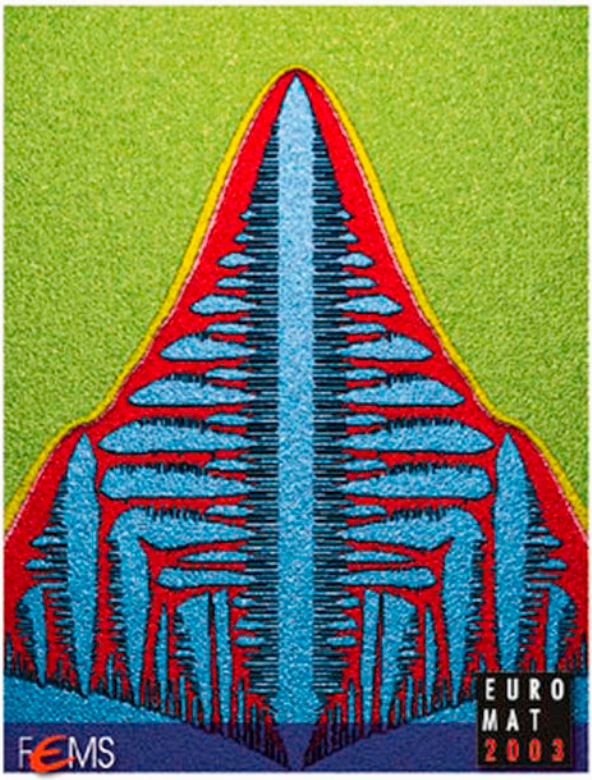

EUROMAT
Publications

Solidification and Crystallization

Edited by
Dieter M. Herlach

DGM

WILEY-VCH

Solidification and Crystallization

Edited by
Dieter M. Herlach

DGM

WILEY-VCH

Related Titles from Wiley-VCH

H.-P. Degischer, B. Kriszt (Eds.)

Handbook of Cellular Metals

2002
ISBN 3-527-30339-1

G. Kostorz

Phase Transformations in Materials

2001
ISBN 3-527-30256-5

K. U. Kainer (Ed.)

Magnesium Alloys and Technology

2003
ISBN 3-527-30570-X

C. Leyens, M. Peters (Eds.)

Titanium and Titanium Alloys

2003
ISBN 3-527-30534-3

Solidification and Crystallization

Edited by
Dieter M. Herlach

DGM

WILEY-VCH Verlag GmbH & Co. KGaA

Edited by

Prof. Dieter M. Herlach
DLR – German Aerospace Center
Institute of Space Simulation
51170 Köln
Germany

Library of Congress Card No.: applied for

British Library Cataloguing-in-Publication Data: A catalogue record for this book is available from the British Library.

Bibliographic information published by Die Deutsche Bibliothek
Die Deutsche Bibliothek lists this publication in the Deutsche Nationalbibliografie; detailed bibliographic data is available in the Internet at <http://dnb.ddb.de>

Printed in the Federal Republic of Germany
Printed on acid-free paper

Composition ProSatz Unger, Weinheim
Printing betz-druck GmbH, Darmstadt
Bookbinding Großbuchbinderei J. Schäffer GmbH & Co. KG, Grünstadt

ISBN 3-527-31011-8

Preface

The Federation of European Materials Societies (FEMS) organized the biannual meeting of EUROMAT conference 2003 in Lausanne, Switzerland. This conference was essentially focussed on materials development and application. One of the conference topic was dedicated to *PHASE TRANSFORMATION* chaired by Professor Wilfried Kurz, Lausanne. It consisted of two symposia S1 on *SOLIDIFICATION* and S3 on *SOLID STATE TRANSFORMATION*.

Papers submitted originally to Symposium S2 *MODELLING* were integrated into Symposium S1. All together 96 abstracts not only from Europe but also from Asia and America were submitted to Symposium S1 with which S1 became the largest symposium of EUROMAT 2003 conference. The papers were distributed to three sessions on *Modelling*, two sessions on *Microstructures* and one session on *Properties of Melts, Nucleation, Dendritic Growth, Phase Selection, Multiphase Alloys* and *Processing Methods*, respectively. In addition there was a poster session.

The symposium was started with a plenary lecture by Professor Michel Rappaz on *Modelling of Solidification with Special Emphasis on the Last Stage Solidification*. The oral sessions and the poster session attracted many attendees and experienced vivid discussions showing that the research area of solidification is carried by a large and very active scientific community. In particular, remarkable progress was reported on new experimental methods and techniques for direct observation and analysis of solidification pathways both under near- and non-equilibrium conditions. Simultaneously, modelling of solidification proceeded to a big step forwards enabling now even the computer assisted description of solidification phenomena in multiphase and multicomponent alloys. Such progress is of fundamental interest for materials science but also very important in developing innovative techniques in materials production routes of improved efficiency in casting processes of foundry industry. Since by far most of the materials are produced from the liquid state as their parent phase even small but steady advances in solidification processing leads to correspondingly large consequences in progress of economy and living conditions of daily human life. It is therefore mandatory for a prosperous society.

The present Publications to EUROMAT 2003 contains selected papers of symposium S1 which have been invited for submission to publication in the present book. Each manuscript was peer reviewed by two independent experts before acceptance for publication. Certainly, the peer review process has essentially contributed to the

quality of the present volume. I appreciate the valuable and important assistance of all experts who delivered reports on submitted manuscripts.

I would like to extend my gratitude to Professor Wilfried Kurz for inviting me as an organizer of the symposium *Solidification* of the topic of *Phase Transformation*, and the colleagues who took over the chairmanship of the different sessions as Andreas Ludwig (Leoben), Michel Rappaz (Lausanne), Heike Emmerich (Dortmund), A. Lindsay Greer (Cambridge), Heiner Müller-Krumbhaar (Jülich), Dirk Holland-Moritz (Köln), Andy Mullis (Leeds), Lorenz Ratke (Köln), Peter Schuhmacher (Leoben) and Britta Nestler (Karlsruhe). I enjoyed the cooperation with Michel Rappaz in his help of combining Symposium S2 (Modelling) with Symposium S1 (Solidification). My thanks are to the local organisers in Lausanne for an excellent conference performance, Peter-Paul Schepp from the Deutsche Gesellschaft für Materialkunde in the preparation of the programme, the Deutsche Forschungsgemeinschaft for support within the priority program SPP1120 and Jörn Ritterbusch and Jörg Wrzesinski from WILEY-VCH for their great help in editing this book.

Köln, August 2004

Dieter M. Herlach
Organizer of Symposium
Solidification of EUROMAT 2003

Contents

Preface *V*

1 Complex Structures: A Symbiosis of Experiments and Numerical Studies *1*
J. H. Bilgram and H. M. Singer
Abstract *1*
1.1 Inotroduction *1*
1.2 Experimental Studies *2*
1.3 Numerical Studies *5*
1.4 Conclusions *6*
Acknowledgements *7*
References *7*

2 Thermal Roughening of a Solid-on-Solid Model with Elastic Interaction *9*
Frank Gutheim, Heiner Müller-Krumbhaar, Efim Brener and Christoph Pütter
2.1 Introduction *9*
2.2 Step Interaction *9*
2.3 Model Description *10*
2.4 Results and Discussion *13*
2.4.1 Height Correlation Function *13*
2.4.2 Energetic Scales *14*
2.4.3 Average Energy *14*
2.4.4 Defect Correlations *14*
2.4.5 Line Energy vs. Step Interaction *15*
2.4.6 Crystal Growth *15*
2.5 Conclusion *16*
References *16*

3 A Phase-Field Model for Crystallization into Multiple Grain Structures *17*
Hamid Assadi
Abstract *17*
3.1 Introduction *17*

3.2 Theoretical Background and Model Development *18*
3.3 Simulations *21*
3.3.1 Temperature Dependence of Interfacial Energy *22*
3.3.2 Crystallization by Inoculation *22*
3.3.3 Crystallization by Homogeneous Nucleation *24*
References *26*

4 Scaling Relations for Dendritic Solidification in Binary Alloys *27*
Heike Emmerich, Matthias Jurgk, Ricardo Siquieri
4.1 Introduction *27*
4.2 Two-scale Modeling for Binary Alloys *28*
4.3 A Novel Scaling Relation Taking into Account Crystal Density *30*
4.4 Numerical Investigations of the Two-scale Model *31*
Summary *32*
References *33*

5 Modeling the Spatial Phase Separation Process in Hypermonotectic Alloys *34*
M. Wu, A. Ludwig, L. Ratke
Abstract *34*
5.1 Introduction *34*
5.2 Numerical Model *35*
5.2.1 Phase Definition *35*
5.2.2 Conservation equations *35*
5.2.3 Droplet Growth and Mass Transfer *36*
5.2.4 Marangoni Force and Hydrodynamic Resistance *37*
5.3 Problem description *38*
5.4 Results and Discussions *39*
5.4.1 Without Gravity *39*
5.4.2 With Gravity *40*
5.5 Conclusions *42*
References *42*

6 Modeling of the Solidification of Immiscible Alloys *44*
J. Z. Zhao, Z. Q. Hu, L.Ratke
Abstract *44*
6.1 Introduction *44*
6.2 Theoretical Model *45*
6.3 Numerical Results and Discussions *48*
6.4 Conclusions *51*
Acknowledgments *51*
References *51*

7 Phase-Field Modeling of Dendritic Solidification: Verification for the Model Predictions with Latest Experimental Data *52*
P.K. Galenko, D.M. Herlach, O. Funke, G. Phanikumar
Abstract *52*
7.1 Introduction *52*
7.2 Governing equations *53*
7.3 Results and Discussion *55*
7.3.1 Dendritic Patterns *56*
7.3.2 Comparison with experimental data *57*
7.4 Conclusions *58*
Acknowledgements *59*
References *59*

8 Phase-Field Modeling of Phase Transitions in Ternary Alloys *61*
Britta Nestler
8.1 Introduction *61*
8.2 Phase-Field Model *62*
8.3 Phase Transitions of Ternary Alloys *64*
8.4 Outlook *68*
Acknowledgements *69*
References *69*

9 Modeling of Heat and Solute Flows during Solidification of Droplets *70*
R. Heringer, Ch.-A. Gandin, G. Lesoult, H. Henein
Abstract *70*
9.1 Introduction *70*
9.2 Experimental *71*
9.3 Modeling *72*
9.3.1 Macroscopic Heat and Solute Flows *72*
9.3.2 Front Tracking and Growth Velocity *73*
9.3.3 Microsegregation and Mushy Zone Solidification *74*
9.3.4 Initial and Boundary Conditions, Numerical Implementation *75*
9.4 Results *76*
9.5 Concluding Remarks *80*
Acknowledgements *81*
References *81*

10 Thermo-physical and Physical Properties for Use in Solidification Modelling of Multi-component Alloys *82*
N. Saunders, Z. Guo, A. P. Miodownik and J-Ph. Schillé
Abstract *82*
10.1 Introduction *82*
10.2 Technical Background *84*
10.2.1 The Scheil-Gulliver Approach with Modification for fast C and N Diffusion *84*

10.2.2 Modelling of Physical Properties *87*
10.3 Example Calculations *88*
10.3.1 Variations in Behaviour Within an Alloy Composition Specification Range *88*
10.3.2 Behaviour of the Liquid in the Mushy Zone *90*
10.4 Discussion *93*
10.5 Summary and Conclusions *93*
References *94*

11 Determination of Solidification Curves Based on DSC Experiments with Improved Heat-transfer Model *95*
Djordje Mirković, Joachim Gröbner, Rainer Schmid-Fetzer
11.1 Introduction *95*
11.2 DSC Experiment and Heat-Transfer Model (DSC-HTM) *96*
11.2.1 DSC Experiment *96*
11.2.2 Heat-transfer Model *96*
11.3 Solidification Curves Determined by Alternative Methods *99*
11.3.1 Quenching and Image Analysis (QIA) *99*
11.3.2 Thermodynamic Calculation of Solidification Curves *99*
11.4 Results and Discussion *100*
Acknowledgement *102*
References *102*

12 Measurement of the Surface Tension of Undercooled Melts by the Oscillating Drop Method in an Electrostatic Levitator *103*
Peter L. Ryder and Nils Warncke
12.1 Introduction *103*
12.2 Experimental Methods *104*
12.2.1 The Levitator *104*
12.2.2 The Oscillating Drop Method *105*
12.2.2.1 Principle *105*
12.2.2.2 Excitation and Detection of the Oscillations *105*
12.3 Results *106*
12.4 Summary and Conclusions *109*
Acknowledgements *109*
References *109*

13 Liquid-liquid Interfacial Tension and Wetting in Immiscible Al-based Systems *110*
Walter Hoyer, Ivan Kaban, Markus Merkwitz
13.1 Introduction *110*
13.2 Experimental Technique *110*
13.3 Results and Discussion *113*
13.4 Conclusions *117*
Acknowledgements *118*

References *118*

14 In-Situ Optical Determination of Fraction Solid *119*
L. Ratke, D. Tscheuschner
Abstract *119*
14.1 Introduction *119*
14.2 Experimental *120*
14.3 Experimental Results *121*
14.4 Mathematical Analysis of the Intensity Curves *122*
14.5 Fraction Solid *124*
14.6 Discussion and Conclusion *125*
References *127*

15 Magnetic Effects on the Nucleation in Undercooled Co-Pd Melts *128*
Dirk Holland-Moritz and Frans Spaepen
15.1 Introduction *128*
15.2 Classical Approach to Describe the Nucleation Behavior of Co-Pd Melts *129*
15.3. Extension of the Classical Nucleation Model by Magnetic Contributions *132*
15.4. Conclusions *135*
Acknowledgements *135*
References *136*

16 Identification of the Substrate of Heterogeneous Nucleation in Zn-Al Alloy Inoculated with ZnTi-Based Master Alloy *137*
Witold K. Krajewski, A. Lindsay Greer, Thomas E. Quested, Waldemar Wolczynski
Abstract *137*
16.1 Introduction *137*
16.2 Experimental Methods *138*
16.3 Results and Discussion *140*
16.3.1 Thermal Analysis and Structure *140*
16.3.2 Crystal Structure and Chemical Composition *142*
16.3.3 Crystal orientation *144*
16.3.3.1 TEM Examination of Thin Foils *144*
16.3.3.2 SEM – EBSD Examinations *144*
16.4 Conclusions *146*
Acknowledgements *147*
References *147*

17 Undercooling and Solidification of Liquid Silicon *148*
C. Panofen, R. P. Liu, D. Holland-Moritz, T. Volkmann, D.M. Herlach
17.1 Abstract *148*
17.2 Introduction *148*
17.3 Experimental *149*
17.4 Results & Discussion *151*
17.4.1 Surface Morphologies and Solidification Mode *151*
17.4.2 Growth Velocity Results *153*
17.5 Conclusion *155*
Acknowledgements *155*
References *155*

18 Two-Phase Equilibrium in Binary Alloy Nano Particles *157*
P. Bunzel, G. Wilde, H. Rösner, J. Weissmüller
18.1 Introduction *157*
18.2 Idealized Model System *158*
18.2.1 The Model Alloy *158*
18.2.2 Particle Shape and Properties of the Phase Boundary *159*
18.2.3 Surface Area of the Phase Boundary *159*
18.2.4 Molar Free Energies *160*
18.3 Size-dependent Alloy Phase Diagrams *161*
18.4 Conclusion *164*
Acknowledgement *165*
References *165*

19 Three-dimensional Reconstruction of Experimentally Grown Xenon Dendrites *166*
H.M. Singer and J.H. Bilgram
19.1 Introduction *166*
19.2 Experimental Setup *167*
19.3 Analytical Models vs. Simulations *168*
19.4 Reconstruction *169*
19.5 Results and Discussion *172*
References *173*

20 Mechanically Deformed Primary Dendritic Structures Observed During the Solidification of Undercooled Melts *175*
Andrew M. Mullis, Kalin Dragnevski, & Robert F. Cochrane
20.1 Introduction *175*
20.2 Experimental Method *177*
20.3 Experimental Evidence for Deformed Dendritic Structures *178*
20.4 Discussion *179*
20.5 Summary & Conclusions *183*
References *183*

21 Effect of Hydrodynamics on Microstructure Evolution of Nd-Fe-B Alloys *185*
R. Hermann, G. Gerbeth, O. Filip, J. Priede, V. Shatrov
Abstract *185*
21.1 Introduction *185*
21.2 Experimental *186*
21.3 Results *187*
21.3.1 Levitation *187*
21.3.2 Magnetic Two-phase Stirrer *190*
21.4 Conclusions *192*
Acknowledgements *193*
References *193*

22 Effect of the Fluid Convection Driven by a Rotating Magnetic Field on the Solidification of a PbSn Alloy *194*
B. Willers, S. Eckert, U. Michel, G. Zouhar
22.1 Introduction *194*
22.2 Experimental Procedure *195*
22.3 Discussion of the Results *197*
22.3.1 Thermal analysis *197*
22.3.2 UDV Measurements *199*
22.3.3 Microstructure *200*
22.4 Discussion, Conclusions *202*
Acknowledgement *202*
References *203*

23 Grain Sedimentation and Melt Convection Phenomena During Globular Equiaxed Solidification *204*
M. Wu, A. Ludwig and A. Bührig-Polaczek
23.1 Introduction *204*
23.2 Brief Description of the Numerical Model *205*
23.3 Experimental procedure *207*
23.4 Results and discussions *208*
23.5 Conclusions and outlook *211*
Acknowledgments *212*
References *212*

24 Metastable Primary Soldification Modes in the Fe-Cr-Ni System During Laser Welding *213*
H. Schobbert, Th. Böllinghaus, M. Wolf
Abstract *213*
24.1 Introduction *213*
24.2 Ferrite – Austenite Type of Primary Solidification Change *214*
24.3 Geometric Analysis of Solidification Structures *218*
24.4 Metastable States and Epitaxial Effects at the Fusion Line *222*
24.5 Metastable Ferritic Solidification *223*

24.6 Conclusions *225*
References *226*

25 Crystallization of the $Nd_2Fe_{14}B$ Peritectic Phase from the Undercooled Melt by Containerless Processing *227*
Shumpei Ozawa, Mingjun Li, Suguru Sugiyama, Itaru Jimbo and Kazuhiko Kuribayashi
25.1 Introduction *227*
25.2 Experimental Procedure *228*
25.3 Results *228*
25.3.1 $Nd_{11.8}Fe_{82.3}B_{5.9}$ ($Nd_2Fe_{14}B$) Alloy *228*
25.3.2 $Nd_{14}Fe_{79}B_7$ Alloy *231*
25.4 Discussions *234*
25.5 Conclusion *237*
Acknowledgements *237*
References *238*

26 Thermomagnetic Analyses of Nd-Fe-B Bulk Alloys Solidified from the Undercooled Melt *239*
S. Reutzel, T. Volkmann, J. Gao, J. Strohmenger, D.M. Herlach
Abstract *239*
26.1 Introduction *239*
26.2 Experimental *240*
26.3 Results and Discussion *241*
26.4 Summary *248*
Acknowledgements *248*
References *249*

27 Analysis of the Solidification Microstructure of Multi-component Gamma Titanium Aluminide Alloys *250*
Viola Küstner, Michael Oehring, Anita Chatterjee, Helmut Clemens, Fritz Appel
27.1 Introduction *250*
27.2 Experiments *251*
27.3 Results *251*
27.4 Discussion *255*
27.5 Conclusions *257*
Acknowledgements *257*
References *257*

28 Formation of Eutectic Cells in Ternary Al-Cu-Ag Alloys *259*
Ulrike Hecht, Victor Witusiewicz, Anne Drevermann, Stephan Rex
28.1 Introduction *259*
28.2 Experimental Procedure *260*
28.2.1 Sample Material *260*

28.2.2 Solidification Process and Sample Analysis *260*
28.3 Experimental Results *261*
28.3.1 Planar Coupled Growth *262*
28.3.2 Cellular Coupled Growth: Elongated and Regular Cells *264*
28.4 Discussion of the Process of Cell Formation *267*
28.5 Summary and Outlook *269*
Acknowledgements *270*
References *270*

29 Lamellar Pattern Formation during 2D-Directional Solidification of Ternary Eutectic Alloys *271*
Markus Apel, Bernd Böttger, Victor Witusiewicz, Ulrike Hecht, Ingo Steinbach
29.1 Introduction *271*
29.2 Phase Field Model *271*
29.2.1 Material Data *273*
29.2.2 Numerical Aspects and Simulation Procedure *274*
29.3 Simulation Results *275*
29.3.1 The Basic State and Tilted Growth *275*
29.3.2 Higher Order Stacking Sequences and Axisymmetric Growth *277*
29.4 Discussion and Summary *277*
Acknowledgement *278*
References *279*

30 Simulation of Stray Grain Formation in Investment Cast Turbine Blades *280*
X. L. Yang, H. B. Dong, W. Wang and P. D. Lee
Abstract *280*
30.1 Introduction *280*
30.2 Model Description *281*
30.3 Simulation Parameters *282*
30.4 Results and Discussion *283*
30.4.1 Effect of Withdrawal Velocity and Isothermal Conditions on Undercooling *283*
30.4.2 Dendritic Growth and Stray Grain Formation *284*
30.4.3 Effect of Withdrawal Velocity on Stray Grain Formation *286*
30.4.4 Effect of Inclination Angle of Isotherms on Stray Grain Formation *287*
30.5 Conclusions *288*
Acknowledgements *288*
References *288*

31 Laser Cladding Applications to Combinatorial Materials Science *290*
R. Vilar, P. Carvalho, R. Colaço
Abstract *290*
31.1 Introduction *290*

31.2 Laser Assisted Synthetic Methods *292*
31.3 Examples of Application *293*
31.3.1 Structure and Properties of Ni-Al-Co Alloys *293*
31.3.2 Metal-matrix-composites for Wear-resistant Coatings *295*
31.4 Conclusions *298*
References *298*

32 Control of Morphological Features in Micropatterned Ultrathin Films *300*
E. Meyer, H.-G. Braun
Abstract *300*
32.1 Introduction *300*
32.2 Experimental *301*
32.3 Results and Discussion *301*
32.4 Perspectives *307*
Acknowledgement *308*
References *308*

Author Index *311*

Subject Index *313*

1
Complex Structures: A Symbiosis of Experiments and Numerical Studies

J. H. Bilgram and H. M. Singer

Abstract

Dendrites are the best studied structures formed during solidification of undercooled melt. Additionally other complex structures have been found in experiments and numerical studies. We perform 2D/3D-numerical simulations of solidification processes and experiments which allow *in situ* investigations of three-dimensional growth of xenon crystals into undercooled pure melt. Dendrites, seaweed, doublons, triplons etc. can be produced in experiments and numerical studies depending on initial conditions. In an interplay of numerical studies and experiments we use simulations to interpret and to plan experiments. Experimental results are used as a basis of model calculations and the development of models of complex shapes. Three-dimensional growth shapes of crystals are reconstructed using sophisticated image processing combined with experimentally determined shape parameters.

1.1
Introduction

Applications in automotive industry call for aluminium castings to be mass-produced without casting defects. Predictive models are necessary to prevent such defects. During the growth of a solid from its undercooled parent melt microstructures are formed. The best-known cases of such structures are dendrites. Microstructural changes can be observed as undercooling is increased, namely the typical length scales like the tip radius decrease with increasing undercooling [1, 2]. These are quantitative changes. In addition to that, for some materials it has been observed that they also undergo an abrupt decrease in microscale with increasing undercooling. This effect is known as spontaneous grain refinement. It has been observed in solidification from undercooled pure metallic melts [3] and alloys [4, 5]. Evidence has been found that spontaneous grain refinement is initiated by changes in the morphology of the microscopic structures [3]. This is in difference to the above mentioned quantitative grain refinement with increasing undercooling. In order to obtain more information on shapes, developed during solidification, numerical modeling and analytical stu-

dies of the solidification process have been performed. Starting with a mathematical formulation of the dendrite problem, the goal is to find out which solutions exist and which morphologies are possible. Namely the stability of solutions has been studied [6, 7, 8]. A very astonishing result was the discovery of a doublon in 2D studies [9]. It is formed by two crystalline tips with a straight channel in between. This is a typical non-equilibrium shape. It was followed up by numerical studies which found a triplet in an 3D channel [8]. In a next step a morphology diagram has been developed for 2D systems [10, 11]. Regions for stable fractal and compact growth of dendrites and seaweed have been determined. Seaweed has been considered to be built up from doublons. In this study the stability regions of morphologies have been determined in a field of supercooling of the melt vs. anisotropy of the surface free energy. Supercooling is given in the range from 0 to 1 in dimensionless units and the anisotropy in the range from 0 to 1. High anisotropies lead to dendritic growth, at low anisotropy and sufficient undercooling seaweed is growing. The amount of noise in the system under consideration may influence the position of the phase boundaries. Therefore the phase diagram has to be considered to be a qualitative one.

To verify predictions, numerical and experimental studies have to be combined. We hope that such combined studies will stimulate the application of theoretical results in the design casting processes.

1.2 Experimental Studies

Existing models for dendritic growth do not predict morphological parameters with sufficient accuracy for reliable calculations to be applied in industrial casting processes. Metallographic techniques show microstructures which have been transformed during solidification and subsequent cooling. The study of decanted structures leads to an overestimation of the fraction of solid and does not provide information of solidification kinetics. Time resolved synchrotron radiation imaging techniques do no not provide a lateral resolution suficient to determine typical length scales of the fine structure and it is not possible to study three-dimensional structures with this technique up to now [12]. Thus the use of transparent materials is the only way to determine growth parameters of morphologies during the solidification process. Two types of experiments have been performed: quasi two dimensional studies on organic alloys [13] and studies of pure materials during free growth in three dimensions [14, 15, 16].

First experimental evidence of doublons has been achieved by Akamatsu et al. [13]. A thin cuvette was used and the material was an mixture of two organic liquids CBr_4 and C_2Cl_6. This system has two properties, which are important for the experiment:
i) An alloy is used. It is well known that in alloys much higher constitutional undercoolings are possible than for bulk undercoolings in a pure melt.
ii) Interface kinetics and surface free energy of the solid-liquid interface are anisotropic. Therefore this system has the great advantage that it is possible to change anisotropy of the surface free energy by changing the orientation of the seed crystal.

In these experiments the growth of seaweed has been observed and phase diagrams of the type as developed by Brener et al. [11] have been verified.

The calculations of Brener et al. have been performed for a 2D system. The experiments of Akamatsu et al. have been performed in a thin cuvette and thus it is a quasi-two-dimensional system. A two-dimensional doublon is topologically different from a doublon in three dimensions, because in 2D there is only one way out of the channel, namely at the tips. In the 3D case it is possible to move out of the channel in a direction perpendicular to the plane defined by the two branches limiting the channel. This fact changes topology significantly and also the possibility for the latent heat to diffuse away.

Experiments in three dimensions to detect doublons and seaweed have been performed in a growth vessel with a volume of 100 cm^3 of pure liquid xenon. We use xenon as a transparent model substance for metals, because it forms a simple liquid, it crystallizes in an fcc-lattice, and it forms a solid-liquid interface which is rough at atomic scale. Details of the experimental setup are described in [16, 17]. At the beginning of the experiment the melt is brought to a homogeneous temperature T_∞ which is below the melting temperature, i.e. the melt is homogeneously undercooled. Then a crystal is nucleated in a capillary and grows through the capillary into the undercooled melt. The dimensions of the growth vessel are sufficiently large to ensure free growth of the crystal. According to the properties of the solid-liquid interface and the undercooling in the range of 10^{-3} to 10^{-2} in dimensionless units, a dendrite grows to a stationary state after several minutes and the temperature distribution around the dendrite reaches a steady state. An important feature of the experimental setup [17] is the possibility to shift this dendrite up and down inside of the growth vessel. Shifting the dendrite in the growth vessel means to disturb the temperature distribution around the crystal and to wash off the isotherms. Immediately after such a shift the crystal is surrounded by melt with a spatial homogeneous temperature. Any surface element of the dendrite tip is in contact with liquid at a temperature close to T_∞. The thermal gradient at the crystal surface is everywhere the same. (Neglecting that the surface has been non isothermal before shifting the crystal.) Therefore any surface element of the crystal is growing with the same growth rate. This leads to an increase in the tip radius of the dendrite (Figure 1.) With increasing tip radius the dendrite reaches a state where the tip becomes unstable and tip splitting is observed. After tip splitting two tips continue to grow and form a doublon with a straight channel between the two tips. A sequence of contours is shown in Figure 1. By this procedure it is possible to grow various morphologies. Figure 2 shows a dendrite, a doublon and a seaweed morphology.

In difference to Brener et al. [11] we distinguish between doublon and seaweed morphology. This difference may originate from the three-dimensional geometry. The three morphologies can be distinguished from symmetry considerations: A dendrite shows a high degree of symmetry. For the seaweed no growth direction can distinguished in the plane of projection. The doublon has an axis of symmetry in the center of the channel.

In three dimensions the morphological transitions are not limited to the three cases shown in Figure 2. In addition to that we find triplons and quadruplons and

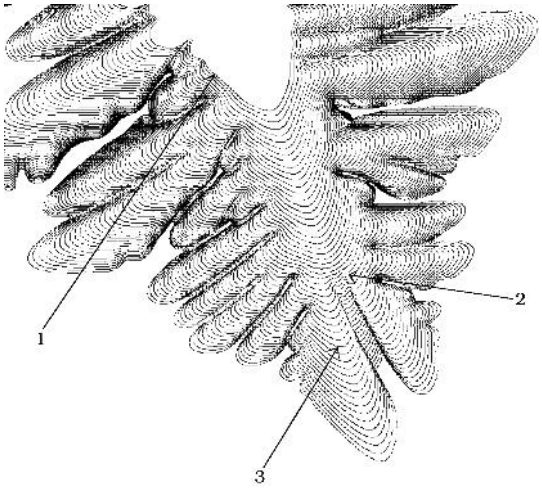

Fig. 1. A sequence of contours taken after the crystal has been shifted in the growth vessel. First we have the shape of the dendrite (arrow 1). During the temporal development the tip radius increases and the tip radius becomes unstable (arrow 2). Finally two tips are formed with a straight channel of liquid in between forming a doublon (arrow 3).

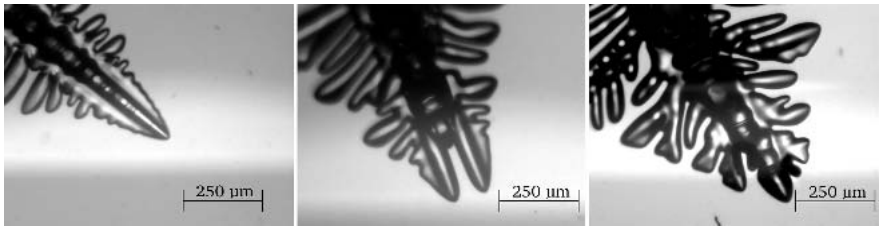

Fig. 2. Three morphologies: A dendrite, a doublon, and a seaweed.

Fig. 3. A crystal with three tips is formed in a similar process as observed in Figure 1.

even higher multiples of tips. Up to now we do not know the precise conditions for the occurrence of a special morphology. Figure 3 shows the development of a triplon out of a dendrite.

1.3 Numerical Studies

In order to verify and refine the qualitative analytical predictions by Brener et al. [11] we have performed phase field simulations with two different phase field models in 2D and 3D. Phase field models are an elegant approach to solve the analytical equations numerically. Instead of calculating a sharp phase boundary between solid and liquid in the Stefan- or sharp interface-problem every grid point holds in addition to the temperature also its phase state. The phase may have arbitrary values between 0 (solid) and 1 (liquid). A thin, but finite region of steep changes between solid and liquid models the interface. This width can be chosen and determines how well the approximation is in accordance with the sharp interface equations.

For our investigations we have chosen the models of Wheeler et al. [18] and Karma et al. [19]. The main difference between the two models is that in the Wheeler model the ratio between kinetic and capillary terms is fixed, where as in the Karma model the kinetic term can be cancelled by appropriately chosen terms for low undercoolings. We have performed simulations on a 2000×2000 grid with different undercoolings and anisotropies. The anisotropy axis goes from 0 to 6.5% as this is the maximal value where a crystal still grows in rough growth. For higher anisotropies the crystal becomes facetted as there occur forbidden growth directions. An initial coarse scan of 100 simulations was used to partition the plane. Subsequently a binary search for the morphology boundary was performed. By this refinement we were able to tie up the uncertainty region for the morphology boundary to up to 10^{-2}%. For lower undercoolings the simulation time increases significantly, therefore the uncertainty becomes bigger. In Figure 4 the results for the 2D simulations can be seen for both models. We have identified 3 regions of different morphologies: for low anisotropies seaweed structures (sw) and for high anisotropies dendrites are observed (den). For intermediate ansiotropies and high enough undercoolings doublons are found (db). Both models show a similar behavior as the analytical predictions for the morphology boundary (seaweed-dendrite): The shape is concave for increasing anisotropy. However there is a big difference to the predictions for low undercoolings: while the predictions state that the whole shape of the boundary is concave we find in our simulations for low undercoolings and anisotropies a convex boundary. Comparing the two phase field models with each other we find qualitative correspondence. However we state that the boundary of the Karma model is slightly more on the left than the one of the Wheeler model. A detailed discussion of this behavior can be found in [20].

Three-dimensional simulations are very time-consuming. Even though we use an adaptive mesh code which runs parallel on 32 processors, it was not possible to obtain the same fine resolutions as for 2D simulations. As we have found qualitative agreement between the two models we have preformed 3D simulations in a domain 400^3 only for the Karma model. The results are qualitatively similar to the 2D case however with two exceptions: i) The morphology boundary for the same parameters as in the 2D case is shifted along the anisotropy axis to the right by an amount of 0.32%. This result can be explained by the topological difference between 2D and

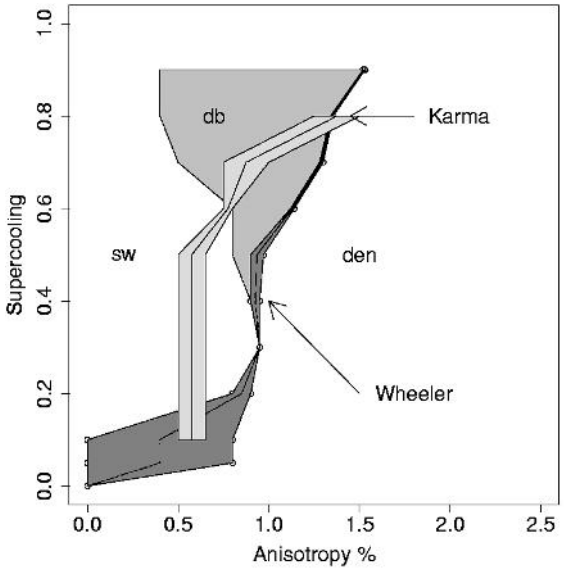

Fig. 4. Morphology diagram in 2 dimensions of the Wheeler model and the Karma model [20]. The zones marked with Wheeler and Karma correspond to the uncertainty regimes given by these models. The dendritic domain is denoted as "den". Seaweed as "sw" and doublon as "db".

3D: in 3D there is one additional dimension where heat can be transported away, therefore more anisotropy is needed to stabilize the structure to be dendritic. ii) No doublon region at all was found in 3D as opposed to 2D where we also started all simulations with the same initial conditions (a small spherical seed) and found a distinct doublon region. When starting with a spherical seed in 3D only seaweeds or dendrites can be simulated. It was however possible to simulate 3D doublons nevertheless by using special initial conditions [20]: by placing two identical seeds at a large enough distance, both start growing as a dendrite. However very soon they start interacting with each other and instead of developing four fins each they grow in parallel and develop only 3 fins each as observed in our experiments (Figure 3).

1.4 Conclusions

Quenching of metals during solidification provides some information on microstructures but not on the dynamics of morphology transitions during the solidification process. Transparent substances have been used to simulate solidification of metals. Rare gases have low melting entropy and form a „simple liquid" similar to metals and can therefore be used as model substances to simulate transparent metals. In these systems the solidification process can be studied *in situ*. Up to now the in-

formation from model experiments with transparent model substances has been limited because no 3D information on the microstructure formed during solidification was available.

Two new features have been introduced into the study of solidification by model experiments: 1.) the study of various morphologies and morphological transitions, and 2.) the possibility to reconstruct the shapes of transparent 3D objects [21]. Morphology changes seem to lead to an explanation of grain refinement in metals, a feature that remained unexplained since a long time. The determination of the 3D shape of objects formed during freezing provides for the first time the possibility to determine 3D shape parameters necessary to apply theories in industrial processes. We have started to determine such parameters and to characterize various morphologies formed during solidification and their transitions. We have the unique possibility to combine theoretical studies with experiments.

The interaction of experiment and theory is crucial. Theoretical studies are stimulated by unexpected experimental observations, and using an expression coined by L. Pasteur, the eye of the experimentalist is trained by theoretical results to see new structures.

Acknowledgements

We thank Professor Dr. H. R. Ott for his support of our experiments. This work was supported by the Swiss National Science Foundation.

References

[1] J.P. Gollub and J.S. Langer, Rev. Mod. Phys. 1999, 71, S396-S403

[2] A. Karma in Banching in Nature (Ed.: V. Fleury, J.-F. Gouyet, and M. Leonetti) Springer, Berlin, 2001, Chapter 9

[3] K. Dragevski, R. F. Cochrane, and A.M. Mullis, Phys. Rev. Lett. 2002, 89, 215502

[4] R. Willnecker, D.M. Herlach, and B. Feuerbach, Appl. Phys. Lett. 1990, 56, 324–326

[5] M. Schwarz, A. Karma, K. Eckler, and D.M. Herlach, 1994, 73, 1380–83

[6] M. Ben Amar and E. Brener, Phys, Rev. Lett. 1995, 75, 561–564

[7] T. Ihle, and H. Müller-Krumbhaar, Phys. Rev. Lett. 1993, 70, 3083–86

[8] T. Abel, E. Brener, and H. Müller-Krumbhaar, Phys. Rev. E, 1997, 55, 7789–92

[9] T. Ihle, Wachstumsmuster unter diffusivem Transport, Berichte des Forschungszentrums Jülich, Jülich, 1996, Vol.3230,

[10] E. Brener, H. Müller-Krumbhaar, and D. Temkin, Phys. Rev. E, 1996, 54, 2714–22

[11] E. Brener, H. Müller-Krumbhaar, D. Temkin, and T. Abel, Physica A 1998, 249, 73–81

[12] R.H. Mathiessen, L. Arnberg, K. Ramsoskar, T. Weitkamp, C. Rau, and A. Snigirev, Metall. Mater. Trans. B, 2002, 33B, 613–623

[13] S. Akamatsu, G. Faivre, and T. Ihle, Phys. Rev. E 1995, 51, 4751–73

[14] M.B. Koss, J.C. LaCombe, L.A. Tennenhouse, M.E. Glicksman, and E.A. Winsa, Metall. Mater. Trans. A, 1999, 30A, 3177–90.

[15] D. P. Corrigan, K. B. Koss, J.C. LaCombe, K.D. de Jager, L.A. Tennenhouse, and M.E. Glicksman, Phys, Rev. E, 1999, 60, 7217–7223

[16] U. Bisang and J.H. Bilgram, Phys. Rev. E, 1996, 54, 5309–26

[17] I. Stalder and J.H. Bilgram, Europhys. Lett. 2001, 56, 829–835

[18] A.A Wheeler, B.T. Murray and R.J. Schaefer, Physica D, 1993, 66 , 243–262

[19] A. Karma and W.-J. Rappel, Phys. Rev. E 1998, 57 , 4323–49

[20] H.M. Singer, I. Loginova, J.H. Bilgram, and G. Amberg, J. Cryst. Growth, submitted

[21] H.M. Singer and J.H. Bilgram, this volume

2
Thermal Roughening of a Solid-on-Solid Model with Elastic Interaction

Frank Gutheim, Heiner Müller-Krumbhaar, Efim Brener and
Christoph Pütter

2.1
Introduction

At low temperatures crystal surfaces are known to assume the shape of a plane facet. With increasing temperature, fluctuations gradually contribute a nonzero thickness to the initially flat facet. This surface thickness finally diverges at a finite temperature, the roughening temperature, where the order of the facet is lost completely. For kinetics of crystal growth and solidification, the roughening transition plays a decisive role. This transition can be described by a set of renormalization group equations first analyzed by Kosterlitz and Thouless [1]. Because of its unusual properties and the relation to the two-dimensional Coulomb gas, this roughening transition has attracted substantial attention.

Various discrete solid-on-solid (SOS) models have been shown to undergo this type of transition. Most of these models incorporate local interactions, at most next-nearest neighbor interactions. Within some of these models a transition involving in-plane disorder is possible, usually referred to as preroughening.

Interaction of surface defects by means of elastic deformation of the crystal, however, is of a long-ranged nature and has apparently not been previously studied in the context of roughening. Leaving the matter of preroughening aside, we will try to elucidate the effects of long-range elastic interactions on the roughening process.

2.2
Step Interaction

Elastic step interaction on the surface of a semi-infinite crystal can be described in terms of elastic force dipoles located at the step edges. Using symmetry arguments one can determine two types of force dipoles that are considered to be present at a step. One type involves in-plane forces perpendicular to the step, the other arises from forces orthogonal to the crystal surface. The former leads to attractive or repulsive interaction depending on the signs of the steps, the latter produces a sign-independent behavior,

which is strictly repulsive. There are materials where the sign-dependent contributions are small compared to the step repulsion caused by in-plane forces. Thus we restrict our model to the case, where we can neglect sign-dependence of the steps [2]. We can make another simplification of the step-step interaction by assuming a scalar $w \sim 1/r^3$ interaction associated with isotropic dipoles at the step. From this, the energy per unit length of the line for a configuration with two parallel steps at distance d is just

$$\tilde{W}_{\text{scalar}} = 4\,\gamma\,\frac{1}{d^2} + 2\,\gamma\,\frac{1}{\varepsilon^2}, \tag{1}$$

where the interaction is limited to distances greater than ε. The factor γ is given by

$$\gamma = \frac{1-\sigma^2}{\pi E}\,Q^2, \tag{2}$$

where Q is the dipole moment per unit length of the step, σ the Poisson ratio and E Young's modulus.

2.3 Model Description

Within the framework of a solid-on-solid model we describe the crystal surface by a simple height field h_i of integer multiples of the lattice constant a. Like in a common SOS model, overhangs are forbidden. We define an elastic step interaction by introducing a field of elastic dipole charges q. To every lattice site k a dipole charge q_k proportional to the number of height differences to the four neighboring sites is assigned. The elastic dipole charges interact, in consequence of Eq. (1), via a modified r^{-3} interaction potential $\Psi_{p_{\max},l}(r)$,

$$\Psi_{p_{\max},l}(r) = \begin{cases} \min\left((a/r)^3, p_{\max}\right) & \text{if } r \le l \\ 0 & \text{if } r > l \end{cases} \tag{3}$$

where r is the in-plane distance between two lattice sites and $p_{\max}$ is a number limiting the interaction potential in vicinity of $r = 0$. We also introduce the cutoff length l, i. e., the potential vanishes for distances greater than l. This gives rise to the elastic energy

$$E_{\text{el}} = \frac{w_{\text{el}}}{2}\sum_{i,j} q_i q_j \Psi_{p_{\max},l}(r_{ij}), \tag{4}$$

where r_{ij} is the distance between lattice sites i and j and w_{el} can be adjusted to give the desired interaction strength. Note that the case $i = j$ is not excluded from the summation. For two straight steps of length L with distance d and without cutoff this elastic energy contribution consists of the self energies of the steps and the expected $\sim d^{-2}$ step interaction term

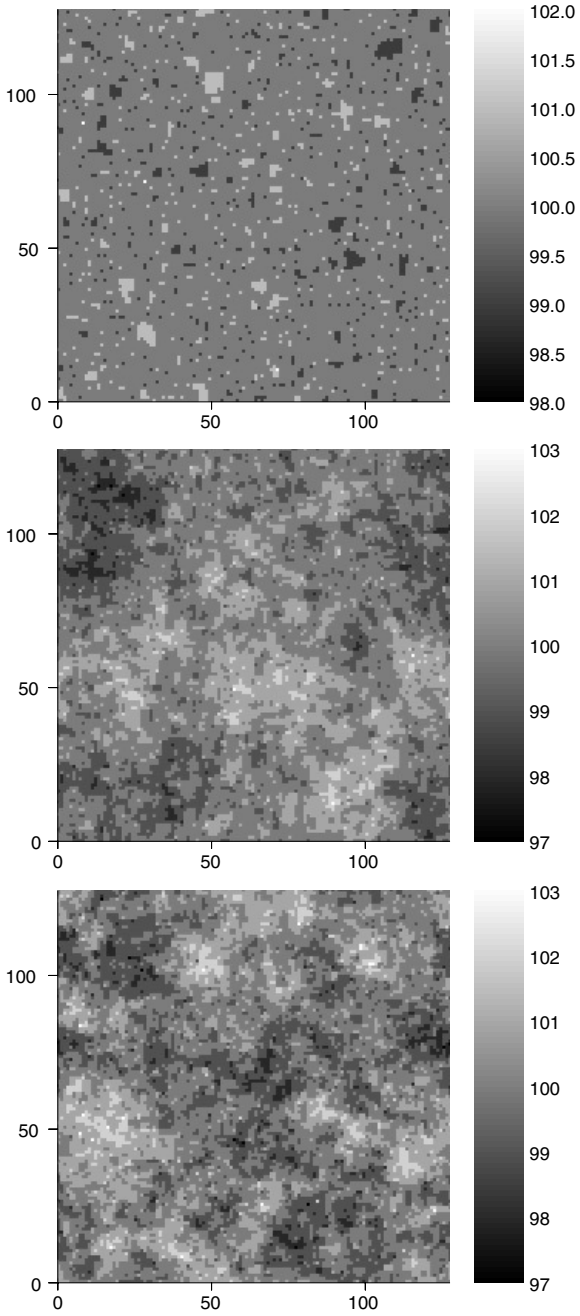

Fig. 1 Roughening transition of a surface under elastic interaction without cutoff. The height field of our model for three different configurations, $T \approx 4.5\ w_{el}$, $T \approx 13\ w_{el}$ (top to bottom), are shown as topviews. The heights are coded in grayscales. The average height corresponds to 100 atomic units.

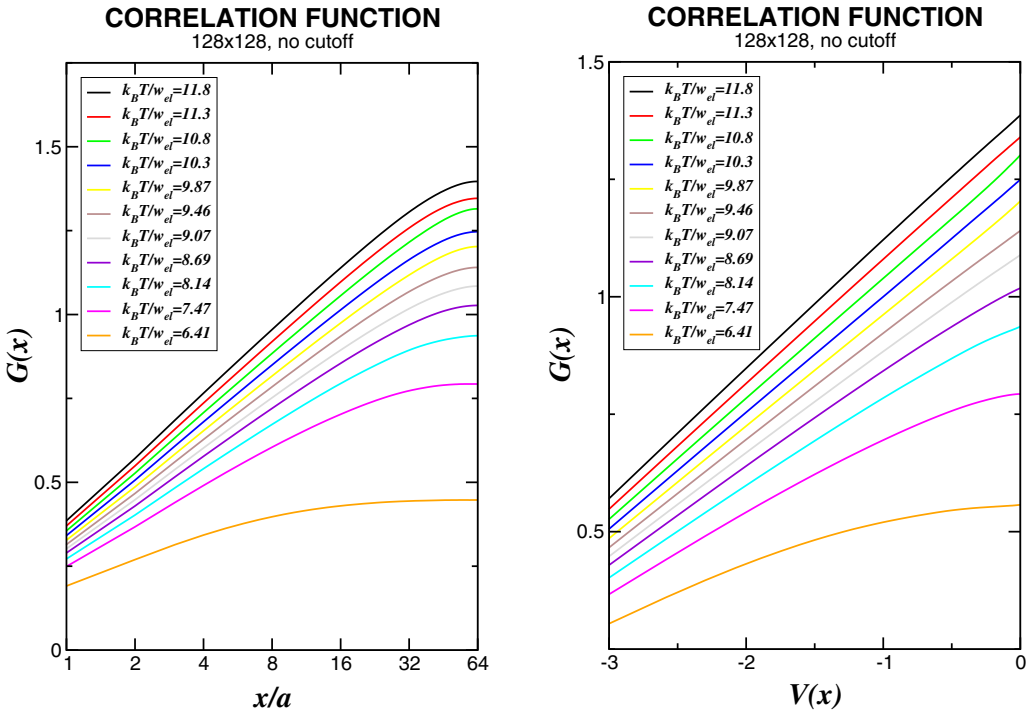

Fig. 2 Height-height correlation function without cutoff along the main directions of the lattice. Left: The correlation function saturates for all temperatures due to the finite size of the system. Right: Same plot, but with finite size correction [2]. The correlation function saturates for small temperatures and shows logaritzmic behavior for $T \geq T_R$. The first straight line gives an estimate of $k_n T_R / w_{el} \approx 9.0$.

$$E_{\text{int}} \approx 8\, w_{\text{el}}\, \frac{L}{d^2}\,, \tag{5}$$

for large distances $d \gg a$.

Modifying $p_{\max}$ the self energy contribution of a straight step can be adjusted to the desired line energy, independently of the step-step interaction amplitude.

For given $p_{\max}$ the relative amplitude of line energy and step-step interaction is fixed and we can concentrate on the crossover from a local to a long-range model depending on the cutoff length l, which is studied using the interaction potentials $\Psi_{1,l}$ where $p_{\max} = 1$. Later, however, other relative amplitudes are studied for the potential $\Psi_{p_{\max},\infty}$ without cutoff.

The simulation is carried out on a square lattice of size $(L/a)^2 = 64 \times 64$ to 128×128. In order to calculate the difference in energy for every metropolis Monte Carlo trial, we apply a multigrid scheme based on Ref. [3], which reduces computational cost and which has already been applied successfully to submonolayer epitaxy [4].

2.4
Results and Discussion

2.4.1
Height Correlation Function

We determine the roughening temperature T_R from the behavior of the height-height correlation function. In order to visualize the roughening transition of a surface Fig. 1 shows the height field of our model for three different configurations. Below roughening, $T < T_R$, the interface is macroscopically flat, i. e., the height-height correlation function

$$G(r) = \frac{\langle [h(0) - h(r)]^2 \rangle}{a^2} \tag{6}$$

approaches a finite value in the limit $r \to \infty$. To be more precise, the correlation length ξ is finite and the interface has a characteristic width. Approaching the transition temperature the correlation length increases and diverges at $T = T_R$. For $T > T_R$ the correlation function $G(r)$ diverges according to the conventional theory of the roughening transition,

$$G(r) \sim K(T) \ln \frac{r}{a}, \tag{7}$$

with an amplitude $K(T)$ depending on the temperature. Plotting $G(r)$ vs. $\ln(r/a)$ one could determine at what temperature the correlation length ξ diverges and the graphs approach a straight line.

In a finite system with periodic boundary conditions, however, the correlation length ξ cannot exceed the system size L, and the height-height correlation function $G(r)$ saturates for $T > T_R$ as well (see Fig. 2, left). In order to overcome this finite-size effect, we define a "periodic logarithm" $V(r)$ by means of Fourier analysis. At a temperature of about $k_B T \approx 9.0\, w_{el}$ the graph for the full $1/r^3$ interaction now becomes straight, indicating the roughening transition (see Fig. 2, right). For finite cutoff lengths the graph of the correlation function becomes straight at lower temperatures. Restricting the elastic dipole charge interaction to distances $\leq a$, one obtains $k_B T_R \approx 3.0\, w_{el}$. The roughening temperature only gradually increases with the cutoff length. Estimates of the roughening temperature from the Kosterlitz-Thouless theory are identical for the two cases with and without cutoff.

From this we conclude that the system with long-range interaction has a much higher transition temperature compared to the model with interaction cutoff. The roughening temperature changes by a factor ~3. We further conclude that the increase of the roughening temperature is not a next-nearest neighbor effect.

2.4.2 Energetic Scales

The increase of the roughening temperature by a factor of ~3 cannot sufficiently be explained by the increase of obvious energy scales of the low-temperature regime. The energy of a straight step, a single kink of such a step or a single adatom on a flat crystal surface does not change by more than 36% where the main contribution to the change comes from short-range interactions. For low temperatures the major energy contribution is local because dipole charges are distributed along steps. For a rough interface, however, the term "step" does not make much sense and dipole charges can be assumed to be rather evenly distributed over the whole plane. The energy of an additional dipole charge then relates to the two-dimensional surface integral

$$\int d^2 r \, \Psi(r), \tag{8}$$

whereas all local energetic scales mentioned above depend on effectively one-dimensional charge distributions. A naive analytic evaluation of the integral suggests a simple $k_B T_R / w_{el} \sim 1 - 2a/3l$ law for the cutoff dependence of the roughening temperature for $\Psi_{1,l}$, which gives already the observed dependence when l varies from a to ∞.

2.4.3 Average Energy

Comparing the average energy E of the system computed with and without restriction of the charge interaction range, the energy for the nonrestricted interaction always stays well below the graph of the restricted system. For high temperatures the average energy E goes linear with temperature T, indicating that the heat capacity becomes constant.

The range of the interaction potential only affects the behavior below the transition temperature significantly. Above the roughening transition all details of the interaction are combined into one single parameter, the roughening temperature T_R. Accordingly scaled graphs $E/k_B T_R$ vs. T/T_R coincide for $T/T_R > 1$.

The decrease in average energy of the system using long-ranged interaction coincides with a smaller number of broken bonds. The number of deviations from a facet or the step length is smaller compared to the system with interaction potential cutoff.

2.4.4 Defect Correlations

Restricting the surface height to $\{-a, 0, +a\}$, one may talk about a surface defect wherever the height deviates from the average height 0. If one analyzes the correla-

tion between these defects, it turns out that in the low temperature regime single holes or islands avoid being close to each other. This anticorrelation effect vanishes with increasing temperature and is much more pronounced for a system with an infinite-range interaction than for a system with a restricted interaction range.

The repulsion between defects cuts down the number of favorable configurations and thus strongly reduces the entropy contribution to the free energy for a given density of defects. From a simple argument one can see that the reduction of the entropy of a system by some factor $\alpha < 1$ gives rise to the increase the roughening temperature by a factor $1/\alpha$.

2.4.5
Line Energy vs. Step Interaction

In comparison to purely local models like the absolute solid-on-solid model or the discrete Gaussian solid-on-solid model, the line energy w_l of a step of length a can be considered as a kind of effective coupling constant J_{eff}. In purely local models the roughening temperature is proportional to the only energetic scale J, i.e., $k_B T_R \sim J$. Therefore the dependence of the quantity $k_B T_R/w_l$ on the ratio of line energy and elastic step interaction strength w_l/w_{el} can tell, whether long-ranged elastic effects are important, or whether the model corresponds effectively to a local model with a coupling constant $J_{\mathrm{eff}} \sim w_l$. The ratio w_l/w_{el} can be varied by changing $p_{\max}$.

Our simulations suggest an reciprocal dependence on w_l/w_{el},

$$(k_B T_R/w_l - 1.9) \sim 5.5 \left(\frac{w_l}{w_{el}}\right)^{-1}. \tag{9}$$

For large ratios w_l/w_{el} the influence of the step-step interaction can be neglected and $k_B T_R/w_l$ approaches the asymptotic value 1.9. If, however, w_l is smaller than the step interaction amplitude, the long-range character of the elastic interaction is important and results in a strong increase of $k_B T_R/w_l$. The crossover ratio between the two regimes lies somewhere near $w_l/w_{el} \approx 3$. A rough estimate of the ratio for certain step configurations on Si(111) and Si(001) yields $w_l/w_{el} \sim 2 \times 10^2$ and $w_l/w_{el} \sim 2$, respectively. This indicates that there probably are materials, for which the ratio w_l/w_{el} is small and the influence of long-range elastic effects cannot be ignored.

2.4.6
Crystal Growth

In order to investigate the kinetics of crystal growth a driving force $\Delta\mu$ has been added to the model recently. Preliminary results show that the growth rate of the height field depends linearily on $\Delta\mu$ above the roughening temperature. Below T_R the driving force needs to overcome a critical strength after which linear growth starts.

2.5 Conclusion

In summary, we have presented a model which contains the essential effects of long-range elastic repulsion between elastic defects on a crystal surface. We conclude that correlations due to these long-range interactions can strongly increase the roughening temperature in solid-on-solid models, mainly by a reduction of the entropy. Since defects prefer to exist in secluded areas, the number of favorable configurations and consequently the entropy contribution to the free energy is diminished, leading to an increase of the roughening temperature. A scaling law, Eq. (9), has been found describing the change of the roughening temperature depending on the ratio of local and long-range energetic scales. Our simulations suggest that the type of transition remains the same, although a rigorous proof lies beyond the scope of this type of Monte Carlo approach.

References

[1] J. M. Kosterlitz, D. J. Thouless, J. Phys. C 1973, 6(7), 1181-1203

[2] F. Gutheim, H. Müller-Krumbhaar, E. Brener, V. Kaganer, Phys. Rev. B 2003, 67, 195404

[3] J. Steinbrecher, H. Müller-Krumbhaar, E. Brener, C. Misbah, P. Peyla, Phys. Rev. E 1999, 45(7), 5600-5605

[4] F. Gutheim, H. Müller-Krumbhaar, E. Brener, Phys. Rev. E 2001, 63, 0410603

3
A Phase-Field Model for Crystallization into Multiple Grain Structures

Hamid Assadi

Abstract

Crystallization into multiple grain structures takes place through stages of nucleation, growth, grain impingement and grain coarsening. The present paper reports on an attempt to incorporate implicitly these four stages into a single model, in which the entire microstructure is described by one structural, and one orientational order parameter. In this model, the evolution of the structural order parameter is governed by an Allen-Cahn equation, whereas the orientational order parameter evolves through a Monte Carlo algorithm. The model is thus aimed to combine the merits of the standard phase-field and the so-called Potts methods. Based on this model, various scenarios of crystallization can be simulated for different combinations of nucleation and thermal conditions. Some of the simulation results are examined qualitatively with respect to the general features of multiple grain crystallization.

3.1
Introduction

The desire to predict and control microstructure formation during solidification has motivated numerous theoretical, computational and experimental research works on various aspects of solidification science, ranging from thermodynamic modeling and interface dynamics to advanced numerical analyses and simulation techniques [1]. There has been particularly much progress in simulating solidification microstructures by using phase-field method [2]. In this method, one or more phase-field variables are used to describe the corresponding liquid and solid phases. A phase-field variable is normally taken to represent the structural order, the chemical order or the local 'crystallographic' orientation of the corresponding phases, and is evolved through minimization of a free energy functional. The scope of application of the phase-field method has been expanding continually over the recent years, and has included problems as complex as the formation of multiple phase or grain structures [3], nucleation [4] and non-equilibrium solidification [5].

Nevertheless, there is still much room left for further work in simulating microstructure formation in various crystallization processes. A challenging example is nanocrystallization from undercooled liquids, where copious nucleation, multiple grain formation, growth and coarsening, and non-equilibrium effects have to be treated simultaneously, all within a robust and physically justifiable model. This paper addresses some of the issues in this area, and examines a hybrid model of crystallization with the above capability. The paper includes a brief assessment of the model, and a few examples of 2D simulations of multiple-grain crystallization.

3.2
Theoretical Background and Model Development

Formation of nanocrystalline microstructures from highly undercooled liquids is associated with extremely high nucleation rates, often orders of magnitudes larger than those predicted from the classical nucleation theory [6]. Diffuse interface models of nucleation provide an explanation for this nucleation behavior, in terms of the variation of the solid/liquid interfacial energy with temperature [7]. Figure 1 shows an example of such variations [8].

Based on these models, the phenomenon of copious nucleation, and the resulting nanocrystalline microstructure, can be attributed to the vanishing of the interfacial energy and hence the barrier to nucleation at a critical undercooling, ΔT_c. The decrease in the interfacial energy with increasing undercooling is a characteristic feature of the diffuse interface models. Thus, phase-field simulation of crystallization would be expected to illustrate appropriately copious nucleation and nanocrystallization. Nevertheless, formation of a nanocrystalline microstructure is not only influ-

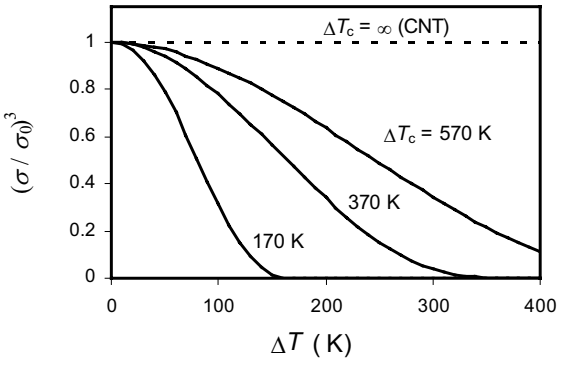

Fig. 1 Variation of the normalized interfacial energy (cubed) with undercooling, calculated based on a diffuse-interface model of nucleation [8]. The dashed line corresponds to the classical nucleation theory. According to non-classical theories of nucleation, the interfacial energy decreases with increasing undercooling and can vanish at a non-zero critical temperature.

enced by nucleation kinetics, but also by subsequent grain growth or coarsening. In order to simulate nanocrystallization, therefore, a model should also be able to treat appropriately the problem of grain growth or coarsening.

Simulation of grain growth has, on the other hand, been the subject of numerous studies. The work started when the idea of Potts model, originally developed to model the evolution of magnetic domain structures, was applied to grain growth in polycrystals [9]. In Potts model, the microstructure is described by a single parameter, indicating the local crystallographic orientation. This parameter evolves through a Monte Carlo algorithm, so as to reduce the number of nearest neighbor pairs of unlike crystallographic orientation. Simulation of grain growth was subsequently tackled by using various phase-field models. Examples include modeling by multiple order parameter phase field. In this method, a finite number of orientations are represented by unique combinations of the same number of order parameters [10]. Multiple order parameter models are robust and are in perfect agreement with Potts method [11]. Nevertheless, in these approaches, the free energy density depends on the orientation of the grains as measured in a fixed frame. Although this assumption secures a finite thickness for the grain boundaries, it has little physical justification. More recently, Kobayashi *et al.* [12] introduced a frame-invariant phase-field model, in which a single order parameter represents crystallographic orientation. In contrast to multiple order parameter models, the local energy density in the latter model is not a function of orientation. The frame-invariant approach is thus based on a more solid physical justification. However, earlier versions of this model [13] ran into the problem of being unstable with respect to a completely diffuse grain boundary. This problem was solved in the later versions of frame-invariant approach [12], ensuring grain boundaries with a finite thickness (Fig. 2).

As shown in Fig. 3, the solution for θ is a step function at the middle of grain boundary, where ϕ is minimal. This solution has clear physical justifications. Nevertheless, it can be shown that, at least for a certain combination of parameters, the model may diverge from the above solution and result in a non-physical solution. This can be examined by calculating the free energy of the system as a function of the non-equilibrium thickness of the 'orientational boundary', as represented by the

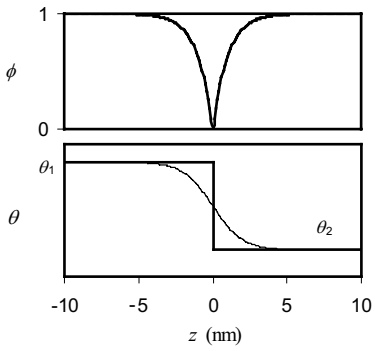

Fig. 2 Profiles of the structural and orientational order parameters, ϕ and θ, across a grain boundary. Solid curves correspond to a typical equilibrium solution for the frame-invariant model of Kobayashi *et al.* [12], showing a discontinuity of orientation profile at the grain boundary. The thin curve shows a hypothetical orientation profile with a finite gradient at the boundary, corresponding to an arbitrary non-equilibrium condition.

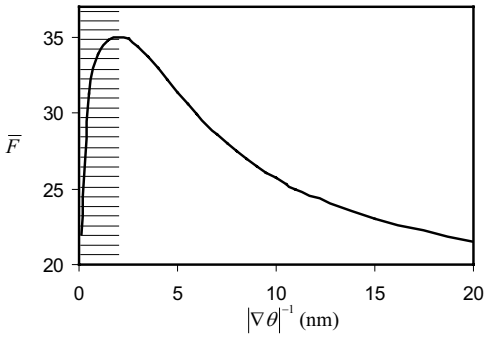

Fig. 3 Variation of the total grain boundary energy with the inverse of orientation gradient at the boundary, calculated for a fixed structural order parameter profile, such as that shown in Fig. 2. The hatch indicates the region where the energy is minimized through an increase of the orientation gradient up to its equilibrium value. For initial gradients lying outside this region, minimization of energy would result in a non-physical decrease of the orientation gradient, and ultimately in a completely diffuse interface.

inverse of orientation gradient. Figure 3 shows the result of such an analysis. As shown in the figure, the energy increases with increasing the thickness up to a maximum point. For such a case, the phase-field equations would converge to the physical equilibrium solution, if and only if the initial orientational boundary thickness is below this maximum point – i. e., if it lies within the hatched region in Fig. 3.

It should be noted that the total free energy is a multi-variable function, as it depends also on the structural order profile, and hence the variation shown in Fig. 3 is only a simplified ‚cross section' of a rather complicated function. Nevertheless, this simple example is sufficient to demonstrate the possibility of obtaining a non-physical solution through frame-invariant formalism. It should also be noted that a largely diffuse grain boundary, even if physically conceivable, would be associated with complex stress fields and dislocation arrangements, neither of which have so far been incorporated into the frame-invariant models.

The present analysis makes use of the frame-invariant phase-field formalism, though with some modifications. The free energy functional employed in the present analysis has the following form:

$$F = \int \left[g(\phi, T) + \frac{1}{2}\varepsilon^2 |\nabla\phi|^2 + \frac{1}{2}\upsilon^2\phi^2 G(|\nabla\theta|) \right] dV, \tag{1}$$

where ε and υ are constants, G is an operator, and g is the local free energy density.

The energy density is assumed to be a forth-order polynomial function of ϕ, as follows:

$$g = 3\phi^2 \left[\Delta g \left(\frac{2}{3}\phi - 1 \right) + \Delta g_c (\phi - 1)^2 \right] \qquad 0 < \Delta T < \Delta T_c, \tag{2}$$

in which Δg and Δg_c are the volumetric free energy difference between solid and liquid at ΔT and ΔT_c, respectively. Outside the specified undercooling range, a slightly different form is used to ensure that the local extrema occur at $\phi = 0$ and 1. The operator G does not change the operand for small gradients, but – to ensure periodicity of the crystal orientation during numerical calculations – it replaces $\delta\theta$ by $\sin(\delta\theta)$ when the difference between orientations of two adjacent cells are large. The kinetic

equation for the evolution of structural order parameter and the heat equation have the standard differential form such as those used in [14].

As pointed out before, the orientational order parameter in the frame-invariant method may evolve into non-physical solutions – an artifact which has to be avoided during numerical simulations. This is particularly important when simulating nanocrystallization; in this process the variety of local initial conditions increases the chance of diverging from the physical solution. To treat this problem, a Monte Carlo algorithm, such as that employed in the Potts model, is used to calculate the evolution of the orientational order parameter. The procedure for the calculation of orientation is as follows. Initially, a new orientation – out of a finite number of orientations – is selected randomly for the designated cell. Then the orientation mismatch energy between this cell and its neighbors is calculated, based on the last term of Eq. (1). Then a probability number is calculated based on the difference between the old and the new mismatch energies as follows:

$$p = 1 - \exp\left(\frac{\Delta F}{kT} + \xi\right), \tag{3}$$

in which ξ represents the thermal noise – taken generally to be a function of temperature. In the next step, a random number, $0 < r < 1$, is generated and compared with p. Finally, the transition to the new orientation is allowed if $r < p$.

Several merits are sought by using a Monte Carlo algorithm for the evolution of orientational order parameter. Most significantly, this method would be suitable to handle discontinuities in the orientation profiles, such as that shown in Fig. 2. In this way, and due to the fact that the number of allowed orientations is finite, formation of non-physically diffuse orientational boundaries is prevented. Moreover, due to the probabilistic nature of the method, not only curvature driven grain coarsening, but also stochastic coarsening can be modeled. The latter is especially relevant for coarsening of grains in the nanometer range [15]. The coupling of Potts and phase-field on one hand eliminates the common limitations of both methods; e.g., problem with non-zero bulk driving force in Potts [16], and with curvature driven coarsening in frame-invariant phase field [12]. On the other hand, this coupling allows implicit modeling of nucleation behavior at high undercoolings – an important feature not offered by Potts.

3.3 Simulations

Numerical simulations were performed in two dimensions of a model system with general properties as shown in Table 1. A 250×250 mesh with 1 nm cell size was used. Different sets of kinetic and interfacial parameters were used for each case of simulation. To control additionally the kinetics of orientation evolution, the number of Monte Carlo steps within each time step of heat transfer and phase-field calculations was varied accordingly.

Tab. 1. General properties of the model system used for simulations.

Parameter	*Unit*	*Value*
Liquidus Temperature	K	1000
Latent Heat	J m^{-3}	10^9
Hypercooling Limit	K	500
Critical Undercooling	K	400
Molecular Volume	m^3 mol^{-1}	10^{-5}

3.3.1
Temperature Dependence of Interfacial Energy

As discussed earlier, not only the absolute value of the solute/liquid interfacial energy, but also its variation with temperature is central to modeling of the nucleation behavior in an undercooled system. In order to examine the model in this respect, interfacial energy in an undercooled liquid was estimated based on the concept of free-growth model of Greer *et al.* [17]. Initially, simulations were carried out of crystal growth from foreign particles. The particles had various sizes, were not allowed to melt and were completely wetted by the solid phase – no boundary formed between solid and particles. The solid/liquid interface was assumed to be isotropic. The simulations showed that growth started initially from all of the particles, but continued only on particles whose diameter were twice as large as the corresponding critical radius at the given undercooling. The critical radius, and hence the interfacial energy could in this way be estimated for a range of undercoolings. Figure 4 shows the resulted variation, indicating a general consistence with non-classical models of nucleation (Fig. 1).

3.3.2
Crystallization by Inoculation

In order to examine the model with respect to general features of multiple-grain structure formation, solidification was simulated in an 'inoculated' system. This system was subject to continuous cooling from the melting temperature. The snapshots of the corresponding microstructure are shown in Fig. 5. The cooling curves asso-

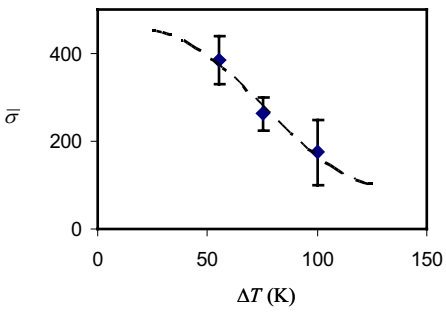

Fig. 4 The effective solid/liquid interfacial energy (normalized) as a function of undercooling, as obtained from free-growth simulations. The dashed line is a guide for the eye. In consistence with non-classical models of nucleation, the interfacial energy decreases with increasing undercooling, and vanishes at a certain critical undercooling (Fig. 1). Nevertheless, the drop in the interfacial energy occurs well above the critical undercooling of 400 K. Such a variation represents nucleation behavior in systems exhibiting copious nucleation.

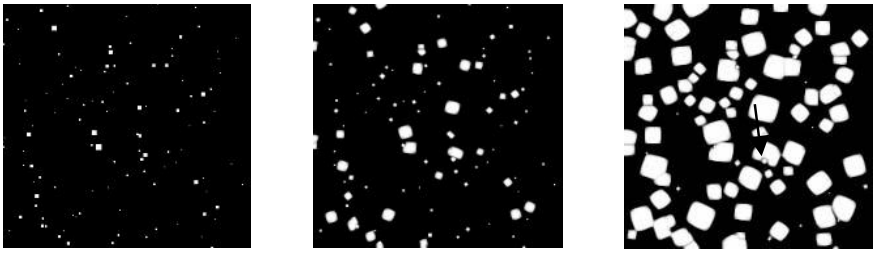

Fig. 5 Simulation of crystal growth from randomly distributed seeds in a continuously cooled melt. The figure shows the initial condition (left) and the structural order parameter before (middle) and after (right) recalescence, i. e. the minimum in the corresponding cooling curve. The seeds have various crystal orientations. A high anisotropy value of 0.05 is assumed, to show non-axisymmetric growth. Some of the seeds are entrapped within the neighboring grains (arrow); despite having reached the undercooling necessary for free growth.

ciated with this simulation showed a characteristic recalescence followed by a plateau region – though this is not shown here. A relatively large anisotropy factor of 0.05 was used to show non-symmetrical growth.

As argued in Greer's model [17] a fraction of particles – which are too small to allow free growth – do not take part in crystallization. This feature is clearly shown by the current simulations. The results also show remelting of some of the grains, leading to sporadic entrapment of larger – 'theoretically potent' – particles during recalescence. This latter feature, also indicated in Fig. 6, could be a source of a discre-

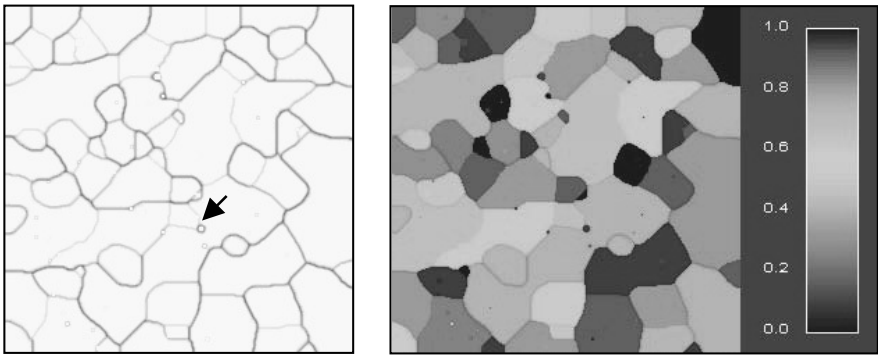

Fig. 6 Simulated grain structure of the fully crystallized system shown in Fig. 5. The left figure shows a map of the structural order parameter, and the right figure indicates the corresponding map of orientation. The darker boundaries in the left figure correspond to grains with larger relative misorientation. The orientation parameter is constant throughout the grains, while it changes abruptly at the grain boundaries. Some of the larger particles (arrow) are also entrapped because of a large misorientation with the entrapping grain.

pancy between the experimental observations and the predictions of the free-growth model at high fractions of grain refiners.

The most important point concerning these simulations is that they do not give an indication of a non-physically diffuse grain boundary. In fact, the orientational order parameter is uniform throughout the grains and discontinues only at the grain boundaries. As shown in the phase-field simulations by Gránásy *et al.* [18] foreign particles with a fixed orientation can, in certain cases of crystallization, disorient a growing solid by forming 'low angle' boundaries which 'radiate' from the pinning particles. This is a feature which can also be observed in the current simulations. Nevertheless, the boundaries thus formed were always found to be sharp.

The model could also show coarsening of grains. It reproduced the power law kinetics $[R^m(t) - R^m(0) = Bt]$ with the growth exponent, m, value of approximately 2.6.

3.3.3
Crystallization by Homogeneous Nucleation

Figure 7 shows three cases of simulations, where crystallization occurs at very high undercoolings without inoculation. To observe 'homogeneous nucleation' within a reasonable calculation time, the system is cooled down to, and slightly below, its critical temperature. Figure 7(a) shows the result of simulations when the model does not include the orientational order parameter. In this case, the initial thermal noise evolves into a high-amplitude order parameter fluctuation, and eventually into a uniform and boundary-free solid. By decreasing undercooling, the amplified fluctuations become scarcer, resembling isolated nucleation events. Such a behavior is also observed at the higher undercoolings regime when the orientational order parameter is taken into account – as shown in Fig. 7(b). Figure 7(c) shows an interesting microstructure, which was obtained at a certain combination of calculation parameters, incorporating low noise amplitude and low grain boundary energy. This feature could nevertheless not be explained. Overall, these results show that (i) crystallization near or beyond the critical conditions can be associated with the formation of isolated nucleation events, as opposed to spontaneous coarsening of 'atom-sized' grains, and (ii) this nucleation behavior would become more prominent when an extra energy contribution concerning the gradient of orientational order parameter is included in the phase-field formalism.

In summary, the present work examines briefly a modified phase-field model as an alternative method for modeling crystallization into multiple grain structures, especially at high undercoolings. The preliminary results encourage further explorations of the model.

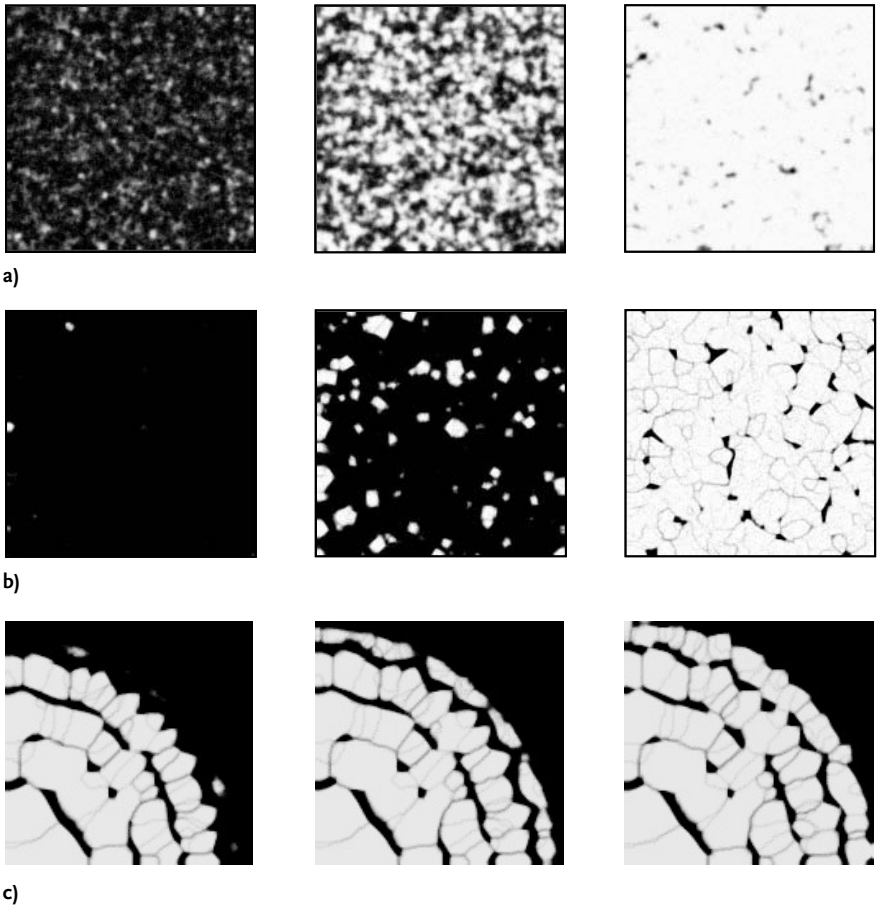

Fig. 7 Simulation of homogeneous nucleation beyond the critical undercooling in the model system. In cases (a) and (b), a global noise term is incorporated into the phase field equations, and in case (c) crystallization starts from a seed placed at the bottom-left corner. In the first case (a) the orientational parameter is uniform and constant throughout the calculations, whereas in the other two cases orientation is non-uniform and evolves with time. In case (a), crystallization starts and continues through amplification of the structural order parameter fluctuations, resulting into a uniform structure with no grain boundaries. In case (b) crystallization starts with isolated nucleation events and continues with growth, impingement and coarsening of solid grains. In case (c) nucleation occurs ahead of crystallization front, which also results in a multiple grain structure.

References

[1] W.J. Boettinger, S.R. Coriell, A.L. Greer, A. Karma, W. Kurz, M. Rappaz, R. Trivedi, *Acta Mater.* 48, 2000, 43.

[2] W.J. Boettinger, J.A. Warren, C. Beckermann, A. Karma, *Annu. Rev. Mater. Res.* 32, 2002, 163.

[3] F. Danan, L.-Q. Chen, *Acta Mater.* 45, 1997, 3297.

[4] L. Gránásy, T. Börzsönyi, T. Pusztai, *J. Crystal Growth* 237–239, 2002, 1813.

[5] S.G. Kim, W.T. Kim, *Mater. Sci. Eng. A* 304-306, 2001, 281.

[6] J. Schroers, R. Busch, A. Masuhr, W.L. Johnson, *Appl. Phys. Lett.* 74, 1999, 2806.

[7] L. Gránásy, F. Igloi, *J. Chem. Phys.* 107, 1997, 3634.

[8] H. Assadi, J. Schroers, *Acta Mater.* 50, 2002, 89.

[9] E.A. Holm, C.C. Battaile, *JOM* 53, 2001, 20.

[10] L.-Q. Chen, W. Yang, *Phys. Rev. B* 50, 1994, 15752.

[11] V. Tikare, E.A. Holm, D. Fan, L.-Q. Chen, *Acta Mater.* 47, 1999, 363.

[12] R. Kobayashi, J.A. Warren, W.C. Carter, *Physica D* 140, 2000, 141.

[13] J.A. Warren, W.C. Carter, R. Kobayashi, *Physica A* 261, 1998, 159.

[14] A.A. Wheeler, B.T. Murray, R.J. Schaefer, *Physica D* 66, 1993, 243.

[15] L. Helfen, D.T. Wu, R. Birringer, C.E. Krill, *Acta Mater.* 51, 2003, 2743.

[16] A.D. Rollett, D. Raabe, *Computational Mater. Sci.* 21, 2001, 69.

[17] A.L. Greer, A.M. Bunn, A. Tronche, P.V. Evans, D.J. Bristow, *Acta Mater.* 48, 2000, 2823.

[18] L. Gránásy, T. Pusztai, J.A. Warren, J.F. Douglas, T. Börzsönyi, V. Ferreiro, *Nature Mater.* 2, 2003, 92.

4
Scaling Relations for Dendritic Solidification in Binary Alloys

Heike Emmerich, Matthias Jurgk, Ricardo Siquieri

4.1
Introduction

Since the late eighty's great progress has been made on the question of what determines the structure of dendritic crystals [1]. The primary interest in this question is twofold: For one thing crystal growth has always been viewed as a paradigm problem of diffusion limited growth in general. In this sense it can be seen as a great success of theory that the precise selection mechanism of dendritic growth was solved [2] even though proven to be beyond all orders of perturbation theory. This result can be summarized best by means of universal scaling relations for the growth velocity of the dendritic tip depending on surface-tension anisotropy, kinetic anisotropy and strength of the undercooling [3].

Scaling relations are the link to the second interest in crystal growth, namely the goal to improve application oriented solidification simulations, as well. As in the more recent analyzes of other multiphase systems, in this context solidification is starting to be modeled using rigorously derived continuum equations [7]. In this regard, the incorporation of proper constitutive relations describing the interface topology and the phase interaction on a microscopic scale continues to be the main challenge. A unified model providing a framework for such an incorporation was developed by Wang and Beckermann recently based on a multiphase approach and volume averaging [8]. Within their approach the key ingredient to enter the dynamics at the micro-scale into the macroscopic continuum equations are exchange terms which account for the transfer of mass, momentum, energy and solute across the dendritic interface. Since the momentum exchange term is a function of the dendritic tip velocity, the model depends on a scaling relation for this velocity as discussed above. This also implies that the accuracy of the unified model is limited by the accuracy of this scaling relation. Thus precise scaling relations fit to the respective applied crystal growth conditions are indispensable for quantitative predictions of solidification.

With respect to the latter the severe shortcoming of all scaling relations obtained so far is that they apply to isolated crystals only. In this contribution we derive for the first time a scaling relation which accounts for the interaction of dendritic crys-

tals in the melt. Following the above argumentation, on the one hand it can be applied to improve the accuracy of the unified model. On the other hand it yields additional insight in the universality of diffusion limited crystal growth in the presence of competing micro-structures.

Our derivation of the scaling relation is based on a two-scale model for alloy solidification, which is a specification of [4] based on a linearization of the underlying phase diagram. We will present our formulation of the model equations in the following section. We will then summarize our analysis resulting in our novel scaling relation itself (section 3). Finally, we compare this new result to numerical simulations and give an outlook on its applicability.

4.2 Two-scale Modeling for Binary Alloys

The solidification process of an alloy is controlled by the diffusion of two properties, heat and solute. Heat-diffusion is usually much faster than the diffusion of solute. This motivates the introduction of two different length scales, i.e. a microscopic scale for the transport of solute and a macroscopic scale for the transport of heat. In this picture the growth of the crystalline interface separating solid and liquid phase takes place on the micro-scale.

Separation of the microscopic and the macroscopic transport scale can be achieved by means of an asymptotic expansion (see [4] for the general procedure), which allows us to derive a homogenized two-scale model. The homogenization procedure maps the full alloy solidification problem, which consists of transport of heat and solute coupled to the growth of all the crystals in a characteristic domain of the alloy (see Fig. 1 left) onto a homogenized heat equation coupled to a representative micro-cell growth problem (see Fig. 1 right)[1]. The numerical gain of this approach is tied to the possibility to solve the homogenized temperature equation on a grid considerably coarser than for the non-homogenized transport equations. The price to pay is the coupling to a representative micro-cell problem at each point of the coarser grid.

The full two scale model obtained via the expansion procedure is given by the homogenized heat equation

$$\partial_t \left(T - \varepsilon_s \frac{L}{c_v} \right) - D_T \Delta T = 0 \tag{1}$$

with boundary condition

$$\partial_n T = Bi\,(T_a - T_I) \tag{2}$$

1) Within the formulation of the original problem (left) μ refers to the chemical potential, L to the latent heat, K to the heat conductivity and $b(T,\mu)$ specifies the relation between μ and T according to the underlying phase diagram. The model equations to the right are explained further in the text.

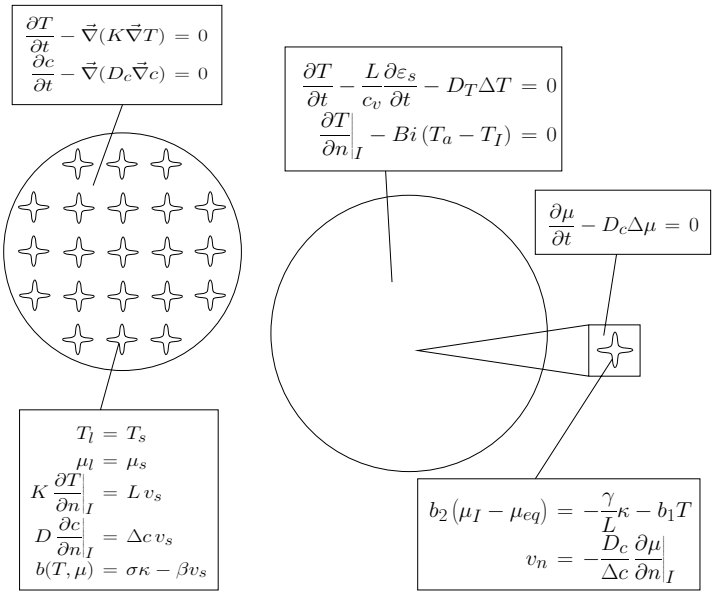

Fig. 1 Left: The original problem posed by alloy solidification in a characteristic domain of a sample. Right: The homogenized two-scale model.

together with the micro-cell problem

$$\partial_t \mu - D_c\,\Delta\mu \;= 0 \tag{3}$$

$$b_2\,(\mu_I - \mu_{\text{eq}}) = -\frac{\gamma}{L}\kappa - b_1 T \tag{4}$$

$$-D_c \partial_n \mu|_I \quad = \Delta c \cdot v_n\,. \tag{5}$$

Here we have introduced the notation ∂_t for $\frac{\partial}{\partial t}$ and ∂_n for $\frac{\partial}{\partial n}$. Within the homogenized heat equation Trefers to the macroscopic temperature field with homogenized diffusion constant D_T, Bi to the Biot number. The term $\partial_t \varepsilon_s \cdot L/c_v$ expresses the local temperature change due to the release of latent heat, which results from the microscopic solidification process. L itself denotes the latent heat per mass unit and c_v the heat capacity for constant volume. ε_s summarizes the solid volume fraction, which is the fraction of solid phase in the total volume. Moreover $T_a - T_I$ refers to the difference of domain wall temperature and external temperature. In the micro-cell problem, the governing field is now the chemical potential. The relation between μ and the concentration field c is given by $\mu_k(c_k) = c_k + \delta_{kj}\Delta c$ ($k,j =$: liquid, solid), with constant miscibility gap Δc. $b(\mu,T)$ has been specified for the part of a phase diagram, where we can approximate the phase-equilibrium curve as linear line, i.e. $b(T,\mu) = b_1 T + b_2\,\mu$. Here $b_2 = T_m/m_l$, where m_l denotes the slope of the liquidus line. b_1 is fixed by the initial conditions. γ refers to the anisotropic surface tension of the solid-

liquid interface and κ to the interface curvature. We assume a fourfold crystalline anisotropy, which applies to *fcc*-crystals. Equation (4) is known as the Gibbs-Thomson relation expressing local thermodynamic equilibrium at the interface. Equation (5) is called the Stefan condition. It summarizes mass and energy conservation. In (5) $\partial_n \mu|_I$ denotes the gradient of the solutal field normal to the interface in direction of the liquid phase. v_n yields the growth velocity in this direction.

4.3 A Novel Scaling Relation Taking into Account Crystal Density

To maintain an equilibrium of surface and volume energy, homogenization theory requires a rescaling of surface tension and diffusion constants. This implies that $\gamma = \varepsilon\sigma$ and $D_T = \varepsilon^2 K$. Moreover curvature scales as $\kappa = \varepsilon^{-1}\kappa_0$, where the subscript 0 refers to the curvature in the original (non-homogenized) problem and ε to the scale of the micro-structure.

The coupling between homogenized heat equation and micro-cell problem runs in both directions: The homogenized temperature T enters the micro-cell problem via the term $b_1 T$ in (4). On the other hand, the growth of the micro-structure as given by the micro-cell problem enters (1) via the solid fraction ε_s.

Equations (1)–(5) are the basis for our analysis employing the Kruskal-Segur reduction [9]. This analysis is simplified if we transform (1)–(5) to dimensionless equations:

$$\partial_t T' = D_T \Delta T' - \partial_t \varepsilon_s \tag{6}$$

$$\partial_t u = D_c \Delta u \tag{7}$$

$$\partial_t u_I = \Delta_c - d_0^c \kappa - \frac{b_1}{b_2}\frac{L}{c_p}\frac{T'}{\Delta c} \tag{8}$$

$$v_n = -D_c \partial_n u\,. \tag{9}$$

Here T' refers to the dimensionless temperature, u to the dimensionless chemical potential, Δ_c to the dimensionless supersaturation and d_0^c to the chemical capillarity length. Equation (6) is an inhomogeneous heat equation for which we can find a solution based on the Greens function formalism. If we insert this formal solution into (8), the problem, which remains to be solved with respect to a scaling relation for the dendritic tip velocity, is given by (7) and (9) together with the following Gibbs-Thompson relation:

$$\partial_t u_I = \Delta_c - d_0^c \kappa - \frac{1}{4\pi D_T}\frac{b_1}{b_2}\frac{L}{c_p}\frac{\partial_t \varepsilon_s}{\Delta c}\cdot N\,. \tag{10}$$

Here N refers to the number of crystal nuclei in the reference domain. Following [8] we set $\partial_t \varepsilon_s = \frac{2}{\lambda_2}\cdot v_n$, where λ_2 is the spacing of secondary dendritic arms. Inserting

this expression in (10) we obtain a Gibbs-Thompson relation, which final term turns out to be of kinetic origin. The respective kinetic coefficient is given by $\beta = \tilde{b}_1 N / 2\pi D_T \lambda_2$, with $\tilde{b}_1 = b_1 L m_l / (T_m c_p \Delta c)$. If we assume the anisotropy of this kinetic effect as well as the anisotropy of surface tension to be small, then the framework to treat this kind of selection problem has been established in successive contributions starting from [11]. A review can be found in [3]. For brevity here we will only report the result of this analysis, which leads to the following expression for the selected tip velocity v_n:

$$v_n = \frac{p_c\,(1 - 2^{-1/2})}{\tilde{\lambda}_0 \beta}\,, \tag{11}$$

where $\tilde{\lambda}_0$ is a constant to be evaluated based on (9.6) of reference [3] and p_c the peclet number of the governing field. Thus in the limit $\Delta_c \to 0$ $v_n \sim \frac{4\Delta_c^2}{N} \frac{1}{\Delta_T Bi}$. The most important new feature of these relations is their dependence on the number of nuclei in a reference domain, i.e. on crystal density. The following section is devoted to a numerical investigation of this new dependence.

4.4 Numerical Investigations of the Two-scale Model

For our numerical investigation of the two-scale model we solve the diffusion problem given by the homogenized temperature (1) on the points of a coarse Euclidean grid, whereas the diffusion problem for the chemical potential driving the growth process is solved independently on a much finer grid. On both grids we employ a first order finite difference scheme. For the micro-scale problem simulations are averaged over four grids rotated with respect to each other to average out numerical anisotropy. Moreover, the crystalline interface is discretized independently as polygon train, where the Stefan condition is solved according to the *method of the steepest ascent* [6].

To investigate our new scaling relation we carried out parameter studies varying undercooling, crystalline anisotropy, crystal density and the Biot number *Bi*. Here we restrict our focus to the crystal density-dependence in the limit of small driving forces, for which an inverse proportionality is predicted by (11). Our numerical results for the respective parameter studies are presented in Fig. 2 by the squared dots. They display the same linear behavior for ρ^{-1}, where ρ refers to the crystal density in the reference domain, as predicted by theory. The interesting feature of our numerical result is that we can identify two different solution branches. In the transition region $\rho^{-1} \in [0.001; 0.00125]$, metastable solutions exist. The morphology of the crystals belonging to the lower branch deviates from the one of the crystals belonging to the upper branch in that it displays considerably larger tip radii. Qualitatively we can understand the origin of the two different solution branches as follows: For the solutions on the upper branch, the transport of latent heat away from the growing crystal can still be accomplished. Thus all the whole reference domain temperature remains

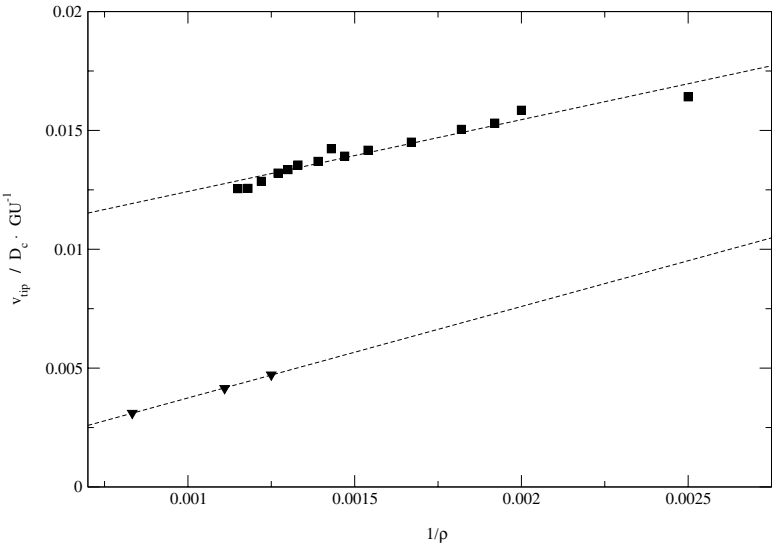

Fig. 2 The $1/\rho$-dependence of the tip velocity as obtained from simulations of the two-scale model. The dotted lines indicate the two qualitatively different solution branches we were able to identify numerically.

small and as a consequence the kinetic term in the Gibbs-Thompson relation of the micro-cell problem, as well. For the lower branch, on the other hand, the term $\partial_t \varepsilon$ dominates the homogenized heat equation. As a consequence, a sudden increase of the macroscopic temperature is encountered, which in turn slows down the crystals via an increased kinetic term in (10). This transition is similar to the transition, which a hydrodynamic field encounters in a region of increasing solid fraction, namely the transition from free flow to Darcy type flow. We will report a more detailed study of the nature of the transition within the metastable regime and point out its impact on ultrasound treatment of solidifying samples in a forthcoming article.

Summary

Here we have demonstrated that the competition of crystals via a macroscopic transport field does not destroy the universality of diffusion limited crystal growth. We expect our new scaling relation to have impact for application oriented solidification simulations employing a multi-scale approach based on volume averaging as e.g. in [8]. In this context this relation, which is fit better to the array-type alignment in a real solidifying sample, should allow for more quantitative exchange terms. We will demonstrate this by simulations of recalescence phenomena in [12].

References

[1] For an early review, see J.S. Langer, in *Chance and Matter*, ed. by J. Souletie (North-Holland, Amsterdam, 1987)

[2] E. Brener, V.I. Melnikov, JETP 1995, 80, 341

[3] For a review see E.A. Brener, V.I. Melnikov, Adv. Phys. 1991, 40, 53

[4] C. Eck, P. Knabner, S. Korotov, J. Comp. Phys. 2002, 178, 58

[5] T. Ihle, H. Müller-Krumbhaar, Phys. Rev. Lett. 1993, 70, 3083

[6] T. Ihle, H. Müller-Krumbhaar, Phys. Rev. E 1994, 49, 2972

[7] C. Beckermann, R. Viskanta, Appl. Mechanics Review 1993, 46, 1

[8] C.Y. Wang, C. Beckermann, Metall. Mater. Trans. A 1994, 25A, 1081

[9] M. Kruskal, H. Segur, Physica 1987, 28D, 228

[10] T.Z. Kattamis, J.C. Coughlin, M.C. Flemings, Tarns. TMS-AIME 1967, 239, 1504-1511

[11] R. Brower, D. Kessler, J. Koplik, H. Levine, Phys. Rev. Lett. 1983, 51, 1111

[12] H. Emmerich, M. Jurgk, in preparation

5
Modeling the Spatial Phase Separation Process in Hypermonotectic Alloys

M. Wu, A. Ludwig, L. Ratke

Abstract

A two-phase model is established to simulate the decomposition, macroscopic spatial phase separation due to sedimentation and Marangoni motion, and monotectic reaction in hypermonotectic alloys. Simulations of a 2D square casting with composition (Al-10wt.%Bi) under normal terrestrial and weightless conditions are made. The results for the weightless condition are found to agree qualitatively remarkably well with experiments performed by Walter in sounding rocket experiments using Al-Bi alloys. The results for the normal terrestrial condition agree to a certain extent with experiment performed by Alkemper and Ratke in chill cast Al-Bi alloys. Understanding to the spatial phase separation phenomena in the hypermonotectic alloys is achieved.

5.1
Introduction

Alloys with a miscibility gap in liquid state, especially for those with gross composition beyond the monotectic point (hypermonotectic), are potential bearing materials for automotive industry [1]. A coarse spatial separation of the minority phase from the parent melt seems unavoidable no matter whether the alloy solidifies under normal terrestrial condition [2] or under reduced gravity situation [3–4]. Two mechanisms are responsible for this phenomenon: the gravity induced sedimentation and the Marangoni (thermocapillary) motion. In order to model the phase separation phenomenon, a two phase volume-averaging model, based on the Beckermann's [5–11] and Ludwig's [12–14] previous works on equiaxed solidification, is developed. The ideal spherical morphology of the decomposed second phase droplets permits describing more precisely the growth kinetics of the droplets, their hydrodynamic behavior (drag force), etc. This paper highlights the decomposition of the secondary phase from the parent phase and the spatial phase separation process under normal and under reduced gravity situations.

5.2
Numerical Model

5.2.1
Phase Definition

As shown in Figure 1, at least 4 phases appear in hypermonotectic solidification: the parent melt ($L = L_1$), the secondary liquid phase (L_2), the solidified monotectic matrix (as one phase) and the solidified secondary phase. For simplicity this model considers only two phases: the first liquid phase L_1 and the second liquid phase L_2. During monotectic reaction the monotectic matrix is transformed directly from L_1. Therefore the solidified monotectic matrix is modeled as L_1 phase in such a way that an enlarged viscosity is applied to the L_1 phase on reaching the monotectic temperature. The latent heat of the monotectic reaction is added to L_1 phase. L_2 droplets appearing at the monotectic reaction front are modeled to be entrapped in the monotectic matrix by applying a similar enlarged viscosity at or below the monotectic point. In addition to the above phase definition, following assumptions are made:

(1) Gravity induced sedimentation is modeled with Boussinesq approach;
(2) Both liquid phases have same viscosity;
(3) Eutectic reaction of L_2 is ignored;
(4) No collision and coalescence (coagulation) of droplets;
(5) Diffusion in a single droplet is infinitive, and between droplets is ignored.

5.2.2
Conservation equations

The conservation equations for a two-phase globular equiaxed solidification system have been described previously [12–14]. Modifications are made for hypermonotectic solidification.

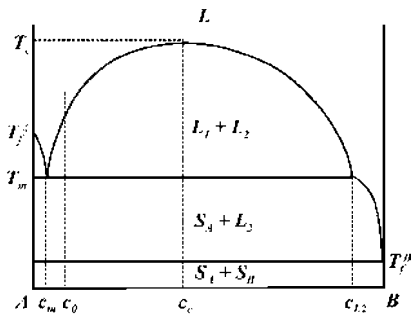

Fig. 1 Schematic phase diagram for systems with a liquid miscibility gap

Mass conservation:

$$\begin{aligned}\frac{\partial}{\partial t}\left(f_1\rho_1\right)+\nabla\cdot\left(f_1\rho_1\vec{u}_1\right)&=M_{21}\\ \frac{\partial}{\partial t}\left(f_2\rho_2\right)+\nabla\cdot\left(f_2\rho_2\vec{u}_2\right)&=M_{12}\end{aligned}\tag{1}$$

Momentum conservation:

$$\begin{aligned}\frac{\partial}{\partial t}\left(f_1\rho_1\vec{u}_1\right)+\nabla\cdot\left(f_1\rho_1\vec{u}_1\otimes\vec{u}_1\right)&=-f_1\nabla p+\nabla\cdot\bar{\bar{\tau}}_1+f_1\rho_1\vec{g}+\vec{U}_{21}-\vec{F}_M\\ \frac{\partial}{\partial t}\left(f_2\rho_2\vec{u}_2\right)+\nabla\cdot\left(f_2\rho_2\vec{u}_2\otimes\vec{u}_2\right)&=-f_2\nabla p+\nabla\cdot\bar{\bar{\tau}}_2+f_2\rho_2\vec{g}+\vec{U}_{12}-\vec{F}_M\end{aligned}\tag{2}$$

where $\bar{\bar{\tau}}_1=\mu_1 f_1\left(\nabla\cdot\vec{u}_1+\left(\nabla\cdot\vec{u}_1\right)^T\right)$ and $\bar{\bar{\tau}}_2=\mu_2 f_2\left(\nabla\cdot\vec{u}_2+\left(\nabla\cdot\vec{u}_2\right)^T\right)$

The subscripts 1 and 2 in above equations stand for L_1 and L_2 phases. Decomposition, i.e. nucleation and growth (or dissolution) as well as coarsening of the L_2 phase in the parent melt, is taken into account through a mass transfer term M_{12} ($=-M_{21}$). $\vec{F}_M$ is the volume averaged Marangoni force on the L_2 droplets. The enthalpy and species conservation equations are described in literature [12–14].

5.2.3 Droplet Growth and Mass Transfer

A 3-parameter law by Rappaz [12, 15] is employed to model the nucleation of the L_2 droplets. The droplets grow or dissolve by diffusion (Figure 2). The diffusion-controlled growth of a precipitate in a supersaturated matrix was described by Zener [1, 16–17].

$$\frac{dR}{dt}=\frac{D_1}{d_2}\cdot\frac{\Delta c}{\Delta c_d}\tag{3}$$

The radius growth rate dR/dt of a droplet is governed by the difference between the far field concentration c_1 and the interface concentration c_1^* of L_1 phase, i.e. $\Delta c=c_1-c_1^*$. The solute partitioning at the L_1/L_2 interface is $\Delta c_d=c_2^*-c_1^*\approx c_2-c_1^*$, where c_2 is the L_2 phase concentration. D_1 is the diffusion coefficient and d_2 is the droplet diameter. When the droplet density n and an additional Avrami-factor f_1 (volume fraction of L_1 phase) are considered, the mass transfer rate M_{12} (kg/m^3/s) is expressed as:

$$M_{12}=n\cdot\pi d_2\cdot\rho_2\cdot\frac{D_1}{c_d}\cdot\Delta c\cdot f_1\tag{4}$$

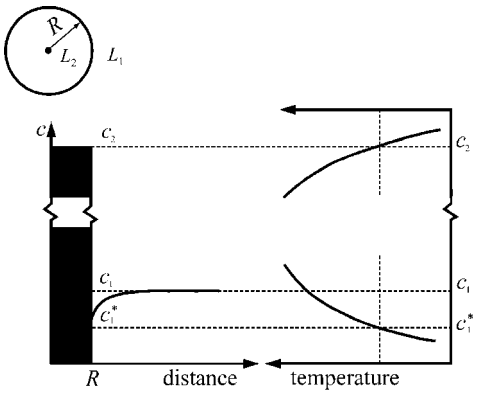

Fig. 2 Schematic of the concentration profile ahead of a growing droplet with respect to the binodal in the phase diagram.

5.2.4
Marangoni Force and Hydrodynamic Resistance

When a droplet is placed in a melt having a temperature gradient, a thermocapillary convection in/around the droplet is induced (Figure 3). The droplet surface is drawn from hotter towards the colder poles in order to lower the surface energy. The consequence is the motion of the droplet towards the hot region. This is called thermocapillary or Marangoni motion. Integration of the thermocapillary force acting on the droplet surface is defined as Marangoni force $\vec{f}_M$ (N). On a droplet having a relative velocity $\Delta\vec{u}$ with respect to the matrix, a hydrodynamic resistance or Stokes force $\vec{f}_{st}$ (N) exists. Based on Stokes-Rybczynski-Hadamard approximation, Young et al [18–20] have deduced $\vec{f}_M$ and $\vec{f}_{st}$ for single droplet.

$$\vec{f}_M = \frac{\pi d_2^2}{(1+\mu_2/\mu_1)\cdot(2+k_2/k_1)} \cdot \frac{\partial\sigma}{\partial T} \cdot \nabla T \tag{5}$$

$$\vec{f}_{st} = 2\pi d_2 \cdot \mu_1 \cdot \frac{1+3\mu_2/2\mu_1}{1+\mu_2/\mu_1} \cdot \Delta\vec{u} \tag{6}$$

Further considering the droplet density n and the relation $f_2 = n \cdot \pi d^3/6$, the volume averaged Marangoni force $\vec{F}_M$ (N/m^3) in Eq. (2) is expressed as:

$$\vec{F}_M = \frac{6}{(1+\mu_2/\mu_1)\cdot(2+k_2/k_1)} \cdot \frac{f_2}{d_2} \cdot \frac{\partial\sigma}{\partial T} \cdot \nabla T \tag{7}$$

An empirical relationship for the Marangoni coefficient $\partial\sigma/\partial T$ is recommended [1, 17, 21].

$$\frac{\partial\sigma}{\partial T} = -1.26 \cdot \sigma_0 \cdot \frac{1}{T_c} \cdot \left(1 - \frac{T}{T_c}\right)^{0.26} \tag{8}$$

where σ_0 is determined experimentally.

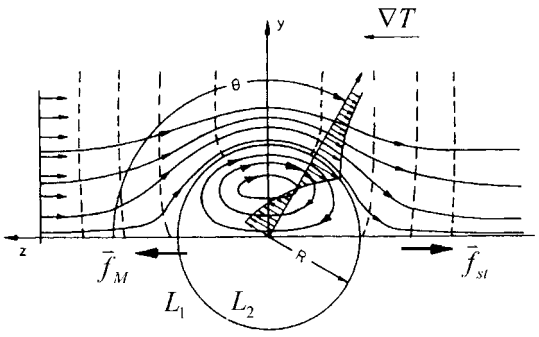

Fig. 3 Thermocapillary convection in and around the droplet.

Momentum exchange $\vec{U}_{12}$ (= $\vec{U}_{21}$) includes two parts: a part due to mass transfer $\vec{U}_{12}^{p}$ and a part due to Stokes force $\vec{U}_{12}^{d}$. Two situations are further considered for $\vec{U}_{12}^{p}$: decomposition (including growth and coarsening) and dissolution respectively. For decomposition, the momentum transferred from L_1 to L_2 is determined according to $\vec{u}_1$, i. e. $\vec{U}_{12}^{p} = \vec{u}_1 \cdot M_{12}$. By analogy we have $\vec{U}_{12}^{p} = \vec{u}_2 \cdot M_{12}$ for dissolution. The Stokes force is expressed as $\vec{U}_{12}^{d} = K_{12} \cdot \Delta\vec{u}$, where K_{12} can be deduced from Eq. (6).

$$K_{12} = \frac{1 + 3\mu_2/2\mu_1}{1 + \mu_2/\mu_1} \cdot \frac{12 f_2}{d_2^2} \cdot \mu_1 \tag{9}$$

Tab. 1 Notation of phase diagram information of Al-Bi system

Monotectic temperature	T_m	930 K	657 °C
Monotectic concentration	c_m	0.47 at. %	3.526 wt. %
L_2 monotectic concentration	c_{L2}	83.4 at. %	97.493 wt. %
Critical temperature	T_c	1310 K	1037 °C
Melting point of Al	T_f^A	933 K	660 °C
Melting point of Bi	T_f^B	543 K	270 °C
Gross concentration	c_0	1.415 at. %	10 wt. %
Slope of liquidus at c_0	m	148.1 K/at.%	20.42 °C/wt.%
Partitioning coefficient	k	51.72	9.55

5.3 Problem description

A 2D square casting (90 × 90 mm^2) with the composition Al-10wt.%Bi is simulated. The mold, remaining at a constant temperature of 290 K, is assumed to be filled instantaneously with melt of initial temperature 1065 K. The heat exchange coefficient at casting-mold interface is 750 W/(m^2.K). The nucleation parameters [15] for L_2 droplets are $n_{\max} = 10^{13}$ m^{-3}, $\Delta T_N = 20$ K, $\Delta T_\sigma = 8$ K. Other thermal physical properties and modeling parameters are listed in Table I-II.

Tab. 2 Thermophysical properties used for the simulation [17, 21–22]

ρ = 2340 kg/m	$c_{p(2)}$ = 124.8 J/kg/K	Δh_d = 10.775 kJ/kg
k_1 = 238 W/m/K	$\mu_1 \approx \mu_2 = 1.03 \cdot 10^{-3}$ Kg/m/s	Δh_M = 383 kJ/kg
k_2 = 15.5 W/m/K	$D_1 = 1.1 \cdot 10^{-8}$ m^2/s	σ_0 = 0.1427 J/m^2
$c_{p(1)}$ = 917 J/kg/K	D_2 = 0.0	

5.4 Results and Discussions

5.4.1 Without Gravity

As shown in Figure 4, phase separation, i.e. decomposition and growth with droplet motion is independent of gravity. Marangoni motion presents the only mechanism for the phase transport in the absence of gravity. Droplets of L_2 start to nucleate and grow in the casting surface as the local temperature drops below the binodal (1062.2 K). The Marangoni force causes the L_2 droplets to move from surface regions towards the casting center. The parent melt moves in reverse direction, because the space of the leaving phase L_2 must be replaced by the parent melt L_1. The movement of L_2 will definitely result in depletion of the L_2 phase (f_2) in the corners and surface regions, and enrichment of L_2 phase in the casting center. As the casting further cools down to the monotectic point, monotectic reaction occurs, the velocity of L_1

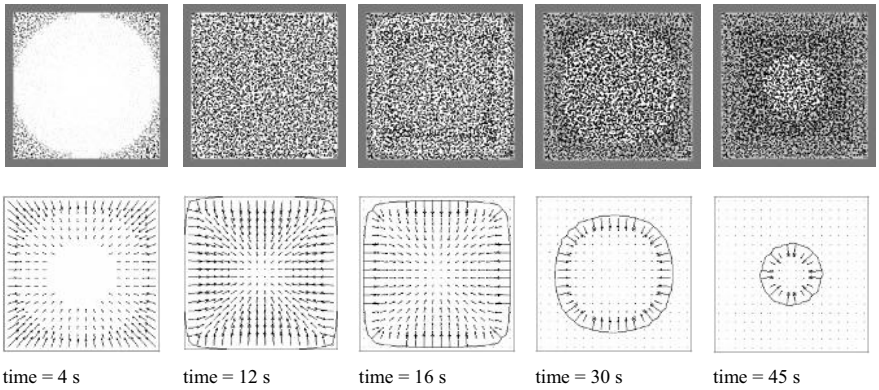

Fig. 4 Solidification sequence without gravity. Top raw: the Bi droplet distribution. The gray matrix means that the alloy has solidified, and the droplets are entrapped in the solid monotectic matrix. Both the droplet density and the diameter of the droplets, shown in this figure, are reduced and enlarged by corresponding factors so that the droplet distribution can be seen with the naked eye. Lower raw: the velocity fields of the second phase droplets together with the monotectic front (T = 925 K).

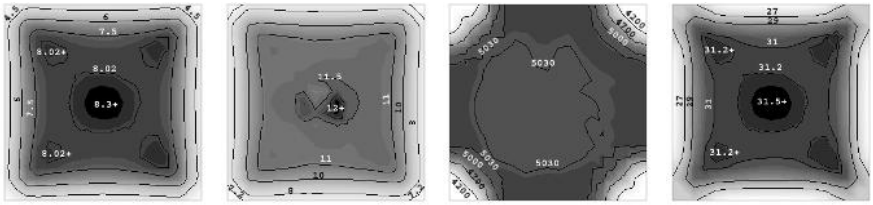

a) f_2 (%) b) c_{mix} (Bi in wt.%) c) n (mm^{-3}) d) d_2 (μm)

Fig. 5 Computer-predicted phase separation, macrosegregation and droplet distribution (without gravity). All quantities are shown with isolines together with 30 gray levels, with dark showing the highest value and bright the lowest.

vanishes and the L_2 droplets are entrapped in the monotectic matrix. When solidification is finished (Figure 5) the surface has a lower volume fraction of L_2 phase ($f_2 <$ 4.5%) and the center has higher volume fraction ($f_2 > 8.3\%$). The spatial separation of the phases is directly responsible for the macrosegregation: $c_{mix} < 7.2\%$Bi in corners, $c_{mix} > 12\%$Bi in center. Both Marangoni motion and diffusion controlled growth contribute to an uneven droplet size distribution. A tendency of finer droplets in the surface regions ($d_2 < 27$ μm) and relatively large droplets in the central region ($d_2 > 31.5$ μm) is predicted. Although the results of Figure 5 have not been experimentally evaluated, the numerically predicted tendency of phase separation agree qualitatively remarkably well with experiments performed by Walter in sounding rocket experiments using Al-Bi alloys [23]

5.4.2
With Gravity

As shown in Figure 6, the droplets of the L_2 phase starts to nucleate in the corners and along the walls, then grow and sink downwards along the vertical walls. As two liquid phases are coupled through the momentum exchange terms the parent melt L_1 phase is drawn by the sinking L_2 phase, forming two vortices: one clockwise in the right half and one anticlockwise in the left half of the casting. The convection currents of L_1 are so strong that they in turn influence the movement and the distribution of L_2 droplets. With the monotectic reaction the L_2 droplets are entrapped in the monotectic matrix, the phase and droplet size distribution remain unchanged afterwards. The final solidification results (Figure 7) show the depletion of L_2 phase in the upper region ($f_2 < 2\%$) and an enrichment of L_2 in the central bottom region ($f_2 > 22\%$ L_2). Strong spatial separation of the phases leads to a strong macrosegregation: $c_{\mathrm{mix}} < 5\%$Bi in the upper region, $c_{\mathrm{mix}} > 25\%$Bi in the lower bottom region. The droplet distribution pattern is the direct outcome of melt convection and droplet transport. A tendency of small droplets in upper region ($d_{\mathrm{s}} < 18$ μm) and large droplets in the lower bottom region ($d_{\mathrm{s}} > 45$ μm) is predicted. This predicted phase distribution agrees to a certain extent with experiment performed by Alkemper and Ratke in chill cast Al-Bi alloys under terrestrial conditions [24].

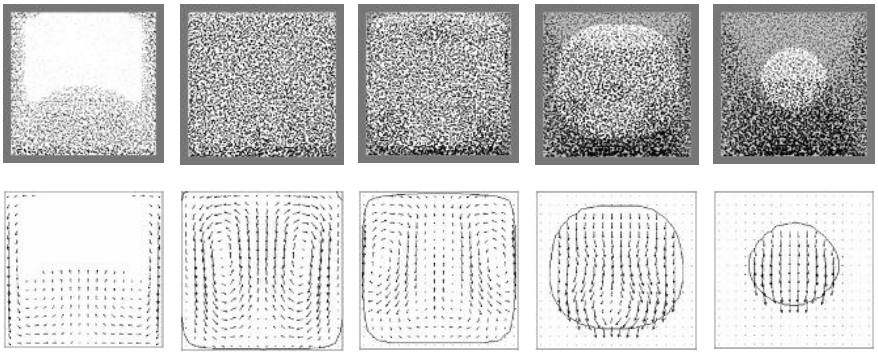

Fig. 6 Solidification sequence with gravity (g = 9.8 m/s^2). Top raw: the Bi droplet distribution. The grey ma trix means that the alloy has solidified, and the droplets are entr apped in the solid monotectic matrix. Both the droplet density and the diameter of the droplets, shown in this figure, are reduced and enlarged by corresponding factors so that the droplet distributi on can be seen with the naked eye. Lower raw: the velocity fields of t he second phase droplets together with the monotectic front (T = 92 5 K).

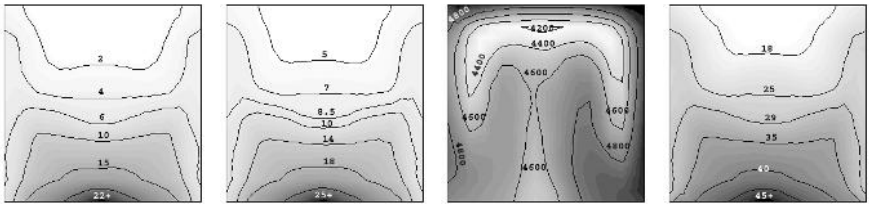

Fig. 7 Computer-predicted phase separation, macrosegregation and droplet distribution (g = 9.8 m/s^2). All quantities are shown with isolines together with 30 gray levels, with dark showing the highest value and bright the lowest.

The convection patterns with and without g are totally different. The convection and spatial separation of the two liquid phases with g (max $\vec{u}_2 \approx 81$ mm/s) is much stronger than that without g (max $\vec{u}_2 \approx 0.44$ mm/s). Although both Marangoni motion and gravity induced droplet motion are considered in the case with g, no influence of Marangoni motion on the solidification result is seen. The function of the gravity overwhelms the Marangoni force under normal terrestrial condition as often anticipated in the experimental literature without proof [1–2].

The recent model is established based on some modeling assumptions. For example, the nucleation parameters used in the above simulations were empirically given, and collision and coalescence (coagulation) of droplets are ignored, etc. In order to

evaluate the modeling results, further parameter studies or improvement on the model by releasing some modeling assumptions may be necessary.

5.5 Conclusions

The two phase model described in this paper is able to simulate the decomposition and the spatial phase separation during solidification of hypermonotectic alloys. Nucleation of the secondary phase droplets, droplet growth, Marangoni motion, gravity induced phase sedimentation, parent melt convection, macrosegregation, monotectic reaction, etc. are included. The simulation results demonstrated:

1) Marangoni force under weightless condition causes the L_2 droplets to move from casting boundary regions towards the casting center, and the parent melt L_1 to move in reverse direction, leading to depletion of L_2 phase in the boundary regions and enrichment of L_2 phase in the casting center.
2) Although both gravity induced sedimentation and Marangoni motion occur under normal terrestrial condition, the gravity induced sedimentation dominate the spatial phase separation process. The final results show depletion of L_2 phase in the top region and enrichment of L_2 phase in the middle bottom region.

Collision and coalescence (coagulation) of droplets are not considered in the recent model.

References

[1] L. Ratke, and S. Diefenbach, *Mater. Sci. Eng.*, **1995**, 15(R), 263–347.

[2] B. Prinz, A. Romero, and L. Ratke, *J. Mater. Sci.*, **1995**, 30, 4715–4719.

[3] L. Ratke, G. Korekt, and S. Drees, *Adv. Space Res.*, **1998**, 22, 1227–1236.

[4] L. Ratke, and G. Korekt, *Z. Metallkd.*, **2000**, 91, 919–927.

[5] C. Beckermann, and R. Viskanta, *Appl. Mech. Rev.*, **1993**, 46, 1–27.

[6] J. Ni, and C. Beckermann, *Metall. Trans. B*, **1991**, 22B, 349–361.

[7] C.Y. Wang, and C. Beckermann, *Metall. Mater. Trans. A*, **1996**, 27A, 2754–2764.

[8] C.Y. Wang, and C. Beckermann, *Metall. Mater. Trans. A*, **1996**, 27A, 2765–2783.

[9] C.Y. Wang, and C. Beckermann, *Metall. Mater. Trans. A*, **1996**, 27A, 2784–2795.

[10] C. Beckermann, *JOM*, **1997**, 49, 13–17.

[11] A.V. Reddy, and C. Beckermann, *Metall. Mater. Trans. B*, **1997**, 28B, 479–489.

[12] A. Ludwig and M. Wu, *Met. Trans A.*, **2002**, 33A, 3673

[13] M.. Wu, A. Ludwig, *Adv. Eng. Mater.*, **2003**, 5, 62

[14] M. Wu, A. Ludwig, A. Bührig-Polaczek, M. Fehlbier, and PR. Sahm, *Inter. J. Heat Mass Transfer*, **2003**, 46, 2819–32

[15] M. Rappaz, *Int. Mater. Rev.*, **1989**, 34, 93–123.

[16] C. Zener, *J. Appl. Phys.* **1949**, 20, 950–953.

[17] S. Diefenbach, *Modellierung der*

Gefügeentwicklung von Monotekta, Ph.D. thesis, Ruhr-University Bochum, **1993**.

[18] N. O. Young, J. S. Goldstein, and M. J. Block, *J. Fluid Mech.*, **1959**, 6, 350–356.

[19] W. Günter, *Über die Dynamik von Fluidpartikeln aufgrund des Marangoni-Effektes*, Düsseldorf: VDI-Verlag, **1993**.

[20] M.G. Velarde, in L. Ratke, H. Walter, B. Feuerbacher (Eds.), *Materials and Fluids under Low Gravity*, Springer Berlin, **1995**, 283–298.

[21] F. Falk, in L. Ratke (eds.), *Immiscible Liquid Metals and* Organics, DGM Informationsgesellschaft mbH, **1993**, 93–100.

[22] L. Ratke et al., in L. Ratke, H. Walter, B. Feuerbacher (eds.), *Materials and Fluid under Low Gravity*, Springer Berlin, **1995**, 115–133.

[23] H. U. Walter, in Järva Krog (eds.), *Proc. RIT/ESA/SSC Workshop*, ESA SP 219, Noordwijk, Sweden, **1984**, 47–64

[24] J. Alkemper, L. Ratke, *Z. Metall.*, **1994**, 85, 365–371.

6
Modeling of the Solidification of Immiscible Alloys

J. Z. Zhao, Z. Q. Hu, L.Ratke

Abstract

A model has been developed by taking into account the common action of the nucleation, the diffusional growth, the collisions and coagulations of the minority phase droplets and the spatial phase segregation to describe the microstructure evolution in an immiscible alloy solidified rapidly under the vertical directional solidification conditions. The model was applied to predict the microstructure evolution in a directionally solidified hypermonotectic Al-Pb alloys. The numerical results show that at a high solidification velocity a constitutional supercooling region appears in front of the solid/liquid interface and the liquid-liquid decomposition takes place there.

6.1
Introduction

Alloys with a miscibility gap in the liquid state are a broad kind of materials. Many of them are excellent candidates to be used as, for instance, self-lubricating bearings (Al-Pb, Al-Bi), electrical power switches (Ni-Ag), etc. These alloys, however, have an essential drawback that just this miscibility gap, as depicted in Fig. 1, poses problems during solidifications. If a homogeneous, single-phase liquid is cooled into the miscibility gap, the liquid-liquid decomposition happens. The phase transformation process begins with the nucleation of the liquid minority phase in the form of droplets. These droplets grow by diffusion of solute in the matrix.

They can also settle due to gravity or migrate due to a temperature or a concentration gradient [1]. In this temperature range large composition and density differences exist between the two liquid phases that lead to a quick spatial phase separation or macrosegregation during solidification processing on earth.

The microstructure evolution during a cooling of an immiscible alloy in the miscibility gap is very complex. Although a lot of works have been carried out the solidification of immiscible alloys remains an unsolved problem. The models existing nowadays are generally developed under some simplified assumptions and were

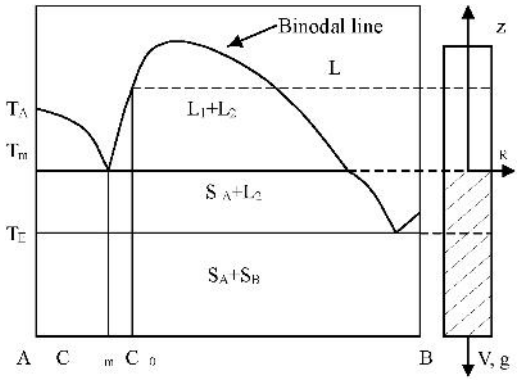

Fig. 1 Schematic phase diagram of an alloy with a liquid miscibility gap.

often not applicable to practical situations [2–10]. Great improvements have been made in recent years. Zhao and Guo et al developed models to simulate the solidification of immiscible alloys under practical situations. But these models were developed either by neglecting the effect of collisions and coagulations of droplets [11–13] or by neglecting the spatial segregation of phases [14]. A model is therefore proposed in this paper to simulate the microstructure evolution under the practical situations of cooling an initially homogeneous single phase liquid of immiscible alloy through the miscibility gap. The technical process we have in mind is the so-called strip casting process, a variant of the more general continuous casting routines, in which thin slabs of approximately 10 mm thickness and 10 cm width are produced with high solidification speeds (around 50 to 100 cm/min.) and high temperature gradients (around 200 K/cm) [17].

6.2
Theoretical Model

Under the conditions of directional solidification there exists a supercooled region in advance of the solidification interface. The nucleation of minority phase droplets in this region can be described with the classical nucleation theory. The stationary nucleation rate, the number of nuclei created per unit of time and volume, was calculated by [15]:

$$I = N_V N_0 O \Gamma Z \exp\left[-f(\Theta)\,\frac{\Delta G_c}{k_B T}\right] \tag{1}$$

with the abbreviation:

$$N_0 = (X_A\,\Omega_A + X_B\,\Omega_B)^{-1}$$

$$O = 4\,n_c^{2/3}$$

$$\Gamma = 6\,D/\lambda$$

$$Z = \left(\frac{\Delta G_c}{3\,\pi\,k_B T n_c^2}\right)^{1/2}$$

$$\Delta G_c = \frac{16}{3}\,\pi\,\frac{\sigma^3}{\Delta G_v{}^2}$$

where N_0 is the number density of atoms per volume, Ω_A, Ω_B are the atomic volumes of A and B components, X_A and X_B are the mole fractions of component A and B, n_c is the number of atoms in a droplet of critical radius $R^* = 2\,\sigma/\Delta G_v$, σ is the interfacial tension between the two liquids, ΔG_v is the gain in free energy per volume on nucleation, D is the diffusion coefficient, λ is the average jump distance of a solute atom due to diffusion, Z is the Zeldovich factor, k_B is Boltzmann's constant, T is absolute temperature and ΔG_c is the energy barrier for nucleation, N_v is the concentration of catalyzing impurities and the function $f(\theta)$ describes the change of the energy barrier to nucleation due to wetting of the nuclei to the catalyzing substance with θ being the wetting angle between the nuclei and the catalyzing surface. $f(\theta) = 1$ for homogeneous nucleation and $0 < f(\theta) < 1$ for heterogeneous nucleation. It is assumed in this calculation that $f(\theta)$ equals 1.

The droplets nucleated are embedded in a supersaturated matrix and thus will grow by diffusional transport of solute in the matrix. If the dimensionless supersaturation $S = (C_m - C_m^\infty)/(C_\beta - C_m^\infty)$ is much less than unity, the growth or shrinkage rate of droplet is given by [11]:

$$\frac{dR}{dt} = D\frac{C_m(t) - C_I(R,t)}{C_\beta(t) - C_I(R,t)}\,\frac{1}{R} + \frac{R}{3}\,\frac{(dC_\beta(t)/dT)/(dT/dt)}{C_\beta(t) - C_I(R,t)} \tag{2}$$

Here $C_m(t)$ is the mean field concentration in the matrix liquid, $C_\beta(t)$ is the concentration of the liquid within the droplet, $C_I(R,t) = C_m^\infty(t)\exp\left(\frac{\alpha_s}{R}\right)$ is the concentration of solute in the matrix at the interphase boundary, R is the droplet radius, $\alpha_s = (2\,\sigma\,\Omega_d/k_B T)$ is the capillary length and $C_m^\infty(t)$ the equilibrium composition in the matrix liquid at a flat interface boundary at time t, Ω_d is the atomic volume in the droplet. The first term on the right hand side denotes the growth or shrinkage rate of a droplet in an isothermal system or at a constant C_β. The second term describes the contribution of the variation of C_β with time.

The motion of droplets leads to the spatial separation of phases accompanied by collisions and coagulations of droplets. The coarsening of droplets due to collisions and coagulations may be described using the collision kernel K [16]:

$$K(R_1, R_2) = E(R_1, R_2)\,W(R_1, R_2) \tag{3}$$

where $E(R_1, R_2)$ is the collision efficiency. It was taken as 1 for simplification. $W(R_1, R_2)$ the collision volume between droplets of radius R_1 and R_2. Under the si-

tuation as illustrated in Fig. 1, the collision volume due to Stokes settlement and Marangoni migration can be calculated by:

$$W_S(R_1, R_2) = \pi (R_1 + R_2)^2 \left| u_S(R_1) + u_M(R_1) - u_S(R_2) - u_M(R_2) \right| \quad [3]$$

The collision frequency M is:

$$M(\mathrm{R}_1, R_2) = K(R_1, R_2)\, n(R_1)\, n(\mathrm{R}_2) \quad [4]$$

where n is the number density of droplets, u_S is the Stokes motion velocity and u_M the Marangoni migration velocity.

The microstructure in front of the solid/liquid interface may be described by a droplet distribution function $f(R,z,t)$ which is so defined that $f(R,z,t)\,dR$ gives the number of droplets per unit volume at time t and position z in a size class from R to $R + dR$. Taking into account the common action of the nucleation, the diffusional growth, the collisions and coagulations of droplets and the spatial phase segregation due to the motion of droplets, $f(R,z,t)$ obeys in the coordinate demonstrated in Fig. 1 the following continuity equation for a sample solidified anti-parallel to the gravity:

$$\frac{\partial f}{\partial t} - V\frac{\partial}{\partial R}\left(\frac{\partial R}{\partial z} f\right) + \frac{\partial (u_M - u_S - V) f}{\partial z} = \left.\frac{\partial I}{\partial R}\right|_{R=R^*}$$
$$+ \frac{1}{2}\int_0^R K(R_1, R_2) f(R_1, t) f(R_2, t) \left(\frac{R}{R_2}\right)^2 dR_1 - \int_0^\infty K(R, R_1) f(R, t) f(R_1, t)\, dR_1 \quad (5)$$
$$R_1^3 + R_2^3 = R^3$$

Where V is the solidification velocity. In this equation the first term describes the time dependent change of the droplet radius distribution, the second term the contribution of the diffusional growth/shrinkage of droplets to the change of the local distribution function. The third term describes the contribution of both the motion of droplets in the melt and the movement of the sample. The fourth term is the source term stemming from nucleation. The last two terms describe the collisions and coagulations of droplets. In the moving interface frame the term $\frac{\partial R}{\partial z}$ can be replaced by $\frac{\partial R}{\partial z} = -v(R, z)/V$. In the two-liquid-phase region the solute transfers through both the diffusion of the solute in the matrix liquid and the motion of droplets. It may be reasonable to assume that outside the two-liquid-phase region the diffusional transport of solute is negligible small. The concentration field in front of the solid/liquid interface can then be obtained by solving the following partial differential equation when the solidification comes into the stable state.

$$\begin{cases} \partial D \dfrac{\dfrac{\partial S}{\partial z}}{\partial z} + V \dfrac{\partial C^m}{\partial z} - \dfrac{4}{3}\pi \left[\displaystyle\int_0^\infty \dfrac{[\partial (uM - u_S - V) f(C^\beta - C^m)]}{\partial z} R^3 dR \right] = 0 \\ \left. \dfrac{\partial S}{\partial z} \right|_{z=z_{L/S}} = 0 \\ C^m(z > z_{L_1+L_2}) = C^0 \end{cases} \tag{6}$$

Where $S(z) = C^m(z) - C^m_\infty(z)$ is the supersaturation, C^0 is the initial Pb content of the alloy. Coupling a given temperature profile and the concentration field given by Eq. (6) with the phase diagram of an immiscible alloy, the droplet distribution function in the melt is determined via a solution of Eq. (5).

6.3 Numerical Results and Discussions

Fig. 2 shows the phase diagram of Al-Pb. For the numerical study we used an alloys with 5 wt.% Pb. The binodal temperature is then around 850 °C giving approximately 190 °C temperature difference between the equilibrium onset of the two-phase re-

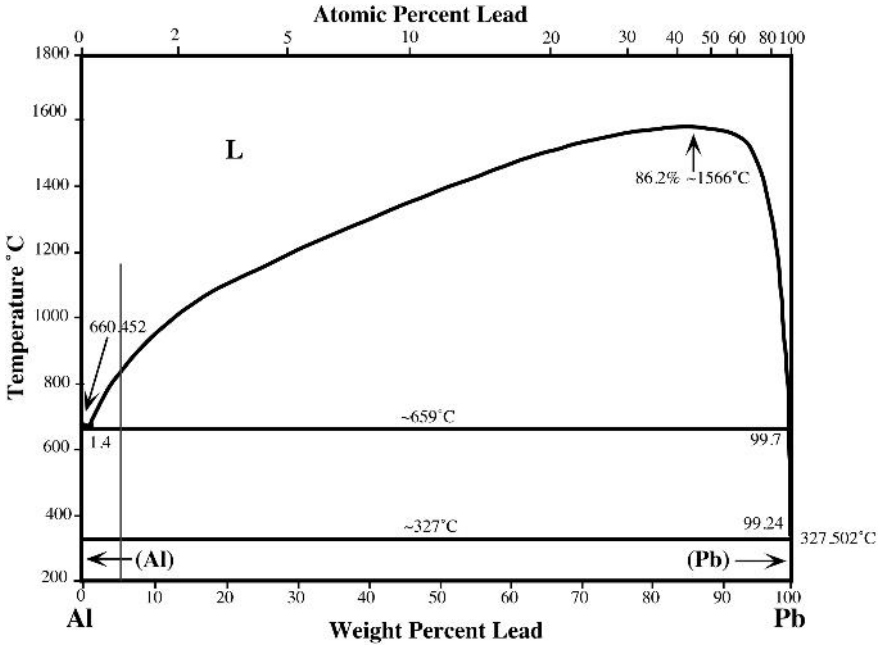

Fig. 2 Al-Pb phase diagram with a vertical line showing the alloy used in this study.

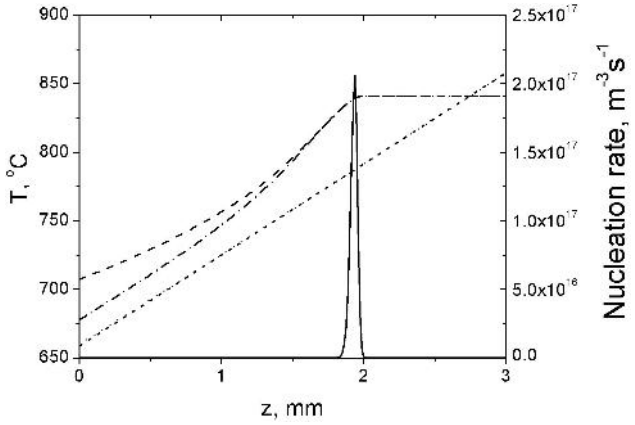

Fig. 3 The temperature profile (dotted line), the upper consolute temperature (dashed line) and the nucleation rate (solid line) in front of the solid/liquid interface. The dash-dots are the upper consolute temperature calculated without taking into account the collisions and coagulations between droplets.

gime and the monotectic reaction front. At a temperature gradient of 660 K/cm there is a region extending 2.9 mm from the monotectic reaction or solidification front into the melt where phase separation can occur.

Fig.3 shows the temperature profile and the upper consolute temperature of the sample together with the nucleation rate of the minority phase drops in front of the solid/liquid interface for the Al-5wt%Pb alloy. The solidification speed is set as 18 mm/s with a temperature gradient of 660 K/cm. It indicates that an undercooled region appears in advance of the interface and the nucleation of the minority phase droplets occurs in a region around the peak of the undercooling.

The collisions and coagulations of droplets have a negligible effect on the nucleation behavior of droplets because during the nucleation period the droplets are very small and their moving velocities are negligible. The average radius and the number density of droplets are shown in Fig. 3. It demonstrates that after nucleation the droplets grow and coarsen as they approach the solid/liquid interface. The effect of droplet motions on droplet number density is duplex. On the one hand, the collisions and coagulations of droplets cause naturally a decrease of the number density with approaching the solid/liquid interface, on the other hand, the motions of droplets lead to an accumulation or depletion of droplets in front of solid/liquid interface depending on the relative magnitude between u_S and u_M. The latter effect can be explained as follows.

Using the fact that the number density of droplets at any position is time independent when the solidification comes into steady state $\left(\frac{\partial f}{\partial t} = 0\right)$, neglecting the effect of collisions and coagulations between droplets and the temperature dependency of the densities and viscosities of the liquids one obtains:

$$(V + \langle u_S \rangle - \langle u_M \rangle)\frac{\partial n}{\partial z} = (\langle u_M \rangle - 2\langle u_S \rangle)\frac{n}{\langle R \rangle}\frac{\partial \langle R \rangle}{\partial z} \tag{16}$$

In the steady state of the solidification all drops should move towards the solid/liquid interface or, in other words, $V + \langle u_S \rangle - \langle u_M \rangle > 0$. They grow as approaching the solidification interface, or in other words, $\frac{\partial \langle R \rangle}{\partial z}$ should always be smaller than 0. Thus $\frac{\partial n}{\partial z}$ if $\langle u_M \rangle - 2\langle u_S \rangle > 0$. Otherwise $\frac{\partial n}{\partial z} > 0$.

Under the conditions assumed for this calculation, u_S is negligible small compared to u_M, see Fig. 5. The motions of droplets cause therefore an accumulation of droplets in front of the solidification interface, see the curve in Fig. 4 for the number density of droplets calculated without taking into account the collisions and coagulations.

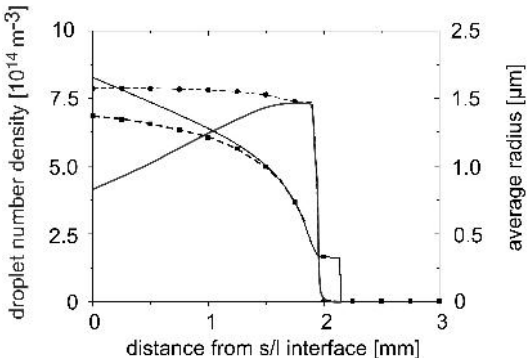

Fig. 4 The number density (dashed line) and the average radius (solid line) of drops in front of the solidification interface. The circles are the number density and the squares the average radius of droplets calculated without taking into account the collisions and coagulations between droplets.

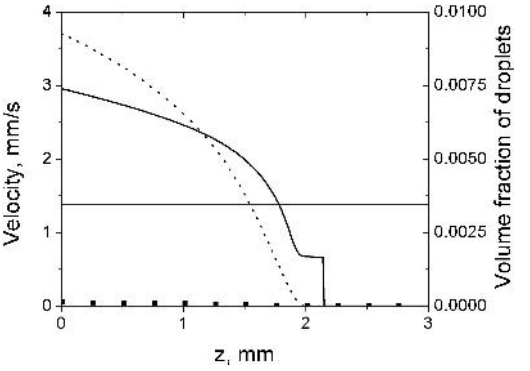

Fig. 5 The Stokes (squares) and Marangoni (thick solid line) velocities of the local average size drops and the volume fraction of Pb-rich phase (dotted line) in front of the solidification interface. The horizontal solid line shows the volume fraction of Pb droplets according to the phase diagram.

6.4 Conclusions

A model has been developed by taking into account the common action of the nucleation, the diffusional growth, the collisions and coagulations of the minority phase droplets and the spatial phase segregation to describe the microstructure evolution in an immiscible alloy solidified rapidly under the vertical directional solidification conditions. The model was applied to predict the microstructure evolution in a directionally solidified hypermonotectic Al-Pb alloys. The numerical results show that at a high solidification velocity a constitutional supercooling region appears in front of the solid/liquid interface and the liquid-liquid decomposition takes place there.

Acknowledgments

The author gratefully acknowledges the financial support from the Sino-Germany Science Foundation (032/1), the National Natural Science Foundation of China (50271076) and the Natural Science Foundation of Liaoning Province of China.

References

[1] J.Z. Zhao, L. Ratke L, J. Jia, Q.C. Li, J. Mat. Sci. Technol. 2002, 18, 197–205

[1] Bergman A; Fredriksson H: In: Materials processing in the reduced Gravity Environment of Space. Rindone G. E (ed), Elsevier science publishing company (1982) 563–577.

[2] L. Ratke, J. Coll. Interf. Sci. 1987, 119, 391–397.

[3] T. Carlberg, H. Fredriksson, Metall.-Trans. A 1980, 11, 1665–1676

[4] L. Ratke, H.F. Fischmeister, A. Kneissl: in: 6th European Symposium on Materials Science in Microgravity, ESA SP-256 (1987) 161–167.

[5] L. Ratke, H.F. Fischmeister, A. Kneissl: in: 7th European Symposium on Materials Science Under Microgravity, ESA SP-295 (1989) 135–140.

[6] J. Alkemper, L. Ratke, Z. Metallkd. 1994, 85, 365–371.

[7] L. Ratke, J. Alkemper, Advances in Colloid and Interface Science, 1995, 58, 151–170.

[8] Zhao J. Z; Guo J. J; Jia J; Li Q. C: Trans. Nonferrous Met. Soc. China, 5 (1995) 67–70.

[9] Zhao J. Z; Guo J. J; Jia J; Li Q. C: Trans. Nonferrous Met. Soc. China, 5 (1995) 105–108.

[10] Zhao J. Z; Guo J. J; Jia J; Li Q. C: Trans. Nonferrous Met. Soc. China, 5 (1995) 85–87.

[11] J. Z. Zhao, L. Ratke; B. Feuerbacher, Modelling Simul. Mat. Sci. Eng. 1998, 6, 123–140.

[12] J. Z. Zhao, L. Ratke; Mat. Sci.Technol. 2002, 18, 306–310.

[13] J. Z. Zhao, S. Drees, L. Ratke, Mat. Sci. Eng. A, 2000, 282A, 262–269.

[14] J.J. Guo, Y. Liu, J. Jia, Y.Q. Su, H.S. Ding, J. Z. Zhao, X. Xue, Scripta Materialia 2001, 45, 1197–1204

[15] J. Christian, The Theory of Phase transformation in Metals and Alloys, 2nd, Pergamon press, Elmsford NY. (1975) Vol. 1.

[16] J.Z.Zhao, PhD thesis, Harbin Institute of Technology, China, 1994

[17] B.Prinz, A.Romero, L.Ratke , J.Mater. Sci., 1995, 30, 4715–4719

7
Phase-Field Modeling of Dendritic Solidification: Verification for the Model Predictions with Latest Experimental Data

P.K. Galenko, D.M. Herlach, O. Funke, G. Phanikumar

Abstract

The results on modeling of dendritic solidification from undercooled melts are discussed. In order to model the details of formation of dendritic patterns we use a phase-field model of dendritic growth in a pure undercooled system with convection of the liquid phase. The predictions of the phase-field model are discussed referring to our latest high accuracy measurements of dendrite growth velocities in nickel samples. Special emphasis is given to the growth of dendrites at small and moderate undercoolings. At small undercoolings, the theoretical predictions deviate systematically from experimental data for solidification of nickel dendrites.

7.1
Introduction

Since several decades now dendritic growth velocities V have been measured during solidification of electromagnetically levitated metal melts. Different techniques have been applied, e.g. the usage of a fast responding photo-double-diode [1,2] or an ultra-high-speed camera system [3]. Following the sharp interface model of dendrite growth by Kurz et al. (LGK/LKT model) [4,5], the prediction of the dendritic growth velocity V as a function of the undercooling ΔT is in good agreement with experimental data for nickel solidification only in the region of medium undercoolings $100\ \mathrm{K} < \Delta T < 200\ \mathrm{K}$ [2]. Recently, we suggested a modification to the sharp interface LGK/LKT model which takes into account the effect of forced convective flow caused by electromagnetic stirring [6]. It is shown that this modification leads to an increase of the calculated velocity when the melt flow is opposite to the direction of the steady-state dendritic growth. However, the effect of forced convective flow alone can still not explain the measured data in a satisfying manner [6]. Therefore, (i) we essentially improved the accuracy of the technique and performed new measurements of dendritic growth velocities in levitated undercooled nickel samples (see Ref. [7] and references therein), and, in the present work, (ii) we present the phase-field model predictions in comparison with the new measurements of dendrite growth ve-

locity measurements for levitated undercooled Ni melts obtained with an advanced capacitance proximity sensor (CPS) technique.

7.2 Governing equations

The phase-field model was suggested and developed for the description of phase transitions in condensed matter with diffuse phase interfaces (see, e. g., overviews in Refs. [8,9]). In the present investigation, we have used the "thin-interface" analysis of the phase-field model [10,11] where the interface thickness W_0 is assumed to be small compared to the scale of the crystal but not smaller than the microscopic capillary length d_0. The thin-interface limit is ideally suited to model dendritic growth in pure materials quantitatively at low undercoolings when used in conjunction with efficient numerical algorithms [12]. The phase-field and energy equations were taken from the model of Karma and Rappel [10,11] with the momentum and continuity equations of motion of the liquid phase taken from Beckermann et al. [13]. Furthermore, in the momentum equation, the additional force for the motion of the liquid phase in an undercooled levitated droplet, i. e. the Lorentz force $\vec{F}_{LZ} = c^{-1}\vec{J} \times \vec{B}$ caused by the alternating electromagnetic field, has been introduced (here is the speed of light, $\vec{J}$ is the electric current density, and $\vec{B}$ is the vector of magnetic induction).

The main governing equations are described by

– *energy conservation*

$$\frac{\partial T}{\partial t} + (1-\varphi)(\vec{v}\cdot\nabla)T = a\nabla^2 T + \frac{T_Q}{2}\frac{\partial \Phi}{\partial t}\,, \tag{1}$$

– *continuity of the liquid phase*

$$\nabla\cdot[(1-\varphi)\vec{v}] = 0\,, \tag{2}$$

– *momentum transfer*

$$(1-\varphi)(\vec{v}\cdot\nabla)\vec{v} = -\frac{1-\varphi}{\rho}\nabla p + \frac{(1-\varphi)}{\rho}\vec{F}_{LZ} + \nabla\cdot\left[\nu\nabla(1-\varphi)\vec{v}\right] + \vec{F}_D\,, \tag{3}$$

– *phase-field evolution*

$$\tau(\vec{n})\frac{\nabla\Phi}{\partial t} = \nabla\cdot\left(W^2(\vec{n})\nabla\Phi\right) + \sum_{w=x,y,z}\frac{\partial}{\partial w}\left(|\nabla\Phi|^2 W(\vec{n})\frac{\partial W(\vec{n})}{\partial(\partial_w\Phi)}\right) - \frac{\partial F}{\partial\Phi}\,. \tag{4}$$

In Eqs. (1)–(4) the following notations are accepted: T is the temperature, T_Q is the adiabatic temperature of solidification defined by $T_Q = Q/c_p$, Q and c_p are the la-

tent heat of solidification and specific heat per unit volume, respectively, Φ is the phase-field variable ($\Phi = -1$ is the liquid phase and $\Phi = 1$ is for the solid phase); $\varphi = (1 + \Phi)/2$ is the fraction of the solid phase ($\varphi = 0$ is for the liquid and $\varphi = 1$ is for the solid), $\vec{v}$ is the fluid flow velocity in the liquid, x,y,z are the Cartesian coordinates, t is the time, a is the thermal diffusivity, ρ is the density, p is the pressure, and ν is the kinematic viscosity of the liquid phase. The dissipative force in the Navier-Stokes equation (3) is defined by $\vec{F}_D = -2\,\nu\,h\,\varphi^2\,(1-\varphi^2)\vec{v}/W_0^2$, where the constant $h = 2.757$ is defined by the asymptotic analysis in Ref. [13]. Furthermore, in the solution of Eq. (3), the Lorentz force has been averaged in time: $\vec{F}_{LZ} \approx |B|^2/(4\pi\delta)$, where $|B| = B_o \cdot \exp[(r - R_o)/\delta]$ is the modulus of the magnetic induction vector, B_o is the time averaged value of the magnetic induction, r is the radial distance of a droplet of radius R_0, $\delta = \left[2/(\omega\sigma_R\mu_0)\right]^{1/2}$ is considered as a skin depth for the alternating magnetic field in the liquid droplet, which decreases for a short distance at which the modulus of magnetic induction $|B|$ decays exponentially, σ_R is the electric conductivity (measured under isothermal conditions), μ_o is the magnetic permeability, and ω is the frequency of the applied current. The phenomenological free energy F is defined by $F(T,\Phi) = f(\Phi) + \lambda\,(T - T_M)\,g(\Phi)/T_Q$. With including the double-well function $f(\Phi) = -\Phi^2/2 + \Phi^4/4$ and the odd function $g(\Phi) = \Phi - 2\,\Phi^3/3 + \Phi^5/5$ itself, the form of the free energy F is constructed in such a way that a tilt λ of an energetic well controls the coupling between the fields of T and Φ.

The time $\tau(\vec{n})$ of the phase-field kinetics and the thickness $W(\vec{n})$ of the anisotropic interface are given by

$$\tau(\vec{n}) = \tau_0\,a_c(\vec{n})\,a_k(\vec{n})\left[1 + a_2\frac{\lambda d_0}{a\beta_0}\,\frac{a_c(\vec{n})}{a_k(\vec{n})}\right], \quad W(\vec{n}) = W_0\,a_c(\vec{n}), \tag{5}$$

where τ_0 is the time-scale for the phase-field kinetics, W_0 is the parameter of the interface thickness with $W_0 = \lambda\,d_0/a_1$, and $a_1 = 5\sqrt{2}/8$. The second term in square brackets of Eq. (5) for $\tau(\vec{n})$ defines a correction for the "thin-interface" asymptotics with adopting a constant $a_2 = 0.6267$ [12] in comparison with the sharp-interface analysis. The functions $a_c(\vec{n})$ and $a_k(\vec{n})$ of interfacial anisotropy are described by

– *the anisotropy of interfacial energy*

$$a_c(\vec{n}) = \frac{\gamma(\vec{n})}{\gamma_0} = (1 - 3\,\varepsilon_c)\left[1 + \frac{4\,\varepsilon_c}{1 - 3\,\varepsilon_c}(n_x^4 + n_y^4 + n_z^4)\right], \tag{6}$$

where $\gamma(\vec{n})$ is the surface energy dependent on the normal vector $\vec{n}$ to the interface, γ_0 is the mean value of the interfacial energy along the interface, and ε_c is the anisotropy parameter,

– *the anisotropy of kinetics of atomic attachment to the interface*

$$a_k(\vec{n}) = \frac{\beta(\vec{n})}{\beta_0} = (1 + 3\,\varepsilon_k)\left[1 - \frac{4\,\varepsilon_c}{1 + 3\,\varepsilon_k}(n_x^4 + n_y^4 + n_z^4)\right], \tag{7}$$

where $\beta(\vec{n})$ is the kinetic coefficient dependent on the normal vector $\vec{n}$ to the interface, β_0 is the averaged kinetic coefficient along the interface which is defined by $\beta_0 = (1/\mu_{100} - 1/\mu_{110})/(2\,T_Q)$, and ε_k is the kinetic anisotropy parameter defined as $\varepsilon_k = (\mu_{100} - \mu_{110})/(\mu_{100} + \mu_{110})$. In Eqs. (5)–(7), the normal vector $\vec{n} = \vec{n}(n_x, n_y, n_z)$ has the components defined by the gradients of the phase-field as follows

$$n_x^4 + n_y^4 + n_z^4 = \frac{(\partial\Phi/\partial x)^4 + (\partial\Phi/\partial y)^4 + (\partial\Phi/\partial z)^4}{|\nabla\Phi|^4} \tag{8}$$

7.3 Results and Discussion

Equations (1)–(8) have been solved numerically by a finite-difference technique on a uniform computational grid with application of the special numerical algorithms. Particularly, we used the multi-grid algorithm for resolving the equations of the phase-field (4), heat transfer (1) and momentum (3) which have the different spatial lengths and time scales of their dynamics. The details of numerical algorithm and computational procedure of solution of dendritic growth with convective flow were the same as given in Refs. [14,15]. Parameters of modeling applicable to pure nickel are given in Table 1. The phase-field modeling of dendritic patterns has been carried out on Workstation – SUN BLADE 1000.

Tab. 1 Material's parameters for pure nickel and characteristics of the electromagnetic facility

Parameter	*Symbol*	*Numerical value*
Equilibrium temperature of solidification	T_M	1728 (K)
Latent heat of solidification	Q	$8.113 \cdot 10^9$ (J/m^3)
Specific heat	c_p	$1.939 \cdot 10^7$ (J/K/m^3)
Interface energy	γ_0	0.326 (J/m^2)
Capillary length	d_0	$1.66 \cdot 10^{-10}$ (m)
Interfacial kinetic coefficient in <100>-direction	μ_{100}	0.52 (m/s/K)
Interfacial kinetic coefficient in <110>-direction	μ_{110}	0.40 (m/s/K)
Density	ρ	8.110^3 (kg/m^3)
Dynamic viscosity	μ	4.310^{-3} (Pa · s)
Thermal diffusivity	a	$1.2 \cdot 10^{-5}$ (m^2/s)
Anisotropy constant	σ_0	1.1 (–)
Parameter of anisotropy	ε	1.810^{-2} (–)
Electric conductivity	σ_R	$4.1 \cdot 10^6$ ($\Omega \cdot$ m)
Magnetic permeability	μ_0	$4 \cdot \pi \cdot 10^{-7}$ (H/m)
Frequency of the applied current	ω	$3.0 \cdot 10^5$ (1/s)

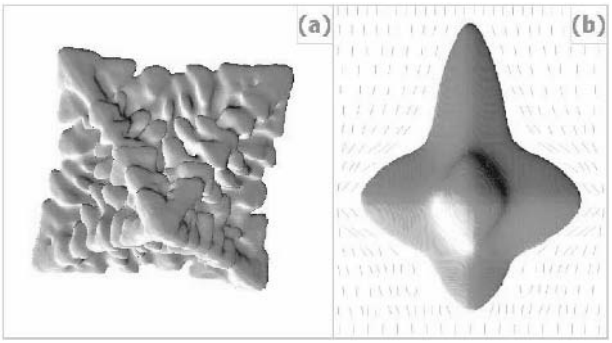

Fig. 1 (a) Dendritic growth pattern with side-branches due to application of finite level of thermal stochastic noise according to Ref. [16]. Dendrite has been obtained for pure nickel with the finite anisotropies of the interfacial energy and kinetics (see Table 1) at the undercooling $\Delta T = 0.55 T_Q$. Pattern has been simulated on a grid of size 650^3 nodes. (b) Growth of nickel dendrite under convective flow at $T = 0.30 T_Q$ and $U_0 = 0.7$ m/s. Growth velocity V of the up-stream branch is most pronounced in comparison with the down-stream branch due to forced convection with the far field flow speed U_0. The speed U_0 has been found from the energy balance within the levitated droplet from Eq. (3) of Ref. [6] and with the parameters of the electromagnetic facility given in Table 1. Dashed lines around the dendrite indicate the flow velocity vectors in the vertical cross-section. Pattern has been simulated on a grid of size $230 \times 330 \times 330$ nodes.

7.3.1 Dendritic Patterns

Solution of the phase-field equations allows us to obtain the complete morphological spectrum of interfacial crystal structures for a wide range of undercoolings. In our modeling, the complete morphological spectrum of the crystal structures has been obtained, which exhibits a crystal changing from grained crystals at very small undercoolings ($\Delta T < 0.15\, T_Q$) up to grained crystals at higher undercoolings ($\Delta T < 1.00\, T_Q$) via the dendritic growth form within intermediate region. Therefore, within the range of undercoolings investigated $0.10\, T_Q \leq \Delta T \leq 1.3\, T_Q$, the growth form of dendrites is dictated by the preferable crystallographic direction. In addition to this, stochastic noise plays a crucial role in the formation of branched crystal patterns of dendritic type. Figure 1(a) shows the dendritic crystal with secondary and even tertiary branches with the application of the thermal noise. With no convective flow, dendrites grow in the stagnant melt in a symmetrical manner with the main stems growing along the preferable crystallographic directions of a crystal. Solidification under the influence of convective flow forced by electromagnetic stirring in a droplet, however produces dendritic growth strongly pronounced in the direction opposite to that of the far field flow velocity U_0 [6]. The results of the present phase-field modeling also confirms this out-

come: with the imposing of the fluid flow, the growth becomes more pronounced in the opposite direction to the flow as shown in Fig. 1(b). For these structures, i. e. with the thermal noise in a stagnant melt and also with imposed flow of the melt (Fig. 1) we compared the results for dendrite growth velocity in pure nickel versus undercooling quantitatively.

The phase-field modeling exhibits an increase of the velocity of the up-stream dendritic branch in comparison with the dendrite tip velocity in a stagnant melt, Fig. 2. The enchanced dendrite velocity due to the melt flow has been found to decrease the disagreement between theory and experimental data, which is present at small undercoolings. Therefore we have compared quantitatively the predictions of the present phase-field modeling with the new experimental data [7] for growth kinetics of nickel dendrites.

7.3.2
Comparison with experimental data

We quantitatively analyzed the models predictions in comparison with previously recorded experimental data on dendritic solidification for nickel obtained with photodiode technique or, respectively, the capacitance proximity sensor (CPS) technique [1,2]. Particularly, it has been shown that the forced melt flow due to electromagnetic stirring in a droplet may increase the dendrite growth velocity if the flow imposed on the dendrite has the direction opposite to the growing dendritic tip [6]. However, the effect of the convective flow alone does still not explain the measured data in a satisfying manner. Therefore, to analyze critically the previous experimental data on dendritic growth, we improved the accuracy of the CPS technique and performed new measurements of dendritic growth velocities in levitated undercooled nickel samples [7]. The measurements were performed for dendritic growth velocity versus the amount of undercooling $T = T_L - T_\infty$ (where T_L is the liquidus temperature, and T_∞ is the actual temperature measured experimentally for the undercooled state of the liquid droplet in an electromagnetic levitation facility [17]). Solidification of the undercooled nickel melt was triggered at undercoolings in the range of $30\ \mathrm{K} < \Delta T < 260\ \mathrm{K}$. The new CPS data reveals high accuracy and low scattering, and showed in this investigation high reproducibility for six individual samples of different masses [7].

New experimental results for dendrite growth velocities in nickel are shown in Figure 2. Comparison of the model predictions, also shown in Fig. 2, with the new experimental results allows one to conclude that the predictions of the phase-field model, Eqs. (1)-(8), are partially agreeable to the experimental data. Particularly, the disagreement still exists in the range of undercooling $35\ \mathrm{K} < \Delta T < 125\ \mathrm{K}$, Fig. 2. Consequently, though the forced convection may drastically influence the thermal field around the growing dendrite and the growth kinetics itself, the disagreement between the modeling and experimental results still exists at small and, in part, moderate undercoolings.

The detailed analysis of the reasons of appearance of such a disagreement lead to the idea that tiny amounts of impurities may play a crucial role in the enhancement of the dendrite growth velocity at small undercoolings. A chemical analysis of the

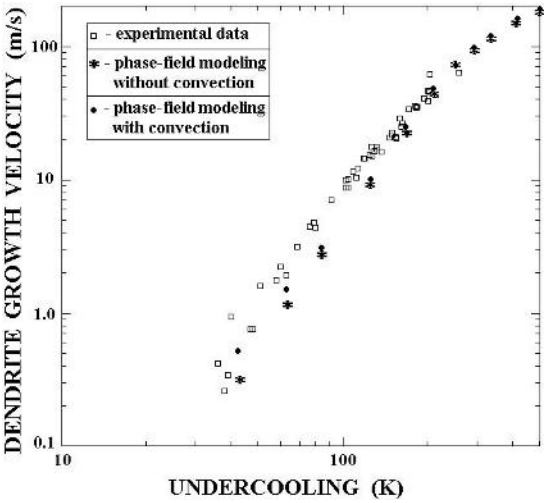

Fig. 2 Comparison of the results of the phase-field modeling for the dendrite tip velocity in stagnant melt, with the melt convection, and with the experimental data on growth kinetics of nickel dendrites. The new experimental data obtained using the improved CPS technique exhibits a smooth kinetic curve in comparison with the previous experimental data [7].

purity of samples used in for the new CPS measurements revealed that the amount of impurities is on the level of 0.01 at.% [7] which might play an essential role in the growth kinetics of nominally "pure" nickel [18]. Therefore we suggest on the basis of the current investigation that the influence of small amounts of impurities on the growth kinetics of nickel dendrites has the different temperature characteristic than of the effect by melt flow. This has allowed us to discriminate between both contributions as it is shown by experimental investigations and modeling within the sharp interface model [19] (for evaluation of the effect of solute diffusion) and the present phase-field modeling as well. The following analysis of these effects on the growth kinetics of nickel dendrites will be given elsewhere [20].

7.4 Conclusions

(i) The results on phase-field modeling for dendritic growth with convective flow are presented. As the phase-field model predicts, the crystal structures are changing from grained crystals at small undercoolings up to grained crystals (with the planar smooth crystallographic grains) at higher undercoolings via the dendritic growth form within intermediate range. Within this range, the branched dendritic patterns occur, Fig. 1(a). With the fliud flow imposed on the growing dendrites, the crystal growth becomes more pronounced in the direction opposite to the flow, Fig. 1(b).

(ii) For comparison of the model predictions with experimental data, the new capacitance proximity sensor CPS data set on dendritic growth velocities in levitated undercooled nickel samples has been chosen [7]. A comparison of the results of the phase-field modeling with the new experimental results shows that though the forced convection may drastically influence on the thermal field around the growing dendrite and the growth kinetics itself, the disagreement between the modeling and experimental results still exists at small and, in part, moderate undercoolings, Fig. 2.

(iii) Very small amounts of impurities existing in nominally "pure" nickel samples may play an essential role in dendrite growth kinetics [7]. Due to the fact that the solute diffusion effect may show a different temperature characteristic than the transport effect by fluid flow, it is possible, as a first approximation, to discriminate between both these effects by investigating growth velocities as a function of undercooling [18]. Good agreement of the models predictions with experimental data on solidification of the nickel dendrites might be obtained when both effects of thermal convection and solute diffusion are taken into consideration [20].

Acknowledgements

We thank Christoph Beckermann and Georg Lohöfer for useful exchanges and discussions. Financial support of this work by Deutsche Forschungsgemeinschaft under the project No. HE 1601/13 is gratefully acknowledged.

References

[1] E. Schleip, R. Willnecker, D.M. Herlach, G.P. Görler, Mater. Sci. Eng. 1988, 98, 39.

[2] K. Eckler, D.M. Herlach, Mater. Sci. Eng. 1994, A178, 159.

[3] D.M. Matson, in Solidification 1998 (Ed.: S.P. Marsh, J.A. Dantzig, R. Trivedi, W. Hofmeister, M.G. Chu, E.J. Lavernia, J.-H. Chun), TMS, Warrendale PA, USA, 1998, p. 233.

[4] J. Lipton, M.E. Glicksman, W. Kurz, Mater. Sci. Eng. 1984, 65, 57.

[5] J. Lipton, W. Kurz, R. Trivedi, Acta Metall. 1987, 35, 957.

[6] P.K. Galenko, O. Funke, J. Wang, D.M. Herlach, Mater. Sci. Eng. A 2003, in press.

[7] O. Funke, G. Phanikumar, P.K. Galenko, M. Kolbe, D.M. Herlach, *New results on dendrite growth velocities during solidification of levitated undercooled Ni melts*, Physical Review E 2004, submitted.

[8] L.Q. Chen, Annu. Rev. Mater. Res. 2002, 32, 113.

[9] W.J. Boettinger, J.A. Warren, C. Beckermann, A. Karma, Annu. Rev. Mater. Res. 2002, 32, 163.

[10] A. Karma, W.-J. Rappel, Phys. Rev. E 1996, 53, R3017.

[11] A. Karma, W.-J. Rappel, Phys. Rev. E 1998, 57, 4323.

[12] J. Bragard, A. Karma, Y. H. Lee, M. Plapp, Interface Science 2002, 10(2–3), 121.

[13] C. Beckermann, H.-J. Diepers, I. Steinbach, A. Karma, X. Tong, J. Comp. Physics 1999, 154, 468.

[14] X. Tong, C. Bekermann, A. Karma, Q. Li, Phys. Rev. E 2001, 63, 061601.

[15] Y. Lu, C. Beckermann, A. Karma, Mat. Res. Soc. Symp. Proc. Vol. 701 MRS, USA, 2002, T2.2.1.

[16] A. Karma, W.-J. Rappel, Phys. Rev. E 1999, 60, 3614.

[17] D.M. Herlach, Annu. Rev. Mater. Sci. 1991, 21, 23.

[18] D.M. Herlach, O. Funke, G Phanikumar, P.K. Galenko, *Free dendrite growth in undercooled melts: experiments and modeling.* In: "TMS (The Minerals, Metals & Materials Society) Proceedings", 2004, accepted for publication.

[19] P.K. Galenko, D.A. Danilov, Phys. Lett. A 1997, 235, 271.

[20] P.K. Galenko, D.M. Herlach, O. Funke, G Phanikumar, *Phase-field modeling of solidification of undercooled melt: a test and comparison for the current models with the new experimental data*, 2004, in preparation.

8
Phase-Field Modeling of Phase Transitions in Ternary Alloys

Britta Nestler

8.1
Introduction

The phase-field methodology has become a powerful methodology to describe phase transition phenomena in alloys with reliable qualitative results in comparison with experimental data. The method has successfully been used to describe solidification processes as well as microstructure evolution in solids and liquid-liquid interfaces. The characteristic property of a phase-field approach is that the phase boundaries are modeled by a diffuse interface of thickness ε. Within the interfacial region, the phase fields and other physical quantities change smoothly on a thin transition layer. Diffuse interface models have been formulated for pure substances, binary alloys for eutectic, peritectic and monotectic systems. Furthermore the evolution of grain boundaries can be modeled by phase-field approaches or order parameter models. In recent years, phase-field models have been derived from thermodynamic principles being now referred to as thermodynamically consistent. In this paper, we present a general formulation of a non-isothermal diffuse interface model (phase-field model) describing phase transformations in alloys with multiple components and phases. The new model is a generalization of earlier phase-field models developed in ref. 1 a).

In section 2, we set up a system of equations to model the solidification of ternary melts. The temporal evolution of the phase boundaries, of the volume fractions of the phases coupled to the heat and mass diffusion during solidification and melting processes is modeled. The phase-field model is derived from an entropy functional in a thermodynamically consistent way. It has been shown by asymptotic expansions in ref.1 b) (H. Garcke, B. Nestler, B. Stinner, SIAM Journal on Applied Mathematics, 2004, in print) that the phase-field model relates to sharp interface models.

Anisotropy, both, smooth as well as facetted types, can be included in the surface energies and in the kinetic coefficients. To numerically solve the set of governing equations in a computational efficient way, we have set up a three dimensional parallel simulator based on a finite difference discretization on a cubic grid with an explicit time marching scheme.

To further improve the performance of the solving algorithm, we applied adaptive strategies for both, the time scales as well as for the length scales.

In section 3, we present phase-field simulations of two and three dimensional crystallization structures in a ternary eutectic system with components (A-B-C), solid phases α, β, γ and a liquid phase L. We constructed a phase diagram of a symmetric ternary eutectic model alloy and incorporated it into the phase-field model through the free energies.

The simulation results illustrate the concentration fields of the three components in the melt ahead of the ternary α-β-γ lamellar growth front. Furthermore, the influence of anisotropy is studied leading to tilted eutectic growth structures, to competition and selection of grains of different crystallographic orientations in three dimensions.

8.2 Phase-Field Model

We propose a new phase-field model for alloys with multiple components and multiple phases. A mathematical analysis and asymptotic investigation of this model is discussed in ref. 1 b). The general formulation of the model allows to describe the phase transformations together with the coupled heat and mass diffusion processes in complex multicomponent alloy systems. Another field of application of the approach is the modeling of grain growth phenomena in systems with multiple grains of different crystal orientations.

In this paper, we apply the phase-field model to ternary phase systems with three components (A-B-C) and four phases (α, β, γ, L) represented by a vector of concentrations $c(\vec{x}, t) = (c_A(\vec{x}, t),\ c_B(\vec{x}, t),\ c_C(\vec{x}, t))$ and by a four component vector of order parameters $\phi(\vec{x}, t) = (\phi_\alpha(\vec{x}, t),\ \phi_\beta(\vec{x}, t),\ \phi_\gamma(\vec{x}, t),\ \phi_L(\vec{x}, t))$, respectively. Another variable of the system is the internal energy density $e(\vec{x}, t)$ which can be related to the local temperature by the thermodynamical relation $e = f + T \cdot s$, where f is the free energy density, T the temperature and s the entropy density. The phase-field model is based on an entropy functional of the form

$$S(e, c, \phi) = \int_\Omega s(e, c, \phi) - \left(\varepsilon a(\phi, \nabla\phi) + \frac{1}{\varepsilon} w(\phi) \right) dx$$

where the gradient energy $a(\phi, \nabla\phi)$ and the multi-well/multi-obstacle type energy $w(\phi)$ determine the thermodynamics of the interfaces, $s(e, c, \phi)$ defines the bulk entropy density and ε is a small length scale parameter related to the thickness of the diffuse interface. By taking the functional derivatives $\frac{\delta S}{\delta \phi_\alpha}$, $\frac{\delta S}{\delta c_i}$ and $\frac{\delta S}{\delta e}$ of the free entropy of the system, the following general set of evolution equations can be derived:

$$\omega\varepsilon \frac{\partial \phi_\alpha}{\partial t} = \varepsilon \left(\nabla \cdot a_{,\nabla\phi_\alpha} - a_{,\phi_\alpha} \right) - \frac{1}{\varepsilon} w_{,\phi_\alpha} - \frac{f_{,\phi_\alpha}}{T} - \lambda\,, \qquad \text{with } \alpha = 1, \ldots, 4$$

$$\frac{\partial c_i}{\partial t} = -\nabla \cdot \left(L_{i0}(T, c, \phi) \nabla \frac{1}{T} + \sum_{j=1}^{3} L_{ij}(T, c, \phi) \nabla \frac{-\mu_j}{T} \right) \quad \text{with } i = 1, \ldots, 3$$

$$\frac{\partial e}{\partial t} = -\nabla \cdot \left(L_{00}(T, c, \phi) \nabla \frac{1}{T} + \sum_{j=1}^{3} L_{0j}(T, c, \phi) \nabla \frac{-\mu_j}{T} \right)$$

These parabolic partial differential equations are used to simulate the solidification and phase transformations of ternary melts. The first equations for the non-conserved phase-field variables ϕ_α describe the dynamics of the phase boundaries and of the volume fractions of the four phases α, β, γ, L in the system. The derivation of the phase-field equations ensures a decrease in the total free energy of the system. The kinetic coefficient ω may depend on the orientation of the interface by $\omega = \omega(\phi, \nabla\phi)$ modeling the effect of kinetic anisotropy. λ is the Lagrange multiplier incorporating the constraint $\sum_{\alpha=1}^{4} \phi_\alpha = 1$. Due to this constraint, the number of phase-field equations that need to be solved can be reduced to three, since $\phi_4(\vec{x}, t)$ can be determined by $\phi_4(\vec{x}, t) = 1 - \phi_1(\vec{x}, t) - \phi_2(\vec{x}, t) - \phi_3(\vec{x}, t)$ at each time step. The notation $a_{,\phi_\alpha}$, $w_{,\phi_\alpha}$, $f_{,\phi_\alpha}$ and $\alpha_{,\nabla\phi_\alpha}$ denotes the derivative of the energy density contributions with respect to ϕ_α and $\nabla\phi_\alpha$ respectively.

The second and third equation for conserved variables describe the dynamics of the concentrations $c_i(\vec{x}, t)$ and of the inner energy $e(\vec{x}, t)$. These equations ensure the conservation of mass and energy.

Applying the thermodynamical relations $e = f + T \cdot s$ and $s = -f_{,T}$ the evolution of the temperature can be determined from the inner energy equation $\frac{\partial e}{\partial t}$. The mobility coefficients L_{ij} with $i, j = 0, \ldots, 3$ are related to the heat and mass diffusion coefficients of the ternary alloy. $\mu_j = f_{,c_j}$, $j = 1, \ldots, 3$ are the chemical potentials that can be obtained from the free energy $f(T, c, \phi)$ by taking the partial derivative with respect to c_j.

Next, we define the expressions for the free energies $a(\phi, \nabla\phi)$, $w(\phi)$, $f(T, c, \phi)$ that we set up for the numerical simulations presented in section 2. The gradient energy has the form

$$a(\phi, \nabla\phi) = \sum_{\alpha<\beta} \frac{\gamma_{\alpha\beta}}{m_{\alpha\beta}} A_{\alpha\beta}(q_{\alpha\beta}) |q_{\alpha\beta}|^2,$$

where $q_{\alpha\beta}$ is an abbreviation for the vector $q_{\alpha\beta} = \phi_\alpha \nabla \phi_\beta - \phi_\beta \nabla \phi_\alpha$. By summing the contribution of each interface, this choice of gradient energy contains enough degrees of freedom to specify the physics of each phase boundary. $m_{\alpha\beta}$ are mobility parameters and $\gamma_{\alpha\beta}$ are surface energies of each pairwise phase boundary. Anisotropy of the surface energies is realized by the factor $A_{\alpha\beta}(q_{\alpha\beta})$ depending on the orientation of the interface.

An example for a three dimensional anisotropy, that is consistent with the symmetry of a material with an underlying cubic symmetry, is given by

$$A_{\alpha\beta}(q_{\varepsilon\beta}) = (1 - \delta_{\alpha\beta}) + \delta_{\alpha\beta} \frac{|q_{\alpha\beta}|_4^4}{|q_{\alpha\beta}|^4} \quad \text{with} \quad |q_{\alpha\beta}|_4^4 = \sum_{i=1}^{3} \left(q_{\alpha\beta}^i \right)^4$$

$$\text{and} \quad |q_{\alpha\beta}|^4 = \left(\sum_{;i=1}^{3} \left(q_{\alpha\beta}^{i} \right)^2 \right)^2$$

where the summation index in this expression denotes the spatial coordinate in a 3 D domain and $\delta_{\alpha\beta}$ is the magnitude of the capillary anisotropy.

As described in ref. 1a$_1$, higher order variants of a multi-obstacle potential of the form

$$w(\phi) = \frac{16}{\phi} \sum_{\alpha<\beta} m_{\alpha\beta}\, \gamma_{\alpha\beta}\, \phi_\alpha\, \phi_\beta + \sum_{\alpha<\beta<\delta} \gamma_{\alpha\beta\delta}\, \phi_\alpha\, \phi_\beta\, \phi_\delta$$

have been proven to show good calibration properties between the model parameters and physical quantities. In addition, the artificial occurrence of foreign phases along two-phase boundaries can be suppressed by the higher order term $\sim \phi_\alpha \phi_\beta \phi_\delta$.

To define the bulk free energy density $f(T, c, \phi)$ we assume the last component $\phi_4(\vec{x}, t) = \phi_L(\vec{x}, t)$ of the phase-field vector to represent the liquid phase. We make the ansatz

$$f(T, c, \phi) = \sum_{\alpha=1}^{4} \sum_{i=1}^{3} \left(c_i L_i^\alpha \frac{T - T_i^\alpha}{T_i^\alpha} h(\phi_\alpha) \right) + \sum_{i=1}^{3} \left(k_B T c_i \ln(c_i) \right) - \mathrm{c}_v T(\ln(T) - 1)$$

with $L_i^4 = 0$ and L_i^α, $i = 1, ..., 3$, $\alpha = 1, ..., 3$ being the latent heats per unit volume of the phase transition from phase α to the liquid phase and of pure component *i*. Furthermore, T_i^α, $i = 1, ..., 3$, $\alpha = 1, ..., 3$ denotes the melting temperature of the *i-th* component in phase α, c_v is the specific heat which is for simplicity assumed to be independent of c and ϕ; k_B is the Boltzmann constant. The function $h(\phi_\alpha)$ satisfies the conditions: $h(0) = 0$ and $h(1) = 1$. Typical examples are $h(\phi_\alpha) = \phi_\alpha$ or $h(\phi_\alpha) = \phi_\alpha^2(3 - 2\phi_\alpha)$. The total free energy $f(T, c, \phi)$ is the sum of the bulk free energies, of the individual phases $f_\alpha(T, c, \phi)$.

8.3 Phase Transitions of Ternary Alloys

To simulate the microstructure formation, the coupled set of governing equations for the phase fields, the concentrations and the energy is implemented and numerically solved. We use a standard explicit time–stepping method with a finite difference representation of the spatial derivatives on a uniform cubic lattice. The modeling of growth structures in large computational domains requires the implementation of methods that reduce the computing time. We subdivide the three dimensional domain in stripes and use message passing concepts (MPI) on distributed memory systems for parallel solving the partial differential equations.The efficiency of the simulating algorithm can further be improved by making advantage of the following specific properties of the model. As described in the previous section, a multi–obstacle potential is used for the energy contribution $w(\phi)$. This type of potential keeps the inter-

facial thickness at a finite width and, hence, allows to solve the phase-field equations exclusively in regions of the interfaces and not in the complete volume. By this, the three dimensional problem is reduced by one dimension. Another performance optimization of the simulator can be achieved by exploiting the multiscale character of the model equations with respect to time and length scales. The three types of equations for the phase-fields, the concentrations and the inner energy equation can be solved using three different time steps Δt_ϕ, Δt_c and Δt_e and three different coarsenings of the mesh Δx_ϕ, Δx_c and Δx_e (being multiples of each others). The values of the variables at intermediate grid points on the finest mesh are calculated by interpolating the values on the coarser meshes. This procedure significantly contributes to the gain of computer time.The 2D and 3D simulations in Figures 1–5 consider ternary eutectic alloy solidificaion involving phase changes of four different phases and diffusion processes of three components. To conduct the simulations, we constructed a ternary eutectic phase diagram by the common tangent method and used the characteristic quantities such as latent heats, melting temperatures and solidus/liquidus compositions as input parameters for the computations. The phase diagram was assumed to be completely symmetric in the three components A, B and C. Below the ternary eutectic temperature, the three solid phases α, β and γ grow into the undercooled melt via the reaction $L \rightarrow \alpha + \beta + \gamma$. Due to the symmetry of the phase diagram, the volume fractions of the solid phases are equal.

The concentration profiles of the components $c_A(\vec{x}, t)$, $c_B(\vec{x}, t)$ and $c_C(\vec{x}, t)$ in front of the solidifying eutectic lamellae are illustrated in Figure 1 for a phase sequence $(\alpha|\beta|\gamma|\alpha|\beta|\gamma|...)$ at three different times. Since the α phase consumes component A out of the melt during the growth, it can be seen that ahead of phase α the concentration $c_A(\vec{x}, t)$ is decreased whereas the concentration of $c_B(\vec{x}, t)$, and $c_C(\vec{x}, t)$, are increased. An analogous observation can be made for the β and γ phases. Keeping the phase sequence $(\alpha|\beta|\gamma|\alpha|\beta|\gamma|...)$, the set of parameters and computational 2D domain unchanged, we investigated the influence of facetted surface energy anisotropy on the ternary eutectic microstructure, Figure 2 by using the anisotropy gradient energy density $a(\phi, \nabla\phi)$ for cubic crystal symmetry. The anisotropy leads to tilted growth in the direction of the ternary eutectic grain.

In Figure 3, a different permutation of phases $(\alpha|\beta|\alpha|\gamma|...)$ is considered. The simulation has been started with nuclei of equal sizes at left border of the domain. This configuration produces initially twice as much volume of phase α than of phase β and γ. Due to the incorporated phase diagram, the time evolution demonstrates that this condition is unstable. The phase boundaries rearrange to adjust at a configuration where the α lamellae have half the width of the β and the γ lamellae. As in Figure 1, the images show the concentrations $c_A(\vec{x}, t)$, $c_B(\vec{x}, t)$ and $c_C(\vec{x}, t)$ in the liquid phase. Caused by the $(\alpha|\beta|\alpha|\gamma|...)$ structure, the periodicity of the contour lines of the concentration $c_A(\vec{x}, t)$ differs from the concentrations $c_B(\vec{x}, t)$ and $c_C(\vec{x}, t)$. Finally, ternary eutectic alloy solidification is computed in three space dimensions. Starting from the initial phase pattern in the left image of Figure 4, the system establishes a regular three phase lamellar growth of $(\alpha|\beta|\gamma|\alpha|\beta|\gamma|...)$ phase sequence.

The initial phase configuration in Figure 5 a) leads to a steady state regular hexagonal shape. During the simultaneous growth, the three solid phases mutually en-

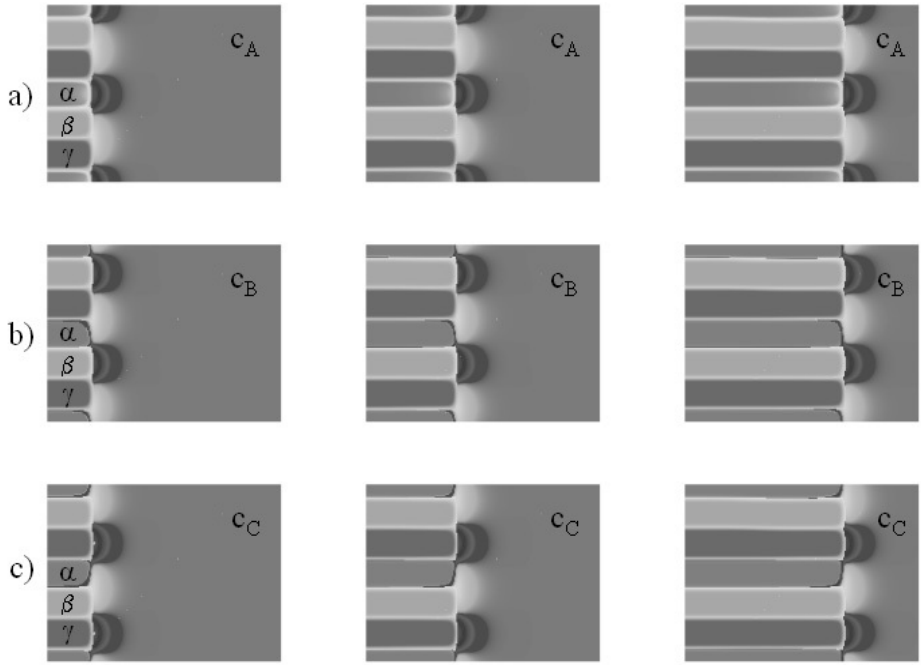

Fig. 1 Phase-field simulation of a ternary $(\alpha|\beta|\gamma|\alpha|\beta|\gamma|...)$ phase sequence that grows into an undercooled melt at three different time steps. The images in a), b) and c) show the concentration profiles of c_A, c_B, c_C ahead of the lamellar eutectic three phase front with dark gray regions of depletion and light gray regions of enrichment of the considered component.

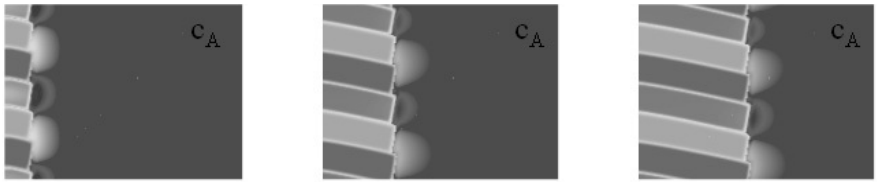

Fig. 2 Tilted solidification front of a $(\alpha|\beta|\gamma|\alpha|\beta|\gamma|...)$ phase sequence resulting from the influence of facetted surface energy anisotropy with cubic symmetry.

hance each other's growth conditions as they reject opposite components of the alloy into the liquid. The optimal pattern in three dimensions for isotropic surface energy and isotropic kinetic is a regular hexagonal rod-like structure. In Figure 5 b), we compare the isotropic growth shape of Figure 5 a) with crystals forming strong facets in preferred directions. The three solid phases have different crystallographic orientations which is realized through the surface energy anisotropy. The dark gray phase

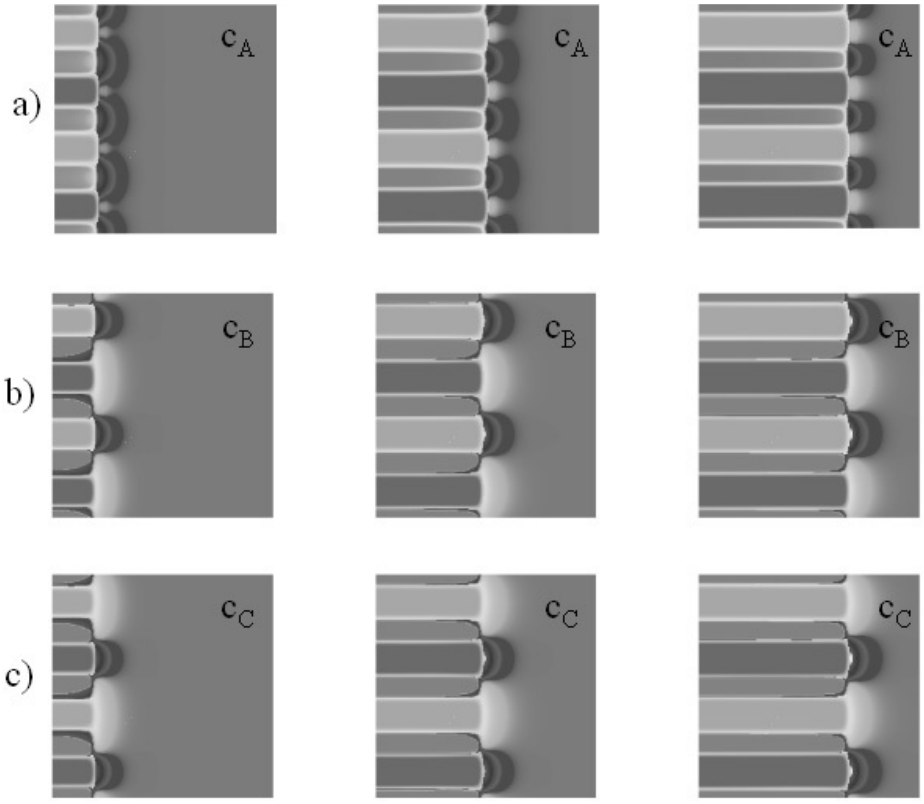

Fig. 3 Simulated solidification structure of a ternary ($\alpha|\beta|\alpha|$-$\gamma|\alpha|\beta|$...) phase sequence illustrating the concentration profiles of c_A, c_B, c_C ahead of the lamellar eutectic three phase front at the same intermediate time step of the computation.

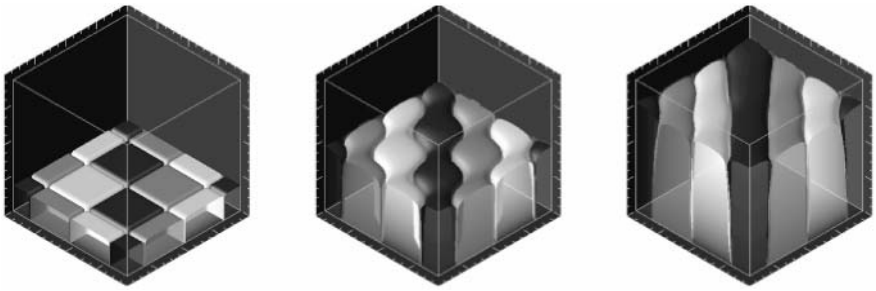

Fig. 4 Three dimensional simulation of a ternary eutectic growth structure. The initial pattern turns into the evolution of steady state lamellar growth in diagonal space direction.

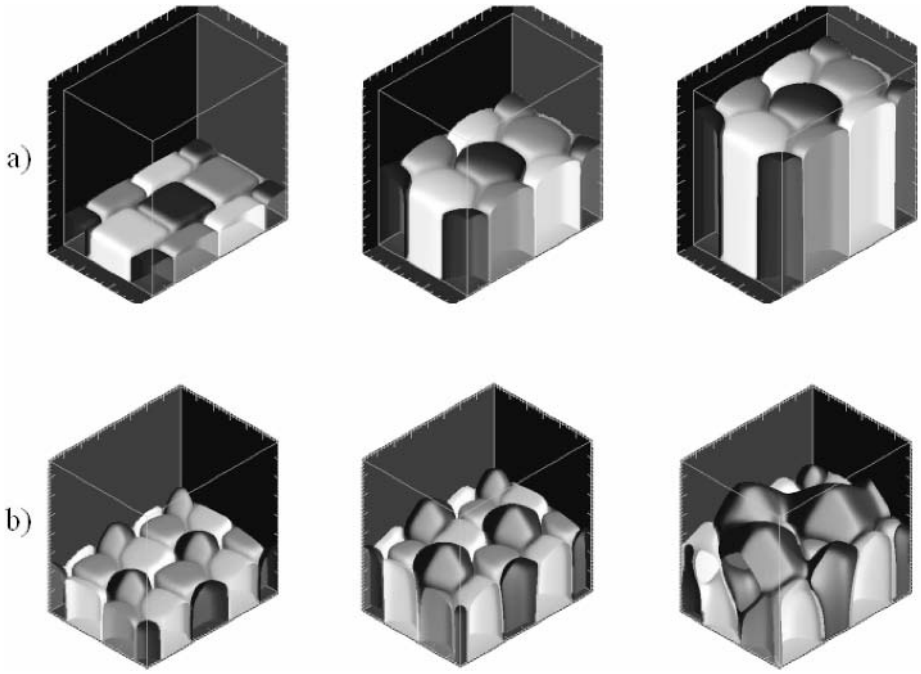

Fig. 5 a) Formation of regular hexagonal rods of alternating solid phases in a symmetric ternary eutectic alloy with isotropic surface energies. b) Formation of strong facets for a crystal evolution with crystalline surface energy anisotropies and different orientations of the three solid phases α, β and γ. The crystal anisotropy has a cubic symmetry.

with its crystal orientation lying in growth directions dominates the microstructure evolution and overgrows the less optimally oriented crystals.

8.4 Outlook

By presenting the phase-field model in its general form, we have indicated the broad potential of possible applications in future work. In a forthcoming paper, a special emphasis of the numerical computations is to analyze the stability of different series of lamellar eutectic phase configurations, e. g. $(\alpha|\beta|\gamma|\alpha|\beta|\gamma|...)$ and $(\alpha|\beta|\alpha|\gamma|\alpha|\beta|...)$. The numerically proposed stability results will be compared with an analytical generalization of the Jackson-Hunt theory to ternary eutectics. Spacing – undercooling relations are discussed for different permutations of the three solid phases.

The application of phase-field simulations to model complex multiscale growth phenomena including several different length and time scales is currently in progress. Examples are the growth of eutectic colonies resulting from small amounts of

ternary impurities and the formation of dendritic networks with interdendritic eutectic substructures. In order to quantitatively describe phase transformations and solidification processes in multicomponent alloys, it is planned to incorporate specific phase diagrams into the phase-field model via the free energies by linking the governing equations to a thermodynamical data base. Another challenge for future work is to include convection into the phase-field model, to investigate the interaction of different physical fields and their effect on the microstructure evolution.

Acknowledgements

The author gratefully thanks Harald Garcke and his group for collaboration over many years. The financial support through the German Research Foundation within the two priority research programs: Phase transitions in multicomponent melts (SPP 1120) and Multiscale problems (SPP 1095) is very gratefully acknowledged.

References

1. Journals

a) with volume number

I. Steinbach, F. Pezolla B. Nestler et al., Physica D 1996, 94, 135–147.

B. Nestler, A. A. Wheeler, Phys. Rev. E 1998, 57, No. 3, 2602–2609.

H. Garcke, B. Nestler, B. Stoth, Interfaces and Free Boundaries 1999, 1, 175–198.

H. Garcke, B. Nestler, Math. Models and Methods in Applied Sciences 2000, 10, No. 6, 895–921.

B. Nestler, A. A. Wheeler, Physica D 2000, 138, 114–133.

B. Nestler,A. A. Wheeler, L. Ratke, C. Stoecker, Physica D 2000, 141, 133–154.

b) without volume number

H. Garcke, B. Nestler, B. Stinner, SIAM J. on Appl. Math. 2004, in print

9
Modeling of Heat and Solute Flows during Solidification of Droplets

R. Heringer, Ch.-A. Gandin, G. Lesoult, H. Henein

Abstract

The solidification of a spherical droplet produced by atomization is studied. Experimental investigation reveals the presence of a macrosegregation, i.e. a segregation taking place at the scale of the particle. A model is developed for the prediction of heat and solute diffusive flows during solidification of an undercooled melt. It is applied to a spherical domain that represents an individual droplet. The range of variation of the composition within the droplet predicted by the model is in agreement with the experimental observation.

9.1
Introduction

Little modeling work is available for the prediction of solidification features of technological relevance of powders produced by melt atomization. Recent experimental results [1] have yet shown that the volume fraction of phases measured in atomized Al-Cu droplets can exhibit deviations with respect to the prediction of usual microsegregation models [2].

Heat flow modeling of a solidifying droplet is found in the literature with either a uniform temperature approximation [1, 3–4] or omission of the mushy zone [4–6]. A model has also been developed by Steinbach et al. in which the heat flow is solved in the liquid surrounding an envelope that represents the extent of the mushy zone [7]. However, it considers a pure material with a constant mushy zone temperature equal to the melting point.

Segregation measurements performed on a 250 μm-diameter particle produced by atomization of an Al-10wt%Cu melt are first presented. Solute heterogeneity is revealed at the scale of the particle. A model is developed based on diffusive flows. The model predicts macrosegregation, ths extending the heat flow analysis proposed by Heringer et al. [8].

9.2 Experimental

Impulse atomization has been conducted in nitrogen on an Al-10wt%Cu melt [1]. Figure 1a presents the dendritic microstructure of a 250 μm-diameter particle observed under a scanning electron microscope. The corresponding segregation map is shown in Figure 1b. It is deduced from microprobe analyses: measurements with a 1 μm-diameter focused beam have been performed on a 4 μm square grid. A large scatter of the composition map is found when simply drawing the 3204 collected data points. This behavior was obviously expected since the focused beam hits either the core of a dendrite arm (in grey in Figure 1 a), a eutectic area (in white in Figure 1 a) or both. Consequently, in order to draw an average composition map over a representative volume of the microstructure, the following filter was applied: on each of the 3204 positions of the square grid, an average value of the composition is calculated by considering all measured values falling within a circle the center of which corresponds to the square grid position. Little variation of the average composition map was found when changing the circle size within 20 μm to 40 μm-radius. Therefore, the value of 30 μm was kept as a reasonable value for the drawing of a meaningful segregation map.

Figure 1 b presents the result of this analysis. The local average composition varies from 7.5 wt% to almost 12 wt%. No obvious direct correlation between the segregation map and the microstructure map is revealed. However, careful comparison between the phase fractions in different regions shows that the volume fraction of eutectic is less where the solute composition is lower.

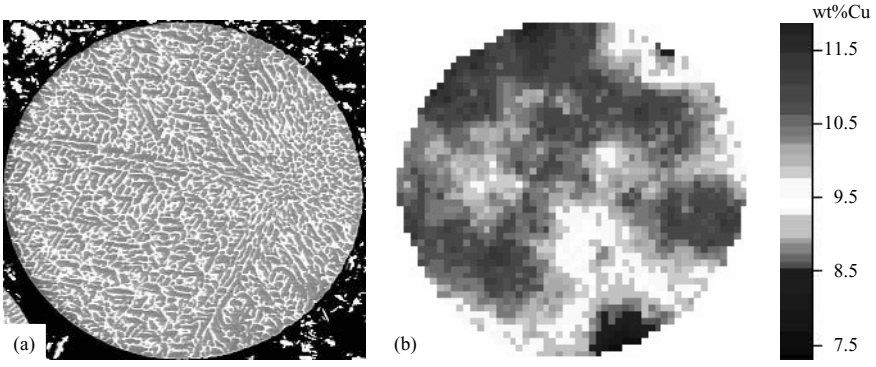

Fig. 1 Cross section of a 250 μm-diameter particle produced by atomization in nitrogen of an Al-10wt%Cu melt: (a) SEM observation of the microstructure and (b) corresponding segregation map deduced from microprobe analysis.

9.3 Modeling

9.3.1 Macroscopic Heat and Solute Flows

The model is based on a solution of the conservation equations for energy and mass fraction of solute written for a representative elementary volume (REV) made of a two-phase mixture (i.e., the mushy zone). The assumptions related to the geometry and the transport phenomena are the following:

h1. Limited representation of the mushy zone using the average volume fraction of the solid and liquid phases, g^s and g^l, with $g^s + g^l = 1$.
h2. Droplet geometry simplified by a spherical domain of radius R.
h3. One-dimensional heat and solute flows along the space coordinate r, with $r \in [0, R]$.
h4. Diffusive flows for both heat and solute (i.e., constant and equal values of the density of the solid and liquid phases).
h5. No diffusion in the solid phase in accordance with Equation (2).

According to the above assumptions, the conservation equations can be written as follows:

$$\frac{\partial \bar{H}}{\partial t} = \frac{1}{r^2}\frac{\partial}{\partial t}\left(\kappa r^2 \frac{\partial T}{\partial r}\right) \tag{1}$$

$$\frac{\partial \bar{w}}{\partial t} = \frac{1}{r^2}\frac{\partial}{\partial r}\left(\frac{(1-g^s)D^1 r^2 \partial \bar{w}^l}{\partial r}\right) \tag{2}$$

with:

$$\bar{H} = \bar{C}_p T + (1-g^s)\,L \tag{3}$$

$$\bar{w} = g^s\,\bar{w}^2 + (1-g^s)\,\bar{w}^1 \tag{4}$$

where $\bar{H}$ is the average volumetric enthalpy, T is the temperature, L is the volumetric latent heat of fusion and t is the time. The average composition of the two-phase mixture, $\bar{w}$, is a function of the average solid composition, $\bar{w}^s$, and the average composition of the liquid, $\bar{w}^l$. The thermal properties of a phase $\varphi \in [s, l]$ are the volumetric heat capacity, C_p^φ, and the thermal conductivity, κ^φ. The corresponding average properties of the mushy zone, $\bar{C}_p$ and $\bar{\kappa}$, are calculated with the relationships:

$$\bar{C}_p = g^s C_p^s + (1-g^s)C_p^1 \tag{5}$$

$$\bar{\kappa} = g^s \kappa^s + (1-g^s)\kappa^l \tag{6}$$

The diffusion coefficient of solute, D^{φ} is calculated using a pre-exponential factor, D_0^{φ}, and an activation energy, Q^{φ}, entering the Arrhenius law:

$$D^{\varphi} = D_0^{\varphi} \exp\left(-\frac{Q^{\varphi}}{RT}\right) \tag{7}$$

The volume fraction of solid, g^s, is a function of both the volume fraction of the mushy zone, g^m, and the internal volume fraction of solid located within the mushy zone, g^{sm}:

$$g^s = g^m g^{sm} \tag{8}$$

These two volume fractions are determined for each volume associated with a given position thanks to a front tracking technique and a microsegregation model as explained hereafter.

9.3.2
Front Tracking and Growth Velocity

The following additional assumptions are made to calculate the fraction of the mushy zone, g^m:

h6. Nucleation at the centre of the spherical domain, $r = 0$, at a given undercooling, ΔT_N, of a single grain.
h7. Radial propagation of the mushy zone.
h8. Dendrite tip temperature, T_d, equals to the local temperature, T, at the position where the growth front is located.

The limit of the envelop defined between the spherical mushy zone and the surrounding undercooled liquid in which it propagates, r_d, is made of dendrite tips. With h3, h6 and h7, the volume fraction of the mushy zone is a direct function of the position of the growth front:

$$g^m = g^m(r_d) \tag{9}$$

Calculation of the position of the growth front, r_d, is conducted by the integration over time of the growth velocity of the dendrite tips, v_d, from the onset of solidification, t_N:

$$r_d(t) = \int_{t_N}^{t} v_d(T_d)\, d\tau \tag{10}$$

The velocity of the dendrite tips is calculated as a function of the temperature of the dendrite tips, T_d, using the following relationship:

$$v_d = \frac{A}{B + w_0} [T_L - T_d]^n \tag{11}$$

$$T_d = T \tag{12}$$

where A, B and n are constants determined by a fit of the velocity-temperature curve deduced from the Kurz et al. [9] model for the alloy of nominal composition, w_0. In the later model, only the solutal and curvature undercoolings have been accounted for. Equation (12) is simply the mathematical translation of assumption h8.

9.3.3
Microsegregation and Mushy Zone Solidification

A microsegregation model is used to calculate the internal volume fraction of solid located in the mushy zone, g^{sm}, as well as the average composition of the solid phase, $\bar{w}^s$, by considering the following additional assumptions:

h9. Uniform composition of the liquid of the mushy zone, w^l.
h10. Local equilibrium at the solid/liquid interface ***during solidification***: for an increase of the volume fraction of solid, the compositions at the solid/liquid interface in the solid, $w^{s/l}$, and in the liquid, $w^{l/s}$, are given by the phase diagram, with $w^{s/l} = k\, w^{l/s}$.
h11. Linear approximation of the binary phase diagram with liquidus slope, m, melting temperature, T_M and segregation coefficient, k.
h12. The average composition entering Equation 4 is also used to write a solute balance at the scale of the mushy zone.

According to the above assumptions, one can write:

$$\frac{d}{dt}(g^{sm}\bar{w}^s) = k\, w^{l/s} \frac{dg^{sm}}{dt} \tag{13a}$$

$$\bar{w} = g^{sm}\bar{w}^s + (1 - g^{sm})\, w^l \tag{14}$$

$$w^l = w^{l/s} \tag{15}$$

$$w^{l/s} = (T - T_M)/m \tag{16}$$

During remelting of the mushy zone (i.e., $g^m = 1$, $g^s = g^{sm}$, $\bar{w}^l = w^l$) while the composition of the interdendritic liquid, w^l, is still calculated using assumptions h9–h11 and thus applying Equations (14–16), the average composition of the solid is interpolated over the composition profile $\bar{w}^s(g^s)$ stored during solidification. Thus, Equation (13 a) is replaced by:

$$\bar{w}^s = \bar{w}^s(g^s) \tag{13b}$$

It should be outlined that such a treatment of remelting does not anymore require knowing the value of the solid composition at the solid/liquid interface.

9.3.4 Initial and Boundary Conditions, Numerical Implementation

The initial and boundary conditions to the heat and solute flows write:

$$T(r, t = 0) = T_0 \tag{17}$$

$$-\bar{\kappa}\,(\partial T/\partial r)_{r=0} = 0 \tag{18}$$

$$-\bar{\kappa}\,(\partial T/\partial r)_{r=R} = h\,[T(r = R, t) - T_e] \tag{19}$$

$$\bar{w}(r, t = 0) = w_0 \tag{20}$$

$$(\partial \bar{w}/\partial r)_{r=0} = 0 \tag{21}$$

$$T(r = 0, t = t_N) = TL - \Delta T_N \tag{22}$$

where T_0 is the initial temperature and w_0 is the nominal composition of the alloy. As can be seen, adiabatic conditions are applied at the center of the droplet for both solute and heat flows. Convection at the surface of the droplet is accounted for by considering a constant heat transfer coefficient, h, and a fixed temperature of the external medium surrounding the droplet, T_e. The unknown in Equation (22) is the time at which nucleation takes place, t_N, for a fixed value of the nucleation undercooling. It obviously depends on the temperature history at the center of the domain and thus on the heat flow through the surface of the droplet.

The finite volume method is used with a regular one-dimensional fixed mesh [10]. The time integration is based on a fully implicit scheme. Enthalpy is chosen as the main variable, while the temperature entering Equation (1) is replaced using a linear relationship $T = T^{\#} + (dT/d\bar{H})^{\#}\,(\bar{H} - \bar{H}^{\#})$, where symbol # refers to the last known value of the variable in an iterative procedure [12]. Definition of the average volumetric enthalpy is used for the calculation of the linear relationship, leading to $dT/d\bar{H} = [\bar{C}_p - (dg^s/dT)\,L]^{-1}$. In fully liquid and fully solid volumes, the later ratio simplifies to $dT/d\bar{H} = [C_p^{\varphi}]^{-1}$, with $\varphi = [s, l]$. An isothermal transformation is assumed for the eutectic microstructure, which is simulated by fixing a sufficiently small value for the ratio $dT/d\bar{H}$ (e. g., $[10\,C_p^{l}]^{-1}$), thus artificially imposing the eutectic temperature, T_E, until the volume is fully solid. Concerning Equation (2), the formulation proposed by Prakash and Voller [11] has been implemented in order to calculate the average composition, w. The three main steps of the iterative procedure consists of solving the heat flow equation assuming an initial value of $(dT/d\bar{H})^{\#}$, the solute flow equation assuming an initial value of $(\bar{w}^{l})^{\#}$, and then all other variables. Iterations are performed up to the convergence of both the temperature and the average composition fields.

The algorithm corresponding to the above treatment is new compared to the methods described in the literature for tracking the position of the dendritic growth front defined by a boundary between an alloyed mushy zone and an undercooled liquid [12–15]. It presents the advantage to treat a non uniform temperature field while the propagation of the growth front within a fixed mesh does not occur at a fixed temperature, e.g., using a vertical truncation of the solidification path. This is a requirement when dealing with a situation of unconstrained growth that leads to reheating of the alloy (positive slope of the curve $g^{sm}(T)$) that prevails during droplet solidification.

Tab. 1 Values of the properties and parameters used for the simulation for an Al-10wt%Cu alloy.

Property/ Parameter	*[Unit]*	*Value*	*Property/ Parameter*	*[Unit]*	*Value*
T_M	[K]	933.6	$C_p^s = C_p^l$	[J m^{-3} K^{-1}]	$3.0 \cdot 10^6$
TE	[K]	817.74	L	[J m^{-3}]	$9.5 \cdot 10^8$
m	[wt% K^{-1}]	–3.37	κ^s	[W m^{-1} K^{-1}]	192.5
k	[–]	0.17	κ^l	[W m^{-1} K^{-1}]	100.
w_0	[wt%]	10.	h	[W m^{-2} K^{-1}]	490.
T_L ($T_M + mw_0$)	[K]	899.9	T_e	[K]	373.
R	[m]	$125 \cdot 10^{-6}$	T_0	[K]	900.9
A	[m s^{-1} K^{-n} wt%]	$2.64 \cdot 10^{-5}$	ΔT_N	[K]	30.
B	[wt%]	–2.6	D_0^l	[m^2 s^{-1}]	$1.05 \cdot 10^{-7}$
n	[–]	2.7	Q^l	[J mol^{-1} K^{-1}]	23804.

9.4 Results

The model is applied to a 125 μm radius size Al-10wt%Cu droplet. The value of the heat transfer coefficient is estimated using the model developed by Wiskel et al. [16]. A 30 K undercooling is chosen for the onset of solidification. Values of the properties and parameters used for the simulation are listed in Table 1. Profiles within the droplet at several times and time evolutions are drawn in Figure 2–4 in order to explain the overall dynamic of the solidification of an undercooled droplet simulated by the model.

Figure 2 a presents the temperature profiles at several time during the propagation of the mushy zone. It is clearly shown that, as soon as nucleation takes place at the center of the droplet (e.g., at 0.0157 s), a temperature increase of the mushy is predicted. It rapidly reheats the whole system. This reheating is due to the latent heat released by the growing mushy zone, which is not counterbalanced by the heat flux imposed at the surface of the droplet. In this figure, the position of the growth front is directly made visible by the profile break down: an almost uniform temperature is found in the mushy zone, whereas a negative temperature gradient ahead of the growth front is predicted. This observation is confirmed by the superimposed tem-

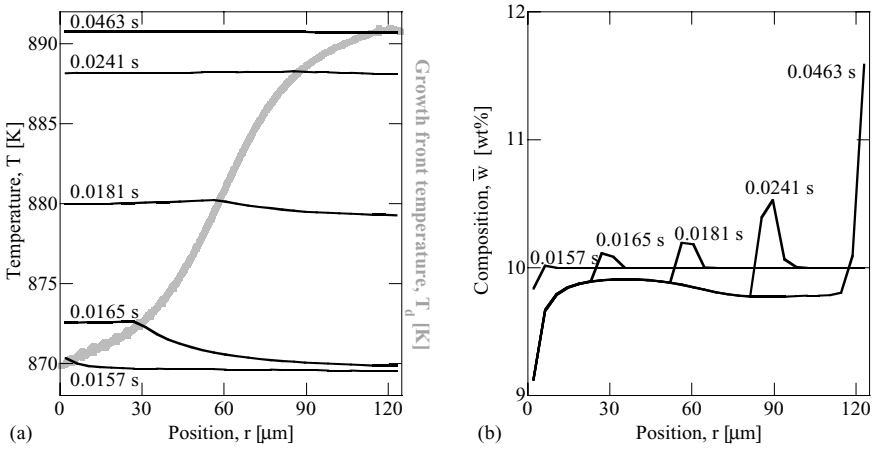

Fig. 2 Profiles of (a) temperature and (b) average composition at several times in an Al-10wt%Cu droplet. The grey curve in (a) shows the temperature evolution of the dendritic growth front as a function of its position during its propagation from the center of the droplet, r = 0 μm, to its periphery, r = 125 μm.

perature at the growth front since it coincides with the position of this break down. It also shows that the highest temperature at a given time is always predicted at the growth front.

The temperature gradient at 0.0165 s ahead of the growth front is of the order of $-10^5\,\mathrm{Km}^{-1}$. It rapidly vanishes during the propagation of the mushy zone and the maximum temperature difference across the whole droplet reaches a few degrees only (typically 2.5 K at 0.0165 s).

The integration of the enthalpy profile over the entire droplet is performed for the calculation of the average volumetric enthalpy of the droplet, $\bar{H}_D$. This allows the estimation of an average droplet temperature, T_D, by using the following heat balance: $\bar{H}_D = \bar{C}_{pD}TD + (1 - g_D^s)L$ where $\bar{C}_{pD}$ is the heat capacity per unit volume whose value is chosen constant and equal in the solid and liquid phases (Table 1) and g_D^s is the volume fraction of the solid in the droplet, i.e. in the whole spherical domain. Figure 3a presents the evolution of both the average volumetric enthalpy of the droplet, H_D, and the corresponding average droplet temperature, T_D. The observations conducted in Figure 2a are retrieved: as soon as the nucleation temperature is reached, a sudden recalescence takes place. It only finishes at the time when the mushy zone approaches the periphery of the spherical domain, i.e. at 0.0463 s. The enthalpy of the droplet decreases almost linearly in Figure 3a. This is due to the fact that an almost constant heat extraction rate, (h [T (r = R,t) – Te] 3/R), is found when T (r = R,t) $\gg$ Te.

The time evolution of the enthalpy and volume fraction of solid are presented in Figures 4a and 4b at the center (r/R = 0), mid-radius (r/R = 0.5) and at the periphery of the droplet (r/R = 1). It can be seen that the intrusion of the mushy zone is accompanied by a sudden decrease of the enthalpy. This is explained by the corresponding

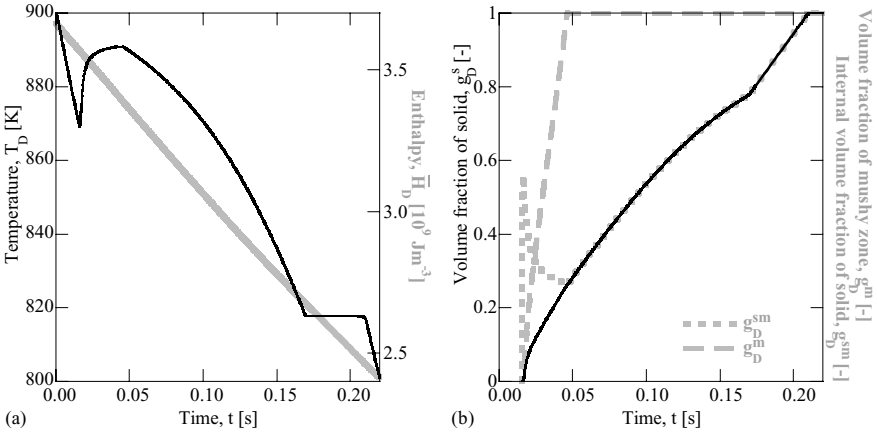

Fig. 3 Time evolutions of quantities averaged over the entire droplet: (a) temperature, enthalpy (dashed grey), (b) volume fraction of solid, volume fraction of the mushy zone (doted grey) and internal volume fraction of solid (dashed grey).

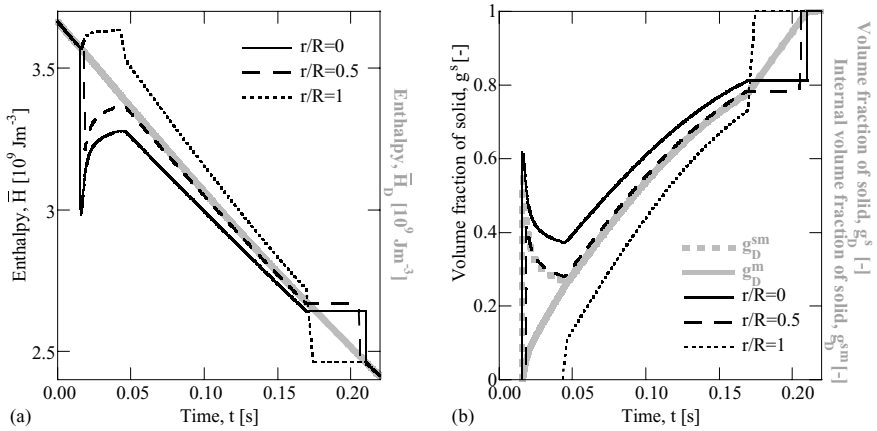

Fig. 4 Time evolutions of (a) the enthalpy and (b) the volume fraction of solid at the center (plain line), at mid-radius (dashed line) and at the surface (doted line) of the solidifying droplet. Additional grey curves correspond to the time evolution of quantities averaged over the entire droplet: (a) enthalpy, (b) volume fraction of solid (dashed line) and internal volume fraction of solid (doted line).

sudden increase of the volume fraction of solid. The same observations can be made for the eutectic transformation. It is noticeable that the eutectic starts to form close to the periphery prior to develop toward the center of the droplet. Such reversion of the propagation of the growth front is due to simple heat flow considerations: the eutectic temperature is reached first at the periphery of the spherical domain.

The local reheating of the mushy zone during its propagation (Figure2 a) results in a local decrease of the volume fraction of solid (Figure 4 b), while the average volumetric enthalpy increases (Figure 4 a). Only the volume located at the periphery of the droplet does not experience remelting (r/R = 1). Since the temperature variation from the center to the outer surface of the droplet is limited (Figure 2 a), the curves predicted in Figure 4 would be almost superimposed in case of no macrosegregation. However, due to solute diffusion in the inter- and extra-dendritic liquid regions, the average composition of the droplet varies from 9 wt% at the center to 12 wt% at the periphery. This difference is sufficiently large to form a volume fraction of eutectic that varies from 0.27 at the center to 0.19 at the periphery, while the overall eutectic fraction, 0.22, remains close to the value predicted by the Scheil calculation when considering the nominal composition of the alloy. In order to explain the built-up of the macrosegregation, one can consider the composition profiles drawn in Figure 2 b at several times. While a solute layer forms in the liquid ahead of the growth front, the average composition in the mushy zone is lower than the nominal composition. It remains almost constant during subsequent remelting/solidification. This is due to the fact that the driving force for solute diffusion in the interdendritic liquid is the temperature gradient according to Equation (13 c and 13 d), which is found to remain very limited in the mushy zone (Figure 2 a).

In Figure 3 b are drawn the volume fraction of the mushy zone, g_D^m, the volume fraction of the solid, g_D^s , and the internal volume fraction of the solid, g_D^{sm}, calculated for the whole droplet. The main purpose of these curves is the comparison with previously developed models in which all these quantities are only calculated at the scale of the droplet [13, 15]. A first comparison conducted by Heringer et al. [8] showed a

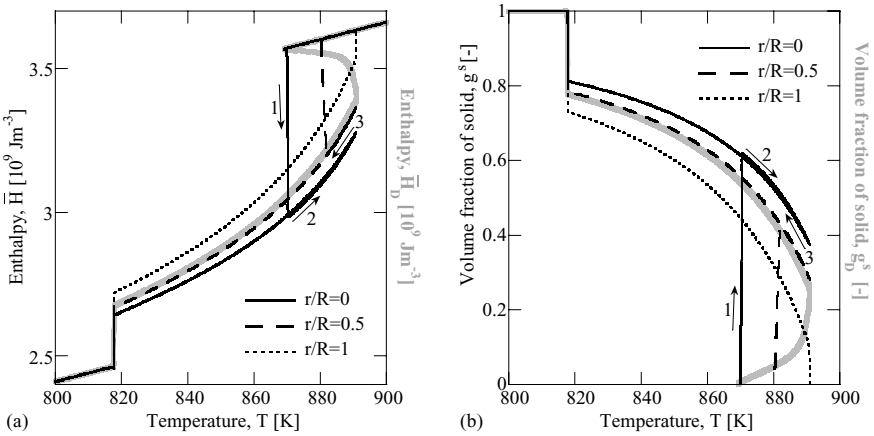

Fig. 5 Temperature evolution of (a) the enthalpy and (b) the volume fraction of solid at the center (plain line), at mid-radius (dashed line) and at the surface (doted line) of the solidifying droplet. Additional grey curves correspond to the evolution of quantities averaged over the entire droplet: (a) enthalpy, (b) volume fraction of solid, as a function of the averaged temperature.

good agreement. Superimposition of these quantities in Figure 4b also shows that large deviations can be expected with the center and the periphery of the droplet.

The resulting enthalpy and solidification paths versus temperature are drawn in Figure 5a and 5b, respectively. Typical back and forth behaviors are predicted: at first the volume fraction of solid increases while the enthalpy decreases abruptly during the propagation of the growth front (arrows labeled 1). During the subsequent increase of the temperature due to the reheating of the whole mushy zone, the volume fraction of solid decreases while the enthalpy increases (arrows labeled 2). Finally, once fully mushy, further cooling simply leads to an increase of the volume fraction of solid in the entire droplet (arrows labeled 3).

9.5 Concluding Remarks

According to the model presented above, the main explanation for the macrosegregation map and the eutectic distribution observed in a particle of powder produced by atomization is the diffusion of solute in the liquid phase. Such diffusion-driven segregation is nothing but the basis of the equiaxed solidification models previously developed by Rappaz and Thévoz [13] and Wang and Beckermann [15]. It leads to a negative segregation in the growing mushy zone due to a solute build-up ahead of the growth front. Thus, the phenomenon must be seen as different from the main cause leading to macrosegregation in casting proposed by Flemings and Nereo [17]. Indeed, the effect of fluid flow due to shrinkage is neglected in the present model and would have led to an inverse segregation, i.e. a positive segregation in the growing mushy zone. In fact, the competition of both effects could be introduced if one considers a model with different values of the solid and liquid densities while accounting for the development of an undercooled growth front. The effect of diffusion in the present configuration of droplet solidification is yet believed to be predominant and explains the choice of the assumptions of the model, in continuation with previous works [13, 15].

Another interesting result is the remelting that accompanies recalescence. Such an expected phenomenon might be seen as one of the basic causes of the fragmented microstructure that is observed in solidified powders. Further work could be considered in this direction based on the present model.

Precise quantitative comparisons between measured and predicted macrosegregation maps and the eutectic distributions are still missing. Although qualitative agreement is achieved, the model should be extended. In particular, the assumption concerning the geometrical propagation of the mushy zone is not realistic since nucleation most probably takes place close to the surface of the droplet. Further extension of the model should also consider the coupling with thermodynamic calculations for a better description of the phase diagram properties and dendrite growth kinetics, as well as kinetics effects that would play an important role at larger growth velocity, i.e. larger nucleation undercooling.

Acknowledgements

R. Heringer is supported by the CAPES Foundation, Brazil.

References

[1] A. Prasad, H. Henein, Ch.-A. Gandin, Light Metals 2002, Metallurgical Society, Montréal, CAN, 2002.

[2] W. Kurz, D. J. Fisher, Fundamentals of Solidification, Trans Tech Pub., Aedermannsdorf, CH, 1998.

[3] G. M. Matson, M. Rolland, M. C. Flemings in Solidification 1998 (Ed.: S. P. Marsh, J. A. Dantzig, R. Trivedi, W. Hofmeister, M. G. Chu, E. J. Lavernia, J.-H. Chun), TMS, Warrendale, PA, USA, 1998, p. 275.

[4] C. G. Levi, R. Mehrabian, Metallurgical Transactions A 1982, 13, 221.

[5] S.-G. Kim, S.-H. Shin, T. Suzuki, T. Umeda, Metallurgical Transactions A 1994, 25, 2815.

[6] V. S. Ajaev, S. H. Davis, Journal of Computational Physics 2003, 187, 492.

[7] I. Steinbach, C. Beckermann, B. Kauerauf, Q. Li, J. Guo, Acta Materialia 1999, 47, 971.

[8] R. Heringer, Ch.-A. Gandin, G. Lesoult, in Modeling of Casting, Welding and Advanced Solidification Processes X (Ed.: D. M. Stefanescu, J. A. Warren, M. R. Jolly, M. J. M. Krane), TMS, Warrendale, PA, USA, 2003, p. 549.

[9] W. Kurz, B. Giovanola, R. Trivedi, Acta Metallurgica 1986, 34, 823.

[10] S. V. Patankar, Numerical Heat Transfer and Fluid Flow, Hemisphere Pub. Co., NY, 1980.

[11] C. Prakash and V. Voller, Numerical Heat Transfer 1989, 15B, 171.

[12] M. M'Hamdi, H. Combeau, G. Lesoult, International Journal of Numerical Methods for Heat & Fluid Flow 1999, 9, 296.

[13] M. Rappaz, Ph. Thévoz, Acta Metallurgica 1987, 35, 2929.

[14] Ch.-A. Gandin, Acta Materialia 2000, 48, 2483.

[15] C. Y. Wang, C. Beckermann, Metallurgical and Materials Transactions A 1994, 25, 1081.

[16] J. B. Wiskel, H. Henein, E. Maire, Canadian Metallurgical Quarterly 2002, 41, 97.

[17] M. C. Flemings and G. E. Nereo, Trans. Met. Soc. AIME 1967, 239, 1449.

[18] A. Karma, International Journal of Non-Equilibrium Processing 1998, 11, 201.

10
Thermo-physical and Physical Properties for Use in Solidification Modelling of Multi-component Alloys

N. Saunders, Z. Guo, A. P. Miodownik and J-Ph. Schillé

Abstract

The thermo-physical and physical properties of the liquid and solid phases are critical components in casting simulations. Such properties include the fraction solid transformed, enthalpy release, thermal conductivity, volume and density, all as a function of temperature. Due to the difficulty in experimentally determining such properties at solidification temperatures, little information exists for multi-component alloys. As part of the development of a new computer programme for modelling of materials properties, JMatPro, extensive work has been carried out on the development of sound, physically based models for these properties. Wide-ranging results have previously been presented for Fe, Ni, Ti, Al and Mg-based alloys. The purpose of the present paper is to look at how changes in composition can substantially affect properties of multi-component alloys during solidification and further demonstrate how properties of the liquid can substantially vary in the mushy zone.

10.1
Introduction

In solidification modelling, there is often a requirement for high quality information concerning thermo-physical and physical properties. Some properties have been measured for specific alloys, but the number of alloys where information is available is limited. Furthermore, the information may be incomplete, in that not all properties measured and, sometimes, disparate information from a variety of sources is used to build up the data for a specific alloy. The latter method can inherit inconsistency as the composition of the alloys used to build up the property database may not be the same and various important temperatures (i.e. solidus, invariant reactions) may differ between the alloys. Furthermore, there may be variations linked to different experimental conditions.

An advantage of using a calculation route to provide properties is that the calculation is internally self-consistent. It can therefore provide extensive information on how the properties of an alloy may change within a specification range as well as

providing detailed information on the properties of the liquid phase in the mushy zone. Furthermore, it will be made clear from the examples presented in this paper that properties experimentally measured in the fully liquid state cannot be extrapolated into the mushy zone with any confidence. Such detail is important in modelling defect formation and is something that is usually beyond the capability of measurement.

The self-consistent calculation of thermo-physical and physical properties is further potentially important in determining unknown properties, such as the heat transfer coefficient at the ingot/mold interface, through inverse modelling. In this case, a full set of consistently calculated properties may lead to a more rigorous estimate and understanding of this property.

It is also noted that, sometimes, experimentally determined properties that are not appropriate to solidification are used. For example, solidus values that are more appropriate to the melting of heat-treated, homogenised alloys [1] rather than the solidus resulting from solidification [2] have been used for solidification modelling of the Ni-based superalloy 718 [3,4]. In this circumstance, the freezing temperature range is likely to be underestimated by more than a factor of 2. Similarly, thermal conductivities are available for 718 [5], but these will also be appropriate for homogenised alloys, rather than for solidification.

Previous modelling work [6,7,8,9,10,11,12,13] has shown that excellent results can be obtained for the phases formed during solidification, as well as their composition and temperature range of formation, by using thermodynamic modelling based on the CALPHAD [14] methodology. Such modelling can be further extended to calculate thermo-physical and physical properties over the complete relevant temperature range for a wide range of alloys [15,16,17,18,19]. The present paper briefly describes the methodology. A significant advantage of the current method is that properties for each phase are calculated so fine detail can be obtained: for example, the density change of the liquid during the solidification, which is governed both by an intrinsic change with temperature and by the composition changes that accompany solidification.

The current work forms part of the development of a more generalised software package (JMatPro) for the calculation of a wide range of materials properties. [19,20] A feature of the new programme is that great store has been placed on using models that, as far as possible, are based on sound physical principles rather than purely statistical methods. Thus, many of the shortcomings of methods such as regression analysis can be overcome. For example, the same models and input parameters are used for density calculations for all alloy types, whether it be for a commercially pure Al-alloy or a complex Ni-based superalloy.

10.2
Technical Background

10.2.1
The Scheil-Gulliver Approach with Modification for fast C and N Diffusion

The SG model can be considered as a complementary limiting case to equilibrium solidification whereby it is assumed that solute diffusion in the solid phase is small enough to be considered negligible and that diffusion in the liquid is extremely fast, fast enough to assume that diffusion is complete. Based on the premise that liquidus and solidus lines are linear, the composition of solid formed during solidification (C_o), as a function of the fraction of solid formed (f_s) can be expressed as

$$C_s = k\,C_o\,(1 - f_s)^{k-1} \tag{1}$$

where C_o is the composition of the alloy and k is the partition coefficient. From this the fraction solid formed as a function of temperature is given by [21]

$$f_s = 1 - \left(\frac{T_f - T}{T_f - T_L}\right)^{\left[\frac{1}{k-1}\right]} \tag{2}$$

where T_L and T_f are the liquidus and solidus temperature. The treatment above is the traditional derivation of the Scheil equation but it has quite severe restrictions when applied to multi- Page 2 component alloys. It is not possible to derive this equation, using the same mathematical method, if the partition coefficient, k, is dependent on temperature and/or composition. The Scheil equation is applicable only to dendritic solidification and cannot, therefore, be applied to eutectic alloys that are common type for Al and Mg-alloys. Further it cannot be used to predict the formation of intermetallics during solidification.

Using thermodynamic modelling all of the above disadvantages can be overcome. The process that physically occurs during 'Scheil' solidification can be envisaged as follows. A liquid of composition C_o is cooled to a small amount below its liquidus. It precipitates out solid with a composition $C_{S,1}$ and the liquid changes its composition to $C_{L,1}$. However, on further cooling the initial solid cannot change its composition due to lack of back diffusion and it is effectively 'isolated'. A local equilibrium is then set up where the liquid of composition $C_{L,1}$ transforms to a liquid of composition $C_{L,2}$ and a solid with composition $C_{S,2}$, which is precipitated onto the original solid with composition $C_{S,1}$. This process occurs continuously during cooling and, when $k < 1$, leads to the solid phase becoming lean in solute in the center of the dendrite and the liquid becoming more and more enriched in solute as solidification proceeds. Eventually, the composition of the liquid will reach the eutectic composition and final solidification will occur via this reaction.

Any appearance of secondary phases can be easily taken into account in this approach with the assumption that no back diffusion occurs in them. Therefore, all transformations can be accounted for, including the final eutectic solidification. The

approach described here is based on an isothermal step process but as the temperature step size becomes small it provides results that are almost completely equivalent to that which would be obtained from continuous cooling. A further and very significant advantage of using a thermodynamic approach is that the heat evolution during solidification is a straightforward product of the calculation.

The limit to the SG simulation is that some back diffusion will take place. However, if its degree is small, good results will still be obtained. For example, Backerud et al. [22] have experimentally studied almost 40 commercial alloys and calculated results have been compared to all of these. Results of the comparisons of fraction solid vs. temperature for some of these alloys are shown in Figure 1. The agreement is most striking and the level of accuracy achieved for these alloys is quite typical of that attained overall in the comparison. A further example is in Ni-based superalloys where differential thermal analysis (DTA) and microstructural studies were done for a 706 alloy and directly compared with calculations [11]. Figure 2 shows the calculated fractions solid vs. temperature plot, while Table I shows the agreement between calculated and experimentally determined critical temperatures. An advantage of the calculation method was the correct prediction that the ç phase would form during solidification. This was observed metallographically in cast alloys, but not determined experimentally by DTA, which was almost certainly because the experiment was insufficiently sensitive to differentiate both the Laves and η formation.

Tab. 1 Comparison between experimentally determined DTA results [11] and a Scheil-Gulliver simulation for a 706 alloy (temperatures all in °C)

	Liquidus	*MC start*	*Laves start*	*η start*	*Solidification end*
Centre (DTA)	1381	1240	1164		
Edge (DTA)	1388	1261			
Calculated	1388	1256	1168	1144	1128

A known weakness of the SG approach is for steels, where fast C and N diffusion causes the model to break down. However, it is noted that the SG model can be modified to take into account the effect of fast C and N diffusion so that steels can be considered [15]. Such a model (SGM) has been implemented in the software package JMatPro [19,20] by considering that C and N will diffuse sufficiently rapidly such that their composition in the growing austenite or ferrite phases will be equal to that of the solid at the growing solid/liquid interface. Within the current model, it is not yet possible to consider the solid state reaction between ferrite and austenite whereby the ferrite is consumed by the growing austenite in a peritectic reaction. However, the kinetics of this transformation may be slow enough such that it is reasonable to assume that the peritectic reaction is not completed during solidification. Having said this, it is clear that in many steels the SGM model provides results that are actually quite close to equilibrium where the full peritectic transformation is complete (Fig.3) and it may be that an equilibrium calculation is the most accurate model to use, as suggested by Saunders [6].

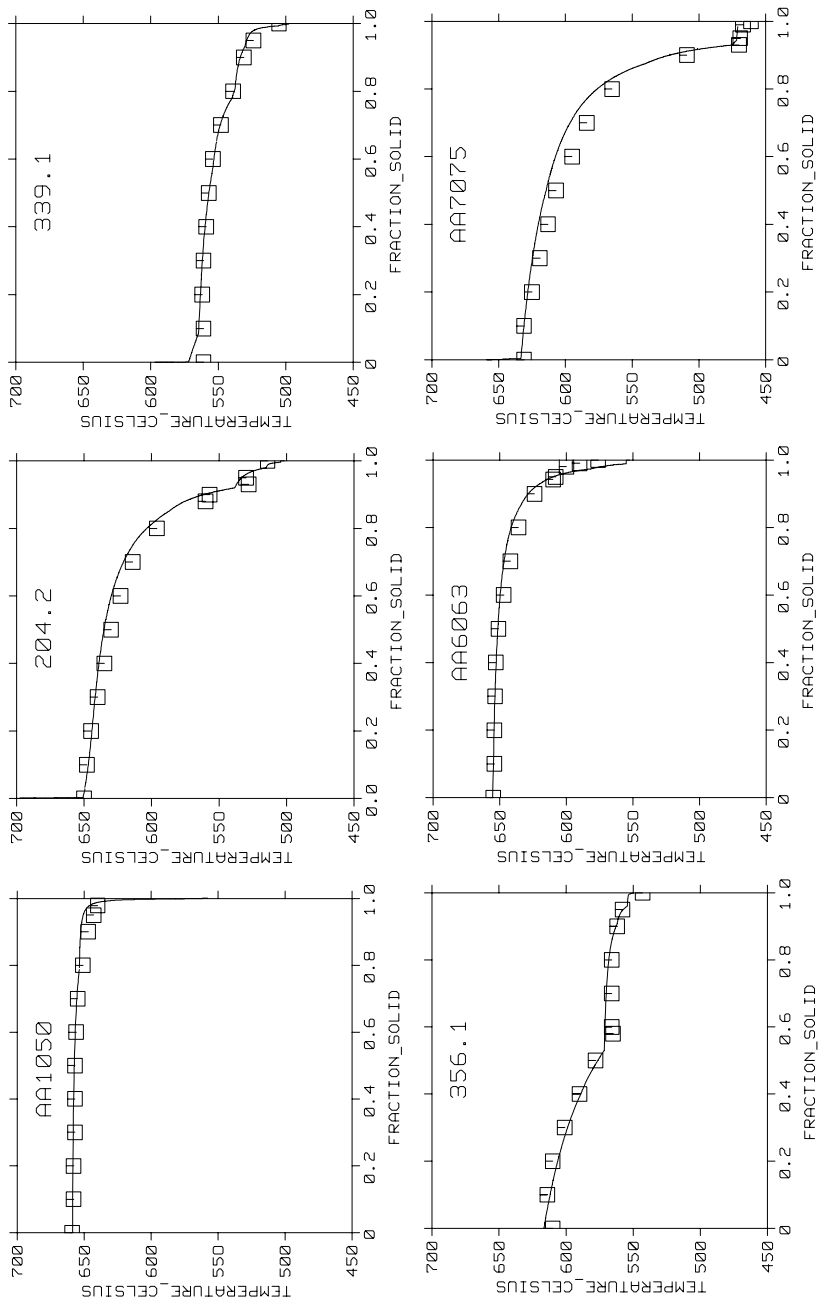

Fig. 1 Fraction solid vs. temperature plots for various Al-alloys calculated under ‚Scheil' conditions with experimental results (□) of Backeruid et al [22] shown for comparison.

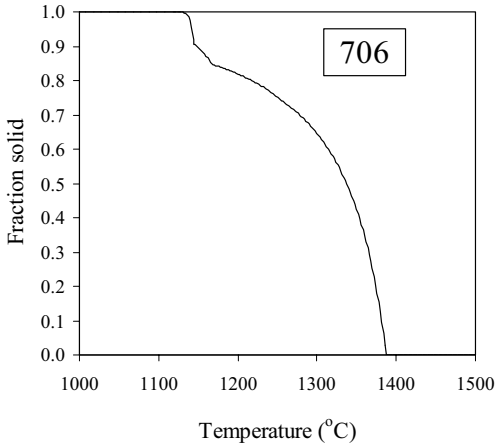

Fig. 2 Calculated fraction solid vs. temperature plot for solidification of alloy 706.

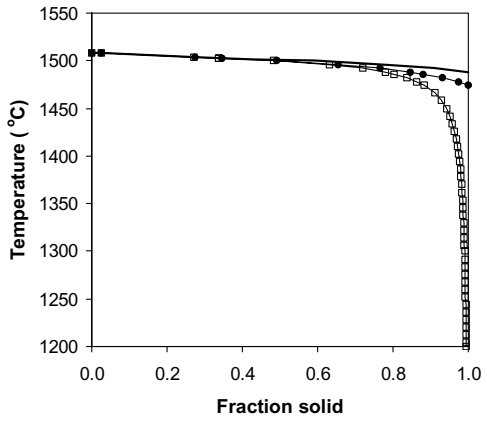

Fig. 3 Fraction solid vs. temperature curves for solidification of a 3310 steel calculated under (—) equilibrium, (□) SG and (●) SGM conditions [15].

10.2.2 Modelling of Physical Properties

A major achievement of the JMatPro software project has been the development of an extensive database for the calculation of physical properties that can be linked to its thermodynamic calculation capability. For individual phases in multi-component systems, properties, such as molar volume, thermal conductivity, Young's modulus, Poisson's ratio etc., are calculated using simple pair-wise mixture models, similar to those used to model thermodynamic excess functions in multi-component alloys [14]. It is possible to include ternary or higher order effects where appropriate. Once the property of the individual phase is defined, the property of the final alloy can be calculated using mixture models that can account for the effect of microstructure on the final property [23,24]. Such models, which were developed for 2-phase systems, have been extended to allow calculations to be made for multi-phase structures [25].

Extensive databases of relevant parameters now exist for most of the major phases in Al-, Fe-, Mg-, Ni- and Ti-alloys, which have been tested both in the liquid and solid state against experimental measurement [15,16,17,18,19,20]. Utilising well established relationships between certain properties, (e. g. thermal and electrical conductivity), minimises the number of property databases that need to be created and allows the following properties to be modelled – volume, density, expansion coefficient, Young's, bulk and shear moduli, Poisson's ratio, thermal conductivity and diffusivity, electrical conductivity and resistivity, liquid viscosity and diffusivity.

10.3 Example Calculations

The ability to calculate thermo-physical and physical properties at will for many type of alloy type is important for a number of reasons. Firstly, information can be readily gained for alloys where measurements are not available. Because there is a distinct lack of reliable measurements for solidification properties of many alloys, this is, in itself, a highly valuable capability. It is also possible to calculate quickly and self-consistently, how such properties may change as the alloy composition varies within the alloy specification. Further a great deal of detailed information comes with the current calculation route that is otherwise either impossible, or extremely difficult, to experimentally determine. For example properties of the liquid in the mushy zone, which is the controlling factor in many types of defect, e. g. freckles, macrosegregation, shrinkage porosity, etc.

10.3.1 Variations in Behaviour Within an Alloy Composition Specification Range

Because for the lack of data concerning thermo-physical and physical properties for multicomponent alloys, properties are often defined for a typical alloy. For example, as for the case of the 718 Ni-based superalloy mentioned in section 1. However, it is not always clear that a typical alloy can be defined. Certain alloys are rather sensitive to small composition variations, while others, for example solid solution alloys, may not be so sensitive. It may also be that the composition specification for that alloy is wide, which is the case for many well-known and wellused alloys. Some excellent examples of the varying behaviour of Al-alloys, of the same designation, are shown by Bakerud et al [22].

We will look here at the Al-alloy ADC12 (Japanese designation). This is a high Si and Cu alloy with quite high allowable levels of other elements such as Fe and Ni. Two compositions have been tested, one at the low level of specification for each element, the other the high level. While such a choice might be expected to show the largest difference in behaviour, it is not necessarily the case. Depending on partition behaviour and effect on invariant reactions, it is possible for an increase in one element to cancel out the effect of another. Having noted this, the difference in behaviour of the two ADC12 alloys is striking enough.

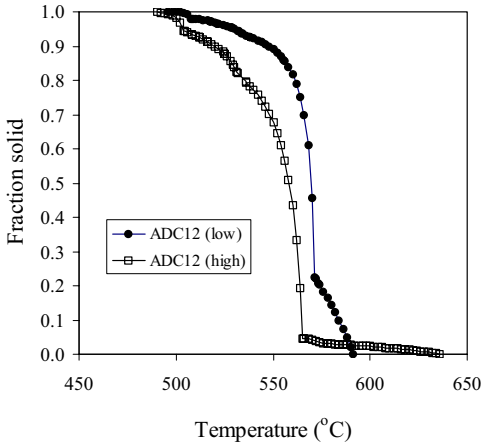

Fig. 4 Calculated fraction solid vs.temperature plots of two ADC12 Al-alloys.

Figure 4 shows fractions solid vs. temperature plots for the two alloys. The high specification (HS) alloy is hypereutectic, with primary Si and intermetallics forming over a significant temperature range, while the low specification alloy (LS) forms about 22% of primary Al. At the start temperature of eutectic solidification for the HS alloy (565 °C) the fraction solid for the LS alloy is ~65%, in comparison to ~5% for the HS alloy. The discrepancies between fraction solid at any temperature remain high for much of solidification, though both finally solidify via a eutectic involving Al2Cu. Due to the very different behaviour of the two alloys, there will be a subsequent effect on all of the properties as a function temperature. An example is the volume change (in the range 450–650 °C), which again for most of the temperature range is quite different for the two alloys (Figure 5).

In the fine detail there can be substantial differences between alloys, with much smaller composition variations producing quite substantial differences in behaviour of the physical property of the liquid. In this case we have taken the Al-alloy 356. In Figure 6 the density of an alloy with the composition Al-0.01Cu-0.2Fe-0.3Mg-

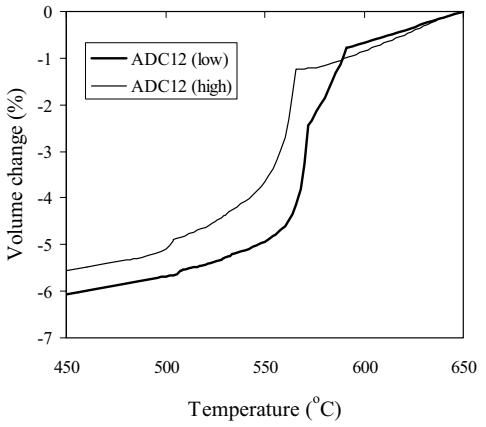

Fig. 5 Calculated volume change vs. temperature plots of two ADC12 Al-alloys.

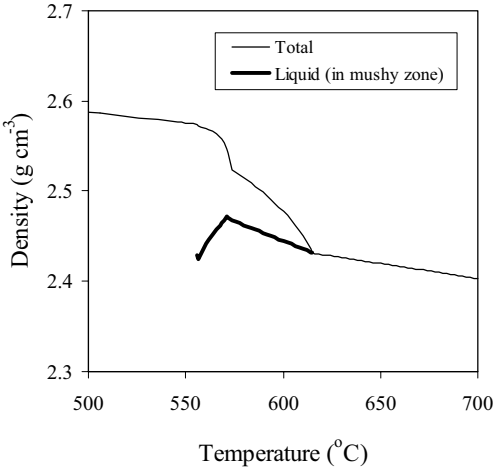

Fig. 6 Calculated density of a 356 Al-alloy (with low Cu, Mn and Zn) during solidification. Bold line shows density of the liquid in the mushy zone

0.02Mn-7Si-0.025Zn (wt%) is shown. In this circumstance, there is a slight density inversion as Mg segregates into the liquid below the Silicon eutectic. However, when Cu, Mn and Zn levels increase to higher levels (0.25%Cu, 0.3Mn, 0.35Zn) the behaviour of the liquid in the mushy zone dramatically changes (Figure 7). During the initial Al solidification the behaviour is little different than before however, the behaviour during the eutectic part of solidification is quite different with the liquid phase now becoming much more dense.

10.3.2
Behaviour of the Liquid in the Mushy Zone

Probably the two most important factors in liquid behaviour in the mushy zone are the density and viscosity. It is possible to measure these in the fully liquid state but

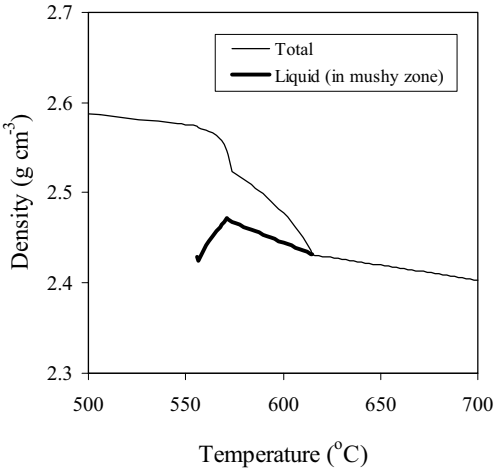

Fig. 7 Calculated density of a 356 Al-alloy (with high Cu, Mn and Zn) during solidification. Bold line shows density of the liquid in the mushy zone

extrapolation of such properties into the mushy zone is dangerous, primarily because the liquid composition changes quite markedly in the mushy zone with subsequent knock-on effects for liquid properties.

The behaviour of the 356 alloys shown in the previous section 3.1 demonstrated how significant variation occurs in the liquid density between alloys of only slightly different composition. However it can also be seen most clearly that the behaviour of the liquid in the mushy zone is markedly different to that extrapolated from the stable liquid. A series of examples will now be shown emphasising this fact.

In Ni-based single crystal superalloys, freckle formation is a significant problem and is caused by a density inversion in the liquid. This caused by segregation of heavy elements such as W and Re into the solid and light elements such as Ti and Al into the liquid. Some segregation of Ta occurs to the liquid, but is insufficient to counterbalance the effect of the other segregation. Figure 8 shows the calculated density of the liquid in the mushy zone for the alloy SRR 99 [18].

The case of SRR 99 is quite a severe case, but not uncommon in such alloys. However, there is a general problem if extrapolations of high temperature properties are used for other alloys, particularly if they have a long freezing range. Figure 9 shows the liquid density of a ZMC 711 Mg-alloy containing Cu and Zn. In this case both Cu and Zn segregate strongly into the liquid causing a rapid rise in density. At the end of solidification the density of the liquid approaches twice that of the original high temperature liquid. The total density of the alloy is counterbalanced by the formation of Mg solid which itself has a lower density than the liquid because almost all of the Cu and Zn segregate to the liquid. As well, the viscosity is strongly affected (Figure 10). In this case there is both the elemental segregation to the liquid increasing the viscosity as well as a natural increase with decreasing temperature causing the viscosity of the final liquid to be almost 5 times that of the high temperature liquid. In steels, freezing ranges can be quite narrow. However, C segregation into the liquid always occurs. Figure 11 shows the liquid density in a low alloy steel, showing the inversion caused by C segregation.

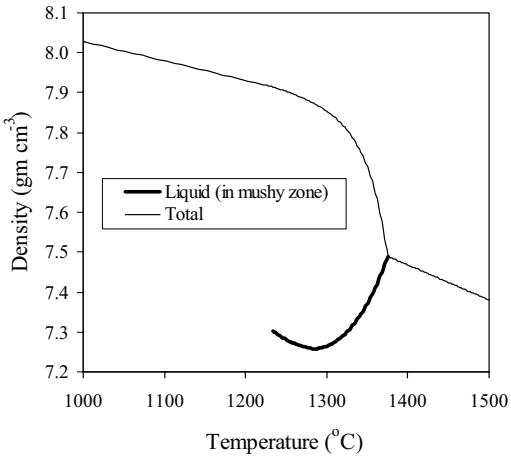

Fig. 8 Calculated density of a SRR99 single crystal superalloy during solidification [18]. Bold line shows density of the liquid in the mushy zone

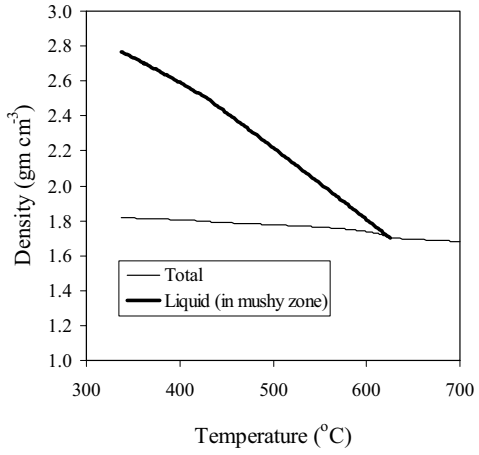

Fig. 9 Calculated density of a ZMC711 Mg-alloy during solidification. Bold line shows density of the liquid in the mushy zone

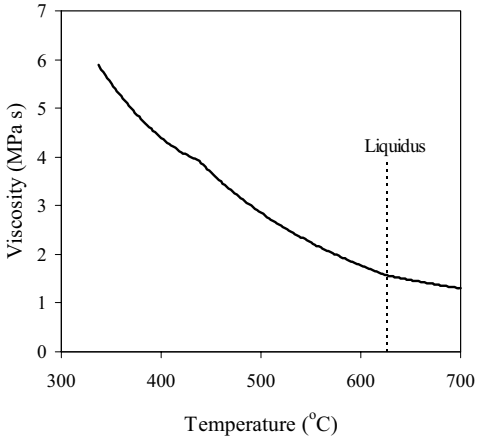

Fig. 10 Calculated viscosity of a ZMC711 Mg-alloy during solidification.

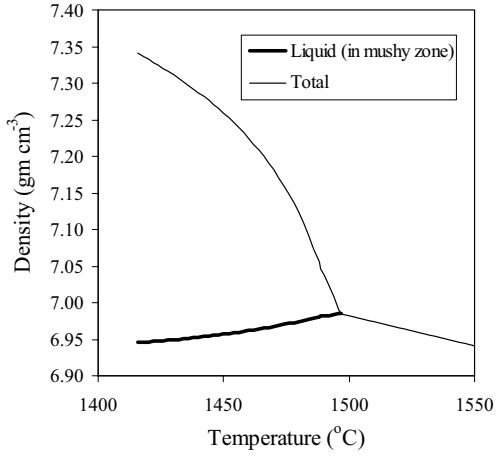

Fig. 11 Calculated density of a B ZMC711 Mg-alloy during solidification. old line shows density of the liquid in the mushy zone

10.4 Discussion

A series of calculations for the physical properties of Al, Fe, Mg and Ni-based alloys have been made and results displayed. The calculations accentuate the fact that the properties of an alloy can substantially change within a composition specification and extrapolation of high temperature liquid properties into the mushy zone will invariably be inaccurate.

To be able, at will, to calculate all critical physical properties during solidification with good reliability is a significant advance. It removes uncertainty both if new alloys are being used and where information concerning existing alloys is incomplete. Further, the calculations invariably provide greater detail than experiment.

While it is recognised that for low-level applications detailed physical properties may not alter casting simulations to a significant degree, for example in shell-freezing type simulations, the physical properties become increasingly important when greater detail is required or when problems to be solved become more complex. For example, for use in various defect models or if accurate cooling rates as a function of temperature are required or if liquid transport through interdendritic regions is being modelled, etc.

10.5 Summary and Conclusions

It is now possible to calculate thermo-physical and physical properties during solidification and previous validation work has shown that good results are obtained in comparison to experiment. This means that properties can now be calculated for many alloys where no experimental information exists. It further means that incomplete experimental information can be augmented and internally self-consistent input can be used as input for inverse models to estimate difficult properties such as heat transfer coefficient at the ingot/mold interface.

In the present paper it is further shown that

(1) substantial differences in properties may occur within a specification range of an alloy designation, and
(2) experimentally determined high temperature liquid properties cannot be extrapolated into the mushy zone with any confidence.
(3) Both of these problems can be overcome by using the present calculation method.

References

[1] P. N. Quested, K. C. Mills, R. F. Brooks. A. P. Day, R. Taylor and H. Szelagowski, *Proc. Conf. Liquid Metal Processing 1997,* Santa Fe, NM, U.S.A., Sept.16–19, American Vacuum Society, **1997**, 1.

[2] W. D. Cao, R. L. Kennedy and M. P. Willis, *Superalloys 718, 625 and Various Derivatives,* (Ed.: E. A. Loria), TMS, Warrendale, PA, **1991**, 147.

[3] W. Zhang, P. D. Lee and M. McLean, *Met. Mater. Trans. A*, **2002**, 33A, 1.

[4] R. M. Ward, M. D. Barratt, M. H. Jacobs and A. L. Dowson, *Proc. Conf. Liquid Metal Processing 2003*, Nancy, France, Sept.21–24, **2003**, 223.

[5] Data downloaded from web address http://metalcasting.auburn.edu/data/data.html.

[6] N. Saunders, *Solidification Processing 1997,* (Eds.: J. Beech and H. Jones), Univ. Sheffield, Sheffield, **1997**, 362.

[7] N. Saunders, *Materials Science Forum,* **1996**, *217–222,* 667.

[8] N. Saunders, *Light Metals 1997,* (Ed.: R. Huglen), TMS, Warrendale, PA, **1997**, 911.

[9] R. A. Harding and N. Saunders, *Trans. American Foundryman's Society,* **1997**, *105,* 451.

[10] W. J. Boettinger, U. R. Kattner, S. R. Coriell, Y. A. Chang and B. A Mueller, *Modelling of Casting, Welding and Advanced Solidification Processes, VII,* (Eds.: M. Cross et al.), TMS, Warrendale, PA, **1995**, 649.

[11] B. A. Boutwell, R. G. Thompson, N. Saunders, S. K. Mannan, and J. J. deBarbadillo, *Superalloys 718, 625, 706 and Various Derivatives,* (Ed.: E. A. Loria), TMS, Warrendale, PA, **1996**, 99.

[12] U. Grafe, D. Ma, A. Engstrom and S. G. Fries, *Modelling of Casting, Welding and Advanced Solidification Processes VIII,* (Eds.: B. G. Thomas and C. Beckermann), TMS, Warrendale, PA, **1998**, 227.

[13] M. S. A. Karunarate, D. C. Cox, P. Carter and R. C. Reed, *Superalloys 2000,* (Eds.: K. A. Green, T. M. Pollock and R. D. Kissinger), TMS, Warrendale, PA, **2000**, 263.

[14] N. Saunders and A. P. Miodownik, *CALPHAD – Calculation of Phase Diagrams,* Pergamon Materials Series vol. 1, (Ed.: R. W. Cahn), Elsevier Science, Oxford, **1998**.

[15] N. Saunders, X. Li. A. P. Miodownik and J.-Ph. Schillé, *Modelling of Casting, Welding and Advanced Solidification Processes X,* (Eds.: D. Stefanescu, J. A. Warren, M. R. Jolly and M. J. M. Krane), TMS, Warrendale, PA, **2003**, 669.

[16] N. Saunders, X. Li. A. P. Miodownik and J.-Ph. Schillé, *Light Metals 2003,* (Ed.: P. Crepeau), Warrendale, PA: TMS, **2003**, 999.

[17] N. Saunders, X. Li. A. P. Miodownik and J.-Ph. Schille, *Magnesium Technology 2003,* (Ed.: H. I. Kaplan), Warrendale, PA: TMS, **2003**, 135.

[18] N. Saunders, X. Li. A. P. Miodownik and J.-Ph. Schillé, *Proc. Conf. Liquid Metal Processing 2003,* Nancy, France, Sept.21–24, **2003**, 253.

[19] N. Saunders, Z. Guo, X. Li, A. P. Miodownik and J-Ph. Schillé, *JOM*, December, **2003**, 60.

[20] N. Saunders, X. Li, A. P. Miodownik and J.-Ph. Schillé., *Materials Design Approaches and Experiences,* (Eds.: J.-C. Shao, M. Fahrmann and T. M. Pollock), TMS, Warrendale, PA, **2001**, 185.

[21] T. W. Clyne and W. Kurz, *Metall. Trans. A,* **1981**, 12A, 965

[22] L. Backerud, E. Krol and J. Tamminen, Solidification Characteristics of Aluminium Alloys: Vols. 1 and 2, Tangen Trykk A/S, Oslo, 1986

[23] Z. Fan, P. Tsakiropoulos and A. P. Miodownik, *J. Mat. Sci.,* **1994**, 29, 141.

[24] Z. Fan, *Phil.Mag.A,* **1996**, 73, 663.

[25] A. P. Miodownik, N. Saunders and J.-P. Schillé, unpublished research.

11
Determination of Solidification Curves Based on DSC Experiments with Improved Heat-transfer Model

Djordje Mirković, Joachim Gröbner, Rainer Schmid-Fetzer

11.1
Introduction

Solidification curves of alloys describe the liquid phase fraction vs. temperature during solidification in a closed control volume. Their knowledge is essential for the control of casting processes and also a very important input parameter for solidification simulation software. In this study an *in-situ* method combining a heat-flux differential scanning calorimeter (DSC) measurement with a mathematical heat-transfer model (HTM) is applied to provide solidification curves of the AZ91 and AZ62 magnesium alloys. These alloys were selected as the prototype Mg alloy and a variation in order to check the applicability of the proposed *in-situ* method.

In earlier work solidification curves were determined by combining a heat flow model with conventional thermal analysis, [1, 2, 3, 4], or differential thermal analysis (DTA) [1, 5, 6, 7, 8], or even DSC [9]. The alloys studied were mainly aluminum alloys [2, 3, 5, 6, 7, 8], but cast iron [1], N4 Ni-based superalloy [10], high speed steel [1] and solders [9] were also investigated. A magnesium alloy (AZ91E) was studied with large sample size in a two thermocouple method resembling the conventional thermal analysis [4].

The present work focuses on the use of DSC, which is superior compared to DTA or thermal analysis, mainly because of the quantitative heat flow measurement and the more stable base line. Compared to earlier work [9] certain improvements enabling a better evaluation of the measured DSC signal are made. This is attained through a more impartial interpretation of the DSC signal as well as the better desmearing of the DSC signal due to separate measurement of the temperature dependence of the time constant of the applied equipment. Due to high oxygen affinity and vapor pressure of investigated magnesium alloys, a special adaptation of the DSC experiments using sealed Ta crucibles was indispensable for generation of reproducible and reliable data. Using this improvement of the technique even the challenging Mg-alloys could be handled.

The present DSC-HTM solidification curves are compared with those measured tediously by using quenching and image analysis and also with those calculated by limiting solidification models (equilibrium solidification model and Scheil model).

The results indicate the high potential of this DSC-HTM method for simple, fast and reliable determination of solidification curves even for highly reactive alloys. It is a truly independent method and does not rely on the knowledge of thermodynamic, kinetic or thermophysical alloy parameters, which are usually very difficult to provide for magnesium alloys.

11.2 DSC Experiment and Heat-Transfer Model (DSC-HTM)

11.2.1 DSC Experiment

The two alloys studied, AZ91 and AZ62, were prepared from master alloys (Norsk Hydro Magnesiumgesellschaft, Bottrop). AZ91 was used directly, the AZ62 alloy was prepared by addition of high purity Zn to an AZ61 master alloy. Due to high oxygen affinity and vapor pressure, a special adaptation of DSC equipment using sealed Ta-crucibles was indispensable for generation of reproducible and reliable data. Cylindrical Ta-crucibles with 6 mm inner diameter and 13 mm height were filled to 50 vol.% with the sample material and sealed under argon by arc welding. Several criteria were considered before tantalum has been selected as crucible material. Details on possible side reactions and other criteria will be published separately [11].

DSC measurements were performed by using a heat-flux twin cylindrical Calvet-type calorimetric system Setaram TG-DSC 111. The DSC scanning program comprised two cycles 300–650–300 °C at heating/cooling rate of 3 K/min under purified Ar atmosphere to protect the Ta capsule.

11.2.2 Heat-transfer Model

The modeling of the heat flow between DSC cells and the furnace applied in this work is based on the so-called Tian equation (Eq. 1) [12, 13] for the heat flow, Φ_r, in J/s produced through reaction or transition inside the sample:

$$\Phi_r = -\Phi - (C_S - C_R)\frac{dT_R}{dt} - R_{FS}C_S\frac{d\Phi}{dt} \quad (1)$$

where t is the time and $\Phi = (\Phi_{FR} - \Phi_{FS})$ is the heat-flow difference between sample and reference which is directly measured during the DSC experiment. The heat-transfer resistance (R) and the heat capacity (C) of the reference (R_{FR}, C_R) and the sample cell (R_{FS}, C_S) will be approximated to be identical ($R = R_{FR} = R_{FS}$; $C = C_R = C_S$). The temperatures (T_R and T_S) are taken to be uniform inside the cells [14]. A schematic diagram of the DSC equipment and the heat-transfer model quantities is shown in **Figure 1**.

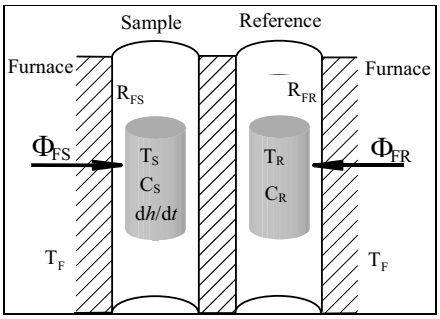

Fig. 1 Schematic view of the DSC (twin cylinder-type), with quantities used in heat transfer model

The heat flow generated by exothermic or endothermic reaction inside the sample, Φ_r can be expressed by the heat evolution, h, which occurs in the sample:

$$\Phi_r = \frac{\mathrm{d}h}{\mathrm{d}t} \tag{2}$$

Chen at al. assumed a linear dependence of heat evolution during solidification h on the solid phase fraction f_S, in their application of the Tian equation to DSC experiment [9] and with a similar heat-transfer model to DTA experiment [5, 6, 7, 8, 15] in order to determine solidification curves. This linearization means

$$\mathrm{d}h = H\,\mathrm{d}\,(1 - f_L) \tag{3}$$

where H is the total latent heat of solidification, assumed to be a constant for each alloy.

This linear dependence is often blamed to be a very rough simplifying approximation. However, if we calculate enthalpy as function of f_L for the example of AZ91 alloy using our thermodynamic Mg-database [16] and Pandat program [17] for two limiting cases, equilibrium and Scheil solidification, **Figure 2** is obtained. Surpris-

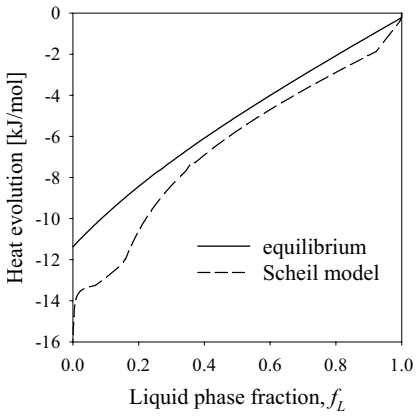

Fig. 2 Calculated heat evolution dependence on molar liquid phase fraction during the solidification of the AZ91 alloy

ingly good linearity, even for the solidification path modeled after Scheil, justifies that the assumption of linear heat release is not too unreasonable. The specific heat contribution, included in Figure 2, is also essentially linear and does not change this statement.

The following equation is derived from Eqs.(1), (2) and (3) after applying all simplifications written in the finite-difference form for numerical solution:

$$\Delta f_L = 1 - \left[\frac{\Delta t}{\mathrm{H}}\left[-\Phi(t) - RC\left[\frac{\Phi(t+\Delta t) - \Phi(t)}{\Delta t}\right]\right]\right] \tag{4}$$

In previous work by Chen et al. [5, 6, 7, 8, 9] the terms H and RC were treated as two adjustable parameters determined from the measured DTA/DSC curve of the sample. The term H, the latent heat of solidification, is obtained by integration of the area under the DTA/DSC experimental curve after the base line was subtracted, and the term RC was iteratively obtained from the after-reaction part of the DSC curve of each sample.

In the present work we make use of the fact that RC is a time constant, which is characteristic for the DSC equipment and experimental conditions. We have measured RC independently as a function of temperature from the solidification curves of pure metals [13, 18].

The signal decay from the inflection point was fitted to an exponential decay as shown in **Figure 3** for the Zn freezing peak at 3 K/min cooling rate. The exponential function can be derived from Eq. 1 since $\Phi_r = 0$ in that part of the DSC curve. This could be tricky in the case of an unknown alloy sample where possible solid state reactions could corrupt the results. In this study Zn, Pb and Sn solidification curves were analyzed using the same Ta crucible setup, scanning rates and other conditions as in the actual alloy experiments. Values of RC = 31 sec at 419 °C (Zn), RC = 29 sec at 327 °C (Pb) and RC = 28 sec at 231 °C (Sn) were determined. These values show a small dependence on temperature in the DSC equipment in contrast to a very strong temperature dependence observed in a DTA equipment [11].

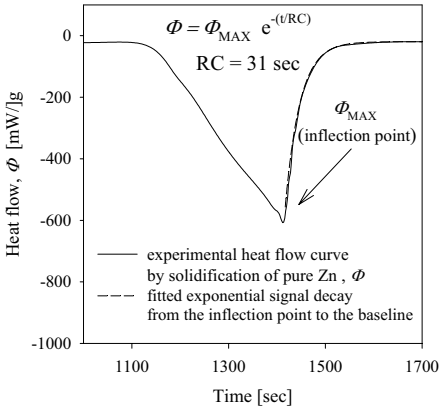

Fig. 3 Determination of the time constant RC from the freezing peak of Zn at the 3 K/min cooling rate.

Based on this knowledge of $RC = RC(T)$ the only remaining alloy-specific parameter in Eq. 4, H, was determined as follows. An initial value of H is obtained by DSC-area integration and can be used to calculate $f_L(t)$ from Eq. 4. A correction of H is then done through an iterative procedure based on the constraint $f_L = 0$ at the end of the solidification, usually assigned to the maximum of the peak with lowest onset temperature.

11.3 Solidification Curves Determined by Alternative Methods

11.3.1 Quenching and Image Analysis (QIA)

For each alloy three samples were encapsulated in a thin-wall mild steel tube, held at 650 °C for 1 hour, slowly cooled in furnace with controlled cooling rate of 2 K/min down to 550, 500 and 450 °C and subsequently quenched into liquid nitrogen. As an example the microstructure of an AZ91 alloy after quenching from the three different temperatures in the freezing range is shown in **Figure 4.** The bright regions were liquid prior to quenching, the dark regions show the slowly grown Mg-solid solution crystals. The area fractions determined by quantitative image analysis are shown as symbols in **Figure 5b**.

11.3.2 Thermodynamic Calculation of Solidification Curves

Solidification curves of the alloys were calculated applying two simplistic, limiting solidification models (equilibrium solidification model and Scheil model) and the resulting curves can be seen in Figure 5b. All calculations in this work have been done with the PANDAT Program [17] and are based on the Mg-Al-Zn-Mn subsystem of the larger database for magnesium alloys which is in ongoing development in our group [16].

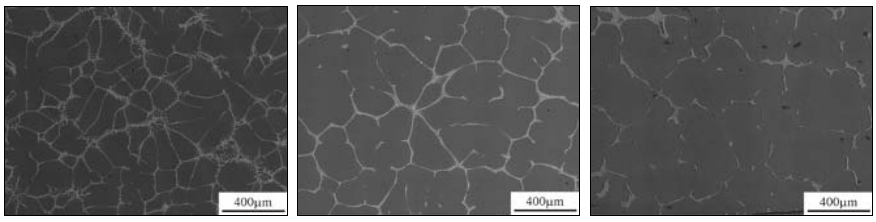

Fig. 4 Microstructure of an AZ91 alloy partially solidified at a cooling rate of 2 K/min from 650 °C to T* and LN2-quenched from a) T* = 550; b) T* = 500 and c) T* = 450 °C. The bright regions show the initially liquid phase prior to quenching.

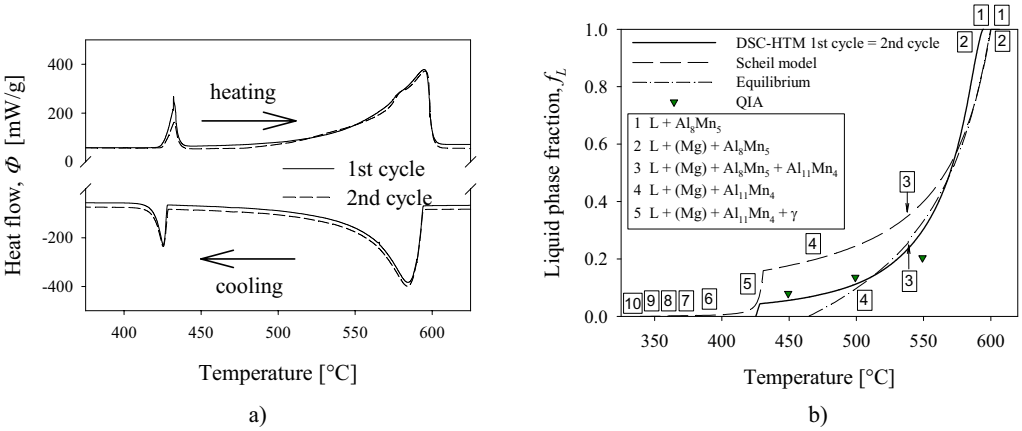

Fig. 5 AZ91 alloy (a) DSC measurement signal; (b) Solidification curves determined in this work by using different methods; the first five solidification steps from Scheil calculation are also shown.

11.4 Results and Discussion

Figure 5a shows the original experimental DSC curves and Figure 5b the liquid phase fraction curves derived from that using the present DSC-HTM for alloy AZ91. It is obvious that these f_L curves are reproducibly obtained from different DSC cycles. Even though the DSC curves may look different in detail, the derived *fL* curves virtually coincide in the graph. For comparison, the solidification curves from the thermodynamic calculation and the present quenching & image analysis (QIA) experiments are also given. Figures 6a and 6b show the analogous data for the alloy AZ62.

A relatively good agreement between DSC-HTM and QIA solidification curves is presented in Figures 5b and 6b. The biggest difference was seen at highest quenching temperature (550°C), presumably due to insufficient cooling rate. Even though liquid nitrogen, a rather capable quenching medium, combined with a thin-wall sample container and a small sample diameter has been used, no sufficient quenching conditions were achieved. Additional growth of the large primary crystals present at the quenching temperature could not be prevented. As this buildup cannot be distinguished from the already present solid phase an overestimation of the fraction of solid (or underestimation of f_L) is unavoidable, especially when quenching from higher temperature. This observation shows the same trend as seen in studies on aluminum alloys [5, 7]. In addition to this inaccuracy the QIA method is very labor intensive and time consuming and, thus, not attractive.

The solidification curves calculated by the Scheil model show a qualitatively similar path compared to those given by DSC-HTM in Figures 5b and 6b. This is in accordance with the metallographic analysis of DTA-cooled samples [11] where even under the slow cooling rate of 1 K/min the non-equilibrium ã particles are precipi-

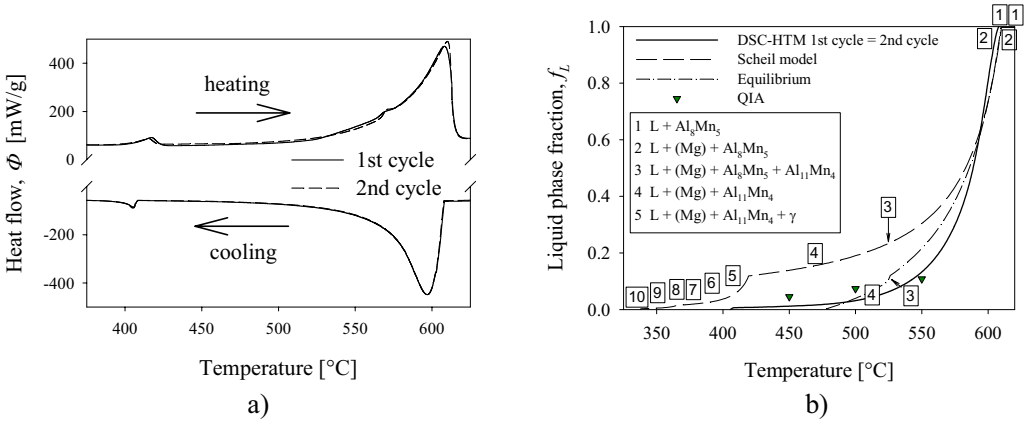

Fig. 6 AZ62 alloy (a) DSC measurement signal; (b) Solidification curves determined in this work by using different methods; the first five solidification steps from Scheil calculation are also shown.

tated, resembling a Scheil solidification mode, rather than equilibrium. The fractions of liquid determined by DSC-HTM are, however, generally below the Scheil calculation and partly even lower than those calculated by equilibrium solidification model. This disagreement requires further studies. It may be due to the not yet completely finished thermodynamic data base of the quaternary Mg-Al-Zn-Mn or to the simplifications inherent in the Scheil model.

The Scheil and equilibrium solidification models simulate two limiting cases of the solidification process. Even these two simple models require a complete thermodynamic description of the alloy system under consideration. Based on that information the enthalpytemperature relation may be calculated and a higher accuracy is obtained using solute-diffusion micromodels additionally as shown by Boettinger and Kattner [19]. Dong et al. [20] also claim the necessity to use microsegregation models [21] to obtain solidification curves on the basis of heat evolution measurements. We are in complete agreement with this approach to use micromodels for a detailed description if all the thermodynamic and kinetic data are available. The crucial point of the present work is to demonstrate that even without knowing any of these data it is possible to determine the solidification curve of a given Mg-alloy by DSCHTM. This is also important in order to provide independent experimental information in order to check more sophisticated microsegregation solidification models of such alloys. Further work is needed to apply this promising technique to other alloys and to further improve the model, for example the assumed linearization of the heat evolution and other aspects.

Acknowledgement

This study is supported by the German Research Council (DFG) under grant no. Schm 588/24. The use of the DSC equipment by courtesy of Prof. Riccardo Ferro, Università di Genova, is gratefully acknowledged.

References

[1] H. Fedriksson, B. Rogberg, Metal Science 1979, 3, 685–690.

[2] L. Bäckerud, E. Krol, J. Tamminen, Solidification Characteristics of Aluminium Alloys; Volume 1: Wrought Alloys, Skan Aluminium, Oslo, Norway, 1986, p. 65–71.

[3] J. Tamminen, Thermal analysis for investigation of solidification mechanisms in metals and alloys, Doctoral Dissertation, University of Stockholm, Stockholm, 1988.

[4] Y. W. Riddle, M. M. Makhlouf in Magnesium Technolngy 2003 (Ed.: H.I. Kaplan), TMS, Warrendale, 2003, 101–106.

[5] S. C. Jeng, S. W. Chen, C. C. Huang in Light Weight Alloys for Aerospace Applications III (Ed.: E. W. Lee, N. J. Kim, K. V. Jata, W. E. Frazier), The Minerals, Metals and Materials Society, Warrendale, 1995, 219–226.

[6] S. C. Jeng, S. W. Chen, Materials Science Forum 1996, 217–222, 283–288.

[7] S. W. Chen, C. C. Huang, Acta mater. 1996, 44, No. 5, 1955–1965.

[8] S. W. Chen, S. C. Jeng, Metall. Trans. A 1996, 27A, 2722–2726.

[9] S. W. Chen, C. C. Lin, C. M. Chen, Metall. Trans. A 1998, 29A, 1965–1972.

[10] S. W. Chen, S. C. Jeng, Metall. Trans. A 1997, 28A, 503–504.

[11] D. Mirkovic, R. Schmid-Fetzer, to be published.

[12] W. Hemminger, H. Cammenga, Methoden der Thermischen Analyse, Springer-Verlag Berlin, Heidelberg, 1989.

[13] G. W. H. Höhne, W. Hemminger, H.-J. Flammersheim, Differential scanning Calorimetry: an introduction for practitioners, Springer-Verlag Berlin, Heidelberg, 1996.

[14] A. P. Gray in Analytical Calorimetry (Ed.: R. S. Porter and J. F. Johnson), Plenum Press, New York 1968, p. 209–218.

[15] S. W. Chen, C. C. Huang, J. C. Lin, Chem. Eng. Sci. 1995, 50, No. 3, 417–431.

[16] R. Schmid-Fetzer, J. Gröbner, Adv. Engineering Mat. 2001, 3, 12, 947–961.

[17] S.-L. Chen, S. Daniel, F. Zhang, Y. A. Chang, W. A. Oates, R. Schmid-Fetzer, J. Phase Equilibria 2001, 22, 373–378.

[18] U. Ulbrich, H.K. Cammenga, Thermochim. Acta 1993, 229, 53–67.

[19] W. J. Boettinger, U. R. Kattner, Metall. Trans. A 1998, 33A, 1779–1794.

[20] H. B. Dong, M. R. M. Shin, E. C. Kurum, H. Cama, J. D. Hunt, Metall. Trans. A 1996, 34A, 441–447.

[21] W. Kurz, D. J. Fisher, Fundamentals of Solidification, Trans. Tech. Publ., Aedermannsdorf, 1989.

12
Measurement of the Surface Tension of Undercooled Melts by the Oscillating Drop Method in an Electrostatic Levitator

Peter L. Ryder and Nils Warncke

12.1
Introduction

In order to be able to simulate solidification processes under non-equilibrium conditions, a knowledge of the thermodynamic properties in the metastable (undercooled) region is required. Undercooling requires *containerless* processing to avoid heterogeneous nucleation. Under microgravity conditions, containerless processing is possible in space flights, parabolic aircraft flights, drop towers, drop tubes, atomising etc. Under earthbound laboratory conditions, some form of levitation is required, such as acoustic, aerodynamic, electromagnetic or electrostatic levitation. All methods have their advantages and disadvantages. The special advantages of electrostatic levitation are

- The specimen is easily accessible for measurements.
- The technique is applicable to all materials, not just metals.
- The specimen is processed in vacuum, thus avoiding oxidation or contamination.
- The levitation and heating powers are independent of one another, so that the temperature range is less restricted than in the case of electromagnetic levitation.
- The electrostatic field does not induce turbulent flow in the melt.

There are, however, a number of disadvantages:

- The specimen position must be actively controlled in three dimensions.
- The time available for measurement is sometimes limited by discharging of the specimen, depending on the material and the temperature.
- Evaporation of material from the specimen may lead to compositional changes during the experiment.

Examples for thermophysical properties which can be measured by containerless processing in the undercooled region are specific heat, emissivity, thermal conductivity, viscosity, density or surface tension. In the authors' laboratory measurements of density and surface tension have been carried out successfully with an electrostatic

levitator. The present paper describes the apparatus and a special technique which was developed for measuring the surface tension continuously during cooling. The results of the measurements of the surface tension of Al, Ni, Sn, Ge, Si and a Cu-Zr alloy by the oscillating drop method are present.

12.2
Experimental Methods

12.2.1
The Levitator

Fig. 1 shows a schematic view of the apparatus viewed from above and a detailed elevation of the central unit with the levitation and position control electrodes. The levitation field is provided by two circular-plate electrodes. For the stability of the levitation, it is very important that the electrodes are adjusted to be parallel and horizontal. The horizontal position of the specimen is controlled by two pairs of rod-shaped electrodes. The temperature of the specimen is measured with a pyrometer from above through a light pipe passing through the center of the top electrode. A second light pipe passing through the lower electrode can be used for irradiating the specimen with UV light to prevent discharging.

The levitator is enclosed in a vacuum chamber with 8 windows for horizontal access to the specimen. Two pairs of windows are used for monitoring the position of the specimen by means of broadened laser beams which cast shadows of the specimen onto position-sensitive detectors. The signals from the detectors are fed to the unit which controls the levitation voltage and the horizontal positioning fields. The specimen is heated by means of a xenon lamp. Fig. 2 shows as an example a cooling curve obtained from a Cu-Zr alloy.

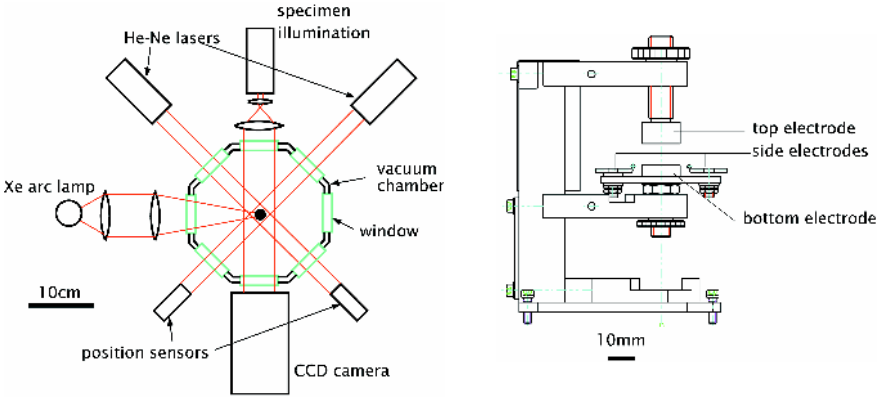

Fig. 1 Left: schematic view of the levitator seen from above. Right: enlarged side view of the central arrangement of the electrodes for levitation and position control.

12.2.2 The Oscillating Drop Method

12.2.2.1 Principle

In the ideal case of a spherical droplet, the oscillation modes are described by spherical harmonics [2]

$$R_{lk} = a \sin(\omega_l t)\, Y_{lk}(\theta, \phi) \quad \text{with} \quad \omega_l^2 = l(l-1)(l+2)\,\sigma/\rho r^3\,, \tag{1}$$

where a is the amplitude, σ the surface tension, r the radius and ρ the density of the droplet. For example, the 3 degenerate modes with $l = 2$ and $k = 0, \pm 1, \pm 2$ are

$$Y_{20} = 3\cos^2\theta - 1; \quad Y_{21} = \sin\theta\cos\theta\cos\phi; \quad Y_{22} = \sin^2\theta\cos(2\theta)\,. \tag{2}$$

For a droplet carrying a charge Q but retaining the spherical shape, Rayleigh [3] showed that the modified Frequency is

$$\omega_l^2 = \frac{l(l-1)}{\rho r^3}\left[\sigma(l+2) - \frac{Q}{(4\pi)^2 \varepsilon_0\, r^3}\right]. \tag{3}$$

However, a levitated droplet is no longer truly spherical due to the different distributions of the electrostatic and gravitational forces. Feng and Beard [4,5] showed how to correct for this distortion with an iterative numerical method. Their technique was used to analyse the results of the present investigation. Details are given in [1].

12.2.2.2 Excitation and Detection of the Oscillations

In the electrostatic levitator, oscillations of the droplet may be excited by modulating the vertical levitation field. Excitation with a sharp pulse leads to the simultaneous generation of several modes, whose frequencies may be determined by Fourier analysis of the oscillations. Alternatively, a sinusoidal voltage can be superimposed on the levitation voltage and tuned to the resonance frequencies. In the present work, the sec-

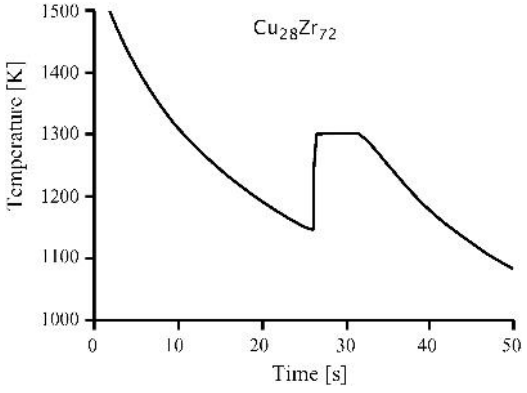

Fig. 2 Cooling curve obtain from a copper-zirconium alloy with the composition $Cu_{28}Zr_{72}$. The solidification at approximately 160 K below the liquidus temperature is accompanied by a marked recalescence, followed by a plateau, during which the remaining melt solidifies.

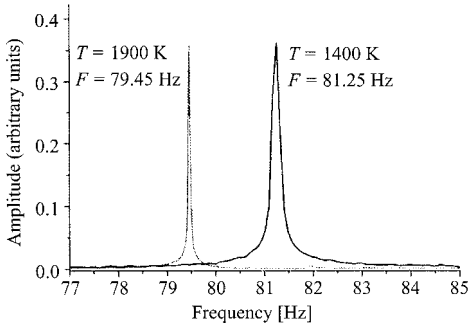

Fig. 3 Resonance curves of a nickel droplet at 1900 K and 1400 K. With increasing temperature, the resonance frequency decreases, and the resonance becomes sharper.

ond method was used, except for some measurements made for comparison in an electromagnetic levitator. The frequency was varied to find the lowest frequency resonance, which corresponded to the mode $l = 2$, $k = 0$. Due to the symmetry of the excitation with a vertical field, the asymmetric modes with $k \neq 0$ are not excited. The position-sensitive detectors were used to measure the amplitude. The alternating voltage also induces translational oscillations of the drop, but their amplitude is negligible at the typical resonance frequencies of the surface oscillations (~100 Hz). Fig. 3 shows two resonance curves obtained from liquid nickel at 1900 K and 1400 K. The figure shows clearly the decrease in resonance frequency – and hence in the surface tension – with increasing temperature (the surface tension vanishes at the critical temperature). The width if the resonance peak is due to damping of the oscillations caused by the viscosity of the liquid and therefore decreases with increasing temperature.

Measurements at constant temperature such as those shown in Fig. 3 are very time-consuming. In addition the heating required to maintain the temperature induces convection in the liquid. The measurements presented below were therefore obtained during cooling after switching off the heating. An electronic frequency control circuit was used to lock the frequency of the driving alternating voltage to the resonance. For this purpose a phase difference of $\pi/2$ between the driving force and the forced oscillations was used as the criterion for resonance, because this is independent of the damping, whereas the amplitude maximum is shifted to lower frequencies at high damping.

For one material – a Cu-Zr alloy with the composition $Cu_{46}Zr_54$ – surface tension measurements were carried out for comparison both in the authors' electrostatic levitator and in an electromagnetic levitator at the Institute for Space Simulation of the German Aerospace Center (DLR) in Cologne. In this case, multiple-mode oscillations were excited, and the frequencies were detected by Fourier analysis.

12.3 Results

The result of the surface tension measurements on nickel and tin are shown in Fig. 4. The filled symbols indicate the uncorrected values calculated by the Rayleigh

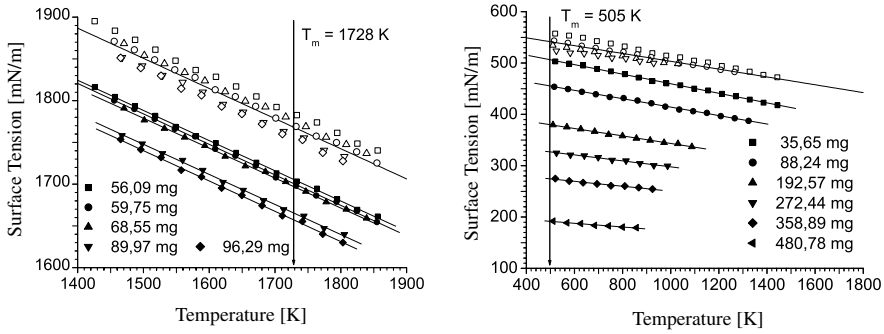

Fig. 4 Surface tension of Ni (left) and Sn (right) as a function of the temperature. The filled symbols denote the uncorrected values from specimens with the indicated masses (see text). In both cases, the melting point (T_m) is marked. In the case of Sn, no undercooling was achieved.

formula for the uncharged, spherically symmetrical case. These values serve as starting points for the iterative correction procedure using the theory of Feng and Beard [4]. The uncorrected values show an apparent dependence on the specimen mass, which is indicated in the legend of Fig. 4. The corrected values (open symbols in Fig. 4) were found to converge quite well to a single curve for all the materials investigated.

Fig. 5 shows the results obtained for germanium and the alloy $Cu_{46}Zr_54$. Again, the uncorrected values (not shown for the alloy) converged well to a common function of temperature after correction. The right part of Fig. 5 includes the results obtained by electromagnetic levitation. They show considerably greater scatter, as indicated by the error bars, probably due to random movement of the specimen during measurement.

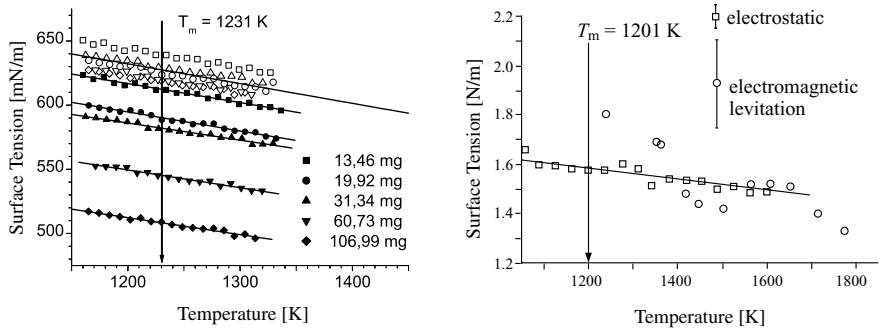

Fig. 5 Surface tension of Ge (left) and $Cu_{46}Zr_{54}$ (right) as a function of the temperature. In the case of the Cu-Zr alloy, the results of the measurements obtained by electrostatic levitation (squares) are compared with measurements obtained by electromagnetic levitation. The latter showed more scatter (indicated by the error bars).

Table 1 summarises the results and includes some figures from the literature for comparison. For each material the table gives the melting point, the range of temperatures investigated, the surface tension at the melting point and the temperature coefficient of the surface tension. It was found possible to undercool all materials except tin. The literature values given in the table are averages of values taken from various sources, quoted in a review article by Keene [6]. They include measurements by different techniques, such as the drop weight, maximum bubble pressure, pendant drop and sessile drop techniques, and also the oscillating drop method with electrostatic or electromagnetic levitation. The agreement is generally good, with the exception of the temperature coefficient for aluminium.

Measurements of the surface tension in the undercooled regime have been performed by Rhim *et al.* on germanium [7], tin [8] and silicon [9], using electrostatic levitation, and by Sauerland *et al.* [10] on nickel, using electromagnetic levitation. These results are shown in Table 2. The results for nickel are in very good agreement with the results of the present investigation, whereas the surface tension values for the semiconductor materials are consistently lower.

Tab. 1 Melting point, temperature range investigated, surface tension at the melting point and temperature coefficient of the surface tension. Comparison with values from the literature.

Material	*Melting point [K]*	*Temperature range [K]*	*Surface tension σ [mN/m]*		*–dσ/dT [mN/mK]*	
			literature[a]	*this work*	*literature*[a]	*this work*
Al	933	921–1506	880 ± 10	890 ± 22	0.168 ± 0.014	0.36 ± 0.03
Ni	1728	1425–1855	1815 ± 19	1769 ± 12	0.36 ± 0.01	0.359 ± 0.003
Sn	505	508–1445	573 ± 12	562 ± 12	0.113 ± 0.10	0.085 ± 0.003
Ge	1233	1159–1335	619 ± 12	626 ± 8	0.12	0.139 ± 0.07
Si	1683	1400–1835	817 ± 42	799 ± 13	0.145	0.146 ± 0.005
$Cu_{46}Zr_{54}$	1200	1052–1770		1490 ± 10		0.30 ± 0.02

[a] Mean of values from various sources, see [6].

Tab. 2 Literature results of the measurements of the surface tension of Ni, Sn, Ge and Si by containerless processing with undercooling.

	Ni	*Sn*	*Ge*	*Si*
Surface tension σ [mN/m]:	1770	541	583	765
Temperature coefficient $d\sigma/dT$ [mN/mK]	0.33	0.09	0.08	0.16
Reference	[10]	[8]	[7]	[9]
Levitation method	electromagnetic	electrostatic	electrostatic	electrostatic

12.4 Summary and Conclusions

A technique has been developed for the continuous measurement of the surface tension of liquid metals during cooling in the stable and undercooled regions. This makes it possible to obtain surface tension data over a wide range of temperatures in a single heating and cooling cycle, thus avoiding problems with specimen discharging or evaporation. A further advantage of the method is that the heating is switched off during the measurement, thus considerably reducing convection currents in the specimen.

Comparison of the results for aluminium, nickel, tin germanium silicon with the literature showed good general agreement when all techniques were considered, except for the temperature coefficient of the surface tension of aluminium. The reason for this deviation is not known. In comparison with literature values from containerless processing (electrostatic and electromagnetic levitation) the surface tension values obtained in the present investigation were higher in all cases. This is a clear indication that the technique used avoids contamination of the specimen.

Acknowledgements

This work was supported by a grant from the German Science Foundation (Deutsche Forschungsgemeinschaft, DFG). Thanks are also due to Professor Ivan Egry of the German Aerospace Center (DLR), Cologne, in whose laboratory the experiments with the electromagnetic levitator were carried out.

References

[1] N. Warncke, Ein Beitrag zur Bestimmung physikalischer Eigenschaften unterkühlter Metallschmelzen mittels elektrostatischer Levitation, Shaker Verlag, Aachen 2003, Chapter 4.

[2] J. W. S. Rayleigh, Proc. Roy. Soc. London 1879, 29, 71.

[3] J. W. S. Rayleigh, Phil. Mag. 1882, 14, 184.

[4] J. Q. Feng, Q. Appl. Math. 1990, 48, 555.

[5] J. Q. Feng, K. V. Beard, Proc. Roy. Soc. Lond. A 1990, 430, 133.

[6] B. J. Keene, Int. Mater. Rev., 1993, 38 157.

[7] W.-K. Rhim, T. Ishikawa, Int. J. Thermophys., 2000, 21, 429–443.

[8] W.-K. Rhim, K. Ohsaka, P. F. Paradis, R. E. Spjut, Rev. Sci. Instr., 1999, 70, 2796–2801.

[9] W.-K. Rhim, K. Ohsaka, J. Cryst. Growth, 2000, 208, 313–321.

[10] S. Sauerland, G. Lohöfer, I. Egry, J. Non-Cryst. Solids, 1993, 156–158, 833–836.

13
Liquid-liquid Interfacial Tension and Wetting in Immiscible Al-based Systems

Walter Hoyer, Ivan Kaban, Markus Merkwitz

13.1
Introduction

Aluminium-based monotectic alloys are intensively investigated during last decades as possible new bearing materials. The idea consists in producing of a hard Al matrix with finely dispersed particles of In, Bi or Pb, for example, as a soft phase with lubricating function. However this is still far from a practical application because the miscibility phenomenon poses problems during solidification [1, 2].

The liquid-liquid interfacial energy effects play a crucial role in solidification processes of the monotectic alloys. Therefore, for understanding, description, and mathematical modelling as well as for prediction of the structure development during solidification in immiscible systems the liquid-liquid interfacial tension and its temperature dependence are to be known. Besides, the mutual wetting of the coexisting phases is of a high scientific and practical interest since this is an important factor of heterogeneous nucleation in the monotectic alloys.

In this work we present the experimental results of the liquid-liquid interfacial tension in the binary Al–Bi, Al–In, Al–Pb as well as in the ternary Al–Bi–Cu ($Al_{82.5}Cu_{17.5}$–Al_8Bi_{92} section) immiscible alloys determined with a sophisticated force method. In addition the interfacial tension in the binary systems is calculated with the help of different models. A correlation between the theoretical and experimental values is studied.

13.2
Experimental Technique

The interfacial tension in the Al–Bi, Al–In, Al–Pb and Al–Bi–Cu monotectic systems was determined by the force method described in [3, 4]. The submerging part was made of alumina in the form of a cylindrical stamp as shown in Fig. 1. Due to such a construction the influence of the free surface of the Al-rich liquids on the experimental data was significantly reduced. Besides, application of the cylindrical stamp allowed using of the radial- symmetrical crucibles as well as chamber and heating

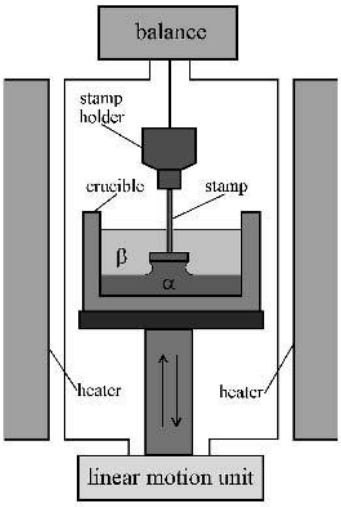

Fig. 1 Scheme of the tensiometer. α and β are the liquid phases.

system. The weight of the meniscus formed by the stamp at the interface was measured as a function of the stamp's position.

The measurements have been performed in a vertical high temperature chamber (1 m of length and 0.1 m of inner diameter) made from a special alloy. The graphite crucible (4 cm of height, 5 cm of inner diameter) was moved by an ultrahigh vacuum manipulating system. The weight of the stamp was measured by a balance with an accuracy of ± 1 mg.

The samples ($Al_{80}Pb_{20}$, $Al_{68}In_{32}$, $Al_{80}Bi_{20}$, $Al_{63.7}Bi_{23.2}Cu_{13.1}$) were prepared from high pure elements (99.999%). Special attention was given to cleaning the samples and prevention of their oxidation. Before heating the chamber was evacuated to better than 1×10^{-5} mbar and then filled with a gas mixture of 90% Ar – 10% H_2 with a total pressure of 1 bar. Nb getter was used additionally for reducing the oxygen that may get into the chamber during measurements. The samples were first heated up to 900–1000 °C and held for about half an hour. Then, it was cooled down to a required temperature, kept for some time to equilibrate the system, and then the measurements were performed. At least three sets of data were collected at every temperature.

The measuring process includes the following steps (see Figs. 2 and 3):

(A) The stamp is being above the upper phase β.
(B) The stamp touches the surface of the phase β and the meniscus is formed.
(C) The stamp moves into the phase β. The buoyancy force and the force of surface tension act on the stamp.
(D) The stamp tears away from the surface of the phase β. Only the buoyancy force acts on the stamp in the section D–E.
(E) The stamp touches the interface and the meniscus is formed.
(E–F) The stamp is further submerged into the phase α.

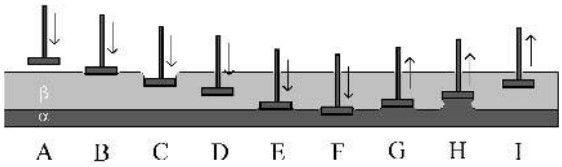

Fig. 2 The main stages of the measuring process.

(F–G) The stamp moves up. Only the buoyancy force caused by the lower phase α is changing in the ranges E–F and F–G.

(G–H) The lower edge of the stamp reaches the contact line. Because of the vanishing contact angle the necking of the meniscus starts. The total force is increasing less and less and it is going through a maximum.

(I) The meniscus at the interface breaks down; the stamp moves up in the phase β.

A typical experimental curve for the Al–Bi alloy at 660 °C is plotted in Fig. 3. It is noteworthy that the forward and the backward measuring curves are smooth and completely coincident. This means that contact angle hysteresis occurred neither at the surface nor at the interface. It should also be noted that the shape of the experimental curves for the binary Al–Bi, Al–In and Al–Pb systems corresponded to the theoretical curve simulated in [3] for the case of zero advancing and receding contact angle and absence of contact angle hysteresis. In the case of the quasi-binary $Al_{82.5}Cu_{17.5}$–Al_8Bi_{92} system this was observed at the temperatures above 950–960 K. At lower temperatures the experimental curves were similar to a modelled curve upon a condition that receding contact angle is more than zero and contact angle hysteresis takes place.

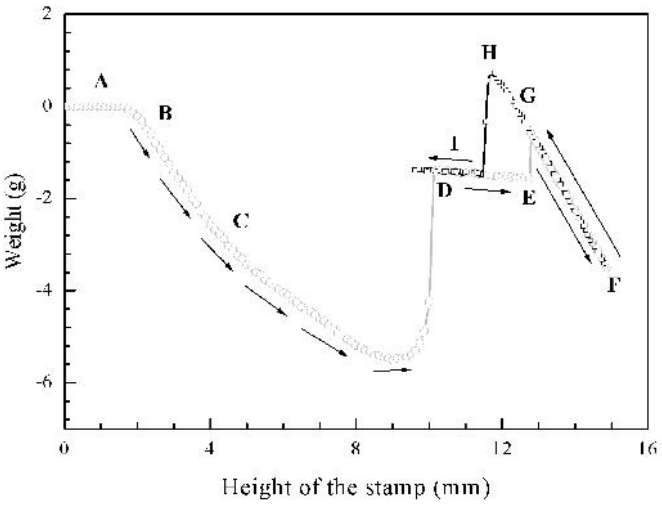

Fig. 3 A typical experimental curve in the Al–Bi system at 660 °C.

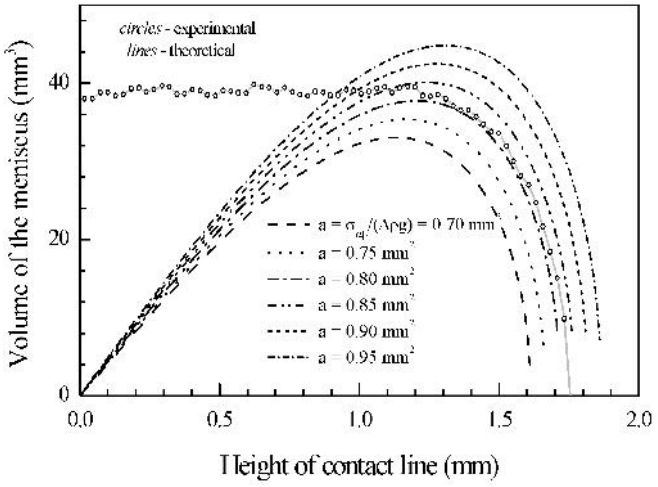

Fig. 4 The experimental meniscus volume curve compared to the theoretical volume curves calculated for various capillary constants.

The experimental data measured at the liquid-liquid interface (stages F–I in Fig. 3) were taken for the mathematical treatment. After subtraction of the buoyancy force and geometrical corrections for limited sample volume and the shape of the stamp, the volume of the meniscus in dependence on the height of the contact line was determined. On the other hand, the meniscus was modelled by the numerical solution of Laplace's equation for different values of the capillary constant $a = \sigma_{\alpha\beta}/\Delta\rho_{\alpha\beta}g$ ($\sigma_{\alpha\beta}$ is the interfacial tension between phases α and β, $\Delta\rho_{\alpha\beta}$ is the difference of the densities of the two liquids, and g is the gravitational acceleration). Due to cylindrical form of the stamp the calculations were reduced to a one-dimensional problem. From comparison of the experimental and theoretical volume curves the capillary constant was determined, and then the interfacial tension was calculated. The density difference $\Delta\rho_{\alpha\beta}$ was determined for each measurement from the buoyancy force (stages D–F in Fig. 3).

Fig. 4 shows as an example the meniscus volume curve calculated from the experimental data for Al–Bi system plotted in Fig. 3 and the respective theoretical functions for various capillary constants. The horizontal part of the experimental curve corresponds to the measurements, where only buoyancy force caused by the lower phase α acts on the stamp and the meniscus shape is not changed (range F–G in Fig. 3).

13.3 Results and Discussion

Fig. 5 shows the liquid-liquid interfacial tensions for the Al-based monotectic alloys in dependence on temperature (the data for Al-In and Al-Pb systems are taken from [5]).

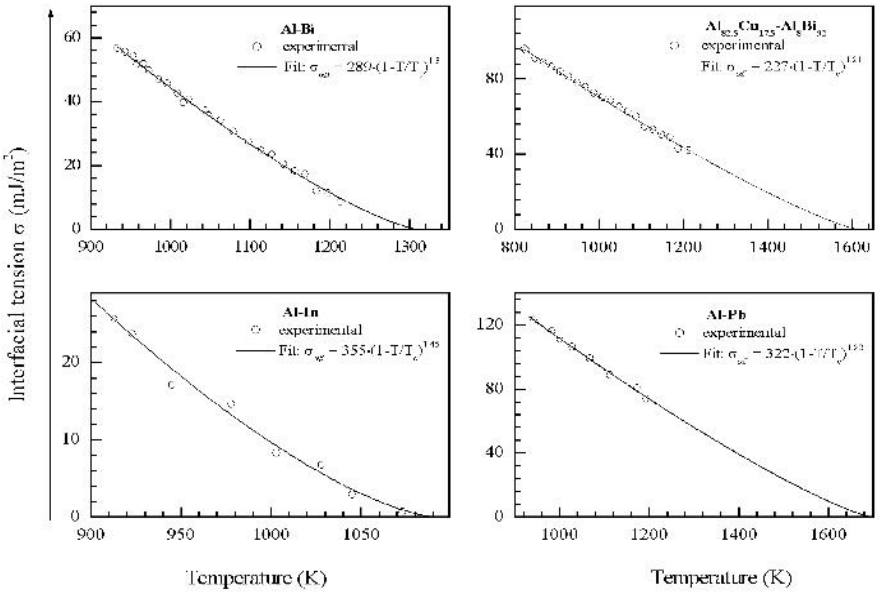

Fig. 5 Liquid-liquid interfacial tension in the Al–Bi, Al–In [5], Al–Pb [5] and $Al_{82.5}Cu_{17.5}$–Al_8Bi_{92} systems.

The experimental values in Fig. 5 are fitted with the power function

$$\sigma_{\alpha\beta} = \sigma_{\alpha\beta 0} \cdot (1 - T/T_c)^{\delta} \tag{1}$$

where $\sigma_{\alpha\beta 0}$ is a constant, δ is the so-called critical exponent, and T_c is the critical temperature. The following absolute values of T_c were taken from the literature: 1310 K for Al–Bi [6], 1110 K for Al–In [7] and 1695 K for Al–Pb [8] system. In the case of the quasi-binary $Al_{82.5}Cu_{17.5}$–Al_8Bi_{92} system the critical temperature was chosen as unknown parameter along with $\sigma_{\alpha\beta 0}$. A fitting procedure yielded $T_c \approx 1613$ K.

Since the temperature dependence of the interfacial tension as well as its first derivative are to be known for description of the structure development in the monotectic systems, the analytical expression [Eq. (1)] is often used in the simulations. However the values $\sigma_{\alpha\beta 0}$ and δ for these purposes should be known. The classical theory of critical phenomena [9, 10] gives $\delta = 1.5$ and the renormalization theory [11] suggests $\delta = 1.26$. The constant $\sigma_{\alpha\beta 0}$ can be found by fitting Eq. (1) to the experimental data. This means that the absolute value of the interfacial tension at least at one temperature is required. Taking into account that experimental measurements in certain systems are not possible at all, a theoretical method for determination of the interfacial tension is needed.

There are two approaches for determination of the liquid-liquid interfacial tension in immiscible systems: semi-empirical and theoretical calculations. In the first case, the interfacial tension is suggested to estimate from experimental values of the sur-

face tension of the coexisting phases or pure constituents; in the second, the interfacial tension can be derived by modelling the interface between two liquids and description of the system by means of statistical thermodynamics.

Antonow [12] suggested that liquid-liquid interfacial tension $\sigma_{\alpha\beta}$ between two liquids α and β can be calculated as the difference between their surface tensions σ_β and σ_α. At first sight this seems to be the easiest way. However, experimental data on the surface tension of individual phases constituting different immiscible systems do not exist and it is also not simple to measure them.

Among the theoretical models the simplest is that of Becker [13], where a demixing system is considered as a regular solution with a sharp interface between two phases, and interactions between atoms are restricted to the nearest neighbours. Following this idea the interfacial tension is equal to an additional energy resulting from the asymmetry of the bonds across the interface.

Cahn and Hilliard [10] supposed that there is no sharp interface between two liquids in an immiscible system and that the concentration profile normal to the interface changes continuously. The Gibbs free energy is assumed to depend not only on the temperature, pressure and local composition but also on the composition gradient, which must be small as compare to the reciprocal of the interatomic distance. After application of the van der Waals model of diffusive interfaces to binary mixtures they have obtained an expression for the interfacial tension in the approximation of a regular solution.

Chatain and Eustathopoulos [14, 15] have modelled the interfacial area in an immiscible system by a definite number of monatomic layers. The interfacial tension is determined as the difference of the free energy of the whole immiscible system and the free energy of a homogeneous system, which could be formed by the same atoms with the same chemical potentials.

For comparing the models the most suitable way is to determine the dimensionless expression $(\sigma_{\alpha\beta} \cdot \Omega_m / W)$, where W is the molar exchange energy, which can be calculated for a regular solution from the experimental critical temperature T_c as $W = 2 \cdot R \cdot T_c$; R is the gas constant; Ω_m is the molar interface averaged over the respective values of the constituent elements. For a component i with the molar volume V_i the molar interface equals

$$\Omega_m(i) = f \cdot N_A^{1/3} \cdot V_i^{2/3} \tag{2}$$

N_A is the Avogadro's number; f is the factor of two-dimensional density or so-called structure factor.

Fig. 6 shows the expression $(\sigma_{\alpha\beta} \cdot \Omega_m / W)$ as a function of the reduced temperature T/T_c determined within the three models in the regular solution approximation. The liquid-liquid interface was identified with the (111)-plane of the face-centered cubic lattice as suggested in [14]. In this case f in Eq. (2) equals 1.091.

It is seen from Fig. 6 that the model of Becker is restricted to the temperatures where the composition at the interface can be assumed to change at a jump, and the model of Cahn-Hilliard is restricted to the temperatures where continuous transition from one to another phase is observed. The model of Chatain-Eustathopoulos as if

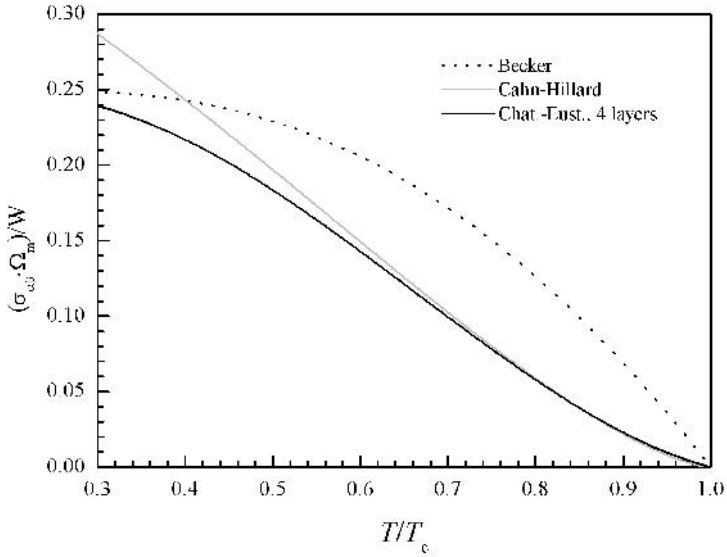

Fig. 6 The expression $(\sigma_{\alpha\beta} \cdot \Omega_m/W)$ as a function of the reduced temperature.

unifying the models of Becker and Cahn-Hilliard gives values $(\sigma_{\alpha\beta} \cdot \Omega_m/W)$, which tend to those of Becker's model at low temperatures and practically coincide with the values of Cahn-Hilliard's model at high temperatures.

The absolute values of the interfacial tension in the Al–Bi, Al–In and Al–Pb systems at the monotectic temperatures determined with the help of the multilayer model of Chatain and Eustathopoulos are given in Table 1. It is noteworthy that the calculated values are approximately 1.5 times less than those measured experimentally.

Tab. 1 The experimental, $\sigma^{ex}_{\alpha\beta}$, and the theoretical, $\sigma^{th}_{\alpha\beta}$, values of the liquid-liquid interfacial tension at the monotectic temperature, T_m; T_c – the critical temperature; W – the molar exchange energy; Ω_m – the molar interface.

System	T_m *[K]*	T_c *[K]*	W *[kJ/mol]*	Ω_m *[m²/mol]*	$\sigma^{th}_{\alpha\beta}$ *[mJ/m²]*	$\sigma^{ex}_{\alpha\beta}$ *[mJ/m²]*	$\sigma^{ex}_{\alpha\beta}/\sigma^{th}_{\alpha\beta}$
Al–Bi	930	1310	21.8	$58 \cdot 10^3$	36	57	1.58
Al–In	912	1110	18.4	$53 \cdot 10^3$	17	26	1.53
Al–Pb	932	1695	28.1	$57 \cdot 10^3$	81	126	1.55
$Al_{82.5}Cu_{17.5}$–Al_8Bi_{92}	819	1613	–	–	–	96	–

To analyze the temperature dependencies of the interfacial tension determined experimentally with the theoretical predictions, the measured data for the Al–Bi, Al–In and Al–Pb systems were fitted to the expression $(\sigma_{\alpha\beta} \cdot \Omega_m/W)$ calculated with the

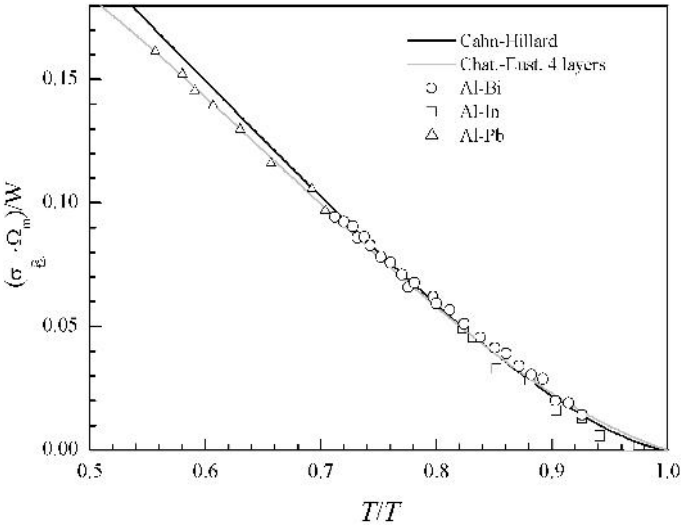

Fig. 7 The temperature dependences of the experimental values of the interfacial tension for Al–Bi, Al–In and Al–Pb immiscible systems fitted to the expression ($\sigma_{\alpha\beta} \cdot \Omega_m/W$) determined with the model of Chatain and Eustathopoulos.

model of Chatain and Eustathopoulos. The results are presented in Fig. 7. It is seen that in fact both models (Chatain-Eustathopoulos and Cahn-Hilliard) describe the temperature dependence of the interfacial tension in the binary monotectic systems very well.

13.4 Conclusions

The liquid-liquid interfacial tension in the binary Al–Bi, Al–In, Al–Pb and quasi-binary $Al_{82.5}Cu_{17.5}$–Al_8Bi_{92} monotectic systems has been determined experimentally using a sophisticated tensiometric technique. The experimental values for the binary systems have been analyzed in frames of the models of Becker, Cahn–Hilliard, and Chatain–Eustathopoulos. Comparison between the measured and calculated data has been made.

It is shown that the temperature dependencies of the liquid-liquid interfacial tension in the Al–Bi, Al–In and Al–Pb binary systems are well described by the continuous model of Cahn-Hilliard or multilayer model of Chatain-Eustathopoulos. The model of Becker can be excluded as a plausible theoretical description.

The absolute values of the interfacial tension calculated within the models of Cahn-Hilliard and Chatain-Eustathopoulos in the approximation of a regular solution with liquid-liquid interface as (111)-plane of the face-centered cubic lattice for the Al–Bi, Al–In and Al–Pb systems are ~1.5 times less than the respective experi-

mental data. Obviously this parameter might be applied to the theoretical calculations for determination of the interfacial tension in those binary systems where experimental measurements are not possible.

From comparison of the shape of the experimental curves measured at the liquid–liquid interface with the theoretical curves it can be concluded that the contact angle at the contact line between the two liquid phases and the stamp was ~0 ° for Al–Bi, Al–In and Al–Pb systems in the whole experimental temperature interval beginning from the monotectic temperature. In the case of $Al_{82.5}Cu_{17.5}$–Al_8Bi_{92} system this was observed at the temperatures ~140 K above T_m. Besides, the upper (lighter) phase of the solidified samples was covered by a layer (~100 μm thickness) of the lower (heavier) phase. These facts are indicative of the wetting phenomena taking place in the investigated immiscible systems.

Acknowledgements

Funding for this research was provided by the Deutsche Forschungsgemeinschaft under grant HO 1688/8-1 in the frame of Schwerpunktprogramm 1120 „Phasenumwandlungen in mehrkomponentigen Schmelzen“.

References

[1] L. Ratke, S. Diefenbach, Mat. Sci. Eng. 1995, R15, 263–347.
[2] R. N. Singh, F. Sommer, Rep. Prog. Phys. 1997, 60, 57–150.
[3] M. Merkwitz, J. Weise, K. Thriemer, W. Hoyer, Z. Metallkd. 1998, 89, 247–255.
[4] M. Merkwitz, Ph. D. Thesis, Technische Universität Chemnitz, 1997.
[5] M. Merkwitz, W. Hoyer, Z. Metallkd. 1999, 90, 363–370.
[6] A. J. McAlister, Bull. Alloy Phase Diag. 1984, 5, 247–250.
[7] F. Sommer, H.-G. Krull, S. K. Yu in Immiscible Liquid Metals and Organics (Ed.: L. Ratke), DGM Informationsgesellschaft mbH, Oberursel, 1993, p. 79–90.
[8] S. K. Yu, F. Sommer, B. Predel, Z. Metallkd. 1996, 87, 574–580.
[9] J. D. van der Waals, Z. Phys. Chem. 1894, 13, 657–725.
[10] J. W. Cahn, J. E. Hilliard, J. Chem. Phys. 1958, 28, 258–267.
[11] S. S. Rowlinson, B. Widom, Molecular Theory of Capillarity, Clarendon Press, Oxford, 1982, p. 249.
[12] G. N. Antonow, J. Chim. Phys. 1907, 5, 372–380.
[13] R. Becker, Ann. Phys. 1938, 32, 128–140.
[14] D. Chatain, N. J. Eustathopoulos, Chim. Phys. 1984, 81, 587–597.
[15] D. Chatain, N. J. Eustathopoulos, Chim. Phys. 1984, 81, 599–609.

14
In-Situ Optical Determination of Fraction Solid

L. Ratke, D. Tscheuschner

Abstract

The fraction solid is a key parameter of solidification describing in an integral way how the mushy zone develops during solidification. In this paper we describe a new technique that measures the fraction solid in-situ, nearly non-invasive optically utilizing a new technique for directional solidification, the aerogel technology developed in the last years. The solidification of an AlSiMg alloy within a transparent silica aerogel mould was observed optically. The intensity readings could be correlated to the temperature profile at the sample surface. Analyzing the intensity profile theoretically yields an expression for the fraction solid as a function of temperature. The results are compared with conventional theories and show remarkable differences that can up to now only explained qualitatively.

14.1
Introduction

A key parameter in solidification is the so-called fraction solid. In a binary alloy the fraction solid is the amount of primary phase that is solidified at a temperature T between the liquidus and the solidus line. Under equilibrium conditions the fraction solid can be calculated from the lever rule. In solidification of castings the fraction solid shows deviations from the lever rule which mainly have their origins in the limited solute diffusion in the solid and the modes of solute transport in the liquid part [1, 2, 3]. Numerous theories have been developed in the past decades to predict the fraction solid. Besides the lever rule the most important model is that of Scheil, in which a perfect mixing of solute in the liquid is assumed and no diffusion of solute in the solid. It is well accepted in the literature that the equilibrium lever rule and Scheil's law describe the theoretically possible extremes of fraction solid. Unfortunately the fraction solid is difficult to determine experimentally.

An often used way is to directionally solidify an alloy and to quench after a certain time the sample rapidly thus aiming to preserve the mushy zone in its morphology. This technique was questioned by Rettenmayr [4]. Another technique is to place a

series of thermocouples either inside the sample or in the sample container and then to derive from the measured temperature profile the fraction solid using analytical or numerical models. A third technique is to decant a partially solidified sample and thus rapidly exhaust the melt out of the mush. In this paper we describe a new technique that measures the fraction solid optically utilizing a new technique for directional solidification, the aerogel technology developed in the last years. The results are compared with conventional theories.

14.2 Experimental

The castings were performed in a wedge completely prepared from so-called silica-aerogels. These are highly transparent, open porous nanostructured materials of pure quartz having an extremely low thermal conductivity of around 5 mW/Km [5]. The aerogel wedge moulds were prepared from silica-aerogel sheets of 28 mm thickness and size 18 cm × 9,2 cm, using a special CNC milling machine. The wedge type is shown in Fig. 1.

The total length is 150 mm and the width is 62 mm. Three steps have a length of 46 mm and one only 12 mm. The depth of the right step is 5 mm, the following 10 mm etc.. The mould filling started on the left hand side in the gate system and ended in the feeding system on the right hand side. The feeder and gate system consisted of a special ceramic CTU 902 and were heated slightly over the casting temperature. The left area with its right ridge served to reduce the flow and thus to con-

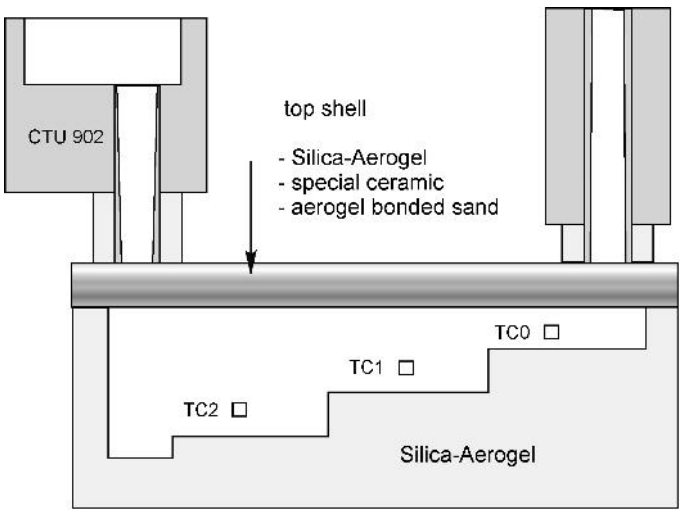

Fig. 1 Sketch of the wedge casting device with a silica-aerogel mould used for casting of AlSiMg alloys (A357. Belwo the aerogel mold a mirror is placed at a distance of 20 cm inclined by 45°.

tribute to a nearly uniform filling of the mould cross section. For all casting experiment we used a AlSi base alloy A357 whose composition was determined by AAS to be in wt.%: Si 6.58, Mg 0.62, Fe 0.017, Ti 0.11 and rest is Al. The mould filling and solidification was observed using a Near Infrared digital camera (InfraVision 500 from Hörotron, Hamburg) mounted below the wedge and observing the wedge bottom via an inclined mirror. The analog signal from the camera was converted into a digital signal by a frame grabber card from Matrox and directly read into the computer with a frequency of 2 frames per second. The camera has 512 × 512 pixel leading to spatial resolution of 0.43 mm/Pixel along the wedge length and 0.31 mm/Pixel perpendicular to it. Its chip has a sensitivity in the wavelength range of 450 to 1400 nm. In addition we placed into each step a thermocouple (TC) at the center in order to compare the TC readings with the intensity readings measured by the CCD camera and also to calibrate it.

14.3 Experimental Results

During solidification we recorded simultaneously the temperature by the TCs and the intensity and thus could correlate both to each other. In addition to this correlation over the whole temperature range there are fix points, namely the onset of primary solidification and the appearance of the eutectic, when the solidification path of the alloy reaches the eutectic valley in the ternary phase diagram.

Fig. 2 shows the result of such a measurement. The first remarkable observation looking at this figure is that the intensity profiles look very similar to the temperature profiles. Let us first discuss the cooling curve as revealed by the TCs. In all steps of the wedge the melt first cools down until the primary α-Al phase starts to solidify. With progress of solidification the temperature decreases until the eutectic valley in the ternary phase diagram is reached and the binary AlSi eutectic solidifies in the interdendritic region. The binary eutectic solidification is finished on reaching the ternary eutectic point. This is hardly to be seen in the temperature readings, since the amount of ternary eutectic is small. The intensity profiles look very similar during the whole time of α-Al solidification but looks quite different to the TC readings when the binary eutectic appears. Instead of having a plateau a continuous increase in intensity can be seen. This has its origin in the emissivity of the Si co-solidifying with Al. Molten Silicon is a metal but becomes a semiconductor on solidification. Thus there is a big change in emissivity during solidification. Since the intensity is directly proportional to the emissivity, we observe a big change in intensity. Its increase with time reflects that the amount of eutectic increases as solidification along the eutectic valley proceeds.

The TC and the intensity readings were taken synchronously such that we can also write the intensity directly as a function of temperature. Since we are interested in the fraction solid of primary phase we show such a correlation only in this temperature range in Fig. 3.

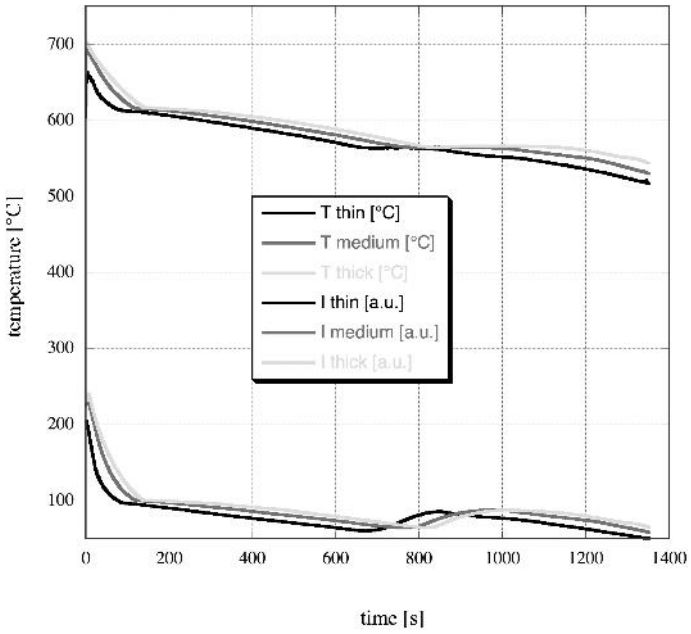

Fig. 2 Cooling curves as measured with thermocouples in the melt at positions indicated in Fig. 1 by boxes and intensity curves measured during the same casting process with the NIR-CCD camera. The upper triple of curves are the TC readings and the lower triple refer to the intensity measurement. In both cases the upper curve belongs to the thin step, the middle one to the medium size step and the lower one to the thickest step.

14.4
Mathematical Analysis of the Intensity Curves

The mathematical analysis of these intensity curves is the basis of the new technique to determine the fraction solid. The intensity measured by the CCD camera and shown in Fig. 2 can be calculated in principle by

$$I(T) = \int_0^\infty \varepsilon(\lambda, T)\, F(\lambda)\, S(\lambda)\, \rho_S(\lambda, T)\, d\lambda \tag{1}$$

where T denotes the temperature, λ the wavelength, $\varepsilon(\lambda,T)$ the emissivity of the sample surface, F (λ) a filter function describing the change of the sample intensity on its way to the CCD detector, S(λ) the wavelength dependent sensitivity of the detector and $\rho_s(\lambda, T)$ is the Planck radiation function of a black body at temperature T. In order to calculate the intensity of eq. (1) several simplifications are necessary. First the filter function F (λ) is set constant as well as the sensitivity of the CCD camera in the wavelength range of interest (450 nm to 1400 nm). The emissivities are also taken as

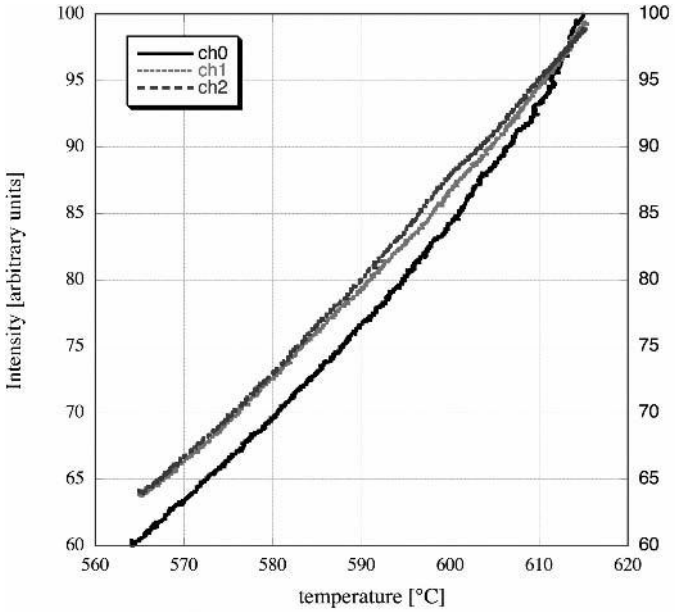

Fig. 3 Intensity versus temperature in the three steps of the wedge taken from the measurement shown in Fig. 2. Ch0 belongs to the thin step, ch1 to the medium and ch2 to the thick step of the wedge.

constant, but different for the three phases, the fully molten state ε_L, the primary α-Al phase ε_α and the eutectic. The intensity within the mushy zone $I_m(T)$ is approximated as a linear weighted average of the primary phase $I_\alpha(T)$ and the fully molten alloy $I_L(T)$:

$$I_m(T) = f_S(T)\, I_S(T) + (1 - f_S(T))\, I_L(T) \tag{2}$$

Instead of using the full Planck curve we made an approximation of the energy density that allows to calculate the integral in eq. (1) analytically. The so-called Wien approximation is an allowed approximation if $\lambda \ll hc/kT$ [7]. For the relevant temperature range between 545 °C und 720 °C we obtain that with hc/kT $\approx$ 20 µm the Wien approximation is allowed. The spectral energy density in the Wien approximation is:

$$\rho(\lambda, T) \cong \rho(\lambda, T)_{Wien} = \frac{8\pi hc}{\lambda^5} \exp\left(-\frac{C_2}{\lambda T}\right) \tag{3}$$

with $C_2 = hc/k = 14390$ µm K. The total power of a black body radiator in the wavelength of interest $[\lambda_1, \lambda_2]$ is then given by:

$$P(T) \cong \int_{\lambda_1}^{\lambda_2} \rho(\lambda, T)_{Wien}\, d\lambda \equiv \sigma_{Wien}(T) \tag{4}$$

The integral can be calculated analytically (the result is suppressed here). With these simplifications the intensities of the liquid and the solid-phase can be expressed as:

$$I_{L,\alpha}(T) = I^0_{L,\alpha}\,\sigma(T)_{Wien} \tag{5}$$

where I^0_L, I^0_α are constants containing the filter factor F, the sensitivity S and the emissivities ε_L, ε_α. The intensity of the mush can now be expressed as

$$I_m(T) = \sigma(T)_{Wien}\left(f_S(T)\,I^0_\alpha + (1 - f_S(T))\,I^0_L\right) \tag{6}$$

This equation can be solved for the fraction solid. Identifying the intensity $I_m(T)$ with the measured intensity the two unknown factors I^0_L, I^0_α can be determined. For the fraction f_s solid we obtain

$$f_S(T) = \frac{I_L(T) - I_m(T)}{I_L(T) - I_\alpha(T)} = \frac{I^0_L\,\sigma(T)_{Wien} - I_m(T)}{I^0_L\,\sigma(T)_{Wien} - I^0_\alpha\,\sigma(T)_{Wien}} \tag{7}$$

At the liquidus temperature T_L the fraction solid is zero and we thus obtain

$$I^0_L = \frac{I_m(T_L)}{\sigma(T)_{Wien}} \tag{8}$$

and at the temperature where the univariant line is hit the fraction solid is known (for instance experimentally from a metallographic analysis) namely $f_s(T_U) = f_{sU}$ and we then obtain the second coefficient as

$$I^0_\alpha = \frac{I^0_L f_S(T_U) - I^0_L}{f_S(T_U)} + \frac{I_m(T_U)}{\sigma(T)_{Wien}(T_U) f_S(T_U)} \tag{9}$$

With these coefficients eq. (6) can be evaluated and the fraction solid determined from the optical measurement.

14.5 Fraction Solid

The experimental result is shown in Fig. 4. The fraction solid as measured optically increases from the liquidus temperature to a maximum value on reaching the univariant eutectic reaction being different for the three wedge step heights. These experimental results are compared with the well known theoretical expression of the Scheil relation

$$f_S^{Scheil}(T) = 1 - \left(\frac{T_m - T}{T_m - T_L}\right)^{\frac{1}{k-1}} \tag{10}$$

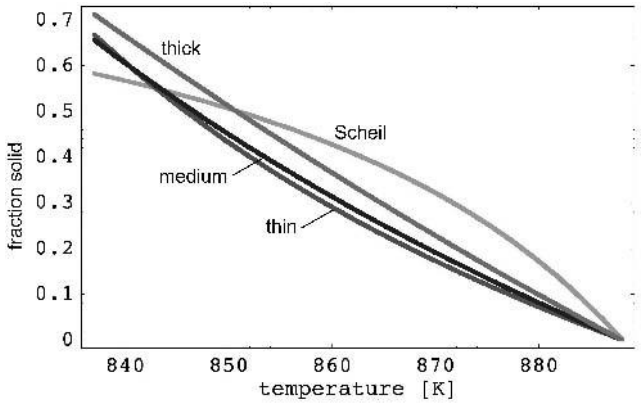

Fig. 4 Optically determined fraction solid as a function of temperature in the three steps of the wedge compared with the Scheil prediction.

in which k denotes the equilibrium partition coefficient (k = 0.132 for a-Al in A357 [1]), T_m the melting point of pure aluminium and T the local temperature of the melt in the interdendritic region and T_L is the liquidus temperature.

The result is astonishing. Whereas the theoretical curve due to Scheil exhibits a convex shape all three experimental curves are concave. In all cases the maximum amount of primary phase is higher than predicted by Scheil's rule. The values were obtained metallographically: On sections taken parallel and transverse to the direction of solidification and also at the bottom and the top of each step we analyzed the fraction primary phase using a Scanning electron microscope (SEM) and standard image analyzing techniques. We observed no difference from top to bottom and between the longitudinal and transverse direction, but difference in all three steps. In the thin step we measure metallographically 66.7, in the medium thick step 65.6 and in the thick step 71.2 Vol.% primary phase (note that in Al-Si alloys the difference between fraction solid calculated on the basis of weight percent eq. (10) and on volume percent is negligible). The accuracy of the metallographic evaluation is estimated to be around ±3 Vol.%. This observation might be explained with macro-segregation, which would mean that the excess concentration is all put into the riser which solidified last. We did not look at the microstructure or composition of the alloy in the gating system. Figs. 5 and 6 shows some representative microstructures observed.

14.6
Discussion and Conclusion

The principal difference between theoretical and experimental observation might suggest that the optical method is wrong. But, we recently used the same method to

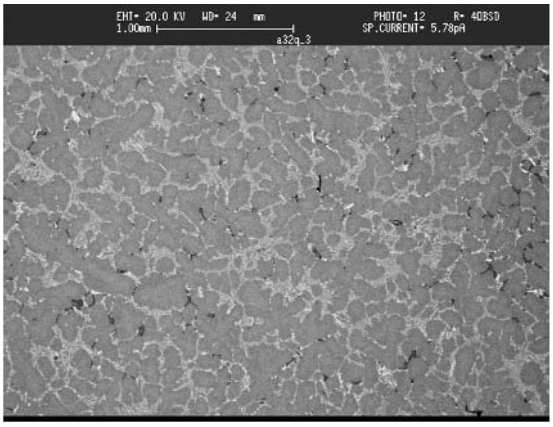

Fig. 5 Microstructure of the AlSiMg alloys solidified in the thick step of the wedge close to the bottom plate. The dendritic structure looks globulithic and equiaxed.

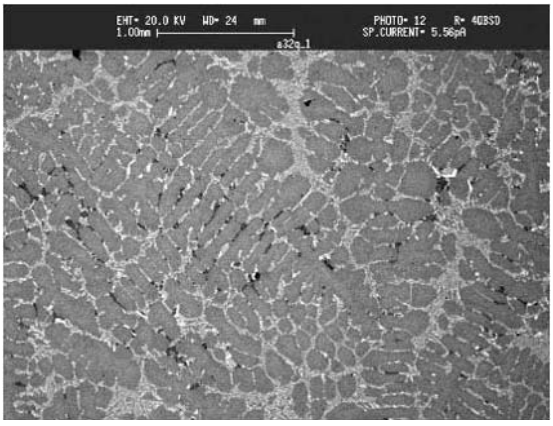

Fig. 6 Microstructure of the AlSiMg alloys solidified in the thick step of the wedge close to the top plate. The dendritic structure looks like a mixture of directed and equiaxed growth.

samples of the same alloy but solidified it directionally and could proof that the fraction solid determined optically behaves exactly as expected, i.e. it follows closely Scheil's prediction [6]. One also might question if eq. (2) is a correct approach. The linear weighting used in eq. (2) is the simplest one being possible. Others using the fraction solid raised to some fractional power (surface equivalent) are possible, but mor complicated to evaluate. We tested such an approach once and did not find any serious difference and thus kept to the simple approach. Since this approach worked well for alloys solidified unidirectionally [6] there is no need to switch to another weighting approach in this case.

Another possibility for the striking differences is fluid flow and sedimentation. Looking at the microstructures, we observe mainly globulithic grains with a dendrite structure. This means that the slow solidification in an aerogel led to more equiaxed than directional growth. Since the density of the solid and liquid are slightly different and especially primary dendritic grains are somewhat heavier than the melt, natural convection could exist ahead of the solidification front with sedimentation of

grains superimposed. This could mean that initially convection rolls lead to a smaller amount of primary phase at the bottom of the aerogel mould, meaning it partially sweeps away the dendrites. At the end of solidification when the eutectic front passes a TC sedimentation has overtaken and more primary phase is observed than possible if the grains would be fixed in space and grow according to Scheil's law. Unfortunately no simple theory is at the moment available describing our observation.

Independent of the observed discrepancy we think that the optical method is valuable to further explore its potential since it is nearly non-destructive. Only one value of the amount of primary phase at the eutectic temperature is needed which can be obtained after complete solidification without further disturbance of the solidification process. In addition we think that our results point to an important question, namely that microsegregation models like the Scheil model, which are well funded and were often confirmed in directional solidification might be not applicable to real castings and their microstructures. If this remark would be true, the modern techniques in numerical casting simulations, in which from local cooling curves the fraction solid is calculated using for instance Scheil or somehow improved models, could be questionable.

References

[1] D.J. Fisher, W. Kurz, Fundamentals of Solidification, Trans Tech Publications Ltd., Switzerland, 1989.

[2] M.C. Flemings, Solidification Processing, McGraw-Hill Book Company, New York, 1974.

[3] C. Beckermann, In: Abbashian R, Brody H, Mortensen A, editors, TMS, Warrendale, PA, 2001, pp. 297–310

[4] O. Pompe, M. Rettenmayr, J. Crystal Growth 1998;192:300; T. Kraft, H.E: Exner, M. Rettenmayr, Modelling and Simulation in Materials Science and Engineering 1996;4:161

[5] J. Fricke, Aerogels, Springer, Berlin, 1986.

[6] S. Steinbach, L. Ratke, Scripta Materialia, 2004;50:1135

[7] H.C. Hottel, A.F.Sarofim, Radiative Transfer, McGraw-Hill Book Company, New York, 1967.

15
Magnetic Effects on the Nucleation in Undercooled Co-Pd Melts

Dirk Holland-Moritz and Frans Spaepen

15.1
Introduction

For all known ferromagnetic metallic materials the Curie temperature, T_C, lies below the liquidus temperature T_L. This is the reason why ferromagnetism has not been observed in any stable metallic melt. However, liquids can be deeply undercooled below T_L even at moderate cooling rates, if heterogeneous nucleation at foreign phases such as container walls or impurity sites is efficiently suppressed [1,2]. By suitable (quasi)containerless processing techniques relative undercoolings of $\Delta T/T_L > 0.2$ can be obtained for a great variety of metallic melts [2]. Therefore, the question arises if it is possible to undercool metallic melts below T_C and if ferromagnetic ordering occurs in such deeply undercooled liquids. Promising sample systems for this kind of studies are some Co-rich alloys because of their small difference $\Delta T_{LC} = T_L - T_C$. For instance, for $Co_{80}Pd_{20}$ $\Delta T_{LC}/T_L \approx 0.21$ which lies within the experimentally accessible range of undercoolings.

Indeed, in undercooling experiments on $Co_{80}Pd_{20}$ melts an attractive interaction between the liquid and an external magnet was observed when the temperature, T, approached T_C, which indicates the onset of magnetic ordering [3]. Studies of the temperature-dependence of the magnetization of electromagnetically levitated $Co_{80}Pd_{20}$ specimens with a modified Faraday balance [4] revealed a Curie-Weiss behavior. The measured Curie temperature of the melt, T_C^L, lies approximately $\Delta T_C^{SL} = 20$ K below that of the solid, T_C^S. These results were confirmed by muon-spin rotation experiments [5].

Most undercooling studies on Co-based alloy melts revealed no undercoolings below T_C^L [3,4,5,6,7,8] although different experimental techniques were used. However, in one experiment [9] on small and comparatively fast-cooled liquid $Co_{80}Pd_{20}$ droplets undercoolings below T_C^L were reported. Moreover, for a bulk sample of pure Co a nucleation temperature $T_N = 1385$ K was measured applying a melt-fluxing technique [6]. This T_N is slightly below $T_C^L = 1388$ K as determined by measurements of the magnetic susceptibility of Co using a high-precision Faraday balance [10]. Nevertheless, this small temperature difference still lies within the error limits of T_N and T_C^L.

Experiments on the composition-dependence of the undercoolability of Co-Pd melts were performed using the techniques of electromagnetic levitation [6,8] and melt-fluxing [6,7]. The maximum relative undercooling $\Delta T/T_L$ depends on the Co-composition, x, in the compositional range in which T_N is near T_C^L ($x > 75$ at. % Co), whereas it is nearly composition-independent at smaller Co-concentrations. The analysis of these findings in the framework of classical nucleation theory with a composition-independent pre-exponential factor delivers a catalytic potency factor for heterogeneous nucleation, $f(\theta)$, that varies as a function of the alloy composition [6]. Such a change of $f(\theta)$ differs from similar undercooling results obtained on other miscible systems like Ni-Cu, in which $f(\theta)$ does not change with alloy composition, independently of sample size and experimental technique [11,12]. This behavior suggests that crystal nucleation in Co-Pd alloys is stimulated by the onset of magnetic ordering.

This idea is supported by statistical investigations of the undercoolability of different Co-Pd alloys which indicate that the nucleation mechanism changes within the narrow compositional range of 70 at.% Co $< x <$ 75 at.% Co [8]. This range separates the regime where T_N approaches T_C from that where T_C is significantly below T_N ($x < 70 <$ at.% Co).

15.2
Classical Approach to Describe the Nucleation Behavior of Co-Pd Melts

Following classical nucleation theory [13], the steady-state nucleation rate of a solid phase in an undercooled melt is given by:

$$I_{SS} = \frac{k_B T \xi N_L}{3\, a_0^3\, \eta(T)} \exp\left(-\frac{\Delta G^* f(\theta)}{k_B T}\right). \tag{1}$$

ΔG^* is the activation energy for the formation of a critical nucleus of the solid phase, a_0 the interatomic spacing, $\eta(T)$ the viscosity of the melt, N_L Avogadro's number, $f(\theta)$ the catalytic potency factor for heterogeneous nucleation and ξ the fraction of atoms that can act as a nucleation site. For homogeneous nucleation $f(\theta) = 1$ and $\xi = 1$. However, if the melt is in contact with foreign phases (e. g. container walls or impurity sites), the formation of a solid nucleus is facilitated by heterogeneous nucleation ($f(\theta) < 1$ and $\xi \ll 1$). As a typical value for heterogeneous nucleation in containerlessly processed metallic specimens we assume $\xi = 10^{-13}$. ΔG^* is given by:

$$\Delta G^* = \frac{16\pi}{3} \frac{\gamma^3}{\Delta G_V^2}. \tag{2}$$

γ denotes the solid-liquid interfacial energy and ΔG_V the difference in Gibbs free energy per unit volume between liquid and solid.

In order to detemine ΔG_V it must be considered that in Co-Pd alloys the Co composition, x_N, of the solid nucleus deviates from the nominal composition, x_0, of the melt. We estimate x_N at a given T_N according to a model by Thompson and Spaepen [14]:

$$x_N(T_N) = \frac{x_0}{x_0 + (1-x_0)\exp\left[\frac{T_L - T_N}{RT_N}\left(\Delta S_f^{Pd} - \Delta S_f^{Co}\right) + \frac{T_L}{T_N}\ln\left(\frac{x_0\,(1-x_S^{eq})}{x_S^{eq}\,(1-x_0)}\right)\right]}\,. \tag{3}$$

x_s^{eq} denotes the Co concentration of the solid phase that is in equilibrium with the melt of concentration x_0 at T_L. R is the gas constant. ΔS_f^{Pd} = 9.61 J/(mol K) and ΔS_f^{Co} = 9.16 J/(mol K) [15] are the entropies of fusion of pure Pd and Co. The difference in Gibbs free energy between the liquid and the solid phase is then given by

$$\Delta G_V(T_N) = (T_L - T_N)\,\Delta S_f^{Co} + RT_N \ln\left(\frac{x_0}{x_N}\right) - RT_L \ln\left(\frac{x_0}{x_s}\right). \tag{4}$$

We estimate the solid-liquid interfacial energy γ within the negentropic model [16,17]:

$$\gamma(T) = \alpha\,\frac{\Delta S_f\,T}{(N_L V_m^2)^{1/3}}\,. \tag{5}$$

V_m denotes the molar volume. The factor α depends on the structure of the solid nucleus. For fcc structures (crystal structure of solid Co-Pd alloys) α = 0.85 is estimated [17].

We assume a linear dependence of ΔS_f on the composition of the nucleus:

$$\Delta S_f(x_N) = \Delta S_f^{Pd}\,(1 - x_N) + \Delta S_f^{Co}\,x_N\,. \tag{6}$$

The viscosity $\eta(T)$ of the melt is expressed by a Vogel-Fulcher-Tammann ansatz:

$$\eta(T) = \eta_0 \exp\left(\frac{A}{T - T_0}\right). \tag{7}$$

We assume A = 2000 as suggested by Battezati, et al., [18], $T_0 = 0.35 \cdot T_L$ [19] and η_0 = 0.004 Pa · s which is motivated by the value of the viscosity of pure Co at T_L [20].

The solidification of a melt sets in at the nucleation temperature T_N, if at least one nucleation event occurs within the sample volume V during the experiment time t_N:

$$I_{ss}(T_N)\;t_N\;V \geq 1\,. \tag{8}$$

Fig. 1 shows the Co-rich side of the phase diagram of Co-Pd inferred from differential thermal analysis (DTA) data [7,6,21] together with the minimum nucleation temperatures measured in undercooling experiments on bulk samples by electromagnetic levitation and melt fluxing [6,7,8,22,23]. A good description of the experimental results at 50 at.% Co is obtained if a value $f(\theta)$ = 0.35 is chosen. Assuming that classical nucleation theory can be applied and that $f(\theta)$ is independent of the Co

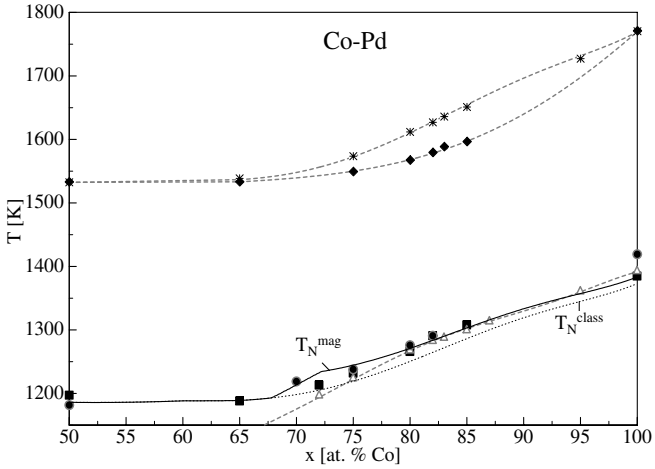

Fig. 1 Phase diagram of Co-Pd. The liquidus-, solidus- and Curie temperatures, T_L, T_S and T_C as determined by DTA [7,6,21] are marked by asterisks, diamonds and triangles, respectively. The dashed gray lines are the interpolations through the measured values of T_L, T_S and T_C. The mimimum nucleation temperatures measured on bulk samples utilizing the electromagnetic levitation technique [6,8,22,23] are depicted by circles and those determined by a melt fluxing technique are marked by squares [7,6]. The dotted line shows the nucleation temperatures T_N^{class} calculated by applying classical nucleation theory under the assumption of a constant catalytic potency factor for heterogeneous nucleation of $f(\theta) = 0.35$, whereas the solid line depicts the nucleation temperatures T_N^{mag} calculated by including a magnetic contribution to the driving force ΔG_V for crystal nucleation.

concentration, as observed for other solid solutions [11,12], it is possible with equations (1)–(8) to predict nucleation temperatures for all other alloy compositions. For these calculations values for T_L and T_S were used that were estimated by interpolation between the data points measured by DTA at different alloy compositions [7,6,21]. The results of these calculations are shown in fig. 1 (dotted curve). The nucleation temperatures T_N^{class} calculated within this classical model are in agreement with the measured values of T_N only for $x < 70$ at.% Co, where T_C is significantly smaller than T_N. At high Co concentrations, nucleation occurs at higher temperatures than predicted, when T is approaching T_C. Obviously, classical nucleation theory must be extended by magnetic contributions in order to describe the observed nucleation behavior. This paper is a summary of our work in this area [24]. Additional calculations pertaining the alloys are presented as well.

15.3. Extension of the Classical Nucleation Model by Magnetic Contributions

Magnetic contributions may influence γ and/or ΔG_V. Our estimations of the magnetic contribution to γ using a broken bond approach have shown that this contribution is negligible compared with the classical contribution according to eq. (5) [24]. The magnetic contribution to ΔG_V, however, turns out to be of fundamental importance.

The magnetic free energy F^+_{mag} of a single spin J (the superscript $^+$ always indicates that a quantity is normalized to one single spin) in an external magnetic field B is defined by [25]

$$e^{-F^+_{mag}} = \sum_{J_z=-J}^{J} e^{-g\mu_B B J_z} = \frac{e^{g\mu_B B(J+1/2)} - e^{-g\mu_B B(J+1/2)}}{e^{g\mu_B B/2} - e^{-g\mu_B B/2}}\,, \tag{9}$$

with $\beta = (k_B \cdot T)^{-1}$, μ_B the Bohr magneton and g Landé's g-factor. For condensed matter at low pressure the pressure-dependent terms of the Gibbs free energy can be neglected, and hence: $G^+_{mag} \approx F^+_{mag}$.

The magnetic contribution S_{mag} to the entropy of the system of N_J spins is given by [25]

$$S_{mag} = N_J\, k_B\, \beta^2 \frac{\partial F^+_{mag}}{\partial \beta} \tag{10}$$

and the magnetization by:

$$M_0\,(T,\, B) = -\frac{N_J}{V}\,\frac{\partial F^+_{mag}}{\partial B} = \frac{N_J}{V}\, g\,\mu_B J\, B_J\,(g\,\mu_B J B)\,. \tag{11}$$

Here, $\mathrm{B}_J(\beta g \mu_B J\, B)$ denotes the Brillouin function.

Within the mean field theory of magnetism [25] the effective field B_{eff} is expressed by

$$B_{eff} = B + \lambda\, M\,, \tag{12}$$

with λ a coupling constant and B the external field. Together with eq. (11) this delivers an expression for the magnetization:

$$\boldsymbol{M}(T) = M_0(T,\, B_{eff}) = M_0(T,\, B + \lambda \boldsymbol{M}(T))\,, \tag{13}$$

which has to be solved self-consistently.

In the molecular-field theory the Curie temperature is expressed by [25]:

$$T_C = \frac{N_J\, g^2\, \mu_B^2}{3\, k_B\, V}\, \lambda\, J\,(J+1) \tag{14}$$

If T_C of a given material is known, this formula enables the calulation of the coupling constant λ. Then, numerical solution of eq. (13) gives the magnetization $M(T)$ as a function of T. From this with eq. (12) the effective field $B_{eff}(T)$ is calculated and from this with eq. (9) and (10) the free energy $F_{mag}(T) \approx G_{mag}(T)$ and the entropy $S_{mag}(T)$.

Our calculations of the magnetic contributions to the thermodynamic quantities of Co-Pd alloys are based on the following assumptions and parameters.

The magnetic moment of Co-Pd alloys per atom was measured as a function of the composition for $x > 78$ at. % Co [26]. These results imply:

$$p_{at}(x) = 1.75\ \mu_B - (1 - x) \cdot 0.926\ \mu_B\ . \tag{15}$$

From this and with $g = 2.17$ and $J = 1/2$, the number j of spins per atom is calculated by $j = p_{at}/(J \cdot g)$ [27]. If N denotes the number of atoms in the sample, the number of spins is given by $N_J = N \cdot j$.

The composition-dependence of T_C^S was inferred by interpolation between the values measured by DTA for various alloys [6,7] (see the corresponding dashed grey line in fig. 1). For pure Co T_C^L lies 6 K below T_C^S [10], while for $Co_{80}Pd_{20}$ the difference amounts to 18 K [4]. Based on these results we assume a linear composition-dependence of $\Delta T_C^{SL} = T_C^S - T_C^L$:

$$\Delta T_C^{SL} = T_C^S - T_C^L = (1 - x) \cdot 60\ \text{K} + 6\ \text{K}\ . \tag{17}$$

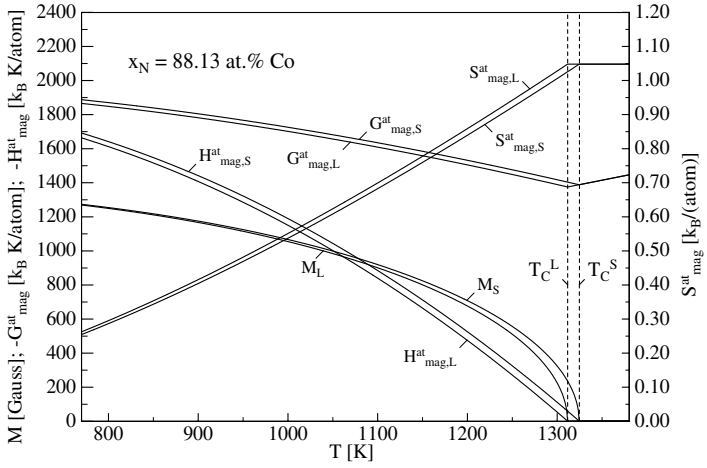

Fig. 2 Magnetic contributions, $G^{at}_{mag,L}$ and $G^{at}_{mag,S}$, to the Gibbs free energies per atom, magnetic contributions, $S^{at}_{mag,L}$ and $S^{at}_{mag,S}$, to the entropies per atom, magnetic contributions, $H^{at}_{mag,L}$ and $H^{at}_{mag,S}$, to the enthalpies per atom and magnetizations M_L and M_S in liquid (L) and solid (S) Co-Pd at a composition of $x_N \approx 88.13$ at.% Co that corresponds to the composition of a solid nucleus in a $Co_{80}Pd_{20}$ liquid at a nucleation temperature of $T_N \approx 1270$ K.

For the calculation of the magnetic contribution on the driving force for nucleation in Co-Pd melts it is crucial to consider that the composition x_N of the nucleus differs from the nominal composition x_0 of the melt. x_N is estimated according to eq. (3).

As an example, we analyze the crystal nucleation in a Co-Pd melt of the nominal composition $Co_{80}Pd_{20}$. As shown in Fig. 1 for this alloy minimum nucleation temperatures of $T_N \approx 1270$ K were experimentally observed. Under these conditions the solid nuclei have a concentration of $x_N \approx 88.13$ at. % Co as calculated by eq. (3). According to eq. (16) at this composition $p_{at} \approx 1.64\ \mu_B$. As inferred from fig. 1 the nuclei of composition $x_N \approx 88.13$ at. % Co are characterized by a Curie Temperature $T_C^S(x_N) = 1324$ K. With eq. (17) a Curie temperature of the corresponding liquid of $T_C^L(x_N) = 1311$ K is estimated.

Furthermore, we assume that no external magnetic field is applied ($B = 0$). Then, numerically solving eq. (9)–(13) with the above parameters gives magnetic Gibbs free energies per atom $G^{at}_{mag,L}$ and $G^{at}_{mag,S}$, magnetic entropies per atom $S^{at}_{mag,L}$ and $S^{at}_{mag,S}$, magnetic enthalpies per atom $H^{at}_{mag,L}$ and $H^{at}_{mag,S}$ (from $G^{at} = j\ G^{+} = H^{at} - T\ S^{at}$) and magnetizations M_L and M_S of the solid and liquid phase at $x_N = 88{,}13$ at. % Co these are shown in Fig. 2. Here, the superscript ^{at} indicates that the quantity is normalized to one atom.

In Fig. 3 the differences $\Delta G^{at}_{mag} = G^{at}_{mag,L} - G^{at}_{mag,S}$, $\Delta S^{at}_{mag} = S^{at}_{mag,L} - S^{at}_{mag,S}$ and $\Delta H^{at}_{mag} = H^{at}_{mag,L} - H^{at}_{mag,S}$ are plotted. For $T > T_C^S$ there is no magnetic contribution to the differences of Gibbs free energy, entropy and enthalpy of liquid and solid phase. However, if T is decreased below T_C^S, ΔG^{at}_{mag}, ΔH^{at}_{mag} and $-\Delta S^{at}_{mag}$ steeply rise

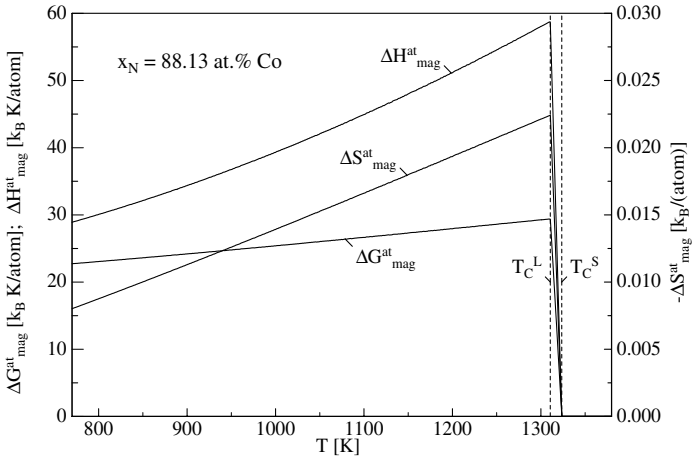

Fig. 3 Differences in the magnetic contributions to the Gibbs free energy, $\Delta G^{at}_{mag} = G^{at}_{mag,L} - G^{at}_{mag,S}$, entropy, $\Delta S^{at}_{mag} = S^{at}_{mag,L} - S^{at}_{mag,S}$, and enthalpy, $\Delta H^{at}_{mag} = H^{at}_{mag,L} - H^{at}_{mag,S}$, between liquid and solid Co-Pd at a composition of $x_N \approx 88.13$ at.% Co that corresponds to the composition of a solid nucleus in a $Co_{80}Pd_{20}$ liquid at a nucleation temperature of $T_N \approx 1270$ K.

to their maximum values at T_C^L. Further lowering T leads to a slight decrease of ΔG_{mag}^{at}, ΔH_{mag}^{at} and $-\Delta S_{mag}^{at}$. A similar estimation was performed for pure Co [24]. The maxima of ΔG_{mag}^{at}, ΔH_{mag}^{at} and $-\Delta S_{mag}^{at}$ are approximately twice as large for the system with a composition of the nucleus of $x_N = 88.13$ at.% Co as for pure Co. This is mainly a result of the composition-dependence of the difference ΔT_C^{SL} ($\Delta T_C^{SL} = 6$ K for pure Co and $\Delta T_C^{SL} = 13$ K at $x_N = 88.13$ at.% Co).

While Fig. 3 shows ΔG_{mag}^{at}, ΔH_{mag}^{at} and ΔS_{mag}^{at} only at the fixed composition $x_N = 88.13$ at.% Co as a function of the temperature, these quantities can be calculated for all possible combinations of x_N and T_N in a similar way. In order to model the nucleation behavior of undercooled Co-Pd melts, $\Delta G_{mag}(T_N, x_N) = \Delta G_{mag}^{at}(T_N, x_N) \cdot N_L / V_m$ must be added to the classical contribution $\Delta G_V(x_N, T_N)$ as calculated with eq. (4).

The nucleation temperatures T_N^{mag} determined by including this magnetic contribution to ΔG_V are shown as a function of the alloy composition in Fig. 1 (solid line). Different from the classical model without magnetic contributions a satisfactory fit to the experimental results is obtained in the full investigated compositional range 50 at.% Co $\leq x \leq$ 100 at.% Co.

15.4. Conclusions

The studies presented above indicate that in magnetically ordering melts the magnetic phase transformation is coupled with the liquid-solid transition by a magnetic contribution, ΔG_{mag}, to the driving force, ΔG_V, for nucleation. The inclusion of this contribution, calculated from simple considerations within the molecular field theory of magnetism, allows a quantitative description of the undercooling behavior of Co-Pd liquids over the *entire* composition range. ΔG_{mag} facilitates nucleation when the temperature of the undercooled liquid falls below the Curie temperature of the solid nucleus. The higher the maximum value, the smaller is the difference between T_C^S and T_C^L.

In the light of these findings, pure Co and Co-Pd alloys with a very high Co content appear to be the more suitable ones for achieving undercoolings below T_C^L.

Acknowledgements

We thank D.M. Herlach, T. Schenk, G. Wilde, G.P. Görler, S. Reutzel, S. Blügel, K. Schneider and T. Volkmann for fruitful discussions. Financial support from the Deutsche Forschungsgemeinschaft (DFG) under contract Nos. Ho1942/1 and Ho1942/2 is gratefully acknowledged by D. H.-M.. F.S. is grateful for funding from the Alexander von Humboldt Stiftung and from the National Space and Aeronautics Administration under contract number NA68-1680.

References

[1] D. Turnbull, J. Appl. Phys. 1950, 21, 1022–1029.

[2] D.M. Herlach, R.F. Cochrane, I. Egry, H.-J. Fecht and A.L. Greer, International Materials Review 1993, 38, 273–347.

[3] D. Platzek, C. Notthoff, D.M. Herlach, G. Jacobs and K. Maier, Appl. Phys. Lett. 1994, 65, 1723–1724.

[4] J. Reske, D.M. Herlach, F. Keuser, K. Maier and D. Platzek, Phys. Rev. Lett. 1995, 75, 737–739.

[5] D. Herlach, C. Bührer, D.M. Herlach, K. Maier, C. Notthoff, D. Platzek and J. Reske, Europhys. Lett. 1998, 44, 98–102.

[6] D.M. Herlach, D. Holland-Moritz, Th. Schenk, K. Schneider, G. Wilde, O. Boni, J. Fransaer and F. Spaepen, J. Non-Cryst. Sol. 1999, 250–252, 271–276.

[7] G. Wilde, Thesis, Technical University Berlin (1997).

[8] T. Schenk, D. Holland-Moritz and D.M. Herlach, Europhys. Lett. 2000, 50, 402–408.

[9] T. Albrecht, C. Bührer, M. Fähnle, K. Maier, D. Platzek and J. Reske, Appl. Phys. A 1997 65, 215–220.

[10] S. Reutzel and D.M. Herlach, Mat. Sci. Eng., in press.

[11] R. Willnecker, D.M. Herlach and B. Feuerbacher, Mat. Sci. Eng. 1988, 98, 85–88.

[12] R.E. Cech and D. Turnbull, J. Metals, 1951, 191, 242.

[13] J.W. Christian, The Theory of Transformation in Metals and Alloys, Pergamon, Oxford, 1975, pp. 418–476.

[14] C.V. Thompson and F. Spaepen, Acta Met. 1983, 31, 2021–2077.

[15] R. Hultgren, P.D. Desai, D.T. Hawkins, M. Gleiser and K.K. Kelley, Selected Values of the Thermodynamic Properties of Binary Alloys, ASM, Metals Park, 1973.

[16] F. Spaepen, Acta Metall. 1975, 23, 729–743.

[17] D.R. Nelson and F. Spaepen, in Solid State Physics (Ed.: Ehrenreich, F. Seitz and D. Turnbull), Academic Press, New York, USA, 1989,Vol.42, p. 1–53.

[18] L. Battezzati, C. Antonione and F. Marino, J. Mater. Sci. 1989, 24, 2324–2330.

[19] G. Wilde, G.P. Görler and R. Willnecker, Appl. Phys. Lett. 1996, 68, 2953–2955.

[20] Smithells Metals Reference Book (Ed.: E.A. Brandes) Butterworths, London, 1983.

[21] G.P. Görler, private communication.

[22] J. Schade, A. McLean and W.A. Miller in Undercooled alloy phases (Ed.: E.W. Collings and C.C. Koch), Metallurgical Society of AIME, Warrendale, PA, 1986, p. 233–248.

[23] T. Volkmann, G. Wilde, R. Willnecker and D.M. Herlach, J. Appl. Phys. 1998, 83, 3028–3034.

[24] D. Holland-Moritz and F. Spaepen, Phil. Mag., in press.

[25] N.W. Ashcroft and N.D. Mermin, Solid State Physics, Saunders College, Holt-Saunders Japan, Tokyo, 1981.

[26] J. Crangle and D. Parsons, Proc. Roy. Soc. 1960, A255, 509.

[27] R.S. Tebble and D.J. Craik, Magnetic Materials, Wiley, London, 1969.

16
Identification of the Substrate of Heterogeneous Nucleation in Zn-Al Alloy Inoculated with ZnTi-Based Master Alloy

Witold K. Krajewski, A. Lindsay Greer, Thomas E. Quested, Waldemar Wolczynski

Abstract

Grain refinement of the primary α′ fcc solid solution in a Zn-25wt%Al casting alloy is achieved by inoculation with a Zn-4.6wt%Ti master alloy. Microstructural studies show the mechanism of the refinement to be heterogeneous nucleation on $Ti(Al,Zn)_3$ particles which have an excellent lattice match with the α′ phase.

16.1
Introduction

The improvement of the properties of conventional materials makes a significant contribution to technological advances. Foundry alloys based on zinc-aluminum were introduced in the 1920s and have been subject to continual development. Because of the demand for higher strength, the aluminum content in these alloys has been increased in the range 6 to 40 wt. %.

Investigations on alloys containing copper in the 1940s and 1950s in Germany [1–4] stimulated the development of alloys introduced into practice in the 1950s and 1960s. These are the ZA alloys – ZA8 (Zn-8Al-1Cu-0.02Mg), ZA12 (Zn-11Al-1Cu-0.025Mg), ZA27 (Zn-27Al-2Cu-0.015Mg) [5–6] and ZA35 (Zn-(30–35)Al-(3–5)Cu-(0.5–1)Si) [7]. Alloys with similar aluminum content were introduced in Poland – Z82 (Zn-8Al-2Cu-0.3Mn), Z105 (Zn-10Al-5Cu), Z284 (Zn-28Al-4Cu-0.04Mg-1.3Mn) [8]. The Zn8Al-based alloys are cast mostly with a ferrous permanent mould, while the Zn12Al-based and Zn27Al-based alloys can be cast by cold-chamber die casting, sand casting and permanent-mould casting [5, 7, 9]. Furthermore, the ZA27 alloy develops its optimum properties when it is sand-cast [9].

High-aluminum zinc alloys with 25–28wt% Al deserve special attention; their high strength, very good casting and tribological properties and wide applicability, can compete with copper-containing alloys. They do, however, tend to have coarse grain structures, especially when cast at the low cooling rates typical of sand moulds. The elongation and ultimate tensile strength (UTS) of the gravity-cast alloys can be

controlled to some extent through the cooling rate. However, depending on the processing and shape of the casting, the microstructural control in practice remains limited [7]. For zinc alloys with high aluminum content the aim is to refine the primary dendritic structure of α′. These dendrites, together with non-equilibrium eutectic, are the basic components of the microstructure of Zn-(25–40)wt%Al [10–11], a binary composition range which is the basis for such industrial alloys as Z284, ZA27 and ZA35.

The α′ phase Zn-Al solid solution is face-centered cubic, with lattice parameter a = 0.402 to 0.405 nm, depending on composition [10]. This phase has the same crystal structure as aluminum and a similar lattice parameter (a_{Al} = 0.404 nm), suggesting that it might be refined using inoculants developed for low-solute-content aluminum alloys. Indeed, grain refinement of Zn-Al has been achieved with additions of 0.03 to 0.05 wt% Ti in the form of Al-Ti or Al-Ti-B master alloys (MA). The change in the α′ morphology from branched dendritic to fine, semi-globular [7, 12–16] increases ductility without reducing tensile strength [7, 15–16]. The observed refinement of the α′ dendrites is attributed to their heterogeneous nucleation on Ti_2Al_5Zn particles (AlTi5 MA) [12] or on $Ti(Al, Zn)_3$ particles (AlTi4 MA, AlTi5B1 MA) [13] which were observed in SEM examinations of the chill-cast and sand-cast Zn-24wt%Al alloy [12] and Zn-25wt%Al alloys slowly cooled in a graphite crucible [13]. The presence of particles of $Ti(Zn_xAl_{1-x})_3$ composition in the centers of refined α′ dendrites was also confirmed in sand-cast Zn-25wt%Al alloy (AlTi4.8 MA) [14].

There are, however, difficulties in making the refining additions. The master alloys require a melt temperature of 700 to 750°C to ensure their rapid dissolution [7, 12–14], whereas the practical limit for holding liquid Zn-Al alloys is 550 to 600 °C. Satisfactory mixing of additions is further impeded by the low density of Al-Ti master alloys (~3 g cm^{-3}, compared to ~5 g cm^{-3} for a Zn – (25–28) wt% Al melt). These difficulties can be avoided by replacing Al-Ti master alloys with those based on Zn-Ti; these have a higher density than Zn-Al melts and they dissolve readily in the melts at temperatures of 450 °C and higher. Importantly, the Zn-Ti inoculants have similar refining effectiveness to those based on Al-Ti, giving a semi-globular microstructure and improved tensile properties [17–19]. The Zn-Ti master alloy introduces particles of $TiZn_3$ phase into the melt. Microstructural studies of inoculated alloys have shown that in the centers of refined α′ particles, there are particles, which probably act as substrates for heterogeneous nucleation.

The present paper focuses on further characterization of these particles and their nucleant action. Attention is paid mainly to their composition and structure, although their size may also be important according to the *free-growth* analysis of grain initiation [20–22] and will be the subject of future work.

16.2 Experimental Methods

A Zn-25wt%Al (ZnAl25) alloy and a master alloy of Zn-4.6wt%Ti (ZnTi4 MA) were prepared from electrolytic aluminum (minimum purity 99.96%), electrolytic zinc

(99.995%) and titanium sponge (98–99.8%, from Johnson Matthey Alfa). The ZnAl25 alloy was slowly melted in an electric resistance furnace, in an alumina crucible of 0.2 liter capacity. The melt was superheated to ~600 °C and ZnTi4 MA was added to give an overall titanium content of 0.05wt%. Five minutes after the addition, the bath was stirred for 2 minutes with an alumina rod, and the alloy was cast into a dried sand mould with two K-type thermocouples (0.25 mm diameter), mounted in the mould cavity (Fig. 1) to monitor the cooling. Temperatures (with precision ± 0.5 °C) were recorded electronically on eight-channels with minimum measurement time 200 ms/channel (MRT-2 instrument, Mediana-Novo, Krakow). The first derivatives of the temperature-time curves were automatically calculated.

From the middle of castings (Fig. 1) samples about 25 mm high were cut for microstructural study. After grinding (on SiC grades 200, 400, 600, 800 and 1000) they were polished using 6 μm and 1 μm diamond pastes and finally using a suspension of 0.5 μm alumina in water-ethanol. Optical metallography (Leica DM IRM microscope) was performed on samples etched in dilute aqua regia.

X-ray diffractometry (Philips PW1710) was performed with CoKα radiation (filtered with a graphite monochromator), step-scanning (0.02°/10 s) over the angular range $2\theta = 20–130^{o}$. The X-ray patterns were analyzed using Philips PC-APD software. The investigations were carried out for bulk samples of ZnAl25 and Zn-25wt%Al-0.05wt%Ti (ZnAl25-Ti) alloys which were ground and polished but not etched. Studies were also made of powder samples of titanium-containing phases extracted from the ZnTi4 MA and ZnAl25-Ti alloys by dissolution in a solution of 2% hydrochloric acid in ethanol at room temperature for 12 hours. After dissolution of the matrix, the solution was filtered and the powder retained on the filter was washed several times with ethanol; for mounting in the diffractometer, it was then dried and transferred to a glass plate thinly coated with amorphous grease.

Thin foils of ZnAl25-Ti alloy for transmission electron microscopy (TEM) were jet-electropolished using a solution of 20% solution of $HClO_4$ at –30 °C. A Philips CM20 microscope was used with an accelerating voltage of 200 kV. Energy dispersive X-ray spectrometry (EDX, Link exL) was performed in a parallel-beam setting, using a LaB_6 electron source. The probe diameter (full width at half maximum) was 5 nm. Analysis times gave a few thousand counts of zinc. Elemental contents of Al Ti and Zn were estimated from the observed peak integrals using Link software.

Scanning electron microscopy (SEM) investigations were performed on unetched samples identical to those used for X-ray diffractometry. Two microscopes with energy-dispersive spectrometry were used: a Philips XL30 with a Link-Isis EDX, and a JEOL JSM 5800 WV microscope with Noran Voyager 3 EDS. The former microscope was also used for electron back-scatter diffractometry (EBSD) orientation determination (version 5.0 HKL Technology ApS, Jobro Denmark).

16.3 Results and Discussion

16.3.1 Thermal Analysis and Structure

The alloy melting temperatures were in good agreement with the latest data on the Al-Zn system [11]. The cooling curves measured by the wall thermocouple (Fig. 1) and their first derivatives are shown in Fig. 2. For the basic ZnAl25 alloy (Fig. 2a) crystallization begins at a nucleation temperature of ~492 °C, as indicated by the sharp rise in the first-derivative curve caused by the release of latent heat. For the ZnAl25-Ti alloy inoculated with 0.05wt%Ti (Fig. 2b) the corresponding nucleation

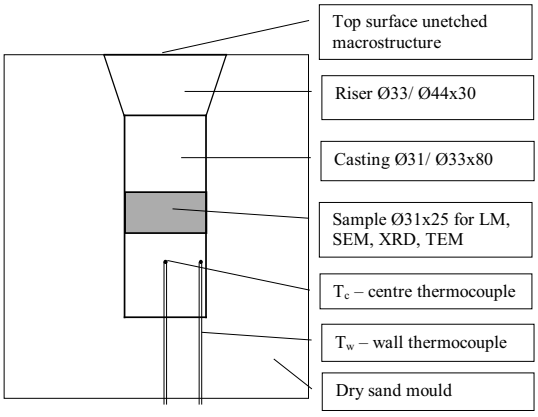

Fig. 1 Schematic diagram of the casting system [18].

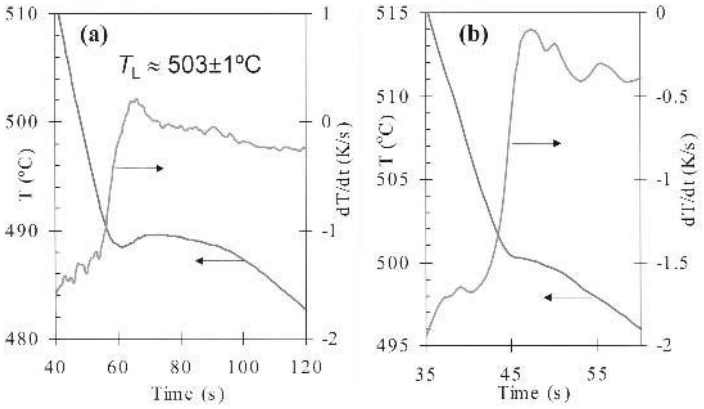

Fig. 2 Cooling curves measured by the wall thermocouple and the first derivatives of the temperature-time data: (a) for the initial ZnAl25 alloy; (b) for alloy ZnAl25-Ti inoculated with ZnTi4 MA to bring the overall Ti content to 0.05 wt% [19].

temperature is ~503 °C. Thus, the addition of the Zn-Ti master alloy reduces the melt undercooling at crystallization onset by ~10 K. Comparison of the macrostructures of the ZnAl25 alloy (Fig. 3 a) and ZnAl25-Ti alloy (Fig. 3 b) shows significant refinement. The increased grain density after inoculation shows that the particles introduced into the melt are effective heterogeneous nucleants. The corresponding microstructures (Fig. 4 a and 4 b) show that the coarse dendrites of the α′ Zn-Al solid solution are refined into semi-globular forms. Close examination of cross-sections of refined primary α′ phase (Fig. 5) reveals intermetallic particles which are the probable substrates for heterogeneous nucleation.

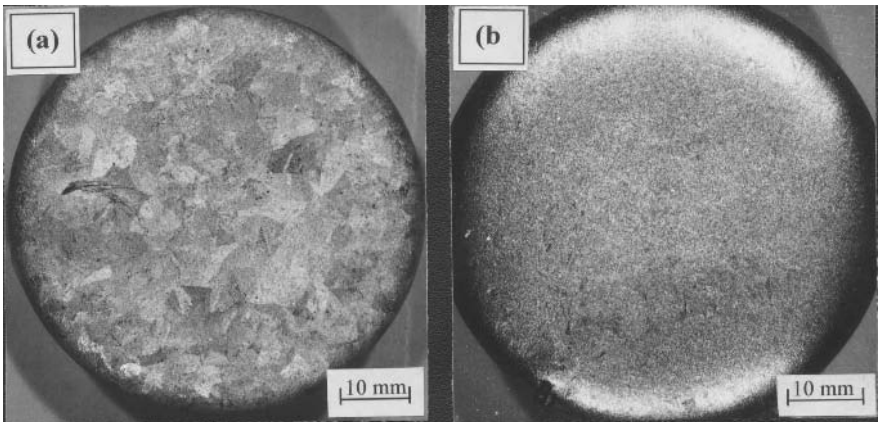

Fig. 3 Macrostructures observed by optical metallography of unetched surfaces of: (a) initial ZnAl25 alloy; (b) alloy ZnAl25-Ti inoculated with ZnTi4 MA to bring the overall Ti content to 0.05 wt% [19].

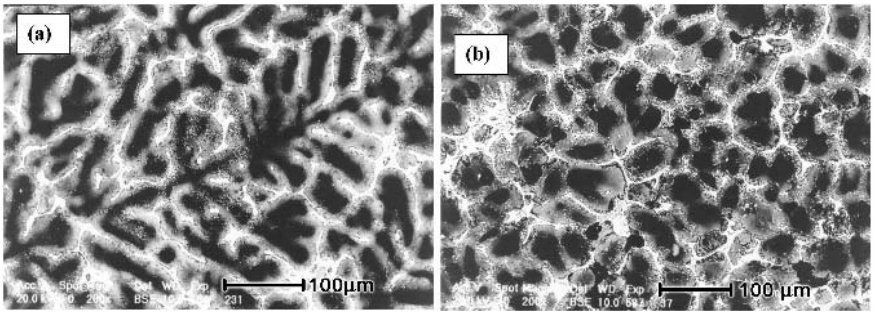

Fig. 4 SEM images of ZnAl25 alloy: (a) without and (b) with inoculation.

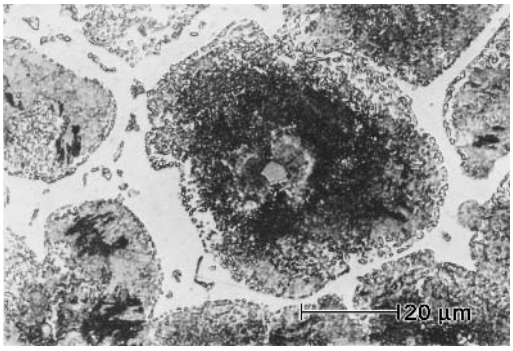

Fig. 5 Optical micrograph showing a Ti-containing particle within refined α′ phase in the inoculated ZnAl25-Ti alloy.

16.3.2
Crystal Structure and Chemical Composition

Scanning electron microscopy of the ZnTi4 master alloy (Fig. 6) displays dark blocky particles, which EDX microanalysis (Table 1) shows to be enriched in titanium compared to the matrix. The measured composition of the particles is consistent with the $TiZn_3$ phase detected by X-ray diffractometry of powder extracted from the master alloy (Table 2). The matrix of the master alloy includes a eutectic mixture of Zn and $ZnTi_{16}$, but these phases dissolve on addition to the ZnAl25 melt. The nucleant particles must therefore be the high-temperature phase $TiZn_3$; this has the cubic $L1_2$ structure and a lattice parameter only ~2.5% less than that of the primary α′ phase in the ZnAl25 alloy. The particle diameter (3 to 5 µm) is sufficiently large that there is not expected to be a significant barrier to free growth of nucleated grains [20]. From the results in Table 2, it is clear that the addition of 0.05wt.%Ti to ZnAl25 does

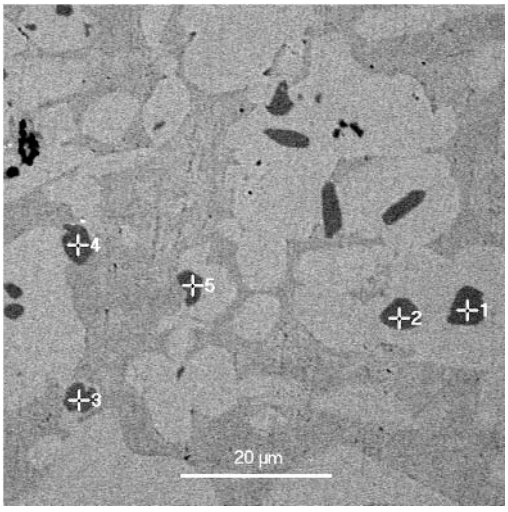

Fig. 6 SEM image showing the microstructure of the Zn-4.6wt%Ti master alloy (ZnTi4 MA). The dark blocky particles are a Ti-containing intermetallic phase.

not significantly change the lattice parameters of the α′ or η phases. On the other hand, the lattice parameter of the $L1_2$ $TiZn_3$ phase in the inoculated alloy is ~0.6% greater than in the master alloy itself. Microanalysis of the particles visible inside the refined α′ phase in the inoculated alloy (Table 3) gives an average chemical composition of 25.1 at% Ti, 15.5 at% Zn and 59.4 at% Al. It therefore appears that the binary $TiZn_3$ in the master alloy undergoes Al substitution for Zn when added to the ZnAl25 melt. The evolution to ternary $Ti(Al,Zn)_3$ occurs without change of crystal structure, but with an expansion of the lattice which reduces its mismatch with the α′ phase in the ZnAl25 alloy from 2.8% to 2.3% (Table 4). Based on these observations, it is expected that the $Ti(Al,Zn)_3$ particles can act as the substrates for nucleation of the primary α′ phase in the solidification of a ZnAl25 melt inoculated with ZnTi4 MA.

Tab. 1 Chemical composition of the eutectic matrix and randomly chosen Ti-containing particles in the microstructure of the ZnTi4 master alloy

	Particle					***Matrix***				
	No. 1	No. 2	No. 3	No. 4	No. 5	No. 1	No. 2	No. 3	No. 4	No. 5
Ti, at. %	24.40	23.72	24.29	24.71	24.04	5.77	6.15	5.53	5.47	6.85
Zn, at. %	73.60	76.11	75.16	74.70	75.15	94.23	93.85	94.47	94.53	93.15
Stoichiometric Formula:			$TiZn_3$					Zn-$TiZn_{16}$		

Tab. 2 Phases identified by fitting the results of X-ray diffractometry. The structures are described according to the *Strukturbericht* classification

Phase	***Crystal structure***	***Lattice parameter [Å]***	***Space group***	***Sample examined***
$TiZn_3$	cubic $L1_2$ ($AuCu_3$ type)	3.9324 ± 0.0019	Pm3m	Powder sample extracted from the ZnTi4 MA
α′	cubic A1	4.0450 ± 0.0008	Fm3m	Bulk sample of the initial ZnAl25 alloy
η	hexagonal A3	a = 2.6629 (+/-0.0003) c = 4.9411 (+/-0.0009) α = β = 90°; γ = 120°	$P6_3/mmc$	Bulk sample of the initial ZnAl25 alloy
α′	cubic A1	4.0434 ± 0.0010	Fm3m	Bulk sample of the ZnAl25–0.05wt%Ti alloy doped with ZnTi4 MA
η	hexagonal A3	a = 2.6633 (+/-0.0003) c = 4.9408 (+/-0.0010) α = β = 90°, γ = 120°	$P6_3/mmc$	Bulk sample of the ZnAl25–0.05wt%Ti alloy doped with ZnTi4 MA
$Ti(Al,Zn)_3$	cubic $L1_2$ ($AuCu_3$ type)	3.9575 ± 0.0003	Pm3m	Powder sample extracted from the ZnAl25–0.05wt%Ti alloy doped with ZnTi4 MA

Tab. 3 Composition of the Ti-containing intermetallic particles found inside the refined α′ primary phase of ZnAl25-Ti alloy inoculated with ZnTi4 MA. (EDX microanalysis)

Sample/ Particle No.	*39/1*	*39/3*	*39/4*	*39/5*	*18/1–1*	*18/1–3*	*37/4*	*40/3*	*40/2*	*18/15*
Ti, at. %	25.92	22.58	24.76	23.17	27.61	26.57	23.33	27.90	26.54	26.97
Zn, at. %	15.53	16.70	14.84	16.14	22.54	24.94	17.12	24.12	25.32	20.21
Al, at. %	58.55	60.73	60.40	60.69	49.85	48.49	59.55	47.98	48.14	52.83
Stoichiometric Formula:				$Ti(Al,Zn)_3$						

Tab. 4 Lattice misfits between the $TiZn_3$ phase in the ZnTi4 master alloy, or the $Ti(Al,Zn)_3$ phase in ZnAl25 alloy inoculated with ZnTi4 MA, and the α′ phase of the original ZnAl25 alloy (for which the lattice parameter a = 4.0450 Å)

Phase	*Lattice parameter, [Å]*	*Lattice misfit*
$TiZn_3$	3.9324	$\delta = \frac{a_\alpha - a_{TiZn_3}}{0.5\,(a_{TiZn_3} + a_\alpha)} = \frac{4.0450 - 3.9324}{0.5\,(3.9324 + 4.0450)} = 2.8\%$
$Ti(Al,Zn)_3$	3.9575	$\delta = \frac{a_\alpha - a_{Ti(Al,Zn)_3}}{0.5\,(a_{Ti(Al,Zn)_3} + a_\alpha)} = \frac{4.0450 - 3.9575}{0.5\,(3.9575 + 4.0450)} = 2.3\%$

16.3.3 Crystal orientation

16.3.3.1 TEM Examination of Thin Foils

TEM was used to investigate the orientation relationship between $Ti(Al,Zn)_3$ particles and the α′ phase surrounding them. The electron diffraction patterns (Fig. 7) show a typical case in which the $Ti(Al,Zn)_3$ and α′ phase are in matching crystallographic orientation. The only differences between the patterns from the two phases are the (100) and (110) reflections coming from the $L1_2$ superlattice of the $Ti(Al,Zn)_3$ (Figs 7c and 7e).

16.3.3.2 SEM – EBSD Examinations

Although TEM provides the best information on the crystallographic relationship between a particle and the phase surrounding it, there are difficulties in acquiring sufficient data. In preparing thin foils there is often loss of intermetallic particles. Furthermore, chemical thinning may induce changes of composition, while in ion-milling phase transformations may occur because of heating of the thin foil. The use of electron back-scatter diffractometry (EBSD) overcomes such difficulties. Figure 8 shows an example where the $Ti(Al,Zn)_3$ particle has the same orientation as the α′ phase surrounding it. On the other hand, there are cases where the orientations do not match; while Fig. 9 shows a particle apparently surrounded by α′, in most cases where the orientations do not match, however, the particles are on the periphery of the α′. Both theoretical and experimental studies of inoculation mostly suggest that the process is inefficient, with only perhaps 1% of the added particles

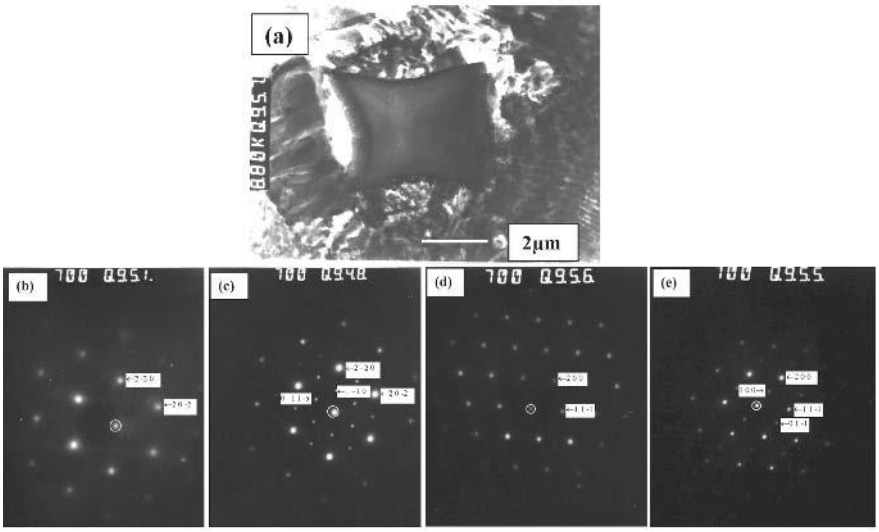

Fig. 7 (a) bright-field TEM micrograph of the microstructure of inoculated ZnAl25-Ti, showing an $L1_2$ structure $Ti(Al,Zn)_3$ particle within the α' Zn-Al solid solution [18]. Corresponding diffraction patterns of: (b) α' phase, zone axis [111]; (c) $Ti(Al,Zn)_3$ particle, zone axis [111]; (d) α' phase, zone axis [011]; (e) $Ti(Al,Zn)_3$ particle, zone axis [011].

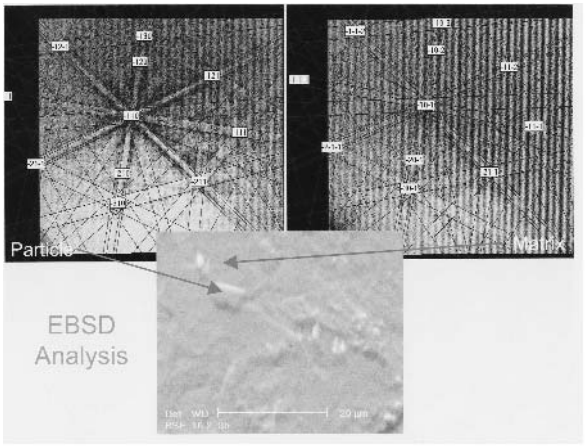

Fig. 8 Backscattered-electron SEM image of the microstructure of inoculated ZnAl25-Ti. The corresponding indexed EBSD patterns show that the α' Zn-Al solid solution and the $Ti(Al,Zn)_3$ particle are in matching crystallographic orientations.

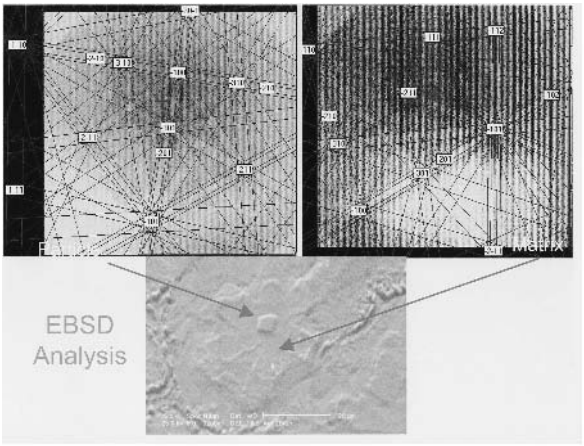

Fig. 9 Backscattered-electron SEM image of the microstructure of inoculated ZnAl25-Ti. In this case (in contrast to Fig. 8), the indexed EBSD indexed patterns show that the α′ phase and the $Ti(Al,Zn)_3$ particle have different crystallographic orientations. Taking into account the overall cuboidal morphology of the $Ti(Al,Zn)_3$ particles observed in optical metallography and SEM, and the cube-cube orientation relationship between the particles and α′ matrix surrounding them, it is reasonable to conclude that each exposed face of the particle can act as a substrate for nucleation. This would be analogous to the nucleation of α-Al on $L1_2$ Al_3Sc particles postulated in the Al–Sc system [24].

acting as nucleation substrates [20]. The remaining particles are pushed ahead of the growing primary phase or are engulfed by it [23], and for these no orientation relationship is expected.

16.4 Conclusions

The primary α′ Zn-Al solid solution is the main microstructural constituent in the high-aluminum casting alloy ZnAl25. When this alloy is inoculated with ZnTi4 master alloy there is a marked increase in the population of primary grains, while the melt undercooling at solidification onset is reduced by ~10 K. The ZnTi4 MA introduces $TiZn_3$ phase into the melt, where it evolves to $Ti(Al,Zn)_3$ as observed within the refined semi-globular α′ phase of the inoculated alloy. The $Ti(Al,Zn)_3$ has the same crystal symmetry as the α′ solid solution and closely matches its lattice parameter. The cube-cube orientation relationship between a particle and the α′ phase surrounding it is strong evidence of the nucleating action of the particle. This orientation relationship was verified both in TEM of thin foils and SEM-EBSD of bulk samples of inoculated ZnAl25-Ti alloy. It is expected that heterogeneous nucleation

of the α' solid solution can take place on any of the exposed faces of the $Ti(Al,Zn)_3$ particles.

Acknowledgements

One of the authors, WKK, thanks the Wasilewski family and Clare Hall, Cambridge for the Roman Wasilewski Scholarship, and the KBN (Polish State Committee for Scientific Research) for financial support under research grant 4 T08A 040 25. The authors acknowledge the provision of laboratory facilities in the Department of Materials Science and Metallurgy, University of Cambridge.

References

[1] E. Gebhardt, *Z. Metallk.* **1941**, *23*, 289.
[2] E. Gebhardt, *Z. Metallk.* **1942**, *34*, 208.
[3] E. Gebhardt, *Z. Metallk.* **1949**, *40*, 136.
[4] E. Peltzel, *Metall* 1954, *8*, 83
[5] E.J. Kubel, *Metal Progress* **1987**, *7*, 51.
[6] R.J. Barnhurst, *Foundry Trade J.* **1991**, *165*, 962.
[7] A.F. Skenazi, J. Pelerin, D. Coutsouradis, B. Magnus, M. Meeus, *Metall* **1983**,*37*, 898
[8] Foundry Zinc Alloys. Polish Standards PN-80/H-87102.
[9] R.J. Barnhurst, Zinc and Zinc Alloys, in *Metals Handbook*, 10th ed. **1992**, *10*, 527.
[10] J.L. Murray, *Bull. Alloy Phase Diag.* **1983**, *4*, 55.
[11] W.M. Li, Y.J. Zhang, *Trans. Nonfer. Metals Soc. China* **1999**, *9*, 611.
[12] W.A. Pollard, K.M. Pickwick, J.T. Jubb, R.H. Packwood, *Can. Metall. Quart.* **1974**, *13*, 535.
[13] A.A. Abdel-Hamid, *Z. Metallk.* **1992**, *83*, 314.
[14] W. Krajewski, *Z. Metallk.* **1996**, *87*, 645.
[15] M. Lamberigts, G. Walmag, D. Coutsouradis, P. Delneuville, M. Meeus, *AFS Trans.* **1985**, *93*, 569.
[16] M. Lamberigts, G. Walmag, D. Coutsouradis, *J. Inst. Met.* **1988**, *116*, 311.
[17] W. Krajewski, *Solidification Metals Alloys* **1995**, *22*, 124.
[18] W. Krajewski, *Archiv. Metall.* **1999**, *44*, 51.
[19] W.K. Krajewski, Shaping the Structure of Zn-Al Alloys by Doping with Zn-Ti Master Alloy. Habilitation Thesis. University of Mining and Metallurgy. ISBN 83–914313-6–3. Krakow, 2001, p. 67 (in Polish).
[20] A.L. Greer, A.M. Bunn, A. Tronche, P.V. Evans, D.J. Bristow, *Acta Mater.* **2000**, *48*, 2823.
[21] A.L. Greer, *Philos. Trans. Royal Soc. London* **2003**, *A 361*, 479.
[22] T.E. Quested, A.L. Greer, P.S. Cooper, *Mater. Sci. Forum* **2002**, *396–402*, 53.
[23] G. Wilde, J.H. Perepezko, *Mater. Sci. Eng.* **2000**, *A283*, 25.
[24] A.F. Norman, P.B. Prangnell, R.S. McEwen, *Acta Mater.* **1998**, *46*, 5715.

17
Undercooling and Solidification of Liquid Silicon

C. Panofen, R. P. Liu, D. Holland-Moritz, T. Volkmann, D.M. Herlach

17.1
Abstract

Containerless processing by levitation techniques was applied to undercool and solidify pure Si melts without disturbing effects by surrounding crucible walls. A pyrometric sensor measured the sample temperature contactlessly. Large undercoolings of up to 330K have been achieved. We stimulated crystallization by triggering with a silicon wafer at the desired temperatures. The velocity of the solidification front as a function of undercooling was directly determined by photo sensors and a high speed camera. We analyzed the growth behavior within current theories of crystal growth in undercooled melts. Special emphasis was placed to a microstructure transition from faceted to non-faceted growth. The results of the growth measurements were correlated to microstructure formation upon undercooling prior to solidification.

17.2
Introduction

Silicon is the element with the highest relevance for the production of electronic components. The fabrication of silicon material ranges from perfect single crystals to polycrystalline material and amorphous thin films with varying properties suited for the needs of the electronics industry.

Due to its high melting temperature and high chemical reactivity the observation of phase transformations and thermophysical properties of undercooled liquid silicon is difficult. Flux processing and containerless processing such as electromagnetic levitation and electrostatic levitation have successfully been applied to deeply undercool liquid silicon melts. The levitation and fluxing techniques allow to significantly undercool liquid materials by avoiding heterogeneous nucleation sites. The first undercooling experiments on silicon were performed by Devaud and Turnbull [1] using uncoated silicon in a quartz tube. Their undercooling of 270 K was exceeded by Shao and Spaepen [2] processing pure silicon droplets of 1 mm diameter in a $SiO_2BaOCaO$ flux and succeeding to undercool their samples to as much as

350 K. Density, hemispherical total emissivity and surface tension of liquid silicon was determined by the electrostatic levitation technique[3]. A transition of growth mode from the growth of faceted twins at low undercoolings to twin free grains at high undercoolings was presented [4]. Liu [5] reported an undercooling of 300 K necessary for this transition. Aoyama and Kuribayashi measured the growth rate of undercooled liquid silicon using photo sensors and a high speed camera with a maximum undercooling of 320 K [6]. In this work we measured the growth rate of undercooled liquid silicon with two photo sensors, monitored the growth front during solidification with a high speed camera and analyzed the surface morphologies of samples solidified at different undercoolings.

17.3 Experimental

Samples of 7–9 mm in diameter were cut from 99.999% pure silicon. We processed our samples in an electromagnetic levitation facility (see Figure 1) evacuated to 10^{-6} mbar and then backfilled with helium gas of 99.999% purity. The levitation coil was driven by a 300 kHz 5 kW RF-power generator. The liquid drop was successively undercooled and solidified by triggered nucleation.

In order to electromagnetically levitate the semi conducting material it had to be preheated to increase its electrical conductivity. We used a graphite heating element covered with an alumina shielding (see Figure 2). The graphite was inductively heated in the electromagnetic levitation coil and the heat conducted towards the

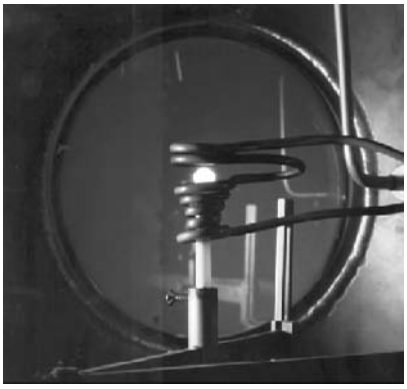

Fig. 1 Electromagnetic levitation setup

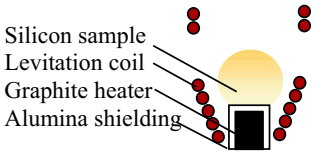

Fig. 2 Sample preheating setup

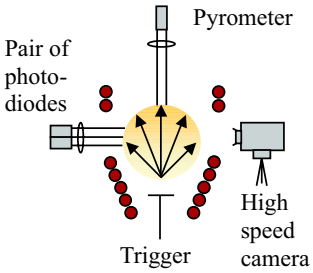

Fig. 3 Growth rate measurement of undercooled silicon triggered with a flat (100) wafer

sample. When the carrier density of the silicon became high enough to couple to the electromagnetic field the silicon sample could be levitated and heated independently from the graphite heater. We then removed the heating element from the levitation coil and set a 5mm x 5mm flat (100) Si-wafer at its place to trigger nucleation from the bottom of the sample (see Figure 3).

The temperature of the sample was monitored by a single color pyrometer using an emissivity of liquid silicon of $\varepsilon = 0.20$ [7, 8] at a wavelength of $\lambda = 800$ nm. Measurements with a two color pyrometer were carried out for comparison (see Figure 4). The temperature of the solid phase is not given appropriately due to the much higher emissivity of $\varepsilon = 0.43$ [7, 8] of solid silicon. The absolute temperature uncertainty in our measurement was ± 10 K. Undercoolings could be determined with higher precision since we determined the undercooling from the difference in temperature prior to solidification and immediately after remelting of the sample.

The temperature rise due to the recalescence event and the change in emissivity between the liquid and solid phase could be used to locate the propagating solidification front. Two high speed photo sensors and a high speed camera with a maximum acquisition speed of 120.000 frames/s (see Figure 3) were used to determine the

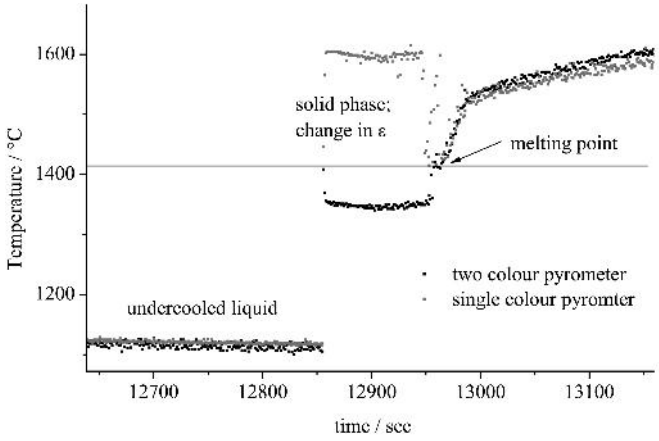

Fig. 4 Temperature – time profile of solidification of a silicon sample at 300 K undercooling measured by single and two color pyrometry

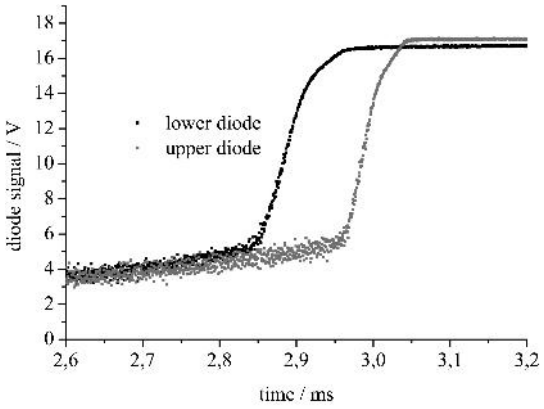

Fig. 5 Photodiode signal of triggered solidification of a silicon sample at 305 K undercooling

growth velocity of the undercooled silicon sample. The difference between start and stop time of each photo diode signal together with the sample geometry and the size of the measurement spot on the sample surface defined the growth velocity (see Figure 5). We used two photo diodes to be able to exclude spontaneous recalescence events.

17.4 Results & Discussion

17.4.1 Surface Morphologies and Solidification Mode

For small undercoolings, e. g. $\Delta T = 85$ K, we clearly observed faceted crystal growth from the surface morphology of the as-solidified sample (see Figure 6). Pronounced edges and faces were visible on a large scale. Twinned crystals were evident on the surface. Layer by layer growth can be concluded from these pictures with atoms attaching to laterally growing edges or kinks. Twin planes serve as preferential sites and re-entrant corners for the formation of a new layer [4, 5]. Solidification was remarkably slow, it took several seconds for the entire sample to crystallize. A solidification front propagating through the sample could not be observed. No dendrites were visible on the surface of the as-solidified sample at low undercoolings.

At higher undercoolings, e. g. $\Delta T = 255$ K, the surface morphology changed drastically. Dendrites became visible on the surface originating from the trigger site as can be seen in Figure 7. The solidification speed increased considerably resulting in a recalescence time of only 0.5 to 10 ms comparing to the time scale of seconds at low undercoolings. During solidification we observed a continuous solidification front propagating from the trigger point through the sample using the high speed camera (see Figure 9). At the undercooling of 255 K the front was wavy and not yet flat on a macroscopic scale. It was not until the highest undercoolings of 300 K that the growth front became flat on a macroscopic scale (see Figure 10). At this undercool-

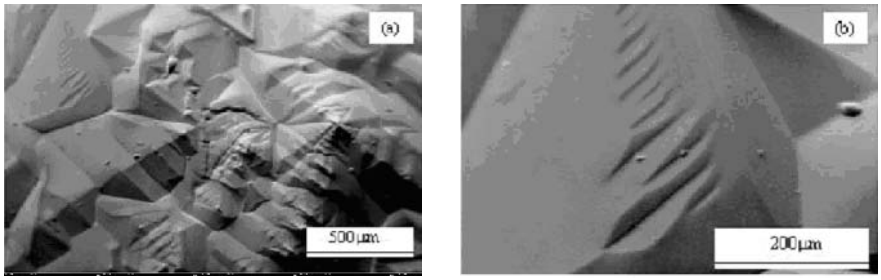

Fig. 6 Surface morphology of a sample solidified at 85 K undercooling

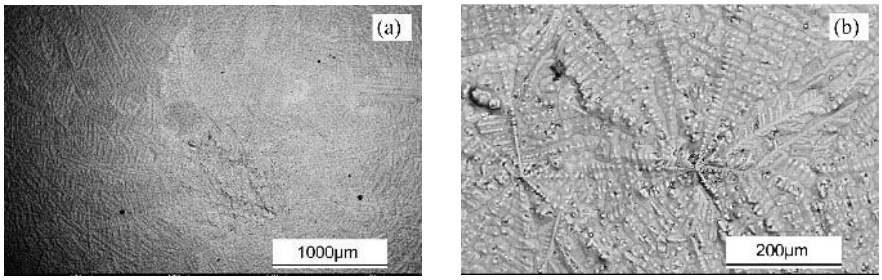

Fig. 7 Surface morphology of a sample solidified at 255 K undercooling

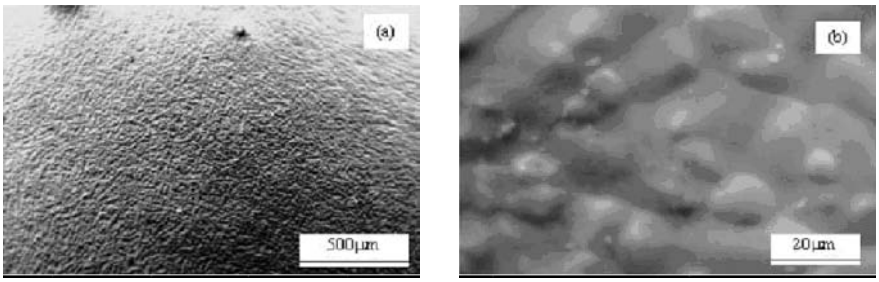

Fig. 8 Surface morphology of a sample solidified at 330 K undercooling

Fig. 9 Solidification of silicon undercooled at 255 K recorded with the high speed camera

Fig. 10 Solidification of silicon undercooled at 330 K recorded with the high speed camera

ing the 2-D projection of the solidification front onto the camera screen was a straight line. We interpret this as due to a high number of dendrites forming a continuous solidification front. An atomically rough surface is required for dendritic growth. Whether an interface is rough or smooth depends on the entropy of melting ΔS [9, 10]. Generally speaking we have an atomically rough surface for $\Delta S \leq 2R$ and an atomically flat surface for $\Delta S \geq 3R$, R is the gas constant. Dendritic growth requires the attachment of atoms at any site on a rough interface in contrast to the layer by layer growth of silicon with $\Delta S \approx 3.3R$. A change in the atomic surface attachment mechanism from atomically flat to atomically rough must be taking place for silicon with increasing undercooling. Since silicon undergoes a transition from faceted to dendritic growth we expect a transition from an atomically flat to a atomically rough solid-liquid surface with increasing undercooling.

The surface morphology of the dendritic structure in Figure 7 shows no traces of edges or faces. Only rounded structures are observable. Whether this is due to surface roughening on the atomic scale or remelting of corners and edges due to a lowering in melting point by curvature effects needs further careful examination. The transition is not abrupt but rather continuous. A mixture of facets and dendrites was observed for intermediate undercoolings [6].

At the highest undercoolings, e.g. 330 K, no more dendrites or faces were visible on the surface of the sample. The surface was homogeneous and further refined, as shown in Figure 8. We interpret this as a dendritic break up and remelting of the truncated dendrite branches resulting in grain refinement of the sample as reported by Schwarz et al. [11].

17.4.2
Growth Velocity Results

We measured the velocity of the solidification front propagating into the undercooled liquid from $\Delta T = 135$ to $\Delta T = 305$ K. The data was recorded with a pair of photodiodes and a transient recorder with a rate of 10 MHz. A lack of a well-determined solidification front at undercoolings below 135 K did not allow growth rate measurements at low undercoolings. If we assume that above $\Delta T = 135$ K the solid-liquid surface is atomically rough due to undercooling we can compare our results with the LKT-BCT Theory [12, 13] for dendritic growth in undercooled pure metallic melts.

$$\Delta T = \Delta T_t + \Delta T_c + \Delta T_k$$

$$\Delta T_k = \frac{v}{\mu}\,; \quad \mu = f\,\frac{\Delta H_m v_s}{R T_m^2}\,,$$

where v is the velocity of the solidification front, ΔT the total undercooling of the sample, ΔT_t the thermal undercooling, ΔT_c the curvature undercooling due to the Gibbs-Thomson effect and ΔT_k the kinetic undercooling. The tetragonal covalent bonding of silicon results in a high kinetic undercooling. In contrast to metals an atomic site factor $f = 0.02$ [14, 15] has been proposed for the growing diamond struc-

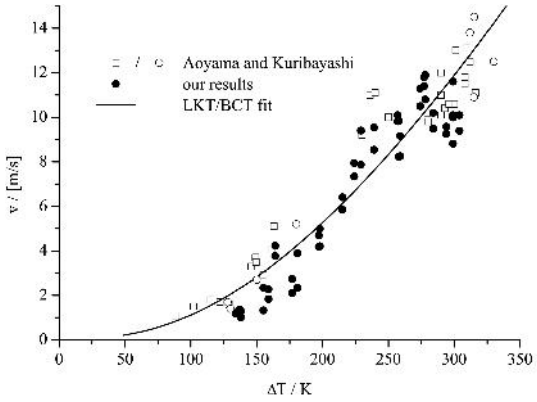

Fig. 11 Growth velocity of the solidification front in undercooled liquid silicon: our results and the previously measured results of Aoyama and Kuribayashi. The solid line indicates the LKT/BCT fit to the data using the thermophysical parameters given in Table 1.

ture of silicon. ΔH_m is the heat of fusion, v_s the speed of sound in the liquid, T_m the melting temperature and R the gas constant.

The growth rate results together with the theoretically predicted data using the thermodynamical values given in Table 1 are shown in Figure 11. At low undercoolings below 135 K we observe only faceted growth which is rather slow and where no solidification front could be observed. From $\Delta T = 135$ K on the growth rate became much faster and we were able to track the velocity of the solidification front with the photo diode setup. In the regime $\Delta T = 135$ to 250 K the measured growth velocity qualitatively follows the theoretically predicted trend. Our measurements compare well with earlier measurements [6] in this regime carried out by Aoyama and Kuribayashi.

At high undercoolings ($\Delta T > 285$ K) our growth velocity results deviate from the theoretically predicted trend and seem to come into saturation. This effect has been observed before for undercooled metallic melts [16]. Whether this is a general trend for crystal growth of undercooled materials or an impurity effect needs further careful examination. Since the solubility of metallic impurities in the solid silicon is negligibly low already tiny amounts of impurities might have a drastic effect on the growth kinetics due to the resulting high partition coefficient.

Tab. 1 Thermophysical parameters used for the LKT/BCT fit to the experimental data

a	$= 1.3 \cdot 10^{-5}$	thermal diffusivity	m^2/s
c_p	$= 2{,}334 \cdot 10^9$	heat capacity of the liquid	J/m^3K
s	= 0.438	solid liquid interface energy	J/m^2
T_m	= 1687	melting temperature	K
ΔH_m	$= 4{,}612 \cdot 10^{13}$	volumetric latent heat of fusion	J/m^3
v_s	= 3400	speed of sound in the liquid	m/s
f_{site}	= 0.02	atomic site factor	

17.5 Conclusion

We applied electromagnetic levitation technique to undercool and solidify liquid silicon. Maximum undercoolings of 330 K have been achieved. From surface morphologies of the solidified samples and high speed camera observations during solidification a transition from faceted to dendritic growth with increasing undercooling could be observed. The onset of dendritic growth in undercooled silicon has been determined to be 135 K.

We believe that surface roughening of the solid-liquid interface at higher undercoolings allows the formation of dendrites growing into the undercooled liquid silicon. A theoretical model and a prediction of the transition temperature still needs to be developed.

In the regime of dendritic growth we measured the velocity of the solidification front using a pair of high speed photo sensors. Our results compare well with other results giver earlier.

The BCT theory for pure metallic melts gave a reasonable fit to our data in the regime $\Delta T = 135$ K to $\Delta T = 270$ K. At higher undercoolings the measured data deviated from the predicted trend. The deviation of the growth velocity results at high undercoolings as well as growth velocity data for undercoolings greater than 305 K will be subject to further investigation. The scatter in the data in our measurements as well as in earlier data from Aoyama is still high. Further experiments carried out with higher precision using a capacitive sensor and a high speed camera will be carried out.

Acknowledgements

This work is supported by DFG under contract No. HE1601/16–1 and the Sino-German Science Center Bejing.

We thank Peter Galenko for helpful discussions.

References

[1] G. Devaud, D, Turnbull, Appl. Phys. Lett., 1985, 46, 844

[2] Y. Shao, F. Spaepen, J. Appl. Phys., 1996, 79, 2981

[3] A.J. Rulison, W.K. Rhim, Metall. Mater. Trans., 1994, 26B, 503

[4] D. Li, D.H. Herlach, Phys. Rev. Lett, 1996, 77, 1801

[5] R.P. Liu, T. Volkmann, D.H. Herlach, Acta Mater., 2001, 49, 439–444

[6] T. Aoyama, Y. Takamura, K. Kuribayashi, Met. And Mat. Trans. A, 1999, 30A, 1333–1339

[7] W.K. Rhim, S.K. Chung, A.J. Rulison, R.E. Spjut, International Journal of Thermophysics, 1997, 18, No 2, 459–469

[8] H. Watanabe, M. Susa, H. Fukuyama, K. Nagata, High Temperatures – High Pressures, 1999, 31, 587–593

[9] K.A. Jackson, D.R. Uhlmann, J.D. Hunt, Journal of Crystal Growth, 1967, 1, 1–36

[10] K.A. Jackson, Journal of Crystal Growth, 1968, 3, 507–517

[11] M. Schwarz, A. Karma, K. Eckler, D.M. Herlach, Phys. Rev. Lett., 1994, 73, 1380–1383

[12] W.J. Boettinger, S.R. Coriell, R. Trivedi, Rapid Solidification Processing: Principles and Technologies IV, ed. R. Mehrabian and P.A. Parrish, Claitor's Baton Rouge, 1988, 13–25,

[13] J. Lipton, W. Kurz, R. Trivedi, Acta Metall., 1987, 35, 957–964

[14] X. Xu, C.P. Grigoropoulos, R.E. Russo, Appl. Phys. Lett, 1994, 65, 1745

[15] F. Spaepen, D. Turnbull, Laser Annealing of Semiconductors, ed. J.M. Poate and J.W. Mayer, Academic, New York, 1982, p. 15

[16] K. Eckler, D.M. Herlach, Mat. Sci. Eng., 1994, A178, 159–162

18
Two-Phase Equilibrium in Binary Alloy Nano Particles

P. Bunzel, G. Wilde, H. Rösner, J. Weissmüller

18.1
Introduction

In macroscopic alloy systems the contribution of the excess free energy of interfaces between different phases to the free energy of an alloy may generally be neglected in the determination of phase equilibriums. By contrast, in sufficiently small alloy particles the interfacial energy may become comparable to the energy of the bulk phases. Studies on small particles of a low melting point metal embedded in a matrix with a considerably higher melting point provide useful experimental model systems for investigations of this issue. The major part of the research published so far is concerned with the melting of elemental particles (see, for instance, Refs. [1][2][3][4][5]). However, in the recent past a small, but increasing number of studies has been concerned with the phase equilibrium in binary alloy nanoparticles. Particles, typically of an alloy with a simple eutectic phase diagram and embedded in an inert matrix, can be prepared by vacuum deposition [6], ion implantation [7], and by melt spinning [8]. A qualitative difference to elemental particles resides in presence of the internal interface between the phases coexisting within the alloy particle. The corresponding interfacial area varies with the fractions of the phases, giving rise to an excess energy which is on top of that of the outer surface of the particle.

Here, we report on the theory part of a study of small eutectic alloy particle melting. In the experimental part of the study, which will be published separately, we have prepared small Bi-Cd alloy particles embedded in an Al matrix using the melt-spinning technique. The Bi-Cd alloy system is of the simple eutectic type with no mutual solubility in the solid state. Furthermore, Bi and Cd are insoluble in solid Al, and the solubility of Al is negligible in solid and liquid Bi as well as Cd.

Figure 1 shows typical transmission electron microscopy (TEM) images of a Bi-Cd alloy particle. In the bright-field image (Fig. 1 a), elemental Bi can be identified by its Z-contrast, and the fcc lattice of Cd gives rise to Moirée fringes due to interference with the Al lattice. The identification of the phases is confirmed by energy-filtered TEM, as evidenced by the example of the Cd map in Fig. 1 b). Thus, the image shows that two phases coexist within the nanoparticle. Geometrically similar internal microstructures were found even for particles with diameters well below 10 nm.

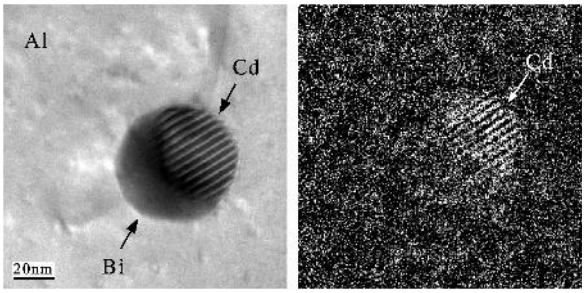

Fig. 1 Left: TEM bright-field picture of an Bi-Cd alloy particle embedded in an Al matrix; right: EFTEM picture using the L-edge of Cd in which the Cd part of the particle can be identified. Sample overall Bi-Cd ratio 69 : 31.

The design of our model was motivated partly by the strive to model – in an intentionally qualitative way – the general features of this type of small particle alloy system. The emphasis is on examining in an exemplary manner the consequences of the energy contributions of the interfaces separating the phases within an alloy particle. As we shall show, the essential difference to a macroscopic system resides in the fact that the total free energy at two-phase coexistence varies nonlinearly as a function of the phase fraction, similar to the free energy of mechanically coherent phases. As a consequence, the common tangent construction which is used to derive phase diagrams for macroscopic alloys based on their free energy functions fails at small size.

18.2 Idealized Model System

18.2.1 The Model Alloy

We consider a simple binary eutectic alloy without mutual solubility in the solid state and with an ideal solution as the liquid phase. We use the simplest equations of state for the bulk phases and the interfaces. For simplicity we assume identical melting temperatures, T_f , for the pure components; the free energy functions are then invariant with respect to replacement of solute and solvent, and the phase diagram is symmetric about the solute fraction $x = 1/2$.The phase diagram of that alloy in the macroscopic case is shown in Fig. 2a. Further we use the identical molar volume, v, for all components in all phases, so that the volume V of the particle will not change during phase transitions, and consequently Clausius-Clapeyron type pressure shifts of phase equilibria may be ignored. Another consequence is that the volume fraction of a phase $i = \alpha, \beta$ is equal to the corresponding fraction of amount of matter of that phase, denoted as the phase fraction, $p = V^i/V = N^i/N$, where N denotes the total amount of matter of both components.

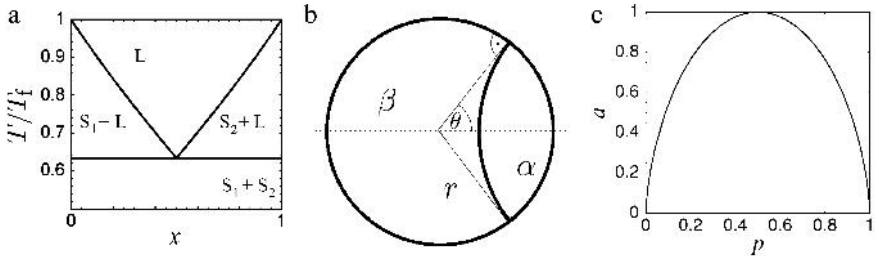

Fig. 2 **(a)** Bulk Phase diagram of the idealized model showing the regions of existence of the liquid, L and of the two solid phases, S_1 and S_2. **(b)** Cross-section of a particle of radius r,showing the definition of the apex angle θ used in computing the area a of the interface between the two phases α and β. **(c)** Plot of a, versus the phase fraction, p.

18.2.2
Particle Shape and Properties of the Phase Boundary

In order to achieve a simple geometry, we fix the external particle shape to be spherical as, for instance, for a fluid particle embedded in a glassy matrix. Furthermore, all interfacial free energies are taken to have a constant and identical value, γ. This has three important consequences: *i*), changes in the interfacial excess free energy arise exclusively from the variation of the internal surface area, A, of the phase boundary; *ii*), there is no solute segregation; *iii*), the dihedral angle at the junction of the internal interface with the outer surface of the particle is 90°, and the internal interface at equilibrium assumes the shape of a spherical cap. Figure 2 b) illustrates the geometry; it is seen to agree qualitatively with that of the Bi-Cd particle in the experimental TEM image, Fig. 1 a). Other geometries are possible when γ is allowed to differ between the different types of interfaces (compare Ref. [7]); these more general cases will be discussed in a separate publication.

18.2.3
Surface Area of the Phase Boundary

To determine the excess free energy of the phase boundary surface, one has to calculate its area as a function of the phase fraction. We found it useful to work with the dimensionless parameter $a = 4\ A/(\pi D^2)$, where D denotes the particle size. By analysis of the cross-section shown in Fig. 2 b we derived two relations, one that connects the phase fraction with the apex angle θ (see Fig. 2 b)),

$$p = \frac{5 + 3\cos\theta + 3\sin\theta)\sin^3(\theta/2)}{2(\cos(\theta/2) + \sin(\theta/2))} \tag{1}$$

and one that connects a to θ:

$$a = 2(1 - \sin\theta)\tan^2\theta. \tag{2}$$

Fig. 2c shows the function $a(p)$ that was numerically evaluated from Eq. (1) and (2), because we found no closed analytical form. We found that the numerically exact $a(p)$ can be approximated by the empirical function:

$$a = 2^{1/3} q^{2/3} + (1 - 2^{1/3})\, q, \quad \text{with} \quad q = 4\, p\, (1 - p)\,, \tag{3}$$

to within an accuracy of better than $\Delta a/a = 10^{-3}$ at all p, and we used the empirical function to simplify the free energy computations.

18.2.4 Molar Free Energies

Adding a constant to the chemical potentials of any one of the components in all phases does not change the equilibrium states. Therefore, we can define the free energies of the elemental solids in the particle at any given temperature T as zero, $g^{S_1} = g^{S_2} \equiv 0$. The molar free energies for intermediate compositions of the system were computed in the following way:

The molar free energy g^{SS} for the two-phase state is simply

$$g^{SS} = \frac{\gamma\, \pi\, D^2}{4\, N}\, a\,(p)\,. \tag{4}$$

As a consequence of the mutual insolubility of the solids, the phase fraction is $p = 1 - x$, where x denotes the fraction of the solute, component 2. For the numerical evaluation it is useful to apply the following substitutions: $N = \pi\, D^3/(6\, \Omega\, N_A)$, where N_A denotes Avogadro's number and Ω the atomic volume, further, formally γ can always be related to Δh_f through $\gamma = c\, \Delta h_f/(\Omega^{2/3}\, N_A)$ with c a dimensionless constant [9]. We shall specify all molar energies in units of the heat of fusion, Δh_f. In this way, we obtain

$$g^{SS}\,(x) = \frac{3\, c\, \Omega^{1/3}}{2D}\, a\,(p)\,. \tag{5}$$

As the liquid is modeled by an ideal solution, the molar free energy g^L of the single-phase liquid state is:

$$g^L = \Delta h_f - T(\Delta s_f + \Delta s_{mix})\,. \tag{6}$$

Here, $\Delta s_{mix} = -R\, ((1 - x)\, \ln\, (1 - x) + x\, \ln\, x)$ denotes the entropy of mixing of a random solution, whit R the gas constant, and Δs_f denotes the molar entropy of fusion. In reduced units for the molar free energy, and using the parameter $\sigma = \Delta s_f/R$, we obtain

$$g^L\,(x, T) = 1 + \frac{T}{T_f}\left(-1 + \frac{1}{\sigma}\,((1 - x)\ln\,(1 - x) + x \ln x)\right). \tag{7}$$

The molar free energy when the liquid of composition x^L coexists with the solid is denoted by $\tilde{g}^{SL}(x, x^L, T)$. Because of the symmetry of the free-energy functions it is sufficient to consider only one of the two solid-liquid equilbria; without lack of generality we consider solid solvent (S_1) plus liquid. With Eq. (5) and (7), and the phase fraction $p = 1 - x/x^L$ of the solid (the solvent, component 1) we obtain

$$\tilde{g}^{SL}(x, x^L, T) = (1 - p)\, g^L(x^L, T) + \frac{3\, c\, \Omega^{1/3}}{2\, D}\, a(p) \tag{8}$$

In order to find the two-phase solid-liquid state of lowest free energy, for given values of T and of the overall composition x, one has to minimize $\tilde{g}^{SL}(x, x^L, T)$ with respect to x^L.

18.3 Size-dependent Alloy Phase Diagrams

To find the equilibrium states of the particle for given x and T, we identify the state with the lowest molar free energy among the three states SS, L, and SL. In macroscopic systems, where the free energy of two-phase states is a linear function of the phase fraction, the common tangent construction may be used to identify the stable two-phase regions of the alloy phase diagram. As we have seen above, the free energy of finite-size systems varies nonlinearly with p, so that the common tangent construction is inapplicable. Here, we used a numerical evaluation of the free energy functions defined above for constructing the equilibrium phase diagram.

As can be seen from the previous section, evaluation of the free energies for our model requires that values are specified for three material parameters, σ, c, and Ω. All three parameters take on roughly similar values for many metals. By using these values, we achieve results that can be compared, in a semi-quantitative way, to experimental results. For σ we use a value of $\sigma = 1.2$; for the atomic volume a value of $\Omega = 0.015\ \mathrm{nm}^3$; typical empirical values of c in metals are $c \approx 0.5$ for solid-liquid interfaces [9] at T_f and $c \approx 1.3$ for grain boundaries [10]. Since we ignore changes in γ, we use an average value for all interfaces, $c = 0.9$.

The molar free energy curves were computed numerically using Eqs. (5)–(8). For solidliquid coexistence one obtains a set of convex free energy curves $\tilde{g}^{SL}(x, x^L, T)$ parametrized by the solute fraction x^L in the liquid, as illustrated by the example in Fig. 3. The molar free energy curve of the most stable solid-liquid state, $g^{SL}(x, T)$, is seen to be given by the lower envelope of the set of functions $\tilde{g}^{SL}(x, x^L, T)$. It is also seen, that the graph of $g^{SL}(x, T)$ ends where it meets the free energy curve of the liquid. Furthermore, it is found that the $\tilde{g}^{SL}$ intersect, so that the composition of the liquid at equilibrium with the solid varies as a function of x. The resulting x^L at equilibrium were used to draw lines of identical composition of the liquid phase that will be presented as a part of Fig. 5 below. It is noted that the situation has some analogs to the equilibrium between coherent phases, where the excess energy is due to stress and strain as opposed to capillarity, and where the coherency strain energy is de-

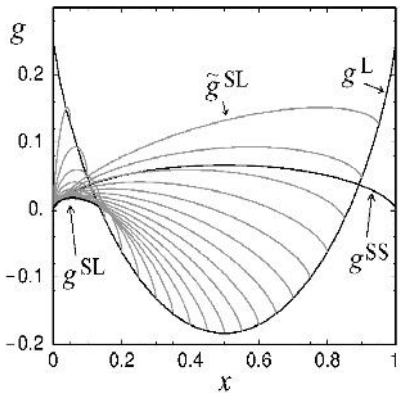

Fig. 3 Molar free energies (in units of the heat of fusion) for the two-phase state solid-solid, g^{SS}, and the single-phase state liquid, g^{L} , as function of the overall composition *x*. Grey lines: array of solid-liquid energy curves $\tilde{g}^{SL}$ for some discrete values of *x*L. Lover envelope, g^{SL}, of the $\tilde{g}^{SL}$ array in that region of *x* , where the two-phases state SL is the one with the lowest energy. The curves are calculated for $T/T_f = 0.75$ and $D = 5$ nm. For clarity the construction of g^{SL} is only shown for the coexistence if the liquid with the solid solvent; the construction for the liquid plus solid solute is analogous.

scribed by convex free energy functions similar to g^{SL} in Fig. 3 [11][12][13]. Also, it should be remarked that for increasing *D*, in the macroscopic limit the function g^{SL} becomes identical with the common tangent.

The alloy phase diagrams are constructed by analysis of the points of intersection of the lowest free energy curves at each temperature. An intersection of g^{SS} and g^{SL} defines a point on the solidus line between the two-phase solid-solid and the two-phase solid-liquid region of the phase diagram; an intersection of g^{SL} and g^{L} (more exact the point, where g^{SL} end at g^{L}) defines a point on the liquidus line; and intersections of g^{SS} and g^{L} define a line in the phase diagram, where discontinuous melting occurs. Fig. 4 illustrates this procedure for the example of the particle size $D = 5$ nm.

An overview of the evolution of phase diagrams for finite-size systems with decreasing particle size *D* is shown in Fig. 5. It is seen that, as the particles size is reduced, the phase diagram undergoes several qualitative changes which are not in accordance with the rules which apply universally to the construction of the phase diagram for macroscopic systems. Firstly, it is observed that the invariance of the solidus temperature is lost in favor of a significant composition-dependence. Secondly, as illustrated by the lines of identical composition x^{L} of the liquid phase at equilibrium (dot, dash, and dot-dash lines in Fig. 5), the compositions of the constituent phases in two-phase equilibria are no longer invariant at constant *T*. Thirdly, the equi-composition lines lose their continuity at the intersection with the liquidus line. This implies that there is a discrete jump in liquid fraction of the alloy particle at the liquidus line, consistent with the observation in Ref. [14] that the ends of the tie lines detach from the phase boundary lines at small particle sizes. The jump in the liquid fraction leads to a discontinuous change in the enthalpy upon heating through the liquidus temperature. This should result in an peak in a DSC measurement, on top of the peak at the solidus. We have simulated DSC signals for the model, convoluting the temperaturederivative of the enthalpy with a Gaussian as a rough approximation of the instrument function. Fig. 6 shows the results for a macroscopic alloy and for an alloy particle with $D = 50$ nm, both at an overall alloy composition $x = 0.2$, confirming the existence of a significant endothermic peak. at the liquidus of the alloy particle.

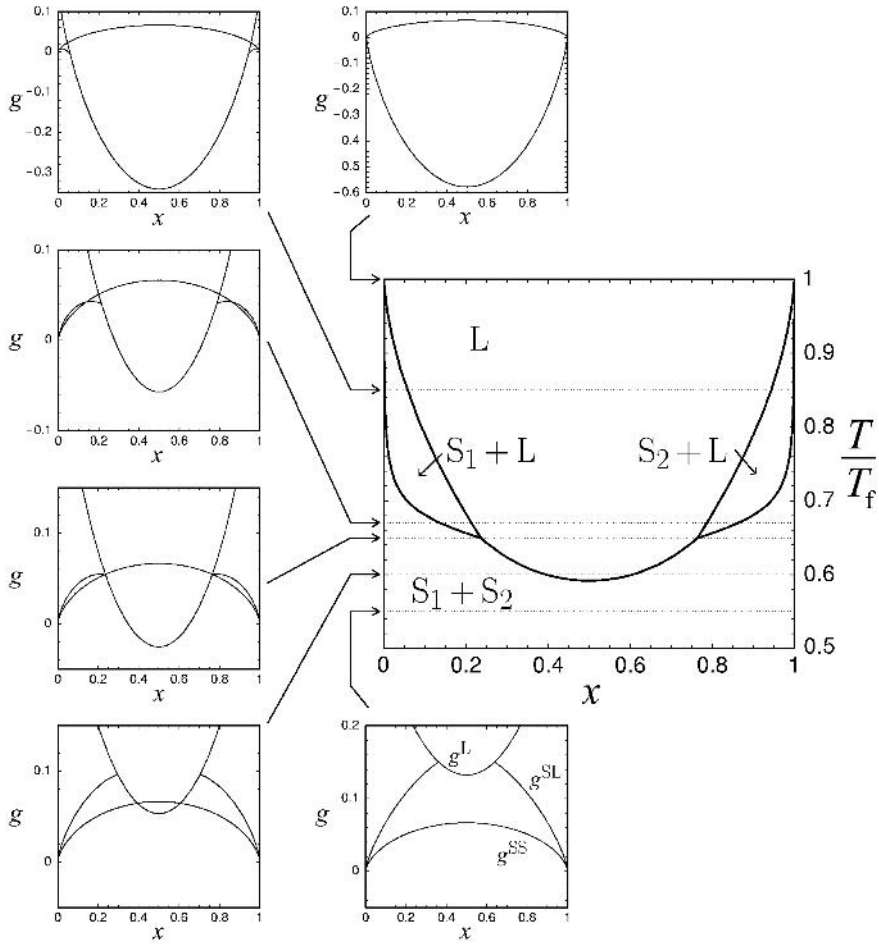

Fig. 4 Construction of a size-dependent phase diagram. Small pictures: computed energy curves of the phase states L, SS, and SL as functions of the overall composition, x , at different temperatures and a particle size of $D = 5$ nm. Large graph: resulting phase diagram; black lines: phase coexistence lines; dotted lines indicate the temperatures of the corresponding energy diagrams.

By inspection of Fig. 5 it is seen that, on top of the changes discussed above, the most fundamental consequence of reducing the systems size is a topological change in the phase diagram, the degeneration of the eutectic point of the macroscopic system into a line representing an interval of composition Δx_d (defined in Fig. 5 c) for which the particle undergoes a discontinuous transition between a two-phase solid-solid state and the singlephase liquid state. In macroscopic binary alloys, three phases coexist at equilibrium at the eutectic point; by contrast, discontinuous melting in our model is a transition between a two- phase equilibrium (solid-solid) and

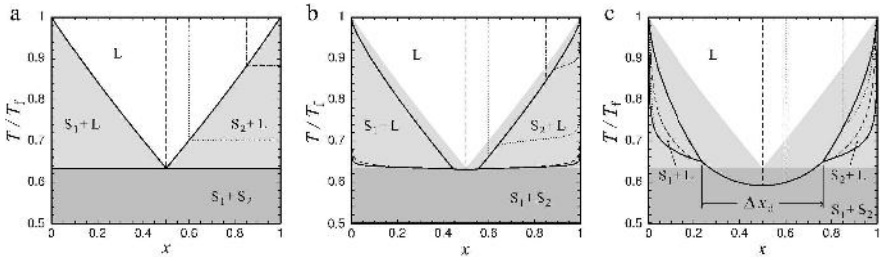

Fig. 5 Computed alloy phase diagrams for different particle sizes: **(a)** $D \to \infty$ (macroscopic limit), **(b)** $D = 50$ nm, and **(c)** $D = 5$ nm. Black lines: phase coexistence lines; dot, dash, and dash-dot lines: lines or equal solute fraction x^L in the liquid phase (in the single-phase liquid and in the two-phase solid-liquid region as well) for three arbitrarily chosen values of x^L. Shaded fields represent the phase regions of the macroscopic alloy.

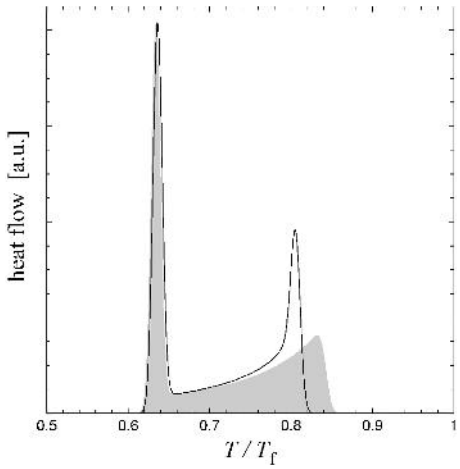

Fig. 6 Computed DSC curve for the idealized model. Black line: heat flow for an nano alloy particle with D=50 nm at an overall composition of $x = 0.2$, shaded field: heat flow for the corresponding macroscopic alloy.

the single-phase liquid state, without three phase equilibrium. It is because of the loss of three-phase equilibrium in the finite-size system that the transition from eutectic *point* to discontinuous melting *line* can be reconciled with the phase rule.

18.4 Conclusion

We have discussed the construction of size-dependent binary alloy phase diagrams for finitesize particles, using free energy functions that take into account the capillary energy of internal interfaces separating the phases within the particle. It was found that several of the rules that apply generally to the construction of phase dia-

grams for macroscopic systems are not longer applicable for small alloy particles. Most notably, the eutectic point is replaced by an interval of composition in which the alloy melts discontinuously at small system size. In the example, which uses material parameters that are characteristic for metals, the width of this interval reaches values in excess of a few atomic percent at particle sizes of roughly 100 nm and below. Simulated DSC curves exhibit characteristic, qualitative changes at small particle size, which makes the predictions open to experimental investigation.

Acknowledgement

The support by Deutsche Forschungsgemeinschaft (Schwerpunkt Phasenumwandlungen in mehrkomponentigen Schmelzen) is gratefully acknowledged.

References

[1] R. W. Cahn, Nature, 1986, 323, 668–669.
[2] R. Kofman, P. Cheyssac, R. Garrigos, Phase Transitions, 1990, 24–26, 283.
[3] K. Chattopdhyay, R. Goswami, Prog. Mat. Sci., 1997, 42, 287–300.
[4] U. Dahmen, S. Q. Xiao, S. Paciornik, E. Johnson, A. Johansen, Phys. Ref. Lett., 1997, 78, 471–474.
[5] H. Rösner, P. Scheer, J. Weissmüller, G. Wilde, Phil. Mag. Lett., 2003, 83, 511–523.
[6] G. L. Allen, W. A. Jesser, J. Cryst. Growth, 1984, 70, 546–551.
[7] S. Hagège, U. Dahmen, Phil. Mag. Lett., 1996, 74, 259–266.
[8] P. Bhattacharya, V. Bhattacharya, K. Chattopadhyay, J. Mater. Res., 2002, 17, 2875- 2883.
[9] Turnbull, D., J. Appl. Phys., 1950, 21, 1002–1028.
[10] Weissmüller, J., Nanostruct. Mater., 1993, 3, 261–272.
[11] R. O. Williams, Calphad, 1984, 8, 1–14.
[12] J. W. Cahn, F. Larché, Acta Metall., 1984, 32, 1915.
[13] A. L. Roytburd, Sov. Phys. Sol. State, 1984, 26, 1229.
[14] W. A. Jesser, G. J. Shiflet, G. L. Allen, J. L. Crawford, Mater. Res. Innovat., 1999, 2, 211–216.

19
Three-dimensional Reconstruction of Experimentally Grown Xenon Dendrites

H.M. Singer and J.H. Bilgram

19.1
Introduction

The solidification of a stable phase at the expense of metastable phase is a multiscale problem. Starting from atomistic considerations of atom attachments over dendritic growth dynamics of a single crystal to grain growth and finally to the influence of material properties of macroscopic cast metals the phenomenon of solidification spans 9 orders of magnitude in length scale. As this huge span cannot yet be described in one general theory there are different models for different scales. Dendritic growth, in the scales of micrometers, has attracted a lot of attention i) in materials science as dendrites crucially influence mechanical and corrosion behavior of the final casting product and ii) in the field of pattern formation as dendrites are considered to be prototypes for the evolution of complex spatio-temporal structures far from equilibrium [1].

Thermal dendritic growth is usually described by the classical sharp interface or Stefan-problem [2]:

$$\frac{\partial u}{\partial t} = D\nabla^2 u \tag{1}$$

$$v_n = D(\nabla u|_{\text{solid}} - \nabla u|_{\text{liquid}}) \cdot \hat{n} \tag{2}$$

$$u|_{\text{interface}} = \Delta - \beta v_n - d\kappa \tag{3}$$

The equations are written in dimensionless units, where $u = \Delta T/(c_p/L)$ denotes the temperature field and Δ the dimensionless supercooling, where ΔT, c_p, L are supercooling specific heat of the liquid and latent heat respectively. These equations are formulated for the "free growth" condition, i.e. the growth vessel is assumed to be infinitely large, so that no boundary effects occur. The temperature of the melt is assumed to be homogenous $T_\infty < T_{melt}$ at the beginning of the growth experiment. Thermal diffusivity is taken to be the same in solid and liquid ($D = D_s = D_l$). The continuity equation (eq. 2) ensures energy conservation at the phase boundary. Eq. 3

describes the non-isothermal case where the temperature at the interface is also dependent on the curvature (Gibbs-Thomson effect) and the velocity of advancement (kinetic effect). d and β are the anisotropic capillary length and anisotropic kinetic coefficient respectively. In the case of an fcc-model a fourfold symmetric anisotropy is assumed. For low supercoolings the kinetic term can be neglected.

Models on dendritic solidification usually can only make predictions of the behavior very near the tip. Further away, where side branches strongly interact with each other, quantitative predictions are almost impossible to make as the behavior is highly nonlinear. For a description of the whole dendrite integral variables such as volume or surface are needed. In order to verify the significance of existing models, it is necessary to compare analytical predictions and simulations with experimentally measured data.

19.2 Experimental Setup

In our *in situ* experiments we are able to observe a growing crystal in three dimensions during the free growth. The rare gas xenon is used as a model substance for metals because i) it forms a "simple liquid", ii) has a low melting entropy to form rough solid liquid interfaces and iii) crystallizes in fcc-structure. Xenon is transparent and therefore allows *in situ* observation, which is not possible for metals up to now. The undercooling of the melt is in the range of $50\,m\mathrm{K} \leq \Delta T \leq 220\,m\mathrm{K}$ (corresponding to about $10^{-3} \leq \Delta T \leq 10^{-2}$ in dimensionless units). The triple point of xenon is $T_t = 161.3897$ K. The experimental setup consists of a high precision cryostat to stabilize the temperature better than $\pm 10^{-4}$ K as long as necessary. Temperature is measured with temperature sensitive resistors (Pt-100). A stirrer producing a laminar flow in the thermostating liquid isopentane is ensuring a homogenous temperature in the heat bath. The actual growth vessel, immersed in the heat bath, has a volume of 100 cm^3 of liquid supercooled xenon in order to ensure "free" growth of the crystal. In order to initiate the growth we use the capillary injection technique proposed by Glicksman et al. [3]: After a local nucleation at the very top of the capillary the crystal is growing downwards through the capillary and after reaching the end, it enters the state of free three-dimensional thermal growth. The experimental apparatus allows us to turn the capillary along its axis in order to orient the crystal to present the maximal projection area. It is also possible to shift the capillary up and down (vertical translation) in order to follow the tip of the crystal during its growth. A sketch of the growth vessel is given in Figure 1.

A self-built periscopic imaging system allows us to observe the crystal during its growth. Its optical resolution has been tested to be 1.22 μm. A spatially homogenous light source illuminates the crystal from the rear. Xenon is optically transparent in solid and liquid state, therefore the crystal is only visible due to the difference of the indices of refraction. A more detailed description of the experimental setup can be found in [4]. The temporal evolution of the crystal is recorded by a digital CCD-camera (1280 × 1024 pixels).

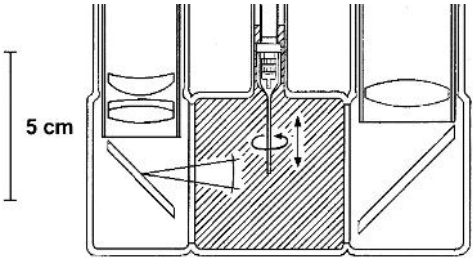

Fig. 1 Close up of the growth vessel in the cryostat. The vessel is filled with supercooled liquid xenon. At the left and right side parts of the optical periscope are visible. The capillary reaches in the growth vessel and can be turned around the capillary's axis and translated upwards and downwards.

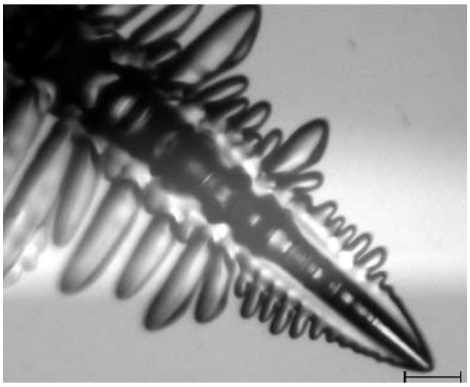

Fig. 2 A typical xenon dendrite oriented so that the maximal projection area can be observed: two fins lie in the image plane and two fins are perpendicular to it, thus only the fin thickness can be seen. The scale bar corresponds to 250 μm.

A typical dendrite grown in our experiments is shown in Figure 2. The dendrite is oriented in such a way that the maximum projection area can be observed: two fins lie in the image plane and two fins grow perpendicular to the focus plane and can only be seen in their thickness.

19.3 Analytical Models vs. Simulations

The first analytical calculations of three-dimensional dendritic growth are due to Ivantsov [5]. He proved that in the isotropic case a rotational paraboloid is a steady state solution of eqs. 1–3. Analytical model calculations of the anisotropic equations [6, 7] of three-dimensional dendritic growth assume at least near the tip that the crystal anisotropy induces only a very small deviation from the isotropic Ivantsov paraboloid. Cross sections of the dendrite perpendicular to the growth direction are therefore predicted to show a convex behavior in diagonal direction ($\pi/4 + n \cdot \pi/2$, $n = 0..3$) as depicted in Figure 3a.

In a thorough asymptotic calculation Brener and Temkin [6] could prove that the outer shape of the fins in their maximal projection area can be described as a power law $z = ax^{5/3}$, where the tip is placed at the origin and z is the height measured from the tip. The thickness of the fins can be described as $z = bx^{5/2}$.

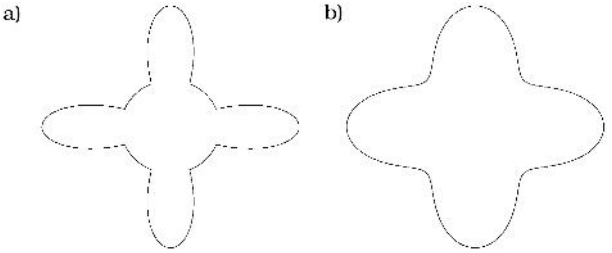

Fig. 3 a) Cross section perpendicular to the axis of growth. The diagonal points $\pi/4 + n \cdot \pi/2$, n = 0..3 show convex behavior, coming from the assumption that near the tip the crystal anisotropy causes only a weak perturbation of the isotropic Ivantsov paraboloid. b) Cross section as deduced from 3D phase field simulations. The diagonal points $\pi/4 + n \cdot \pi/2$, n = 0..3 show a concave behavior: the fins entirely cover the stem, thus they are an inherent part of the dendrite and cannot be treated as a mere perturbation.

On the other hand also numerical simulations have been performed. Solving equations 1–3 directly is very tedious, as the moving boundary must be tracked in every time step. A more elegant approach is the phase field model. Instead of assuming a sharp transition between solid and liquid phase at the interface a new variable ϕ is introduced which is defined over the whole domain. ϕ indicates the state at every point and can vary between the values for solid (0) and liquid (1). The transition is continuous but usually very steep over a choosable length, the interface thickness. This method provides a set of two coupled partial differential equation. The advantage in this approach is that the interface does not have to be tracked explicitly.

Three-dimensional phase field simulations performed by Karma et al. [8] have shown that cross sections perpendicular to the growth direction behave in a different way as predicted by the analytical studies. In the anisotropic case it was found that the fins are an inherent property of the dendrite. The cross sections are concave (Figure 3 b) in the angles $\pi/4 + n \cdot \pi/2$, n = 0..3. Thus the sign of the curvature is opposite to the one predicted analytically. This difference is important as it might indicate that the assumption of a weak perturbation of the paraboloid base shape of the isotropic Ivantsov solution might not be entirely valid.

19.4 Reconstruction

In order to contribute results from the experimental side to the ongoing discussion on the shape of dendritic cross sections we have decided to reconstruct the three-dimensional shape of our dendrites based on different projections.

Many different algorithms for the reconstruction of 3D shapes exist. All of them rely however on the assumption of reflective material properties and fixed points (e. g. [9–11]). The major problem in our case is however that xenon is transparent in

solid and liquid state. The light intensity distribution changes therefore drastically upon turning, as parts of the crystal being in the light beam show angle dependent lens effects.

The commonly used method of confocal microscopy for 3D shapes [12,13] is not applicable either due to geometrical restrictions of the "free growth" condition. A very similar serial sectioning technique (destructive) is however used for reconstructing the dendritic microstructure of opaque materials [14].

We have developed new algorithms that allow a non-destructive reconstruction of *in situ* growing transparent dendrites. The reconstruction consists of three distinct phases: i) qualitative reconstruction of cross sections based on image processing techniques applied to our gray scale images. ii) First quantitative reconstruction of the tip region by fitting to measured parameters of the dendrite. iii) Second quantitative reconstruction of the whole dendrite considering also the growth of side branches.

The qualitative reconstruction is based on the following assumptions [15]:

- There is a visible fourfold symmetry of the crystal for the fins, but obviously not for the side branches (Figure 2).
- The fins are planar symmetric (same elongations from the symmetry planes). This is easily visible in Figure 2 for the fins perpendicular to the focus plane.
- The crystal is oriented in the maximal projection area. One pair of fins is entirely visible, the other one is visible only as fin thickness. We assume that the light intensity found in the crystal is directly related to the angle of the tangential planes relative to the axis of illumination.
- The shape of the dendrite is continuous.
- The height relative to the focal plane at the contour is 0.

With these assumptions it is possible to construct a qualitative height field of a gray scale image. An introduction into the basic idea of the image processing algorithm is given in [15] and more detailed in [16].

By using two projections turned by 90° and superimposing them we have found that cross sections perpendicular to the axis of growth are concave (like in Figure 3 b). Therefore we conclude that at least for xenon dendrites the fins are an integral part of the dendrite. The stem is completely hidden by the fins except from 4 distinct points ($\pi/4 + n \cdot \pi/2$, n = 0..3).

Once the basic shape of our experimental dendrites was found a first quantitative reconstruction was attempted by scaling the heights of the base shape by measured parameters of the dendrite. We have found that for a given distance from the dendrite tip z a fitting function

$$\overrightarrow{f(\theta)}|_{z=\text{const}} = (c + d\cos(4\theta)) \cdot \begin{pmatrix} \cos\theta \\ \sin\theta \end{pmatrix} \tag{4}$$

can fit our data smoothly. The parameters c and d are chosen such that for maximum values (c + d) at angles $n \cdot \pi$, n = 0..3 the fin elongations given by the contour

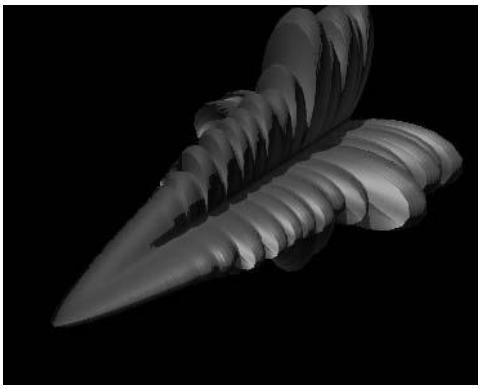

Fig. 4 Three-dimensional reconstruction of an experimentally grown xenon dendrite. The tip region, where side branches are still very small is very accurate, however for larger side branches the reconstruction becomes inaccurate, as the data is not bijective any more.

lines of the two projections and for minimum values (c – d) at $\pi/4 + n \cdot \pi/2$, $n = 0..3$ the elongations given by Brener's asymptotic calculations for the thickness of the fins $x(z) = (z/b)^{2/5}$ are recovered. We assume here that the thickness of the stem increases with the same power law as the thickness of the fins. The parameters for the thickness of the fins can be determined from the images. An example of a first quantitative reconstruction is given in Figure 4.

This reconstruction is very precise in the region of the tip where no side branches grow. With the increase of the size of side branches however, the reconstruction becomes more and more inaccurate. The main reason for this is the experimental observation that the side branches do not grow exactly perpendicular to the axis of growth. The first quantitative reconstruction is based on constructing slices of the dendrite perpendicular to the growth direction and then combining the individual slices to a 3D model. It is assumed that every slice is described as one continuous shape. Therefore non-perpendicular side branches generate a non-bijective description of the individual slices: For a given polar angle within a slice there might be more than one value as parts of side branches from a higher region reach into the slice leading to several continuous or eventually even mutually intersecting contour lines.

In order to overcome this problem and to reconstruct the whole dendrite including side branches correctly a different (second) quantitative reconstruction scheme was applied: instead of slicing the dendrite perpendicular to the growth axis we have developed algorithms to construct projections of the dendrite starting from the actual contour line of the gray scale image which contain the axis of growth. Doing so we avoid the bijectivity problem. The idea is that these projections correspond to polar projections. For every polar angle we construct an interpolation between two known projections: i) the contour of the crystal and ii) the contour of the stem visible only in the angles $\pi/4 + n \cdot \pi/2$, $n = 0..3$. We have taken special care that all the polar projections when superimposed in a 2D plot are strictly contained in the domain spanned by the known projections and that there is a monotonic transition between the two projections, i. e. no intersection between any projections in the superimposed 2D plot is allowed. A plot of such superimposed polar projections is shown in Figure 5 a.

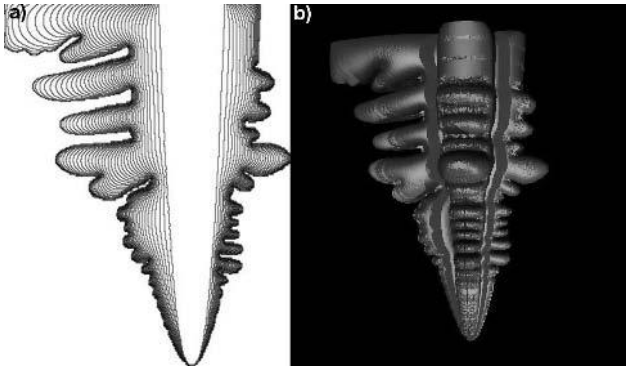

Fig. 5 a) Superimposed constructed polar projections. All projections contain the axis of growth. Therefore the problem of bijectivity is circumvented. b) A mesh constructed with the polar projections in 3 dimensions allows to fully resolving all the side branch curves. The plate-like structure of the side branches is now easily visible.

By reordering the calculated projections so that they run from one loose end to the other one and placing them at their corresponding polar angle it is possible to construct a mesh between two adjacent contour lines and to render a 3D dendrite. Such a dendrite, which contains all the side branches, is shown in Figure 5 b.

The polar projections do not a priori recover the desired cross section in the tip region, which are suitably described by eq. 4. Therefore we have applied a mixed strategy considering the results near the tip region from the first reconstruction: The angles of the polar projection are rescaled in such a way that cross sections perpendicular to the growth direction correspond to the first quantitative reconstruction. Figure 5 b also shows impressively that the side branches can be fully resolved and shows the plate-like shape as expected due to the fact that they are mostly influenced by their adjacent neighbors on the same fin.

19.5 Results and Discussion

After having reconstructed the quantitative three-dimensional shape of our experimental xenon dendrites it was possible to do quantitative measurements on the reconstructions. We have applied two measuring methods: a static and a dynamic one. In the static measurement one single dendrite is reconstructed and the surface area and the volume measured from the tip up to a certain height z was analyzed. We have found that for both surface and volume a power law is recovered: the surface can be described as $S \sim z^{\gamma_1}$ and the volume as $V \sim z^{\nu_1}$. The exponents are $\gamma_1 = 1.66$ and $\nu_1 = 2.13$. The dynamic measurement is based on a sequence of reconstructed shapes of an evolving dendrite. An initial height z_0 is chosen. For every successive image the volume and surface up to a height where the initial height has moved is

measured. Indeed there is a simple relation between the measured height and the tip velocity: $z = z_0 + vt$, where t is the time and v is the constant tip velocity. This measurements leads to different results: $S \sim t^{\gamma_1}$ and $V \sim t^{\nu_1}$ with $\gamma_2 = 1.89$ and $\nu_2 = 2.44$. The difference in the exponents between the static and dynamic measurement can be explained from the fact that in the static case the lateral growth of the side branches is not considered, as only one reconstructed shape is analyzed. Including the lateral growth leads in both cases to an increase of the exponent of ~0.23–0.31. A simplified model to calculate surface and volume of three-dimensional dendrites from their projections was presented by Li and Beckermann [17]. They also have found that volume and surface growth can be described by a power law. In their model only the dynamic measurement is considered: for the surface they find $\gamma_{2,\mathrm{model}} = 1.92$ and $\nu_{2,\mathrm{model}} = 2.10$. It is easy to see that the surface estimation is in good agreement with our findings. However the volume exponent in the model is considerably smaller than the one we have found. Thus the model seems to neglect a vital part that contributes to the volume of the dendrite.

With our quantitative reconstruction of experimentally grown three-dimensional dendrites it was possible to show how cross sections of xenon dendrites look like. We have shown that in our experiments the fins of the dendrites are an inherent part of the shape and may not be treated as a mere perturbation of an isotropic Ivantsov paraboloid. We find good agreement with Brener and Temkin's asymptotic calculations for the fin shape and their thickness. It was shown that the cross section of the dendrites are in gratifying qualitative agreement with phase field simulations, however they seem to point out discrepancies to the analytical predictions.

With the proposed quantitative reconstructions it is possible to analyze integral parameters such as volume and surface and their temporal development in *in situ* observed dendrites. We have shown that for both presented measurement methods a power law for volume and surface is found. While the surface exponents are in good agreement with simplified models the exponents for the volume is considerably larger. Therefore existing models seem to lack a vital part in order to fully describe the volume growth behavior of three-dimensional dendrites.

We thank Professor Dr. H. R. Ott for his support of our experiments. This work was supported by the Swiss National Science Foundation.

References

[1] Solids Far From Equilibrium (Ed.: C. Godrèche), Cambridge University Press, Cambridge, 1992.

[2] L.I. Rubinstein, The Stefan Problem, American Mathematical Society, Providence, Rhode Island, 1971.

[3] M.E. Glicksman, R.J. Schaefer, and J.D. Ayers, Metall. Trans. A 1976, 7A, 1747- 1759

[4] U. Bisang, and J.H. Bilgram, Phys. Rev. E 1996, 54, 5309–5326

[5] G.P. Ivantsov in Growth of Crystals (Ed.: A.V. Shubnikov and N.N. Sheftal) Consultants Bureau, New York, 1958, Vol. 1, p. 76–85

[6] E. Brener and D. Temkin, Phys. Rev. E 1995, 51, 351–359.

[7] G.B. McFadden, S.R. Coriell, and R.F. Sekerka, J. Crystal Growth 2000, 208, 726–745.

[8] A. Karma, Y.H. Lee, and M. Plapp, Phys. Rev. E 2000, 61, 3996–4006.

[9] J. Y. Zheng, IEEE Trans. on Pattern Analysis and Machine Intelligence 1994, 16(2), 163–178

[10] Y. Sun, I. Liu, and J. K. Grady, IEEE Trans. on Pattern Analysis and Machine Intelligence 1994, 16 (3), 241–248

[11] M. Chan, D. Metaxas, and S. Dickinson, 12th Int. Conf. on Pattern Recog 1994, 1, 432–436

[12] S. Inoué in Handbook of Biological Confocal Microscopy (Ed.: J.B. Pawley), Plenum Press, New York, 1989, p. 1–14

[13] F. Mayinger and O. Feldmann (eds.), Optical Measurements 2nd Ed., Springer, Berlin, 2001

[14] J. Alkemper and P.W. Voorhees, J. Microscopy 2001, 201, 388–394

[15] H.M. Singer, and J.H. Bilgram, Phys. Rev. Lett., submitted

[16] H.M. Singer, and J.H. Bilgram, Phys. Rev. E, submitted

[17] Q. Li, and C. Beckermann, Phys. Rev. E 1998, 57, 3176–3188

20
Mechanically Deformed Primary Dendritic Structures Observed During the Solidification of Undercooled Melts

Andrew M. Mullis, Kalin Dragnevski, & Robert F. Cochrane

20.1
Introduction

In a previous paper [1] we reported that samples of Cu-Sn and Cu-O alloys that had been subject to rapid solidification processing appeared to show evidence of extensive deformation, or bending, of their secondary dendrite arms. Moreover, this deformation was restricted to a very narrow window of undercoolings, typically no more than 15 K, centred around $\Delta T = 75$ K. It seems without question that these deformed structures arise due to flow in the melt, although the exact mechanism is controversial. We have previously argued [2] that the most probable cause of this deformation is mechanical bending of the solid by motion of the fluid while the two co-existed during the post recalescence 'plateau' phase of cooling, that is the extended period in which the residual mush following rapid dendritic growth solidifies due to loss of heat to its surroundings. The most compelling evidence for this seems to us to be that the deformation is restricted to a narrow window of undercooling and that this window centres of the range of undercoolings in which it is predicted that the dendrite tip radius passes through a local minimum. However, we also considered the possibility that the deformation arose due to morphological bending, that is the tendency of the dendrite to bend into the flow due to local redistribution of the solute field during the growth phase. However, using a free boundary model of dendritic growth in a flow, originally developed to study rosette formation during semi-solid forming [3], we found that this possibility could effectively be discounted. At $\Delta T =$ 75 K the observed growth velocity in Cu-3 wt.% Sn alloy is 2.3 m s^{-1}, simply two high for this effect to have any observable influence [2].

It is well established from experiments in transparent analogue systems [4, 5], that even when grown under widely different conditions dendrites tend to be self-similar. Therefore, many of the common dimensions of the dendrite, including trunk radius and radius of the secondary arms prior to ripening, tend to be simple multiples of the tip radius, R. It is a relatively straightforward matter to show that the skin stress exerted on a cylindrical dendrite arm in a flow-field scales as $1/r^3$, where r is the radius of the cylinder. Consequently, the skin stress on a dendrite due to the electromagnetically induced flow of the residual liquid remaining in the mush following

recalescence will peak sharply as the tip radius, and hence most of its other dimensions, passes through a local minimum. Using these arguments we were able to show good quantitative agreement between a model of mechanical bending of a *secondary dendrite arm* and the region where deformed dendritic structures were observed. The general trend is illustrated in Figure 1a, which shows how the skin stress in the dendrite will increase sharply as its radius decreases. In particular, for flow velocities >0.1 m s^{-1} the calculated skin stress exceeds the estimated yield stress within a narrow window centred around the location of the radius minimum. Details of the calculation giving rise to this curve are given in [2], the model geometry assumed for the secondary arm is shown in Figure 1b.

Motion of the liquid is likely to result from electromagnetic stirring, a common side-effect of the inductive heating used during the containerless processing of undercooled melts. These velocities have variously been estimated as being from 0.3 m s^{-1} [6] to in excess of 1.4 m s^{-1} [7, 8] prior to nucleation of solidification. However, during undercooling experiments it is normal that electromagnetic power is still applied to the sample during the plateau stage, and consequently forced motion of the residual liquid through the post recalescence mush may result. The volume fraction of solid formed during the recalescence phase of solidification is given by the ratio $\Delta T/\Delta T_{hyp}$, where $\Delta T_{hyp} = L/c_p$ is the hypercooling limit, L the latent heat on fusion and c_p the specific heat capacity. For dilute Cu alloys $\Delta T_{hyp} \approx 420$ K, giving a volume fraction solid, f_s, of around 18% at $\Delta T = 75$ K. At these relatively low solid fractions, although some attenuation of the flow velocity is to be expected, it is likely that significant flow may still persist. In addition our experimental apparatus gives rise to around 50% electromagnetic screening of the undercooled sample (see Section 2 below). Taking these two effects into account we believe that a conservative estimate would be to assume residual flow velocities in the mush which are reduced by a factor of 10 over those present in the pure liquid without electromagnetic screening. That is post-recalescence velocities could be as high as 0.14 m s^{-1}.

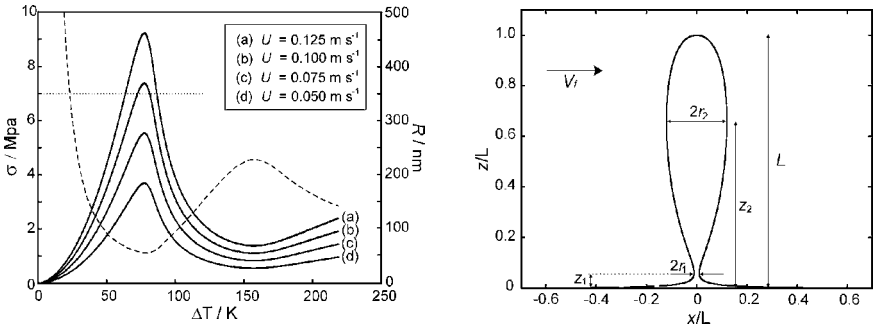

Fig. 1 Results from our previous analysis of the mechanical deformation of secondary dendrite arms showing (a) how the skin stress peaks sharply as the tip radius, R, passes through a local minimum and (b) the model geometry assumed for the secondary arm, including narrowing at the 'neck'.

We have previously assumed the bending occurs at the thinned neck of secondary arms. However, more recent experiments suggest that we may have significantly underestimated the extent of dendritic deformation in our undercooled samples. In particular, we now have compelling evidence of deformed primary dendrites. As it cannot be argued that primary dendrites have the same narrow neck as a secondary dendrite we here re-evaluate our original analysis to determine if we can still account for bending occurring by a mechanical deformation process. The implications of the analysis in terms of the fluid-flow that exists within undercooled melts during containerless processing will also be discussed.

20.2
Experimental Method

Undercooling experiments were performed within a stainless steel vacuum chamber evacuated to a pressure of 10^{-6} mbar and backfilled to 500 mbar with N_2 gas. Samples were heated, in silica crucibles, by induction heating of a graphite susceptor contained within an alumina radiation shield. Viewing slots were cut in the susceptor and alumina to allow the sample to be viewed during the experiment. A commercial soda-lime glass was employed as the flux to reduce the number of potential sites for heterogeneous nucleation. The temperature was monitored by means of a k-type thermocouple positioned at the base of the crucible, which had been thinned, thus reducing the thermal lag between the sample and the thermocouple. Heating and cooling curves were obtained by using a chart recorder. A schematic diagram of the fluxing apparatus is shown in Figure 2. By using this method it was possible to achieve temperatures of up to 1473 K, thus easily accommodating melting and superheating of the alloy systems that were to be investigated, ensuring that the samples were completely contained within the glass flux. Further details of the experimental apparatus and the techniques for measuring growth velocity in fluxed samples can be found in [9].

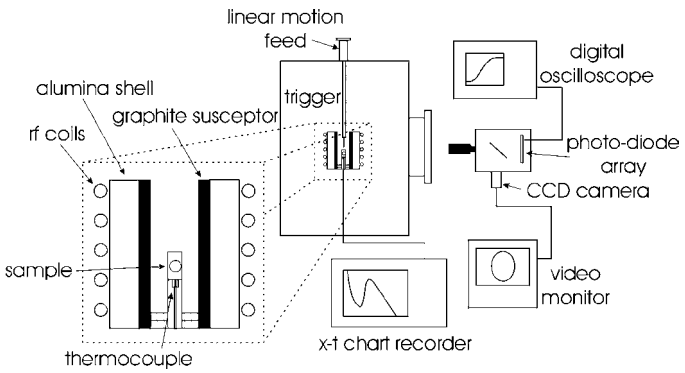

Fig. 2 Schematic diagram of the melt fluxing apparatus used to undercool samples of Cu-3wt%Sn alloy.

Cu-3wt%Sn alloy was prepared by arc melting the elemental constituents under argon. All starting materials were obtained from ALFA (Johnson Matthey) and were of 99.9999% purity. In order to ensure complete mixing of the elements and to eliminate any segregation the alloy was re-melted and finally annealed at 1023 K for 30 min.

After undercooling, the as-solidified droplets were mounted in Bakelite, then polished and finally etched in an appropriate solution to reveal structure and substructure. Optical microscopy was carried out on a Nikon Optiphot microscope using bright field (BF), differential interference contrast (DIC) mode and polarized light.

20.3
Experimental Evidence for Deformed Dendritic Structures

Figure 3a shows a dendrite grown in Cu-3wt%Sn alloy at an undercooling of ΔT = 85 K prior to nucleation of solidification, which was performed by touching the sample surface with a thin alumina needle. The micrograph is shown with the sample (a $\approx$ 6 mm, near spherical droplet sectioned along its axis) oriented as it would have been during the experiment, with the region shown being the bottom of the sample. The dark area on the image is the edge of the specimen. Nucleation was triggered at the top of the sample and consequently the region shown is the last to solidify. The

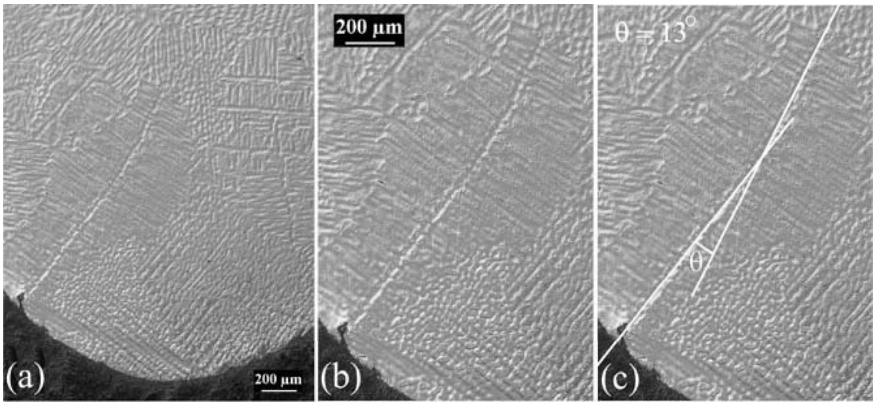

Fig. 3 Micrograph of a Cu-3wt%Sn sample undercooled by 85 K prior to nucleation, showing a highly deformed dendrite. The bulk solidification direction is vertically downwards for the sample orientation shown, so the region containing the deformed dendrite was one of the last to solidify. The figure shows (a) the position of the dendrite in relation to the sample, (b) close up of the deformed dendrite and (c) the dendrite with overlaid guidelines. These show that the dendrite bends through a total angle of $\approx 13^\circ$ and that most of the bend is confined to a region < 200 µm long close to the centre of the dendrite.

bulk growth direction, determined from the trigger point on the sample, is vertically downwards. The interesting region of this sample is towards the lower left-hand side of the micrograph in which a primary dendrite trunk with numerous secondary arms is clearly shown with a significant bend. This region of the micrograph is shown in more detail in Figure 3b. The total length of the primary trunk visible in the section is ≈ 1.7 mm, yet as shown by the guidelines imposed over the image in Fig. 3c the deformation, which is of the order of 13°, is restricted to a region < 200 μm long. If the bending is mechanical, such extensive deformation of a primary dendrite has significant implications for the fluid flow regime that existed in the droplet during solidification.

The measured growth velocity, V, for this sample was 2.6 m s^{-1}. Moreover, because we use a linear photodiode array which measures the growth velocity along the whole solidification path [9], we can assert with reasonable confidence that the growth velocity was constant throughout the whole sample. Consequently, any kinetically induced switch in the growth direction during solidification can, effectively, be ruled out.

20.4 Discussion

We now consider a model in which the dendrite is considered as a simple cylinder of radius r and length, L, which will bend at z_b due to the flow of fluid past it at velocity U. The coordinate system we consider here is as shown in Figure 1b, although now the dendrite is modelled as a cylinder of uniform radius r. It has been shown by Pilling & Hellawell [10] that the force per unit length, F, on such a cylinder is

$$F = 3\pi\eta U \tag{1}$$

where η is the viscosity of the fluid. The skin stress in the dendrite arm, as a function of position z, may be written as

$$\sigma(z) = \frac{M(z)\, r}{I} \tag{2}$$

where M is the bending moment and I the moment of inertia which are given respectively by

$$M(z) = -\frac{1}{2} F z^2 \tag{3}$$

and

$$I(r) = \frac{1}{4}\pi r^4 . \tag{4}$$

The calculation of the bending moment can be formulated in a non-dimensional manner, thus avoiding the problem of defining a length scale for the problem. However, if we are to convert the bending moment into a skin stress that can be compared with experimentally determined yield stresses, this problem must be addressed. No well-defined route exists for calculating dendrite trunk radii. In our previous paper [2] we assumed that this could be estimated by taking a constant multiple of the tip radius [11, 12]. However, for the dendrite shown in Figure 3 the primary trunk is sufficiently well defined that it is possible to estimate its diameter directly from the micrograph of the as-solidified sample. This yields a minimum diameter of around 15 μm.

The viscosity, η, of liquid Cu at its melting temperature is given by Brooks *et al.* [13] as $\eta = 4.36$ mPa s. In the absence of data for Cu-Sn alloy in the undercooled state we have assumed pure Cu melt to be representative of the alloy.

The flow shear stress of the solid, as a function of the homologous temperature, T/T_l, can be obtained from the deformation maps of Frost & Ashby [14]. At the low undercoolings at which dendritic deformation was observed, the plateau time, that is the time between recalescence and complete solidification of the sample, will be of the order of a few seconds. For bending equivalent to that observed in Figure 3 to have occurred within the available time the shear strain rate would have been of the order $10^{-1} - 10^{-2}$ s^{-1}. At these strain rates the required shear stress for pure copper at its melting temperature is estimated as $(2.3 - 3.5) \times 10^{-4}\ \mu_s\,(T_l)$, where $\mu_s\,(T_l)$ is the shear modulus at the liquidus temperature. Over most of the homologous temperature range μ_s decreases linearly with T. Certainly this appears to be a very good approximation up to $T/T_l = 0.6$. As far as we are aware the shear modulus of copper has not been measured close to its melting point. If the linear trend from low temperature data were continued, we estimate, from the data of Frost & Ashby, that $\mu_s\,(T_l) \approx 24$ GPa. However, in many materials the elastic moduli decrease rapidly as the melting temperature is approached and this value may thus be considerably in excess of the true value. Using this value we deduce that an upper bound on the flow stress for pure copper at its melting point may be of the order 7 MPa. In the absence of experimental data we have assumed that the value for the dilute Cu-O and Cu-Sn alloys will be of the same order.

With reference to Figure 3 we note that the dendrite bends around 1 mm from its tip, which we will therefore take as z_b. For a dendrite trunk radius of 7.5 μm, Equations (1–4) with $z = z_b = 1$ mm give a skin stress equal to the yield stress of 7 MPa for a flow velocity that is ≈ 0.11 m s^{-1}. Although it may seem incongruous that we are predicting that the much thicker primary dendrite will bend at the same flow velocity as it's narrower secondary arms, the radius effect is negated by the much longer length of the primary trunk. In this case the primary trunk extends for around a third of the entire length of the sample.

Consequently, mechanical bending of a long primary dendrite such as that shown in Fig. 3 appears to be a feasible prospect. However, we should also consider whether any other physical process can give rise to the observed level of bending at the growth velocities appropriate to these samples. In particular, thermo-solutal advection gives rise to 'morphological bending', that is the tendency for a growing den-

drite tip to bend into a flow due to disturbance of the isotherms and/or isoconcentrate lines ahead of the solid-liquid interface. At low growth velocities this is far more effective than mechanical deformation at rotating the growth direction of the dendrite. We have previously invoked morphological bending as a means of explaining the formation of rosette structures during semi-solid processing [3], finding that the bending or tip rotation rate was a function of the Peclet number for growth and flow. In particular we found that

$$\Phi = \frac{Pt_f}{Pt_g^{1.85}} \tag{5}$$

where Φ is the tip rotation rate in rad m^{-1} and $Pt_{g,f}$ are the Peclet numbers for growth and flow given by

$$Pt_{g,f} = \frac{(U, V)\, R}{2\, D} \tag{6}$$

where D is the diffusivity in the liquid. The implication of Equation (5) is that the effectiveness of the morphological bending mechanism drops off very rapidly with increasing growth velocity. Using the methodology employed in our previous paper [2] we estimated that at a growth velocity of 2.6 m s^{-1} and a flow velocity of 1.0 m s^{-1}, morphological bending could give rise to a maximum deflection of 0.06 rad m^{-1}. For a primary dendrite 1 mm long this equates to a likely bend of 0.003°, which is clearly negligible in the context of the sample shown in Fig. 3. Note that here we have used the higher flow velocity which would be characteristic of the liquid prior to nucleation of solidification.

However, while we see no reason to repeat the calculation of morphological bending rates given in our previous paper, we can now provide additional arguments to support the view that while highly effective at 'conventional' solidification rates, morphological bending does not operate in the rapid solidification regime. Firstly, the direction in which bending occurs is different for mechanical and morphological bending. A dendrite subject to mechanical deformation will bend in the direction of the flow while a dendrite subject to morphological bending will rotate into the flow, that is the bending will be in the opposite direction to that of the flow. Thus, as both the position of the dendrite in the sample and the orientation of the sample in the apparatus is known, any inference concerning the likely flow direction should help to distinguish between mechanical and morphological bending. The two situations are depicted schematically in Fig. 4. We note that the orientation (a), which is appropriate to mechanical bending, is the direction that corresponds with hydrodynamical simulations [6, 15] of the likely flow patterns resulting from containerless processing. Conversely, we are not aware of any reports that the flow pattern resulting from containerless processing could adopt orientation (b).

Secondly, although thermo-solutal advection gives rise to 'morphological bending' there are other morphological changes which could distinguish this from mechanical deformation. Most noticeably, side-branch development occurs preferentially into

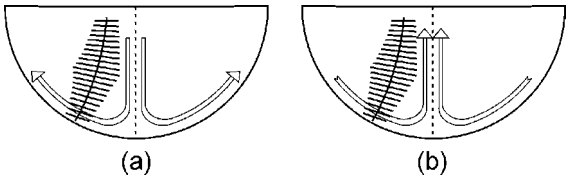

Fig. 4 Schematic diagram of the flow patterns that would give rise to a dendrite deformed in the manner observed

Fig. 5 Phase-field simulation of dendritic growth in a flow, showing that the predominant morphological effect is an asymmetry in the side-branch structure, with side arms growing preferentially into the flow.

the flow. This is seen both in phase-field simulations of dendritic solidification in a flow field [16, 17] (see Fig. 5) and in analogue casting systems [18]. Consequently, if the flow velocities present in the sample can give rise to morphological effects (i. e. if the deformation is the result of morphological bending) we would expect to see a significant elongation of the side-branches on the side of the dendrite facing the flow, which with reference to Figure 4 b is the concave side. Conversely, if morphological effects are unimportant at the observed growth velocity and the deformation is mechanical we would expect the side branch envelope to be approximately symmetric on the convex and concave sides of the dendrite. In our Fig. 3 we note that the envelope of the secondary arms is approximately symmetric in the region of the observed deformation.

To quantify this we have plotted the visible extent of the side-branch envelope as a function of the length of arc along the primary trunk on both the convex and concave sides of the dendrite (Fig. 6). In fact, it is apparent from Figure 6 that there is no systematic difference in the extent of the side-branch envelope. Side-branching is actu-

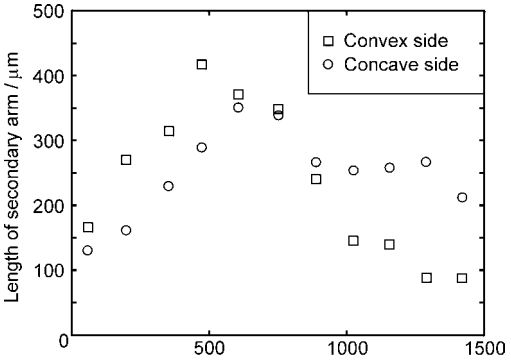

Fig. 6 The measured extent of the side-branch envelope on both the convex and concave sides of the deformed dendrite.

ally better developed on the convex side of the dendrite up to and including the point of maximum bending but is subsequently better developed on the concave side. We would therefore conclude that there is no evidence of flow induced morphological growth effects in the observed dendrite and that bending is likely to be mechanical in origin.

20.5 Summary & Conclusions

Microstructural investigation of as-solidified samples of a Cu-3wt%Sn alloy solidified from its undercooled parent melt show that in a narrow range of undercoolings, typically 75–90 K, deformed dendritic structures can be observed. These deformed structures extend not only to secondary dendrite arms, as identified in our pervious papers, but also to primary dendrites as now reported here. For realistic estimates of the flow velocities that might exist within our undercooled liquid droplets, we find that mechanical deformation seems to be a plausible mechanism for the observed bending. In contrast, morphological bending, that is the tendency of a growing dendrite to bend into a flow due to local redistribution of the solute field, appears to be ineffective at the high growth velocities (2.6 m s^{-1}) relevant to our samples. Moreover, the direction of the bending is consistent with the flow patterns produced in recent hydrodynamic simulations of containerless processing only if the origin of the bending is mechanical.

References

[1] A.M. Mullis, D.J. Walker, S.E. Battersby & R.F. Cochrane, Mater. Sci. Eng. A, 2001, 304, 245–249.

[2] K.I. Dragnevski, A.M. Mullis, D.J. Walker, & R.F. Cochrane, Acta Mater., 2002, 50, 3743–3755.

[3] A.M. Mullis, Acta Mater., 1999, 47, 1783–1789.

[4] D.P. Corrigan, M.B. Koss, J.C. LaCombe, et al., Phys. Rev. E, 1999, 60, 7217.

[5] U. Bisang & J.H. Bilgram, Phys. Rev. E, 1996, 54, 5309.

[6] E. Schwartz, J. Szekely, O. Ilegbusi, J. –H. Zong & I. Egry, in 'Magnetohydrodynamics in process metallurgy' (ed. J. Szekely *et al.*) pp. 81–87, Metallurgical Society of AIME, Warrendale, PA 1992.

[7] P. Galenko, Mid-Term activity report to the NEQUISOL project under ESA MAP project AO 99–023, European Space Agency, 2003.

[8] P. Galenko, Oral presentation at Euromat 2003, Laussane CH, 1–5 September 2003.

[9] S.E. Battersby, R.F. Cochrane & A.M. Mullis, J. Mater. Sci., 1999, 34, 2049–2056.

[10] J. Pilling & A. Hellawell, Metall. Mater. Trans. A, 1996, 27, 229–232.

[11] M. Schwarz, K. Karma, K. Eckler, D. M. Herlach, Phys. Rev. Lett., 1994, 73, 1380.

[12] E. Kaufmann, Ph.D. Thesis, Swiss Federal Institute of Technology, Zurich, 1999.

[13] R.F. Brooks, I. Egry, S. Seetharama & D. Grant, High Temp. High Press., 2001, 33, 631.

[14] H.J. Frost & M.F. Ashby, in 'Deformation-mechanism maps' pp. 24–25, Pergamon, Oxford, UK, 1982.

[15] O. Filip, R. Hermann, G. Garbeth, J. Priede & V. Shatrov, Oral presentation at Euromat 2003, Laussane CH, 1–5 September 2003.

[16] X. Tong, C. Beckermann, A. Karma & Q. Li, Phys. Rev. E, 2001, 63, 061601.

[17] A.M. Mullis, Scripta Mater. to be published.

[18] M.E. Glicksman, S.R. Coriell & G.B. McFadden, Ann. Rev. Fluid Mech., 1986, 18, 307–335.

21
Effect of Hydrodynamics on Microstructure Evolution of Nd-Fe-B Alloys

R. Hermann, G. Gerbeth, O. Filip, J. Priede,V. Shatrov

Abstract

The influence of melt convection on the microstructure formation of Nd-Fe-B alloys, mainly the volume fraction and grain size of the α-Fe phase, has been investigated experimentally using the electromagnetic levitation technique and a specially designed floating-zone arrangement. Samples were subjected to a strong rotation during levitation and compared to fixed samples without additional sample rotation in the levitation facility. A controlled influence on the melt flow is possible via tailored magnetic fields which enable enhancement or suppression of the melt convection using the floating-zone arrangement. A specially designed magnetic two-phase stirrer offers a strong influence on the melt flow in the floating-zone facility. The microstructure pattern, mainly the volume fraction and grain size of the α-Fe phase, vary strongly with the strength of the internal flow motion in both types of experiments. The melt flow in a levitated droplet was studied numerically under the additional effect of a global sample rotation resulting in a strong suppression of internal motions. The electromagnetically driven flow in the inductively heated melt zone of the floating-zone arrangement turned out to be of strong influence on the resulting microstructure. Numerical simulations are essential in order to understand and design the various flow structures.

21.1
Introduction

High performance Nd-Fe-B magnets are of enormous economic interest and they will continue to play a key role in the development of electronics and motors, in biophysics and medicine [1]. Rare-earth magnets are commercially produced by sintering, rapid quenching or HDDR [2–4]. The excellent ferromagnetic properties of the rare-earth magnets are due to the hard magnetic $Nd_2Fe_{14}B$-phase (ϕ-Phase) with high saturation polarisation and magnetocrystalline anisotropy. Crucial problems during industrial processing are the formation of dendritic α-Fe and the grain growth during heat treatment processes. Furthermore, the sensitivity of the micro-

structure to the processing parameters makes it difficult to produce magnets with uniform magnetic properties. Numerous publications consider the influence of additions and the variation of process parameters on microstructure and magnetic properties. Although induction heating is widely used in metals processing the influence of melt convection and fluid flow dynamics is not yet fully understood. In metallurgical processing it is well-known that electromagnetic stirring during the solidification of metals leads to morphology changes of the microstructure. For example, the recent paper [5] describes the positive effect of magnetic field induced convection on grain refinement and improved homogenization of alloying elements. However, systematic studies on the relation between the convection (flow direction, intensity, shear rate at the phase boundary, etc.) and the resulting solidified microstructure are still very scarce [6].

The electromagnetic levitation technique is a useful tool for the in-situ observation of the solidification kinetics [7]. It has been used in order to investigate the influence of melt rotation and turbulence on the microstructure formation of Nd-Fe-B alloys, mainly the volume fraction and grain size of the undesired α-Fe phase. Recent publications have shown the strong dependence of the α-Fe phase formation on processing parameters during cooling, which starts to nucleate at about 50 K below the liquidus temperature [8]. Furthermore, a specially designed floating-zone arrangement with an additional magnetic two-phase stirrer enables a controlled influence of the melt flow via tailored magnetic fields ranging from an enhancement up to a significant suppression of the melt convection. The aim of the present work is to investigate the influence of melt convection on phase and microstructure formation during the solidification process of Nd-Fe-B alloys.

21.2 Experimental

Stoichiometric $Nd_{11.8}Fe_{82.3}B_{5.9}$ alloys were prepared from pure Nd, Fe and Fe-B alloy in a cold crucible induction furnace under argon atmosphere and cast to rods with 6 mm diameter. Cubic samples with a side length of 6 mm and about 1.5 g mass were molten containerlessly and solidified in an electromagnetic levitation facility under helium gas atmosphere. The levitation of the molten spherical samples is facilitated by the oscillating magnetic field which is produced due to an applied RF-alternating current in the cone-like induction coil. Eddy currents are induced in electrically conducting samples and the sample is molten by the absorbed power whereas the magnetic force compensates the gravitational force. The samples were then cooled by a He gas stream. The temperature of the sample was monitored by a two-colour pyrometer with a sampling rate of 50 Hz and a relative accuracy of ± 3 K. The cooling procedure was additionally observed using a video camera. Samples were subjected to strong rotation during levitation and compared with fixed samples without such a global sample rotation.

For the floating-zone experiments with an additional magnetic two-phase stirrer, the rods with 6 mm diameter were vertically adjusted in the floating zone facility [9].

Part of the rod was then molten containerlessly by an RF induction heater under argon atmosphere. In order to achieve a strong and flexible control of the melt motion, an external magnetic field was applied in the form of a two-phase stirrer which allows to control the melt motion in a wide range. The induction heating causes a flow in the melt which typically consists of a double vortex in a cylindrical configuration. The two-phase stirrer is made up of an additional coil which is superimposed to the primary induction coil. The additional coil is part of a secondary circuit with adjustable capacitor and resistance but it is not connected to any power supply. The current in the secondary coil is solely induced by the primary coil, thus creating an electromagnetic pump effect. Its intensity and resulting flow direction can easily be adjusted to the process needs. The flexible system parameters are the location and distance of the secondary coil with respect to the primary one, and the capacitor and resistance of the secondary circuit. Different fluid flow patterns were set up experimentally by varying the parameters of the two-phase stirrer. The molten part of the rod remained in the liquid state for 3 min prior to solidification in order to provide for a steady fluid flow. The solidification of the molten part was initiated by switching off the induction coil system. The solidified melt drops and the molten rod parts were investigated by scanning electron microscopy (SEM) and digitally enhanced KERR microscopy. The volume fraction of α-Fe was determined using a 2.8 T vibration sample magnetometer (VSM). Half of a sample was crushed to powder and sieved. Particle size fractions of 350 to 500 μm were selected and filled into a boron nitride (BN) crucible. Assuming, that only two magnetic phases, α-Fe and $Nd_2Fe_{14}B$ phase exist, the measurement was carried out at 340 °C, well above the Curie temperature of the $Nd_2Fe_{14}B$ phase, up to 1.5 T magnetic field strength under Argon atmosphere.

21.3 Results

21.3.1 Levitation

During electromagnetic levitation, spontaneous global instabilities occur because of the coupling between the sample motion and the induced electric current, leading to sample rotation or oscillation [10]. The levitation of the Nd-Fe-B samples was accompanied by a global rotation rate of about 6–8 Hz. The effect of rotation on the solidification phenomenon was studied and the results compared with fixed samples without global sample rotation. The latter was obtained simply by placing the sample on a BN plate, thus suppressing the global rotation development by a direct contact to a substrate.

Though the detailed relation between the convection and the resulting microstructure is still a challenging task, it is obviously useful to know the related flow fields, at least for a qualitative discussion of the observed tendencies. As the electromagnetic levitation field enters the problem with the two independent parameters of field am-

plitude B and field frequency $\omega = 2\pi f$, the flow is determined by the two non-dimensional parameters skin-depth $\delta = (2/\mu_0 \sigma \omega R^2)^{1/2}$ and interaction parameter $N = \sigma B^2 \omega R^4/\rho \nu^2$ (μ_0 – vacuum permeability, σ – electrical conductivity, R – drop radius, ρ – density, ν – kinematic viscosity). A Reynolds number $Re = Rv_m/\nu$ is defined based on the maximum flow velocity v_m inside the drop. As shown in [11] for various types of levitation fields, the basic axisymmetric flow field becomes typically oscillatory unstable at Re ~ 100 in a three-dimensional way characterized by azimuthal wave-numbers of m = 2, 3, 4. Our levitation experiments have been performed with R = 3.5 mm, f = 200–300 kHz and B ~ 10 mT which corresponds to $\delta \sim 0.25$, $N \sim 3 \times 10^6$ where the material data of pure iron have been used due to the lack of material data for Nd-Fe-B. For a drop globally at rest, these parameters correspond to an induced internal flow of about $Re \sim 10^3$. Now, what is the influence of a global drop rotation on this internal flow field? Assuming again a spherical drop, the basic flow Reynolds number of the internal flow is shown in Fig. 1 for $\delta = 0.1$ and various values of N as a function of the Ekman number $E = \nu/\Omega R^2$ where Ω denotes the global rotation rate of the sample. It is seen that higher rotation rates corresponding to $E < 10^{-2}$ may drastically reduce the internal motion. The interpretation is that a high-speed rotation forces the fluid to rotate more and more as a solid body, thus suppressing the relative internal motion like in a centrifuge. Our levitation experiments revealed global rotation rates of 6–8 Hz corresponding to an Ekman number in the order of $E \sim 2 \cdot 10^{-3}$ which gives an internal flow with Re ~ 10. That means, compared to the non-rotating case the global drop rotation suppresses the internal melt motion significantly by about two orders of magnitude.

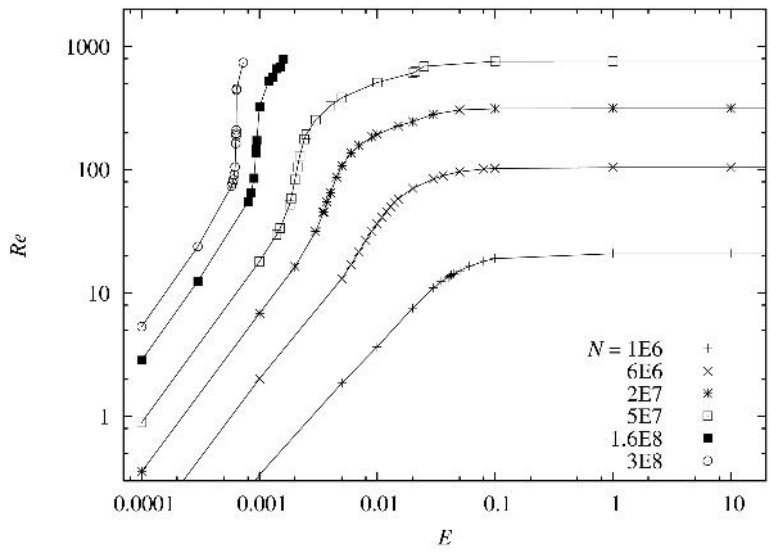

Fig. 1 Reynolds number of the meridional flow inside the drop versus Ekman number for various interaction parameter N. Skin-depth $\delta = 0.1$.

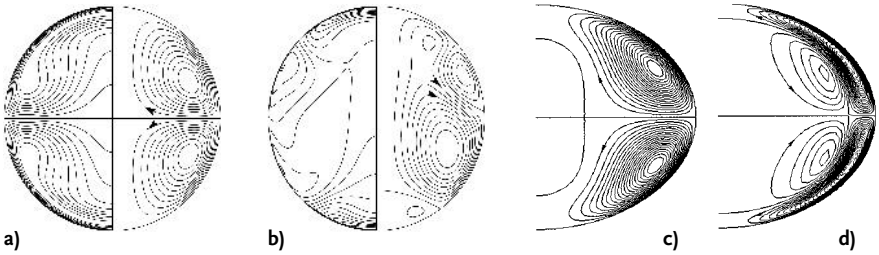

Fig. 2 **a)** Streamlines (right) and angular vorticity (left) in a uniform levitating field of $N = 6 \times 10^6$. **b)** Streamlines (right) and angular vorticity (left) in a linear levitating field of $N = 4.5 \times 10^9$. **c)** Streamlines in a levitated drop with global rotation, $N = 6 \times 10^6$, $E = 10^{-2}$. **d)** Streamlines in a levitated drop with global rotation, $N = 6 \times 10^6$, $E = 10^{-3}$.

Figs. 2a–d show the flow fields for the cases without and with global rotation for a skin-depth of $\delta = 0.1$. Besides the different strength of the flow velocities, it is seen that also strongly different flow structures arise due to the global rotation.

Moreover, SEM micrograph investigations of samples solidified during levitation with simultaneous global sample rotation and without global sample rotation revealed slight refinement of α-Fe dendrites with decreased dendrite arm spacing under global sample rotation. The observation was validated by measuring the magnetic moment at 340 °C using a 2.8 T VSM, yielding a volume fraction of about 35% α-Fe in the fixed sample whereas only 23% α-Fe was determined in the rotating sample. It should be remarked that the rotating samples presented a homogeneous α-Fe dendrite formation while a quite inhomogeneous microstructure was observed in samples processed on a BN plate(see also [12]).

It can be concluded that a strong sample rotation diminishes the α-Fe volume fraction as well the α-dendrite dimension. The grain size of the solidified samples was investigated by KERR microscopy. A grain refinement of the $Nd_2Fe_{14}B$-phase during solidification under strong sample rotation could be observed.

The sample rotation seems to retard rapid dendrite growth. It is assumed that the fine structured Fe dendrites provide numerous nucleation centers for the succeeding solidification of the residual melt, the peritectic growth of the $Nd_2Fe_{14}B$-phase from properitectic γ-Fe and the surrounding melt resulting in a reduced grain size.

These results emphasize that the increase of the α-Fe volume fraction in the fixed sample is due to the stronger melt convection compared to the rotating sample case.

21.3.2
Magnetic Two-phase Stirrer

The application of additional magnetic fields offer a powerful tool for a contact-less influence on the melt motion during solidification. The present approach of a modified float-zone configuration, called magnetic two-phase stirrer, is shown in Figs. 3a–d. The pumping effect due to the two-phase stirrer is capable of transferring the double vortex flow structure (Fig. 3 b) to a single vortex (Fig. 3 d). The flow direction of this single vortex can be reversed by exchanging the primary and secondary coils. Besides the capacitor and the resistance in the secondary circuit, the vertical distance between the two coils is a control parameter of significant influence on the resulting flow field. A maximum strength of the single vortex flow is obtained if this distance equals the radius of the rod. Change of the vertical coil distance as well as changes of the secondary circuit parameters offer the possibility to regulate the flow in a wide range from a

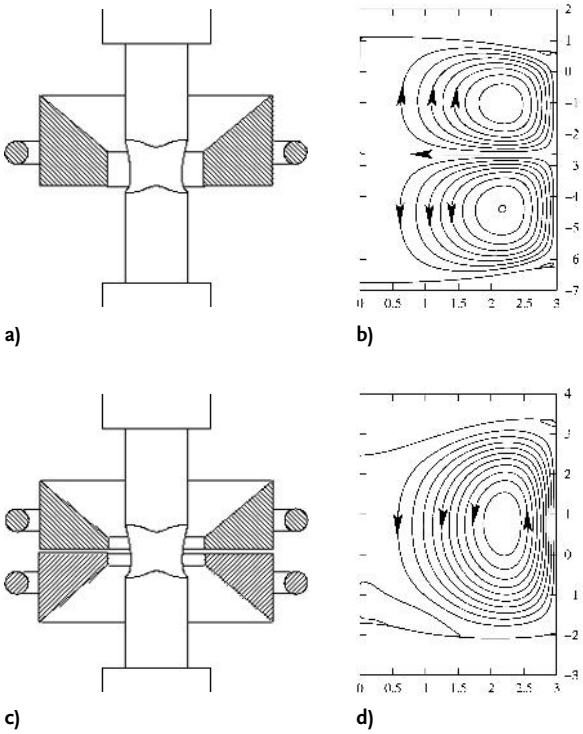

Fig. 3 **a)** Sketch of the standard float-zone configuration. **b)** Numerical simulation of the electromagnetically driven double vortex flow for the standard case of Fig. 4 a. **c)**. Sketch of the magnetic two-phase stirrer with a secondary coil above the primary one. **(d)** Numerical simulation of the resulting single vortex flow due to the action of the two-phase stirrer.

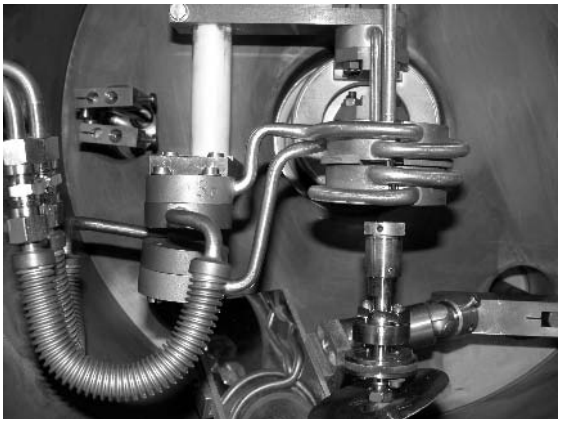

Fig. 4 Photo of the two-phase stirrer realization at the float-zone facility.

strong single vortex flow up to a significant reduction of the internal velocity. In the present experiments, different fluid flow pattern were set up mainly by varying the capacitor in the secondary circuit, thus varying the phase shift between the two coils. A photo of the two-phase stirrer realization at the float-zone facility shows Fig. 4. The molten part of the rod remained in the liquid state for 3 min. prior to solidification in order to install a steady fluid flow. The solidification of the molten part was initiated by switching off the induction coil system.

Fig. 5 a shows the microstructure of the master alloy prepared in a cold crucible induction furnace without any additional magnetic field. The first configuration was chosen to generate a strong stirring of the internal melt. The as-solidified microstructure exhibits large globular α-Fe particles (black), visible in Fig. 5b. Simultaneously, Nd-rich phase (white) appears on a large scale partially unhinged during preparation (black shaded area). In the other two configurations, the melt motion was reduced stepwise from a medium (Fig. 5 c) to a strongly reduced one (Fig. 5 d) compared to the arrangement without any additional magnetic field by a proper choice of parameters of the two-phase stirrer. A strong refinement of the microstructure with small-sized α-Fe dendrites is generated, clearly apparent in Fig. 5 d.

The α-Fe volume fraction amounts to 26.4 wt% for the configuration with strong melt stirring and 11.6 wt% for the microstructure under reduced melt motion. For comparison, the α-Fe volume fraction for the master alloy amounts to 22.5 wt% (Fig. 5 a). Again, the strong dependence of the microstructure on the hydrodynamics of the melt is obvious.

21.4 Conclusions

The microstructure pattern, mainly the volume fraction and grain size of the α-Fe phase, vary strongly with the strength of the internal motion in both types of experiments. The melt flow in a levitated droplet was studied numerically under the addi-

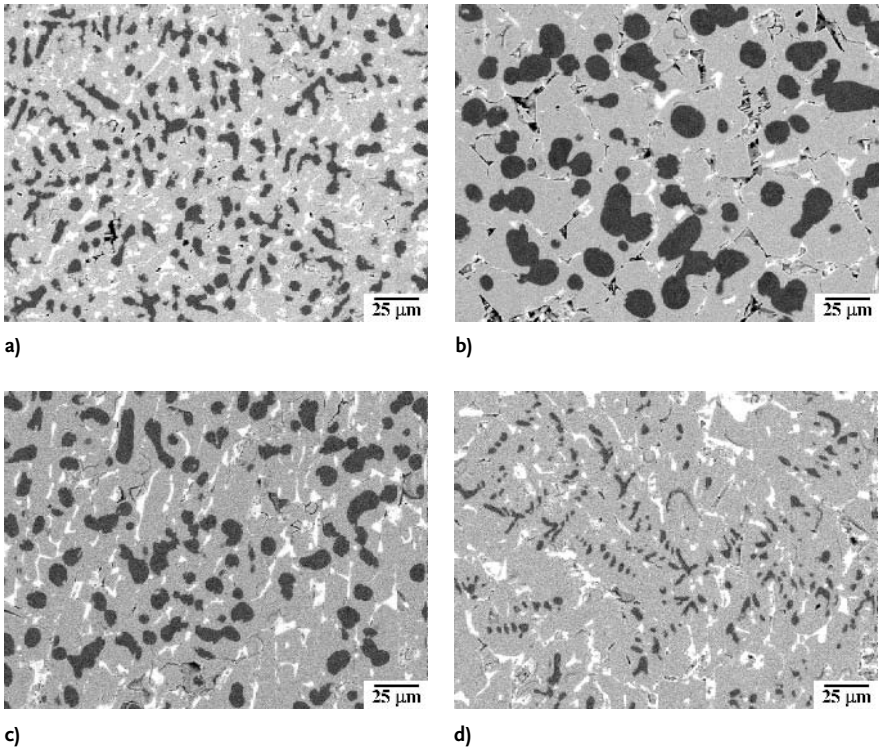

Fig. 5 SEM micrographs of Nd-Fe-B samples, a) master alloy cast in a cold crucible induction furnace, b–d) reducing melt convection from strong to smooth by varying the parameters of the two-phase stirrer. Black: α-Fe phase., white: Nd-rich phase, grey: $Nd_2Fe_{14}B$-phase.

tional effect of a global sample rotation giving rise to the assumption of strong suppression of internal motions leading to reduced α-Fe volume fraction and grain refinement. The electromagnetically driven flow in the inductively heated melt zone of the floating-zone arrangement turned out to be of strong influence on the resulting microstructure. Numerical simulations are essential in order to understand and design the various flow structures.

Acknowledgements

This work was supported by Deutsche Forschungsgemeinschaft in the framework of the Priority program 1120 "Phase Transformations in Multicomponent Melts" under contract no. HE2955/2-1 and Sonderforschungsbereich 609 „Elektromagnetische Strömungsbeeinflussung in Metallurgie, Kristallzüchtung und Elektrochemie".

References

[1] Yuji Kaneko, In: Rare – Earth Magnets and Their Applications, Proc. 16th Int. Workshop on Rare-Earth Magnets and their Applications, Sendai, Japan, 10.–14, September 2000.

[2] M. Sagawa, S. Fujimura, N. Togawa, H. Yamamoto, Y. Matsuura, J. Appl. Phys. 1984, 55, 2083.

[3] J. J. Croat, J. F. Herbst, R. W. Lee, F. E. Pinkerton, J. Appl. Phys. 1984, 55, 2078.

[4] I. R. Harris, C. Noble, T. Bailey, J. Less-Common Met., 1985, 106, L1.

[5] T. Kozuka, M. Kawahara, Proc. 3rd Int. Symposium on Electromagnetic Processing of Materials, Nagoya, Japan 2000, 519.

[6] B. Willers, S. Eckert, U. Michel, G. Zouhar, P. Nikritjuk, K. Eckert, 4th Int. Conference on Electromagnetic Processing of Materials, Lyon, France, Oct. 2003, paper A2-3.7.

[7] E. Schleip, R. Willnecker, D. M. Herlach, G. P. Görler, Mat. Sci. Eng. 1988, 39.

[8] R. Hermann, I. Bächer, D. Matson, W. Löser, L. Schultz, IEEE Transactions on Magnetics 2001, 37, No. 3, 1100.

[9] R. Hermann, J. Priede, G. Behr, G. Gerbeth, L. Schultz, J. Crystal Growth 2001, 223, No. 4, 577–587.

[10] J. Priede, G. Gerbeth, IEEE Trans. Magn. 2000, 36, 349–357.

[11] V. Shatrov, J. Priede, G. Gerbeth, Phys. Fluids 2003, 15, No. 3, 668–678.

[12] R. Hermann, O. Filip, J. Magn. Magn. Mat. 2003, 263, 15–20.

22
Effect of the Fluid Convection Driven by a Rotating Magnetic Field on the Solidification of a PbSn Alloy

B. Willers, S. Eckert, U. Michel, G. Zouhar

22.1
Introduction

The fluid flow during the solidification of metallic alloys results from either natural or forced convection or is driven by the shrinkage of the solidifying material. The natural convection arises from density variations due to differences in the temperature and/or composition. Forced convection in the bulk liquid can be generated by mechanical or electromagnetic stirring.

The benefit of electromagnetic stirring in metallurgical processes such as continuous casting or rheocasting has been discussed in the literature during the last decades. Early investigations have shown a decrease in grain size with increasing strength of forced convection [1–3]. Moreover, the bulk liquid flow promotes the transition from a columnar to an equiaxed dendrite growth (CET) [3,4] and macrosegregation can be reduced [5]. The fluid flow also increases the heat transfer rate and decreases the temperature gradients in the bulk liquid ahead of the solidification front.

The role of the flow in the melt during solidification is complex and the physical mechanisms how the flow field affects the structure and segregation on both macro- and microscale are not fully understood until now. In numerous cases it is difficult to obtain relationships between solidification or microstructure parameters and the fluid velocity because detailed information about the flow field especially in the vicinity of the solidification front is not available. On the other hand, a better understanding of the physical mechanism is strongly required to be able to find an optimized flow structure and finally a configuration of the external magnetic field resulting in favorable properties of the casting ingots.

Different kinds of time-dependent magnetic fields such as rotating, travelling and pulsating field can be used to produce a wide variety of flow fields in the melt which may influence the nucleation and growth process during the solidification.

An experimental program was started aimed to contribute to a better understanding of the influence of a forced bulk flow on the solidification of metallic alloys. At the beginning of the activities a rotating magnetic field (RMF) was chosen to generate a forced convection in a cylindrical melt column because for this case a number

of theoretical and experimental data about the flow pattern are already available [6–10], although for isothermal conditions, only.

The RMF creates a clearly dominating angular component of the Lorentz force which drives a swirling flow of the melt [6]. This primary flow in the horizontal plane is superimposed by a secondary flow showing a double vortex structure in the radial-meridional plane occurring due to the centrifugal force and the no-slip condition at the vertical walls. The secondary flow is found to be a factor of about 5 to 7 times smaller than the angular velocity component. In the low induction and low frequency limit the magnetic Taylor number *Ta* has to be considered as the dominating non-dimensional parameter for describing the flow field:

$$Ta = \frac{\sigma\,\omega\,B_0^2\,R^4}{2\,\rho\,\nu^2} \tag{1}$$

where B, $f = \omega/2\pi$, σ, ρ and ν denote the magnetic field strength, the field frequency, the electrical conductivity, the density and the kinematic viscosity of the fluid.

22.2
Experimental Procedure

In the experiments a Pb85wt%Sn alloy was used prepared from Sn and Pb with a purity of 99.99 pct. The alloy was solidified directionally using the experimental set-up shown in figure 1. A cylindrical stainless steel mould was used having an internal diameter of 50 mm, a height of 100 mm and a wall thickness of 3 mm. The side walls were covered by a 10 mm thick heat insulation to prevent a radial transfer of heat from the mould. The filling height for each charge was 60 mm. The mould is covered at the top by a stainless steel lid. The volume between the lid and the free surface of the melt is filled with air.

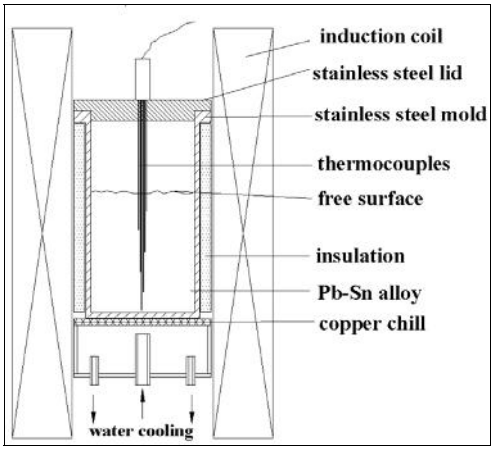

Fig. 1 Scheme of the experimental apparatus for directional solidification of Pb-Sn alloys exposed to a rotating magnetic field

The alloy was heated up by an electrical furnace to a temperature of about 300 °C corresponding to a superheat of 90 K. Then the mould was taken from the heater and set immediately on a copper chill. Water was circulated through a cooling jacket keeping the temperature of the copper plate during the solidification at a constant value of about 25 °C and thus inducing an axial heat transfer from the mould. A special heat conducting gel was used to optimize the heat contact between the steel mould and the copper chill. For the same reason the inner wall of the mould bottom was chemically treated with a mixture of HCl and HNO_3. By this special honing procedure a stable wetting between the steel wall and the liquid Pb-Sn melt was achieved. This wetting is essential to guarantee constant heat transfer conditions during the entire solidification process. Previous measurements were carried out confirming that the described experimental set-up fulfils the requirement of an unidirectional heat flow in vertical direction.

The entire configuration is placed concentrically inside a magnetic inductor. The magnetic system consists of six induction coils generating a rotating magnetic field where the maximum field strength amounts to 25 mT. Moreover, it is possible to vary the frequency of the field between 10 and 400 Hz. For our measurements a frequency of 50 Hz was selected being small enough to neglect the skin effect and to guarantee a homogeneous magnetic field distribution in the entire ingot.

During the solidification continuous temperature measurements inside the melt were performed by means of a set of six type K thermocouples installed in the center of the mould at vertical positions of 1.5, 11.5, 22, 32, 41.5 and 51.5 mm measured from the base of the ingot. The overall scan rate for the temperature measurements was selected as 1 Hz.

Solidification parameters such as the temperature gradient G and the average velocity of the liqidus isotherm V_{TL} have been deduced from the recorded cooling curves following the procedure described by Gandin [11].

The ultrasound Doppler velocimetry (UDV) was applied to measure the velocity inside the liquid phase as well as the position of the solidification front. The technique is based on the ultrasonic pulsed echo method. An ultrasonic pulse is emitted from a transducer along the measuring line. The same transducer receives the echo reflected from tracers suspended in the flow. A profile of the velocity component along the measuring line can be reconstructed from the information contained in the echo. The velocity can be calculated from the measured Doppler shift frequency f_D using the well-known Doppler relation. The origin of the signal can be derived from the time delay τ between the start of the ultrasonic burst and the reception of the corresponding echo. For a detailed description of this measuring technique and their application in liquid metal flows we refer the reader to Takeda [12] and Eckert et al. [13], respectively. Profiles of the liquid velocity were determined using the well-known Doppler relation. The position of the solidification front was detected using an indirect method. In the measured profiles of the vertical velocity the distance from the transducer was determined where the velocity value became identical to zero. So, the qualitative assumption was made that the position where the liquid bulk flow vanishes should be identical with the interface solid-liquid.

The solidified samples were sectioned longitudinally along its midplane, grinded and polished. A solution composed of 150 ml H_2O, 25 ml HNO_3 and 10 ml CH_3COOH was used to etch the surface. After etching the microstructure was examined by light microscopy.

22.3 Discussion of the Results

22.3.1 Thermal analysis

In Figure 2 cooling curves are compared for the case without RMF and a Taylor number of $2 \cdot 10^7$, respectively. If a magnetic field is applied temperature fluctuations can be observed in the cooling curves above the liquidus temperature indicating the existence of a turbulent bulk flow.

The heat flow from the solidifying ingot to the copper chill is mainly determined by the heat transfer coefficient at the solid-liquid interface. The convection in the

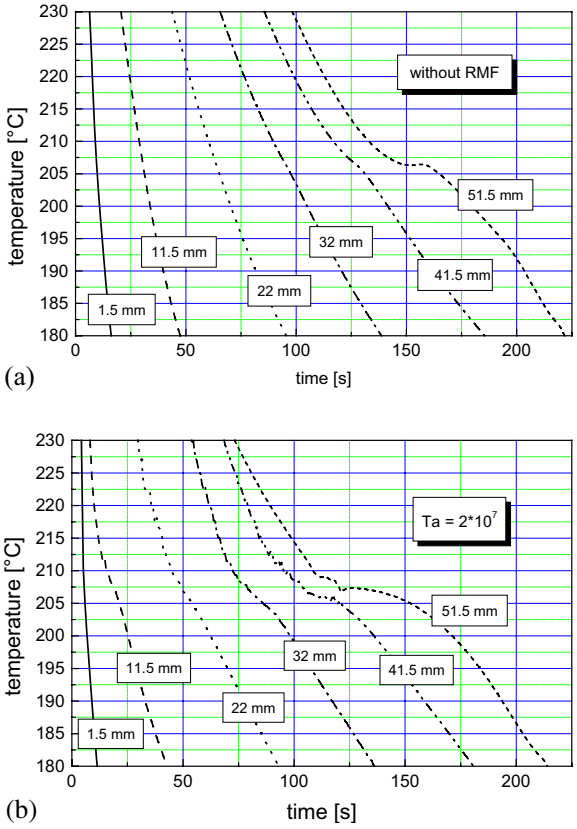

Fig. 2 Cooling curves obtained in Pb85wt%Sn alloy solidified directionally without (a) and with an electromagnetically driven convection by RMF (b)

melt enhances the heat transfer coefficient significantly. Consequently, near the bottom of the ingot a distinct increase of the cooling rate and a reduction of the temperature gradient can be observed with increasing Taylor number *Ta*. The figures 3 and 4 show the cooling rate and the temperature gradient, respectively, obtained when the liquidus temperature T_L was registered at the particular thermocouple.

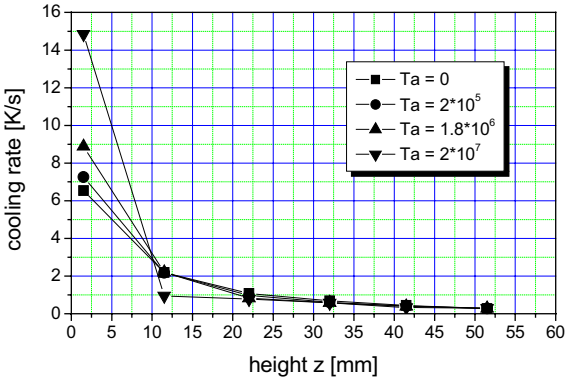

Fig. 3 Cooling rate $-dT/dt$ as a function of the z-position along the ingot axis for different Taylor numbers *Ta*

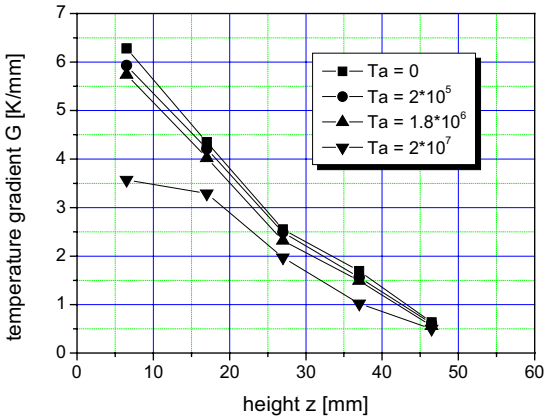

Fig. 4 Temperature gradient *G* as a function of the z-position along the ingot axis for different Taylor numbers *Ta*

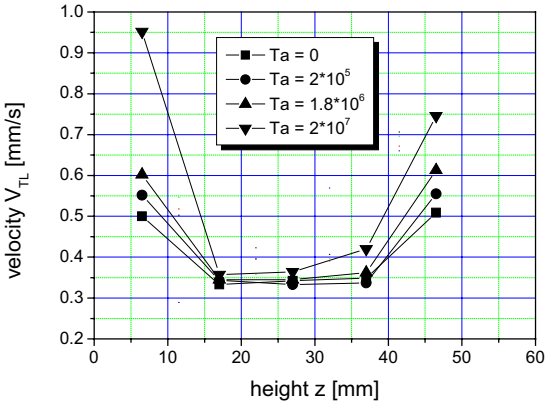

Fig. 5 Average velocity of the liquidus temperature V_{TL} as a function of the z-position along the ingot axis for different Taylor numbers *Ta*

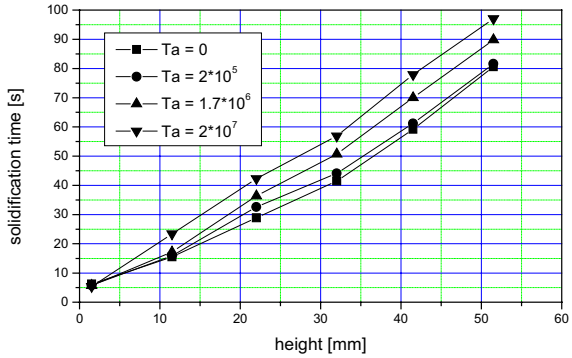

Fig. 6 Solidification time τ_S as a function of the z-position along the ingot axis for different Taylor numbers *Ta*

The corresponding velocity of the liquidus temperature V_{TL} is displayed in figure 5. Figure 6 shows the solidification time measured for different Taylor numbers as the time difference between the two moments where the liquidus temperature T_L and the solidus temperature T_S, respectively, have been detected at the same thermocouple positions. The application of the RMF increases the solidification time and therefore the extension of the mushy zone.

22.3.2
UDV Measurements

Figure 7 shows UDV measurements of the azimuthal velocity component as a function of the temperature obtained at solidification experiments with applied RMF. The measuring position was set at z = 50 mm and r = 20 mm. The solidification process starts at 300 °C at the right hand side of the diagram. The RMF was switched on at the same moment. In the first period of the experiment the flow need some time to develop due to the inertia of the fluid. At a temperature of about 270 °C a maximum velocity value was reached before a continuous damping of the convection can be observed. The reason for that has not to be sought in an increase of fluid viscosity but the reduction of the aspect ratio of the liquid column with ongoing solidification.

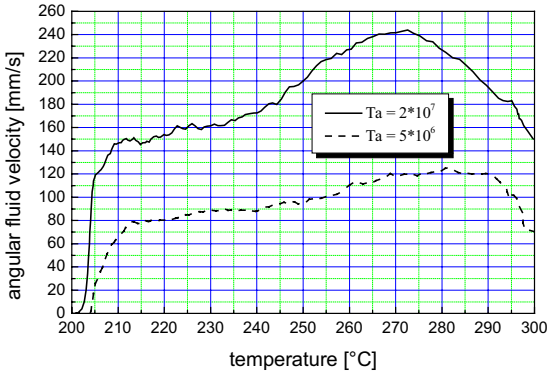

Fig. 7 Azimuthal velocity component during solidification measured at the position r = 20 mm, z = 50 mm

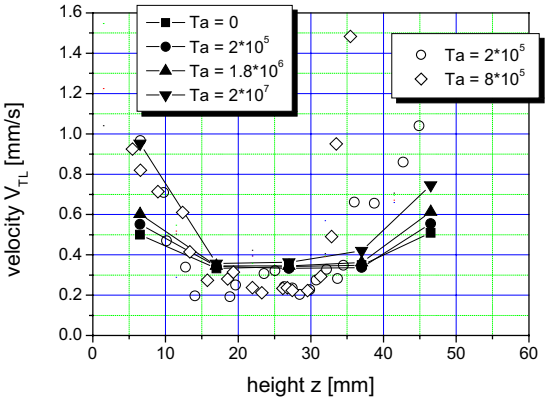

Fig. 8 Comparison of the velocity of the liquidus isotherm as shown in figure 5 (closed symbols) and velocity of the solidification front obtained by UDV (open symbols)

If approaching the solidification front, the velocity decreases and drops steeply to zero if the liquidus isotherm ($T_L \approx 210\,^{\circ}C$) has passed the measuring position.

In figure 8 the average velocity of the liquidus isotherm is compared with the velocity of the solidification front as deduced from the UDV measurements. Whereas the results obtained from the thermal and the UDV measurements agree very well until a height of about 35 mm, the UDV investigations lead to a distinct larger velocity in the upper regions of the specimen. This difference is caused by the method to detect the solidification front as the position where the macroscopic fluid convection disappears. If a RMF is applied during solidification a transition from a columnar to an equiaxed growth as discussed later on is observed at the positions where the curves in figure 8 starts to diverge. In the case of an equiaxed growth a rapid damping of the flow can already be expected for regions of the mushy zone where the solid fraction reaches values of about 0.4 [14].

22.3.3 Microstructure

The Pb-85wt%Sn alloy shows a microstructure with primary tin-crystallites and eutectic. Specimens solidified without RMF showed a columnar dendritic microstructure which is orientated vertically along the heat flux direction. The tin crystallites and the eutectic are homogeneously distributed over the whole sample.

If the alloy solidifies in a rotating magnetic field the columnar dendrites change their direction of growth into the upstream flow direction. Moreover, a transition from columnar to equiaxed growth (CET) is found (see also figure 9). With the same cooling conditions the vertical position of the CET varies with the Taylor number as shown in figure 10.

Looking at the microstructure in figure 9 it becomes obvious that the amount of eutectic differs significantly between the equiaxed and the columnar region. For a quantitative analysis the volume fraction of primary tin crystals and eutectic was measured at several heights (z-direction) along the axis (r = 0) of the cylindrical ingot. The change of the eutectic fraction in z-direction is displayed in figure 11 for a

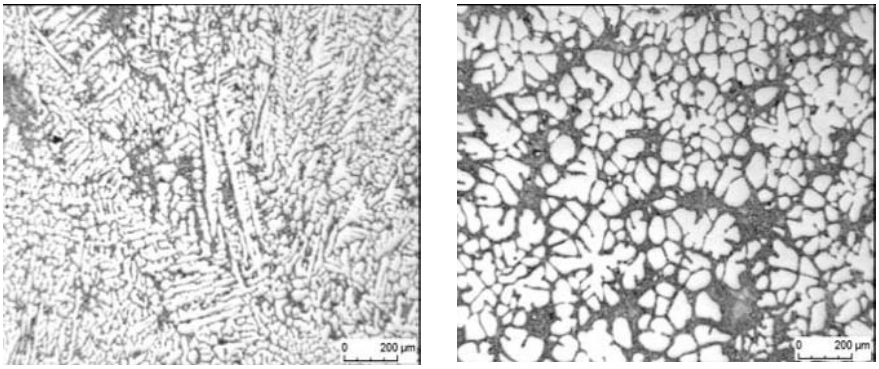

a) b)

Fig. 9 Microstructure of a Pb85 %Sn alloy solidified under the influence of electromagnetic stirring by means of a RMF ($Ta = 8 \cdot 10^6$), a) r = 0, z = 10 mm (below CET), b) r = 0, z = 35 mm (above CET)

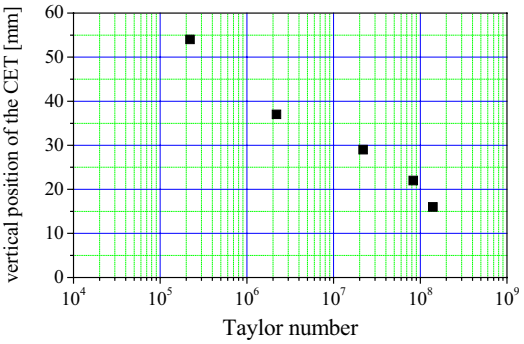

Fig. 10 Position of the CET as function of the magnetic Taylor number *Ta*

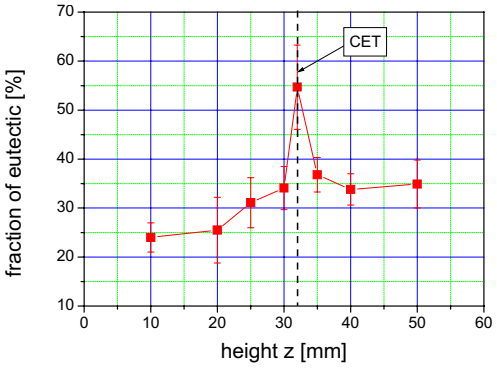

Fig. 11 Volume fraction of the eutectic in the microstructure along the axis of the ingot for $Ta = 8 \cdot 10^6$

Taylor number of $8 \cdot 10^6$. A distinct peak with the highest concentration of eutectic is found at the position of the CET. The eutectic fraction in the equiaxed region is determined to be about 10% higher as found for the columnar structure.

22.4 Discussion, Conclusions

A Pb85%Sn alloy was solidified directionally in a cylindrical mould under the influence of a rotating magnetic field (RMF). The RMF drives a convection in the bulk liquid showing a distinct influence on the solidification parameters and the properties of the microstructure of the ingots. The fluid flow increases the heat transfer rate and decreases the temperature gradients in the melt. Such small temperature gradients reduce the probability of remelting of solid fragments ahead of the solidification front required for the promotion of the CET. Moreover, the temperature measurements also revealed the occurrence of strong temperature fluctuations arising from the turbulent flow in the vicinity of the solidification front. These fluctuations may promote a localized remelting of dendrites and thus the creation of solid fragments.

Velocity measurements have been obtained in the melt during the solidification process with applied RMF by means of UDV. The occurrence of a bulk flow can be observed even if the temperature falls below the liquidus isotherm. However, the strong decrease of the velocity amplitude indicates an rapid increase of the fluid viscosity due to an increase of the solid fraction. The position where the velocity becomes zero can be approximately identified with the position of the solidification front as long as a columnar front grows.

If the ingot is solidified under the influence of forced bulk flow induced by RMF a CET can be observed. The CET position is also affected by the convection. An enhancement of the magnetic Taylor number *Ta* results in a reduction of the length of the columnar region.

The distribution of the eutectic in the microstructure is not homogeneous. In the equiaxed domain an up to 10% higher eutectic content is observed as compared to the columnar region. The highest concentration of eutectic is found directly at the CET position.

The described phenomena are currently under investigation. A more detailed account will be published elsewhere.

Acknowledgement

The research is supported by the Deutsche Forschungsgemeinschaft (DFG) in form of the SFB 609 "Electromagnetic Flow Control in Metallurgy, Crystal Growth and Electrochemistry". This support is gratefully acknowledged by the authors.

References

[1] G.S. Cole, G.F. Boiling, Trans. Met. Soc. AIME 1966, 236, 1366–1368

[2] W.C. Johnston, G.R. Kofler, S. O'Hara, H.V. Ashcom, W.A. Tiller, Trans. Met. Soc. AIME 1965, 233, 1856–1860

[3] C. Vives, Hydrodynamic, Int. J. Heat Mass Transfer 1990, 33, 2585–2598

[4] W.D. Griffiths, D.G. McCartney, Mat. Sci. Techn. 1996, A216 , 47–60

[5] P.J. Prescott, F.P. Incropera, D.R. Gaskell, Exp. Heat Trans. 1996, 9, 105–131

[6] P. A. Davidson, J.C.R. Hunt, J. Fluid Mech. 1987, 185, 67–106

[7] I. Grants, G. Gerbeth, J. Fluid Mech. 2001, 431, 407–425

[8] Y.M. Gelfgat, J. Priede, Magnetohydrodynamics 1995, 31, 188–200

[9] R.U. Barz, G. Gerbeth, U. Wunderwald, E.Buhrig, Y.M. Gelfgat, J. Crystal Growth 1997, 180, 410–421

[10] A. Cramer, S. Eckert, Ch. Heinzelmann, D. Lampe, G. Gerbeth, 4th Int. Conference on Electromagnetic Processing of Materials EPM 2003, Forum Editions, Lyon (France)

[11] Ch.-A. Gandin, Acta mater. 2000, 48, 2483–2501

[12] Y. Takeda, Nucl. Eng. Design 1991, 126, 277–284

[13] S. Eckert, G. Gerbeth, V.I. Melnikov, Exp. Fluids 2003, 35, 381–388

[14] M.C. Flemings, Metall. Trans. 1991, 22 b, 269–293

23
Grain Sedimentation and Melt Convection Phenomena During Globular Equiaxed Solidification

M. Wu, A. Ludwig and A. Bührig-Polaczek

23.1
Introduction

Grain sedimentation and melt convection play very important roles in the solidification and macrostructure evolution, especially in the presence of free-moving grains. A new and promising multiphase model based on the volume-averaging theorem was developed by Beckermann's group [1–7] to calculate the velocity fields of both liquid and moving solid phases explicitly. This model was further modified by Ludwig et al for the globular equiaxed solidification [8–13], and the spatial phase separation phenomenon during hypermonotectic solidification [14–16], where two unmixable liquid phases appear before solidification starts.

In this multiphase model different phases appearing during solidification are explicitly treated as separate interpenetrating continua, the transport equations (mass, momentum, energy and solute) for each phase are established and solved simultaneously, thereby it permits a rigorous description of phase velocities, interactions, thermal and constitutional non-equilibrium, and many other microscopic phenomena between the phases.

With the multiphase model an aluminum ingot (plate) casting with alloy Al-Cu4Mg1Ti0.5 is here simulated. As shown in Figure 1, evaluation effort is made by comparing the numerical simulation with the experiment. As part of an interdisciplinary research project "Integral Materials Modeling" in the frame of the Collaborative Research Center SFB 370 (Germany), the goal of the solidification simulation is to predict the grain size distribution and macrosegregation of the casting, and these information will serve as initial condition for the downstream process simulations i.e. homogenization treatment and forming [17]. The emphasis of the recent paper is placed on the influence of grain sedimentation and melt convection on the grain size distribution and macrosegregation formation after casting.

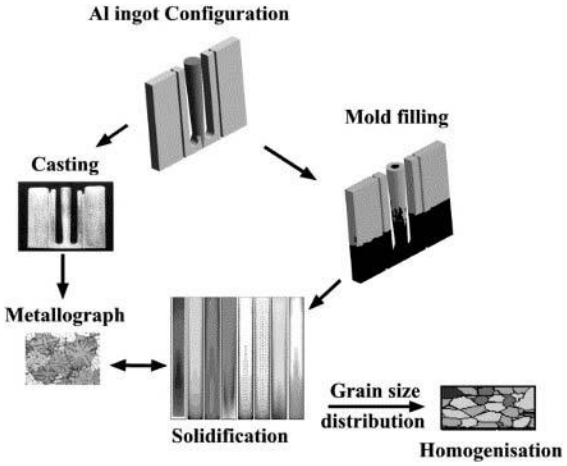

Fig. 1 Integral simulation procedure for an aluminum casting. Casting trials are made to evaluate the simulation results. The numerically predicted grain size distribution is further transferred to the subsequent homogenization simulation procedure.

23.2
Brief Description of the Numerical Model

The conservation equations, source terms, exchange terms and some auxiliary terms used for modeling the aluminum plate casting are shown in Table 1. Only two phases (liquid and solid) and two components (Al and Cu) are modeled. In the Al-Cu4Mg1Ti0.5 alloy system Ti acts as grain refiner, influencing significantly the nucleation parameters, hence by choosing the nucleation parameters the function of Ti can be taken into account. Mg has strong influence on the precipitation of the third phase, but not so obvious on the grain size evolution, hence it is assumed that ignoring the Mg does not influence the grain evolution significantly. We do not treat the stationary grains and free-moving grains as separate phases by assuming that the 'viscosity' of the solid phase (dispersedly distributed grains) as function of volume fraction of solid [8]. As local fraction solid is less than packing limit ($f_s \leq 0.637$), the grains are allowed to move, but beyond the packing limit the solid phase becomes rigid.

The liquid and solid phases are transported according to the mass conservation Eq. (1), taking solidification into account through a mass transfer term M_{ls} ($= -M_{sl}$), which is defined in Eq. (7). The volume fractions of both phases are subject to $f_l + f_s = 1$. Momentum exchange $\bar{U}_{ls}$ ($= \bar{U}_{sl}$) in Eq. (2) consists of two parts: one due to mass transfer $\bar{U}_{ls}^{p}$ and the other due to drag force $\bar{U}_{ls}^{d}$. Details about the drag force model are given elsewhere [8, 12]. The solute concentration in the liquid and solid are calculated by solving Eq. (3). The solute partitioning at the liquid-solid interface due to phase change C_{ls}^{p} is taken into account, while the solute diffusional exchange at the liquid-solid interface C_{ls}^{d} is neglected. A mix concentration c_{mix} is defined in

Tab. 1 Conservation equations, source and exchange terms and auxiliary equations for the numerical model of globular equiaxed solidification

Conservation equations

Mass:

$$\frac{\partial}{\partial t}\left(f_l\,\rho_l\right)+\nabla\cdot\left(f_l\,\rho_l\,\vec{u}_l\right)=M_{sl} \tag{1}$$

$$\frac{\partial}{\partial t}\left(f_s\,\rho_s\right)+\nabla\cdot\left(f_s\,\rho_s\,\vec{u}_s\right)=M_{ls}$$

Momentum:

$$\frac{\partial}{\partial t}\left(f_l\,\rho_l\,\vec{u}_l\right)+\nabla\cdot\left(f_l\,\rho_l\,\vec{u}_l\otimes\vec{u}_l\right)=-f_l\,\nabla p+\nabla\cdot\bar{\bar{\tau}}_l+f_l\,\rho_l\,\vec{g}+\vec{U}_{sl} \tag{2}$$

$$\frac{\partial}{\partial t}\left(f_s\,\rho_s\,\vec{u}_s\right)+\nabla\cdot\left(f_s\,\rho_s\,\vec{u}_s\otimes\vec{u}_s\right)=-f_s\,\nabla p+\nabla\cdot\bar{\bar{\tau}}_s+f_s\,\rho_s\,\vec{g}+\vec{U}_{sl}$$

$$\text{where } \bar{\bar{\tau}}_l=\mu_l f_l\left(\nabla\otimes\vec{u}_l+\left(\nabla\otimes\vec{u}_l\right)^T\right) \text{ and } \bar{\bar{\tau}}_s=\mu_s f_s\left(\nabla\otimes\vec{u}_s+\left(\nabla\otimes\vec{u}_s\right)^T\right)$$

Species:

$$\frac{\partial}{\partial t}\left(f_l\,\rho_l\,c_l\right)+\nabla\cdot\left(f_l\,\rho_l\,\vec{u}_l\,c_l\right)=\nabla\cdot\left(f_l\,\rho_l\,D_l\,\nabla c_l\right)+C_{sl} \tag{3}$$

$$\frac{\partial}{\partial t}\left(f_s\,\rho_s\,c_s\right)+\nabla\cdot\left(f_s\,\rho_s\,\vec{u}_s\,c_s\right)=\nabla\cdot\left(f_s\,\rho_s\,D_s\,\nabla c_s\right)+C_{ls}$$

Enthalpy:

$$\frac{\partial}{\partial t}\left(f_l\,\rho_l\,h_l\right)+\nabla\cdot\left(f_l\,\rho_l\,\vec{u}_l\,h_l\right)=\nabla\cdot\left(f_l\,k_l\,\nabla\cdot T_l\right)+Q_{sl} \tag{4}$$

$$\frac{\partial}{\partial t}\left(f_s\,\rho_s\,h_s\right)+\nabla\cdot\left(f_s\,\rho_s\,\vec{u}_s\,h_s\right)=\nabla\cdot\left(f_s\,k_s\,\nabla\cdot T_s\right)+Q_{ls}$$

$$\text{where } h_l=\int_{T_{ref}}^{T_l} c_{p(l)}\,dT+h_l^{ref} \quad \text{and} \quad h_s=\int_{T_{ref}}^{T_s} c_{p(s)}\,dT+h_s^{ref}$$

Grain transport:

$$\frac{\partial}{\partial t}n+\nabla\cdot\left(\vec{u}_s\,n\right)=N \tag{5}$$

Source terms:

Nucleation:

$$N=\frac{d\,\Delta T}{dt}\cdot\frac{n_{\max}}{\sqrt{2\,\pi}\cdot\Delta T_\sigma}\cdot e^{-\frac{1}{2}\left(\frac{T-T_N}{T_\sigma}\right)^2} \tag{6}$$

Exchange terms

Mass transfer:

$$M_{ls}=g_\alpha\cdot\Delta c\cdot\left(n\cdot\pi\,d_s^2\right)\cdot\rho_s\cdot f_l \tag{7}$$

Momentum:

$$\vec{U}_{ls}=\vec{U}_{ls}^{\,d}+\vec{U}_{ls}^{\,p} \qquad \vec{U}_{ls}^{\,p}=\vec{u}^*\cdot M_{ls} \qquad \vec{U}_{ls}^{\,d}=K_{ls}\left(\vec{u}_l-\vec{u}_s\right) \tag{8}$$

Species:

$$C_{ls}=C_{ls}^d+C_{ls}^p \qquad C_{ls}^p=c^*\cdot M_{ls} \qquad C_{ls}^d \text{ neglected} \tag{9}$$

Enthalpy:

$$Q_{ls}=Q_{ls}^d+Q_{ls}^p \qquad Q_{ls}^p=h^*\cdot M_{ls} \qquad Q_{ls}^d=H^*\cdot\left(T_l-T_s\right) \tag{10}$$

Auxiliary terms

Mix concentration:

$$c_{mix}=\frac{c_l\cdot\rho_l\cdot f_l+c_s\cdot\rho_s\cdot f_s}{\rho_l\cdot f_l+\rho_s\cdot f_s} \tag{11}$$

Grain diameter:

$$d_s=\left(\frac{6\cdot f_s}{\pi\cdot n}\right)^{\frac{1}{3}} \tag{12}$$

Solid viscosity:

$$\mu_s=\begin{cases}\dfrac{\mu_l}{f_s}\cdot\left(\left(1-f_s/f_s^c\right)^{-2.5\cdot f_s^c}-\left(1-f_s\right)\right) & \text{when } f_s<f_s^c\\ \infty & \text{else}\end{cases} \tag{13}$$

Eq. (11) to describe the macrosegregation. The enthalpy conservation Eq. (4) for both phases are also solved separately, hence we get two different temperatures T_l and T_s. With a relatively large diffusional heat exchange term C_{ls}^d between the liquid and solid phases, the temperature difference can be leveled out, and an thermal equilibrium ($T_l \approx T_s$) is obtained. The enthalpy difference ($h_l - h_s = \Delta h_f$) defines the latent heat. Details to handle the latent heat in this model is also described previously [8, 12]. An additional conservation Eq. (5) is solved to obtain the grain density distribution n. The grains are transported according to $\bar{u}_s$. An empirical 3-parameter nucleation law Eq. (6) is used [18]. With the known n and f_s, the averaged grain size d_s is estimated by Eq. (12).

The conservation equations are solved with a control-volume based finite difference method by using a CFD solver FLUENT (Fluent Inc, USA) version 4.5.6. The exchange and source terms are defined with the user defined subroutines, which are compiled into the main solver FLUENT. As simulation results all the necessary volume-averaged variables describing the globular equiaxed solidification are obtained: temperature T and constitutional undercooling ΔT, nucleation rate N, grain density n and grain size d, grain movement velocity and melt convection velocity $\bar{u}_l$, concentrations in solid phase c_s and liquid phase c_l.

23.3 Experimental procedure

The castings with the same configuration as Figure 1 were cast in a steel die. The pouring temperature is 700 °C, and the mold preheating temperature is 300 °C.

In order to investigate the grain size distribution, samples at different positions along the casting central line were taken (Figure 2 a), and metallurgically analyzed. With Baker etching the grain size distribution can be obtained under light optical microscope. Across the section of the plate, a photo series were made. With the computer graphic processing technique all the photo series were put together. A typical micrograph across the section from one casting surface to another surface at position 2# is shown in Figure 2 b). The average grain sizes at intervals of 2 mm were manually measured. Around each measure point, 10 artificial grains were selected, measured, and finally an averaged value was used to represent the grain size at the corresponding point. A typical experimentally measured grain size distribution at position 2# was shown in Figure 2 c). The measured grain size distribution shows finer grains in the central region, and coarser grains near the surface region. The same casting section is also energy dispersive X-ray (EDX) analyzed for macrosegregation.

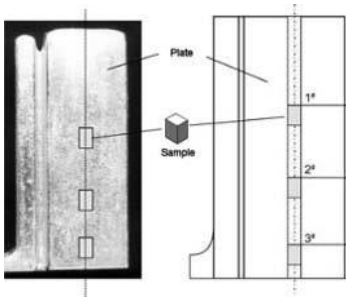

a) Metallographical samples

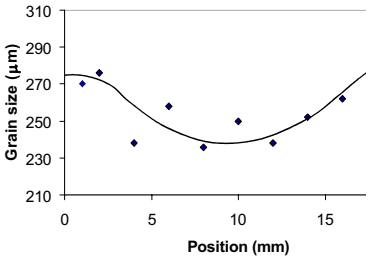

c) Measured grain size distribution

b) Micrograph across the section

Fig. 2 Typical micrograph and the measured grain size distribution across the section of the plate casting (AlCu4Mg1Ti0.5) at the sample position 2#.

23.4 Results and discussions

A 3D mold filling simulation is made with MAGMASOFT (MAGMA Gießereitechnologie GmbH, Germany) to provide the initial condition for the solidification simulation. The temperature distribution across the central section of the plate is predicted to be relatively uniform. The temperature of the most part of the cross section lies between 651 and 654 °C, i. e. a few degrees above the liquidus (651 °C).

Due to the high calculation cost the solidification simulation with the multiphase model is carried out in 2D in the central cross section of the plate (20×164 mm^2). The thermal physical and thermodynamic properties refer to alloy Al-4.0wt%Cu [8].

The typical simulation results are shown in Figure 3–4. With the start of cooling, temperature at the casting surface drops quickly down below the liquidus, and the grains nucleate on the casting surface. Because of the higher density of the solid, the grains sink along the mold wall. The sinking grains drag the surrounding melt together with them. The melt at the bottom region moves inwards and then rises up, providing space for the oncoming grains and melt. Consequently, two vortices forms. In return the vortices have a strong impact on the movement (transport) of the grains. The movement of the grains leads to an increase of the fraction solid f_s in the lower regions. Here the packing limit ($f_s^c = 0.637$) is quickly exceeded and the grain movement is stopped. This phenomenon is known as grain settlement or sedimentation. The grain movement and sedimentation influence the solidification sequence. As shown in Figure 4, grains pile up in the bottom, and the f_s isolines proceeds upwards.

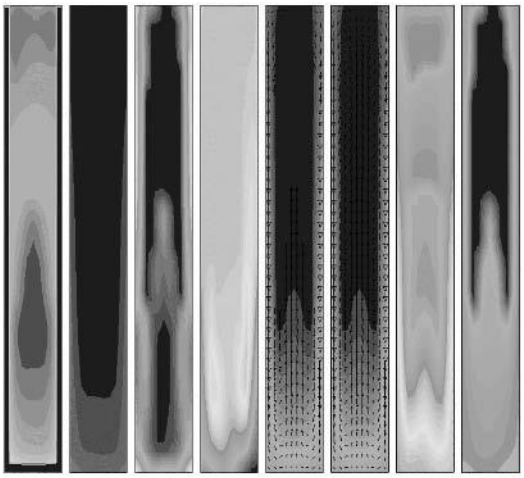

Fig. 3 Results of a simulation 7 s after the cooling has started. The arrows of both velocity fields are continuously scaled starting from zero to the maximal value given. All other quantities are scaled equidistantly by 30 colors, with blue representing the lowest and red the highest value.: T: 900~919 K, c_l: 0.04~0.2, M_{ls}: –1.7~227 kg/m^3/s, c_{mix}: 0.037~0.042, f_s: 0~1, $\vec{u}_s$: 0~21 mm/s, $\vec{u}_l$: 0~20 mm/s,n: 0~130 mm^{-3}, d_s: 0~0.37 mm.

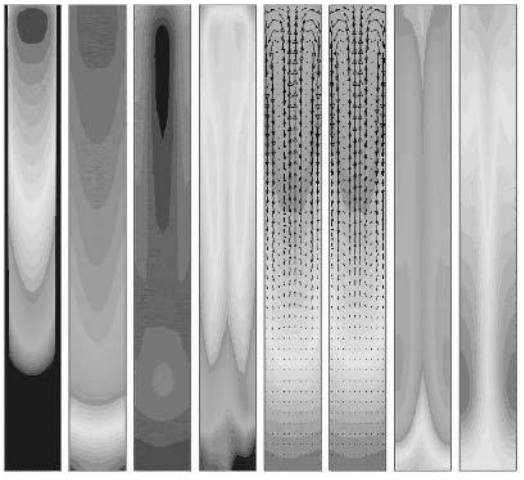

Fig. 4 Results of a simulation 50 s after the cooling has started. The arrows of both velocity fields are continuously scaled starting from zero to the maximal value given. All other quantities are scaled equidistantly by 30 colors, with blue representing the lowest and red the highest value.: T: 900~919 K, c_l: 0.04~0.2, M_{ls}: –1.7~227 kg/m^3/s, c_{mix}: 0.037~0.042, f_s: 0~1, $\vec{u}_s$: 0~5 mm/s, $\vec{u}_l$: 0~5 mm/s, n: 0~130 mm^{-3}, d_s: 0~0.37 mm.

The macrosegregation is quantitatively described with a mixture concentration c_{mix}. The negative macrosegregation (c_{mix} smaller than the gross concentration 4.0wt%Cu) is the direct outcome of the grain sedimentation. Near the side walls, the solute-poor grains sink downwards, and settle in the bottom region, resulting in negative segregation. On the other hand the solute-enriched melt is carried by the flow current into the center of the vortex, which move gently upwards with solidification proceeds. Therefore, positive segregation (c_{mix} larger than the gross concentration 4.0wt%Cu) is predicted in the upper part of the casting.

Both the grain movement and the melt current have strong impact on the grain density and grain size distributions. The final grain size distribution are predicted as shown in Figure 5 a). As mentioned above, grains nucleated near the wall sink to the bottom region, and sedimentation occurs there. Therefore, in the bottom region there are high grain density n, and grains are fine. Some grains in the bottom region, however, are brought to the casting central region by the current. Because the temperature T in the central region is higher than the surface region, the mass transfer rate M_{ls} is lower in the central region. Therefore, grains which are brought to the central region grow rather slowly, some of them are even re-melted there. The grains in the central region are finer than the surface region. It is also noticed that there are two large grain zones near the casting surface about 30 mm above the bottom. The grains near the upper regions sink along the mold wall. In the mean time they grow while sinking. In the late stage of solidification, as they reach the lower region they become relatively large. As the local packing limit is exceeded, they settle there.

Comparison of the numerically predicted and the experimentally measured grain size distribution is made (Figure 5b–c). The grain size distributions of the experiment and the simulation show a reasonable agreement. At the position 2# and 3#, both experiment and simulation show that large grains near the casting surface and fine grains in the central region. At the position 1#, a 'M' curve distribution is observed in both the numerical simulation and the experiment.

The casting is EDX analyzed. The experimentally measured data on macrosegregation are relatively scatter. It is difficult to fit the experimental data to the numerical results quantitatively. However, the measured result shows the same tendency as the simulation. There is a lower concentration in casting bottom region and a higher concentration in top region.

The variation amplitude of the grain size in the experiment, especially in the casting central region, is not so large as predicted by the simulation. The absolute value of the grain size is numerically predicted 262~390 μm, but the experimentally measured value lies between 230 ~ 300 μm. One reason for this quantitative difference is the inaccurate parameters used for the simulation. For example, nucleation parameters in Eq. (6) were empirically given: $n_{\max} = 1.5 \cdot 10^{12}\,\mathrm{mm}^{-3}$, $\Delta T_\sigma = 8\,\mathrm{K}$, $\Delta T_N = 20\,\mathrm{K}$. According to Rappaz et al [18], reliable nucleation parameters must be determined experimentally by measuring the grain density (i. e. the grain size) and the corresponding maximum undercooling at recalescence, $\Delta T_{\max}$. Other reasons are the model assumptions and simplifications. For example, only sedimentation-induced flow is recently considered, the thermo-solutal convection and feeding flow are not included; the multi-component system is simplified as a binary system; the recent simulation is car-

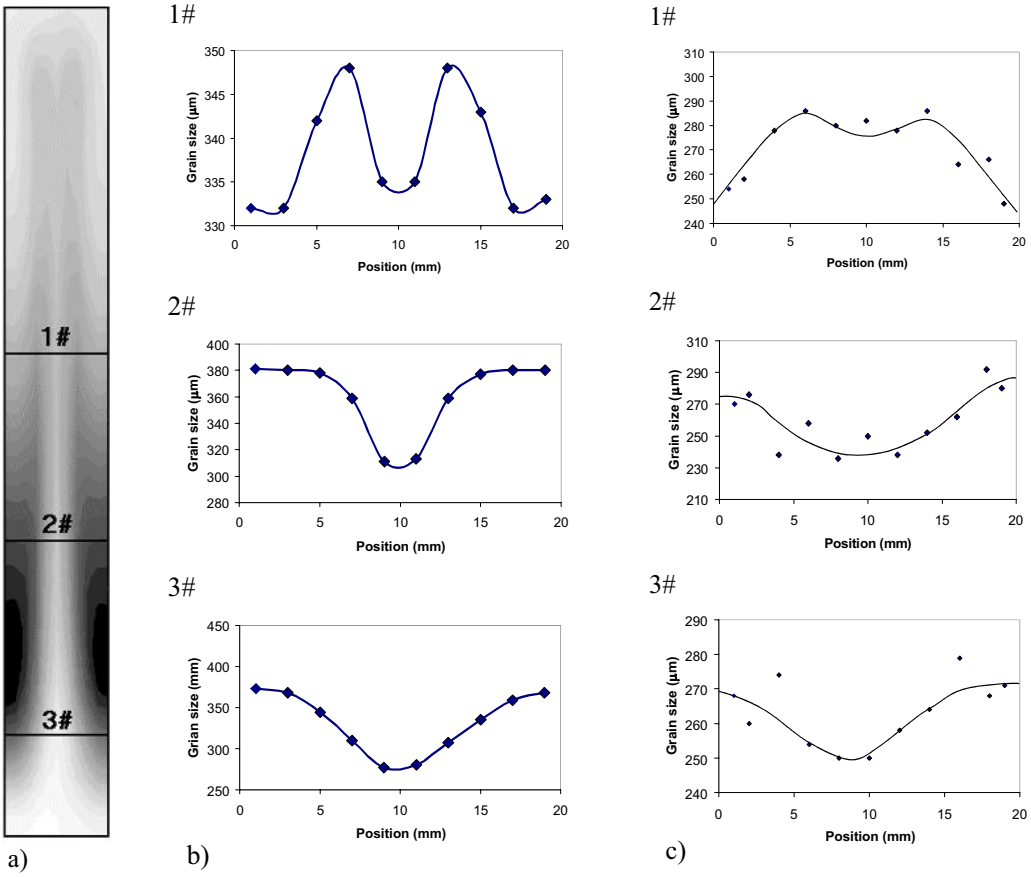

Fig. 5 Comparison of the numerically predicted grain size distribution to the experimentally measured results. a) Simulated grain size distribution, scaled equidistantly by 30 colors, with light representing the smallest (262 µm) and dark the largest (390 µm) grains; b) Simulated grain size distribution across the section; c) Experimentally measured grain size distribution across the section.

ried in 2D instead of 3D. Therefore, further studies are necessary to improve the simulation accuracy.

23.5 Conclusions and outlook

A two-phase volume averaging model for the globular equiaxed solidification considering grain movement and melt convection is applied to simulate an aluminum plate casting. The simulation result is evaluated by comparing with the experiment.

Reasonable agreement was obtained between the numerically predicted grain size distribution and the experimentally measured one. The EDX-analyzed macrosegregation shows the same tendency as the simulation. Understanding to the grain evolution and macrosegregation formation under the influence of grain sedimentation and melt convection is achieved.

In order to improve the simulation accuracy further studies are suggested: e. g. to obtain reliable modeling parameters, to include thermo-solutal convection and feeding flow, to deal with multi-components and use 3D calculation.

Acknowledgments

Financial support for this research has been provided by the German Science Foundation (DFG) as part of the Collaborative Research Centers SFB 370.

References

[1] C. Beckermann and R. Viskanta, *Appl. Mech. Rev.* **1993**, 46, 1–27.

[2] J. Ni and C. Beckermann, *Metall. Trans.* B **1991**, 22B, 349–361.

[3] C.Y. Wang and C. Beckermann, *Metall. Mater. Trans.* A **1996**, 27A, 2754–2764.

[4] C.Y. Wang and C. Beckermann, *Metall. Mater. Trans.* A **1996**, 27A, 2765–2783.

[5] C.Y. Wang and C. Beckermann, *Metall. Mater. Trans.* A **1996**, 27A, 2784–2795.

[6] C. Beckermann, *JOM* **1997**, 49, 13–17.

[7] A.V. Reddy and C. Beckermann, *Metall. Mater. Trans.* B **1997**, 28B, 479–489.

[8] A. Ludwig, M. Wu, *Metall. Mater. Trans. A* **2002**, 33A, 3673–3683.

[9] A. Ludwig, G. Ehlen, M. Pelzer, P.R. Sahm in Proceedings of 9th Int. Conf. on McWASP-IX (Ed.: P.R. Sahm et al), Shaker Verlag, Aachen, Germany, **2000**, 175–182.

[10] A. Ludwig and M. Wu in Proceedings of "Modellbildung und Simulation in der Werkstoff-, Schweiß- und Umformtechnik"(Ed.: H. Cerjak), TU-Graz, Austria, **2003**, 11–20.

[11] M. Wu and A. Ludwig, *Adv. Eng. Mater.*, **2003**, 5, 62–66.

[12] M. Wu, A. Ludwig, A. Bührig-Polaczek, M. Fehlbier, P.R. Sahm, *Int. J. Heat Mass Transfer.*, **2003**, 46, 2819–32.

[13] M. Wu, A. Ludwig, P.R. Sahm and A. Bührig-Polaczek in Proceedings of 10th Int. Conf. on McWASP-X(Ed.: D. Stefanescu et al), TMS Publication, Warrendale, PA, **2003**, 261–268.

[14] M. Wu, A. Ludwig and L. Ratke, *Modell. Simul. Mater. Sci. Eng.*, **2003**, 11, 755–769.

[15] M. Wu, A. Ludwig and L. Ratke in Proceedings of 10th Int. Conf. on McWASP-X (Ed.: D. Stefanescu et al), TMS Publication, Warrendale, PA, **2003**, 141–148.

[16] M. Wu, A. Ludwig and L. Ratke, *Metall. Mater. Trans.* A, **2003**, 34A, 3009–3019.

[17] L. Neumann, R. Kopp, M. Wu, A. Bührig-Polaczek, M. Schneider, G. Gottstein and A. Ludwig, *Modell. Simu. Mater. Sci. Eng.*, **2003**, in press.

[18] M. Rappaz, Int. Mater. Rev., **1989**, 34, 93–123.

24
Metastable Primary Soldification Modes in the Fe-Cr-Ni System During Laser Welding

H. Schobbert, Th. Böllinghaus, M. Wolf

Abstract

Austenitic stainless steels widely used in industry have been examined regarding their hot cracking resistance with respect to their short-term metallurgical behaviour during laser welding. The results demonstrate for a series of materials with a chemical composition located on the ferritic side near the eutectic rim in the Fe-Cr-Ni system, that they might exhibit a change to a metastable austenitic primary solidification under conditions of rapid solidification which adversely affects their hot cracking resistance. This effect is considerably enhanced by potential nitrogen pick-up during welding. As a specific item, it turned out that also a metastable ferritic crystallization can occur in undercooled austenitic melts, due to the specific kinetics during laser welding. Additionally, laser weld pool geometries have been modelled by an approach based on the relation between the solidification rate as determined from respective transverse sections and the weld pool shape.

24.1
Introduction

Innovative laser processes and also arc-coupled hybrid welding are attracting growing industrial attention for an enhanced fabrication of austenitic stainless steel components. A fundamental aspect for component fabrication with the help of such processes is that the welds are produced largely without any imperfections. In this respect, hot cracks must be regarded as a most critical factor comprising the risk of strongly restricted weldability. Since the hot cracking susceptibility of materials in the Fe-Cr-Ni system is substantially determined by the type of primary solidification, a deeper understanding of the specific short-term metallurgical microstructures formed during welding using high-power radiation sources is required. For this reason, the primary solidification mode change during laser welding of specific austenitic stainless steels and its effects on hot cracking are highlighted in the present contribution.

In this respect, the distance of a respective Fe-Cr-Ni melt to the eutectic rim while reaching the liquid/solid transition phase during cooling has to be considered as well as the fact that such alloys are subdivided into areas of primary ferritic and primary austenitic solidification depending on their location to the eutectic rim. Austenitic stainless steels on the ferritic side at first reach the liquidus temperature of the body-centered cubic crystal during cooling which means ferritic phase selection. The liquidus point of an austenitic transition phase which has to be regarded as metastable ranges at lower temperatures and thus, cannot be reached by a melt without undercooling. Such phenomena reversely apply to the austenitic side for the face-centered cubic crystallization, i. e. to the other side of the eutectic rim.

However, in the case of rapid solidification occurring during beam welding of austenitic steels near the eutectic rim, specific metallurgical short-term mechanisms have to be considered [1, 2], in particular the kinetic undercooling and the supersaturation of the melt ahead of the liquid/solid interface. The interface response function [3] for a given temperature gradient describes the growth temperature of the possible morphologies. It has to be considered that during solidification the metastable phase, as for instance the γ-mixed crystal, might compete with the stable phase, represented by the δ-mixed crystal. Following the considerations of Kurz [2], that phase will be formed which solidifies at the highest liquid solid interface temperature. This is one explanation for a primary ferritic solidification altering into an austenitic one at high solidification rates under the presumption that the nucleation for such a process is not impeded. It has also to be assumed, however, that weld pools provide a sufficient number of nuclei to initiate or change, respectively, the solidification mode.

24.2
Ferrite – Austenite Type of Primary Solidification Change

In order to investigate to what extent austenitic stainless steels change their solidification mode based on short-term metallurgical effects, remelting experiments were carried out with the alloys listed in Table 1 using a 6 kW CO_2 laser as well as the tungsten inert gas (TIG) process [4]. The welding power and speed were selected under the presumption that the solidification rate is the decisive process parameter influencing the primary solidification mode being identified by respective colour etched weld cross sections. It turned out that the investigated heats of the austenitic stainless steels AISI 304L (1.4306), 309 (1.4828) and 316L (1.4404) tend to change their solidification from the primary ferritic to the primary austenitic mode during laser welding at low heat inputs, i. e. at high solidification rates. For the material AISI 316 Ti (1.4571) no change was found. Microstructures with respective primarily solidified austenitic portions can be distinguished by their light colour and thus, can be evaluated quantitatively in the cross sections, as shown for the materials AISI 304L and 309 in Figure 1. It turned out that the size of these portions increases with the welding speed. At high welding speeds and low penetration depths, weld metals with almost complete primary austenitic microstructure are produced. To the dia-

Tab. 1 Chemical composition of the test materials [wt-%] (kinetic phase selection)

Material	*Thickness [mm]*	*C*	*Si*	*Mn*	*P*	*S*	*Cr*	*Ni*	*Mo*	*Ti*	*Nb*	*N*	*Cu*
1.4306 (304L)	6	0.019	0.354	1.355	0.026	0.001	17.88	10.10	0.375	0.013	0.013	0.044	0.299
1.4404 (316L)	2	0.038	0.275	1.300	0.028	0.002	15.94	10.26	1.950	0.025	0.001	0.040	0.230
1.4571 (316Ti)	2	0.049	0.410	1.100	0.030	0.002	15.93	9.82	1.950	0.360	0.006	0.040	0.230
1.4571 (316Ti)	2.5	0.039	0.524	1.236	0.024	0.001	16.39	10.62	1.946	0.491	0.020	0.014	0.230
1.4571 (316Ti)	5	0.034	0.574	1.034	0.024	0.003	16.34	10.61	1.981	0.288	0.019	0.021	0.260
1.4571 (316Ti)	6	0.038	0.430	1.187	0.027	0.001	16.52	10.59	2.047	0.379	0.021	0.014	0.239
1.4828 (309)	3	0.054	1.907	0.674	0.023	0.002	18.93	10.81	0.223	0.013	0.012	0.044	0.098

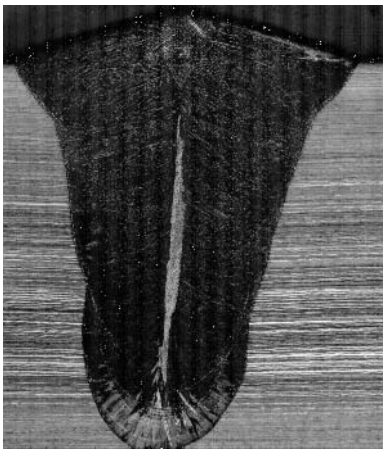

a)

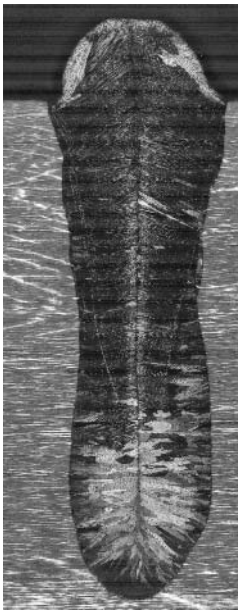

b)

Fig. 1 Cross section of austentitic stainless steel welds showing a change of the primary solidification mode by primary ferritic (dark) to primary austenitic (light) cells in the weld metal. a) AISI 309 steel, plate thickness: s = 3 mm, laser power: P_L = 3 kW, speed: V_s = 3 m/min, focal point: Δf = –1 mm, gas pressure: p_{He} = 0.5 bar; b) AISI 304L steel, plate thickness: s = 6 mm, laser power: P_L = 10 kW, speed: V_s = 10 m/min, focal point: Δf = –1 mm, gas pressure: p_{He} = 0.5 bar

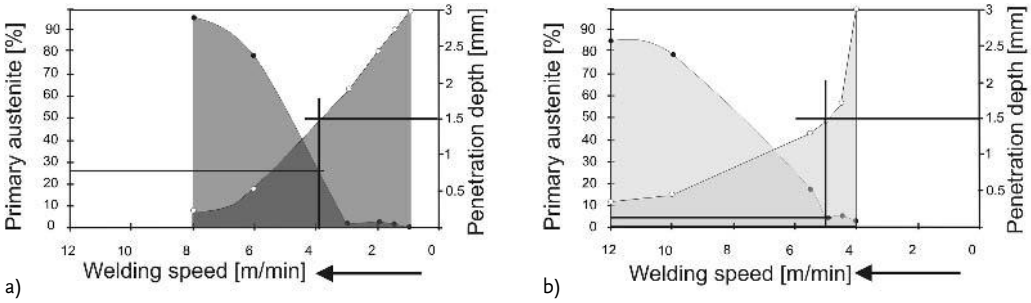

Fig. 2 Portion of primary austenite and penetration depth in the weld metal of the remelted stainless steel AISI 309 dependent on the welding speed and the laser power. a) Laser power: P_L = 2 kW; b) Laser power: P_L = 5 kW

grams in Figure 2, the primary austenitic portions of the entire weld cross section were assigned dependent on the welding parameters and compared with the respective penetration depths. By such diagrams, parameter combinations required for sufficient penetration at a minimum of primary austenite targeted at hot cracking avoidance can be determined. If, for instance, a depth of 1.5 mm is required this can be achieved with a welding speed of about 3.8 m/min at a laser power of P_L = 2 kW, but at a 25 % portion of primary austenite in the weld. In contrast, the same depth can be reached at higher laser power of P_L = 5 kW, reducing the primary austenite amount to 5 % and thus, at a relatively low hot cracking risk.

EDX analyses (Figure 3) demonstrated typical unidirectional segregation in Ni and Cr in microstructure areas with primary austenitic solidification, in contrast to the oppositely directed segregation in the areas with primary ferritic solidification of the parent material. This again evidently shows that the rapid solidification paths and, in particular, the concentrations of the residual melts differ markedly from those predicted by constitutional diagrams. In order to investigate the influence of

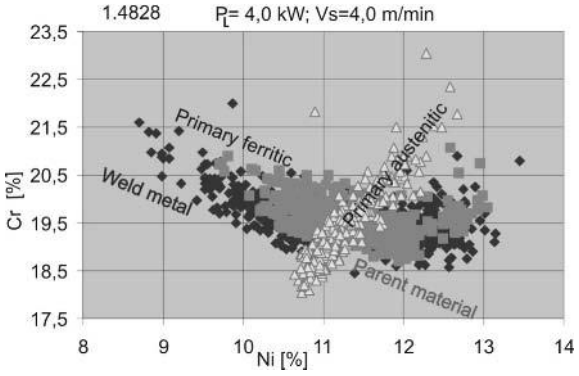

Fig. 3 EDX-microprobe analysis of stable and metastable segregations

Tab. 2 Chemical composition of the test materials [wt-%] (influence of nitrogen)

Nr.	*Material*	*Thickness [mm]*	*C*	*Si*	*Mn*	*P*	*S*	*Cr*	*Ni*	*Mo*	*Ti*	*Nb*	*N*	*Cu*	*V*
1	1.4828 (309)	3.0	0.052	1.645	1.319	0.027	0.007	19.29	10.66	0.197	0.005	0.019	0.024	0.354	0.085
2	1.4828 (309)	3.0	0.053	1.915	0.677	0.024	0.005	18.70	11.02	0.231	0.014	–	0.046	0.098	–
3	1.4828 (309)	3.0	0.050	2.110	0.670	0.024	0.003	19.00	11.00	0.290	0.016	0.013	0.057	0.120	0.017
4	1.4571 (316Ti)	3.0	0.026	0.613	1.749	0.024	0.002	16.80	9.90	2.068	0.305	0.019	0.018	0.214	0.053
5	1.4571	2.5	0.039	0.524	1.236	0.024	0.001	16.39	10.62	1.946	0.491	0.020	0.014	0.230	–

nitrogen, known as an austenite stabilizer, on the solidification mode change [4], nitrogen was added to the process and shielding gas, respectively, during various remelting processes of the materials listed in Table 2. Such nitriding was predominantly performed by laser welding in one, two or three passes, respectively, lying closely side by side. Subsequently, these welds were homogenized by a slow TIG process using argon. Primary austenitic solidification of such homogenized laser welds has to be regarded as a clue for the shift of the composition to the eutectic rim or even beyond and thus, represents an indication for respective nitrogen pick-up. Assuming a stable solidification front, the solidification rate orthogonally to the solidification front versus the weld pool shape is less than/equal to the welding speed (next section). For the discussion of the nitrogen impact it is therefore sufficient to determine the solidification rates dependent on the welding speeds. For the material 1.4828(1), the diagram in Figure 4 shows the influence of nitrogen on the solidification rate necessary for the change of the solidification mode. The base material with a nitrogen content of 0.024 wt % changes the solidification mode from primary ferritic to austenitic at a laser power of 1.5 kW and welding speeds above 0.5 m/min. With higher nitrogen contents and, appreciably greater primary austenitic portions appear which even at an extrapolation to $V_s = 0$, i.e. at slow equilibrium solidification, still differ from zero. Hence, with a nitrogen content of approximately 0.05 wt

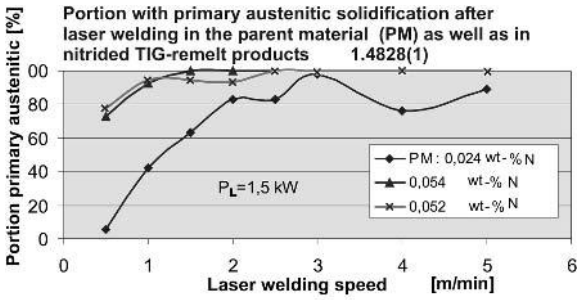

Fig. 4 Influence of the nitrogen content on primary solidification

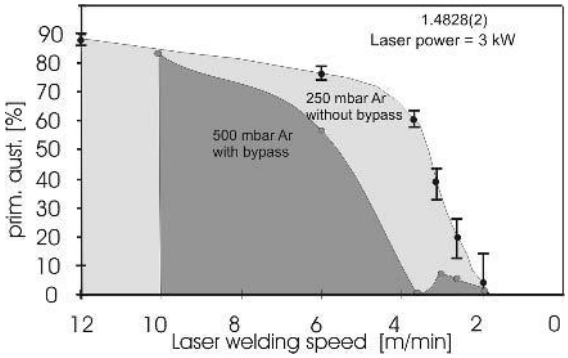

Fig. 5 Effect of air introduced via the welding nozzle

%, this material has an eutectic composition which allows both solidification modes coexisting even in equilibrium without undercooling. From the practical viewpoint undesirable nitrogen pick-up particularly during laser welding might occur, if the process gas is coaxially led to the beam through a welding nozzle and air is sucked in from the beam guidance system. As illustrated in Figure 5, a modification by which process gas overpressure was generated via a bypass at the beam entrance in front of the nozzle to reduce the air entering from the beam guidance system causes a shift of the beginning of the phase change is towards higher welding speeds.

24.3
Geometric Analysis of Solidification Structures

The geometric structures produced during solidification of a melt are affected by a multiple variables given by both the cooling conditions and by epitaxial effects at the solidification front. Rappaz et al. [5], for instance, reported that during remelting processes in single-crystals materials, the crystal orientations of the parent material in the preferred solidification directions conditioned by crystallographic prerequisites, in conjunction with different remelting directions, are distinctly represented in the microstructures of a solidified melt. In the present study aimed at modelling the solidification geometry it is additionally intended to establish a relationship between the solidification rates in various weld metal cross sectional areas and the change of the primary solidification mode. In this context, epitaxial phenomena as well as temperature gradient effects on the change of the solidification mode completely disregarded as a first approach. A perfect solidification front is presumed to be formed under structural orientation conditions that does not affect the solidification process, i.e. permit undisturbed solidification progress into the melt area ortogonally to the front surface. The investigation focuses on a stationary case in which the solidification front constantly advances with consistent geometry in x-direction at a welding speed V_s. Consequently, for the solidification rate V placed perpendicularly on the solidification front, the relationship

$$|V| = |V_S| \cos\theta \tag{1}$$

can be anticipated, where θ is the angle between the solidification rate vector, i.e. between the area normal of the solidification front at the solidification position (x,y,z) and the welding speed. The solidification rate vector is fully given by this angle θ, by the amount V and by the angle φ. φ is the angle between the projection of the solidification rate to the y-z plane and the y-axis:

$$\vec{V} = \begin{pmatrix} V\cos\theta \\ V\sin\theta\cos\varphi \\ V\sin\theta\sin\varphi \end{pmatrix} \tag{2}$$

The shape of the solidification front at the weld surface, i.e. at z = 0, is quite well represented in the so-called end craters and can be dimensioned at these locations. The geometric modelling conditions are illustrated in Figure 6. It is assumed that the x-y contours of the solidification front can be represented by

$$\frac{x^2}{a^2} + \frac{(y-y_0)^2}{b^2} = 1 \qquad b = B - y_0$$

$$M1: \ldots \frac{(B-y_0)^2}{b^2} = 1 \qquad a = A\sqrt{\frac{(B-y_0)^2}{B^2 - 2By_0}} \tag{3}$$

$$M2: \ldots \frac{A^2}{a^2} + \frac{y_0^2}{b^2} = 1 \qquad y_0 = -\left|\frac{B^2}{A\tan\alpha - 2B}\right|$$

$$\tan\alpha = \left.\frac{\partial y}{\partial x}\right|_{x=A}$$

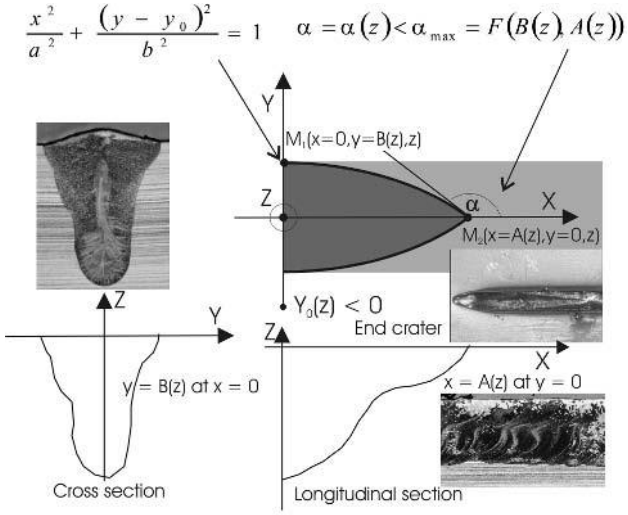

Fig. 6 Geometric modelling of the solidification front

ellipses or segments of ellipses in the sections with z = const. Segments of ellipses are applied to take account of the fact that different weld pool trailing edge sharpnesses are obtained depending on the welding speed. The relationships (3) are true for the ellipse segment. The widths B are measurable in the transverse section. The functions A(z) and $\alpha(z)$, i.e. the weld pool length and edge curvature are first unknown. In order to keep the number of free parameters low, a test function A(z) (in the form of a table) is used to match with the contours appearing in the longitudinal section (Figure 6), with the penetration depth and with the weld pool surface length. The angle $\alpha(0)$ can be measured at the surface at z = 0. Measurements at several end craters reveal for different welding speeds that angles with values near those of the maximum possible angles are always obtained which allow it at given length/width ratios to realize a geometry still with ellipse segments, $\tan(\alpha_{max}) = -\frac{2B}{A}$. For reasons of convergence, a slightly reduced angle $\alpha = \alpha_{max} - \varepsilon$ is inserted into the equations (3).

It is intended to assign to the transverse section positions (y,z) the respective solidification rates V according to the equations (1) and (2), in order to evaluate the angle θ. The solidification front position vector R is given by the equations (3) which can be used to calculate the unit vector e_R of the solidification front area normal. This vector is identical with the unit vector e_V of the solidification rate.

$$\vec{R} = \begin{pmatrix} X(y,z) \\ y \\ z \end{pmatrix} \tag{4}$$

The unit vector of the area normal is derived from (4) with the relationships (3):

$$\vec{e}_R = \frac{\frac{\partial \vec{R}}{\partial z} \times \frac{\partial \vec{R}}{\partial y}}{\left| \frac{\partial \vec{R}}{\partial z} \times \frac{\partial \vec{R}}{\partial y} \right|} = \begin{pmatrix} \frac{1}{\sqrt{1 + X_y^2 + X_z^2}} \\ \frac{X_y}{\sqrt{1 + X_y^2 + X_z^2}} \\ \frac{X_z}{\sqrt{1 + X_y^2 + X_z^2}} \end{pmatrix} \tag{5}$$

From a component by component comparison with the unit vector V/|V| according equation (2), the orientation terms of the solidification rate can be derived:

$$\cos\theta = \frac{1}{\sqrt{1 + X_y^2 + X_z^2}}$$

$$\tan\varphi = \frac{X_z}{X_y} = k1 \tag{6}$$

$$V/V_S = \cos\theta = k \in [0;1] \tag{7}$$

Assuming a fixed value k for the solidification rate/welding speed ratio, these equations constitute a relationship F (y, z) = 0, i. e. they determine a curve in the cross sectional y,z-plane in which the solidification rate corresponds to a predetermined value. When equation (7) is inserted into equation (6) and solved with respect to y, for example, the required set of curves y = y (z, k) are resulting. Such fourth order polynomials can be solved numerically.

The calculated result for a weld on material 1.4828 produced at a welding speed of V_s = 4 m/min using a laser power of 3 kW is illustrated as an example in Figure 7. A limiting curve is plotted for k = 0.3, i. e. with equation (7) for V = 1.2 m/min. In addition, isoplots are shown for some angles φ. Primary austenitic solidification areas (bright) can clearly be identified in the transverse section within the limiting curve k = 0.3, suggesting that the assumption V > 1.2 m/min for a change of primary ferritic to primary austenitic solidification is justified. But the same solidification rate must then also be expected at other welding speeds. Figure 8 shows the solidification front modelling results for a welding speed of 9 m/min, indicating that also in this case the solidification rate V = 1.2 m/min with the associated k = 0.13 yields a good limiting curve for the change of the primary solidification mode. The results confirm that this method of determining the transition rate is, conversely, also a good tool for weld pool shape modelling, even though the important function x = A (z) still consti-

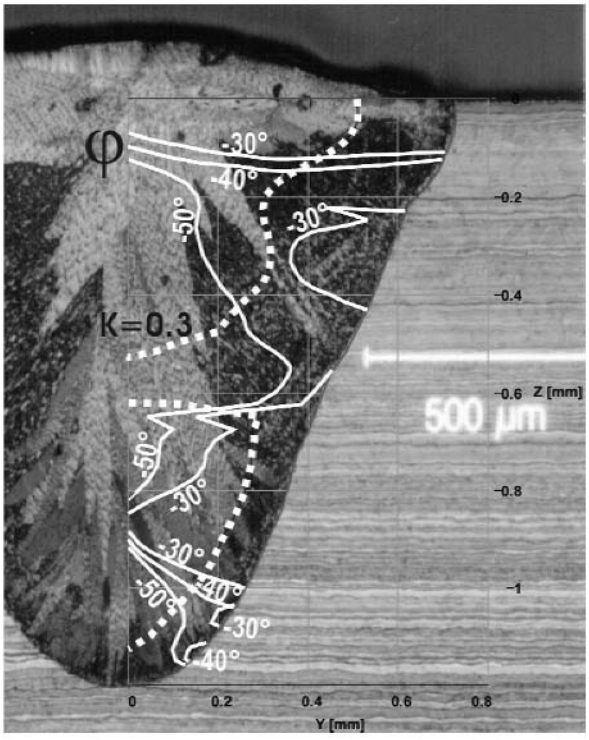

Fig. 7 Example of a calculation: 1.4828, V_S = 4 m/min, P_L = 3 kW

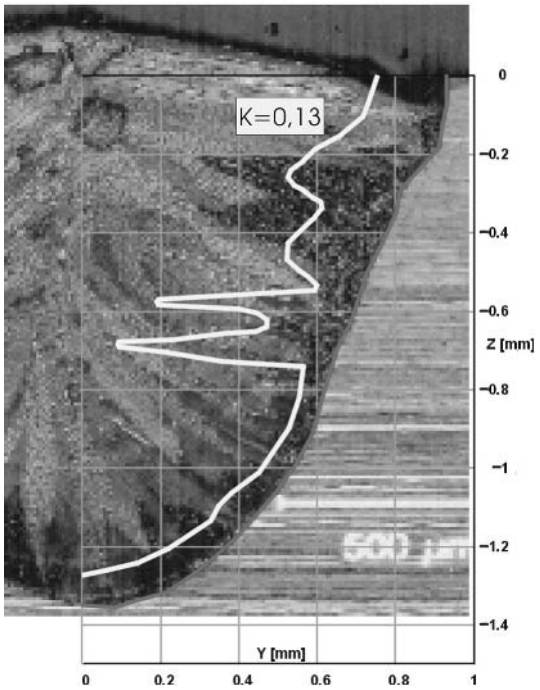

Fig. 8 1.4828, V_S = 9 m/min, P_L = 4.5 kW

tutes a relatively unclear influencing factor. It should be mentioned that the functions y = y(z, k) may, for example, provide information about a turning point in a third order function A(z) in transverse sections, thus permitting also parameter-free back front modelling.

24.4
Metastable States and Epitaxial Effects at the Fusion Line

In the context of a solidification change in laser welding it has to be considered that in the parent material areas adjacent to the fusion line the diffusion-controlled austenite-ferrite transformation in solid state is largely incomplete as a result of the rapid heating processes. Thus, for epitaxial crystallization of the melt, predominantly austenitic nuclei are present at the fusion line. Due to the lack of ferritic nuclei for ferritic equilibrium solidification, the melt may, also in these areas of very low solidification rates, be undercooled and retain this state up to the metastable austenitic solidification area. It can be seen from Figure 9 that primary austenitic borders are formed at the fusion line of material 1.4571, for which no kinetic-specific change of the primary solidification mode was found even at high welding speeds, and which is hence relatively far away from the eutectic rim on the ferritic side. But this austenitic solidification ends after a relatively short time because it is replaced by the ferritic equilibrium solidification enabled by elevated temperatures. In laser welds of materi-

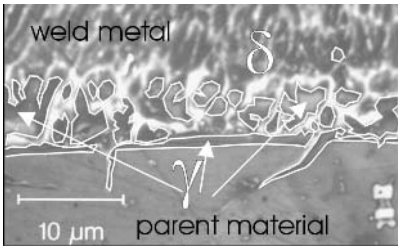

Fig. 9 Primary austenitic border (γ) at the fusion line, 1.4571 (5), V_S = 10 m/min, P_L = 3 kW

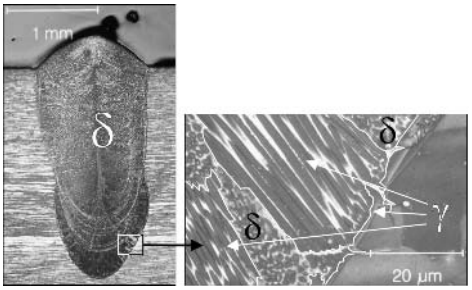

Fig. 10 Epitaxial primary austenitic solidification (γ) at the border, 1.4828(3), V_S = 4 m/min, P_L = 3 kW

als which, by contrast, exhibit a kinetic-specific change of the primary solidification mode, cellular austenitic morphologies may, in case, adjoin an austenitic border at the fusion line and extend over larger areas. Figure 10 illustrates a laser weld for steel 1.4828 with otherwise completely primary ferritic solidification, however with marked primary austenitic zones starting directly at the fusion line. This effect must be considered as critical, particularly in conjunction with smaller isolated hot cracks which cannot be excluded in such areas. If the material to be welded is austenitized by any arising nitrogen pick-up, the epitaxy- and kinetic-specific effects may combine and form pronounced primary austenitic morphologies involving the risk of hot cracking.

24.5
Metastable Ferritic Solidification

The occurrance of metastable ferritic solidification of a austenitic melt has already been confirmed in non-chambered undercooling and quenching experiments, respectively [6, 7]. The fact that the nucleation energy for ferritic crystallization is lower than that for austenitic solidification turned out to be propitious to the crystallization of metastable ferritic states from undercooled melts. It was thus the goal of the present study to elucidate whether such undercooling is reached also in beam welding processes. Accordingly, gradual nitriding and the associated austenitization of a base material with originally ferritic solidification has deliberately been used to create austenitic melts near the eutectic rim to elucidate their solidification behaviour during

rapid kinetic undercooling. The respective investigations were performed with the material 1.4571(4). Two-fold CO_2-laser welding with nitrogen process gas and subsequent homogenizing TIG-overwelding still engenders completely primary ferritic solidified weld metal, as marked by the symbol δ in Figure 11 a. The material nitrided in this way has subsequently been subjected to a further rapidly executed laser weld feeding additional nitrogen to it. This further nitriding entails nearly complete primary austenitic solidification which is marked in Figures 11 a and b by the symbol γ. But, at the end of the weld pool, i. e. in the weld centre (Figure 11 b), large numbers of equiaxed dendritic crystals are formed. These clearly had been identified as primary ferritic solidification products owing to the irregularly enclosed residual ferrites (Figure 11 c). Undercooling and supersaturation, respectively, are confirmed by the equiaxed dendritic morphology and, in particular, the undercooling is so pronounced that it allows equiaxial dendritic crystallization. Such effects require that the solidification heat is carried away to the outside and led into the undercooled melt. In this connection, metastable *ferritic* solidification favoured by energetics during nucleation is obviously predominant. This means that a thermodynamically instable area for the existence of ferrite at temperatures below the solidification interval in solid state must exist for an austenitic initial composition. In this region particularly no area of coexistence for ferrite and austenite in equilibrium, i. e. no transformation area, is likely. Thus, a ferrite, formed in the metastable state, having an austenitic composition is immediately forced in a non-equilibrium reaction to transform into austenite and to freeze in a most unstable state, respectively. This unstable residual ferrite is represented by the ultra-thin black inclusions in the equiaxed dendrites in Figure 11 c. Post-heating of the specimen containing such solidification products in a furnace to about 800 °C and subsequent cooling at a slow rate prompts the black ferrites in the equiaxed dendrites in the weld centre to nearly totally disappear (Figure 12 a), i. e. to completely undergo austenitization. The co-annealed stable residual delta ferrites (δ-area in Figure 11 a), however, clearly maintain, as can be seen

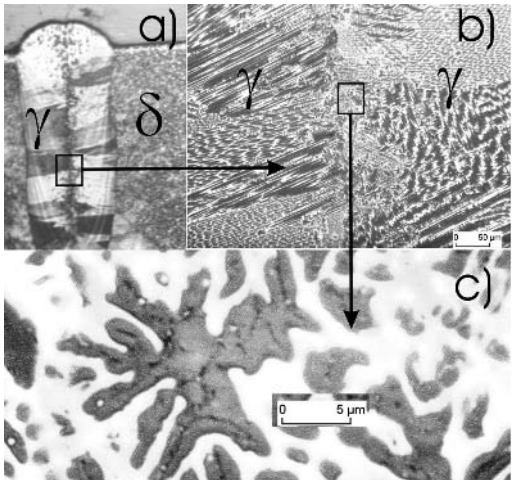

Fig. 11 Metastable ferritic crystallization of equiaxed dendritic morphologies in an austenitic melt. 1.4571 4, nitrided), V_S = 10 m/min, P_L = 5 kW

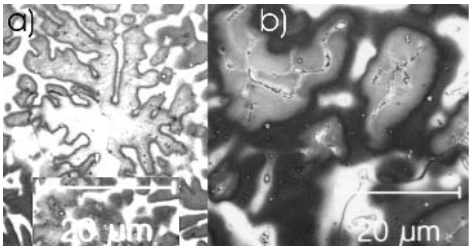

Fig. 12 Metastable (left hand side) and stable ferritic solidification products after annealing up to 800 °C

from Figure 12 b. This fact, too, confirms the metastable primary ferritic solidification mode of the morphologies in the weld centre (Figure 11 c). The repetition of this procedure for a specimen with a higher nitrogen content, which exhibits stable austenitic solidification already in the TIG-homogenized area, yielded comparable results.

24.6 Conclusions

From the present state of laser welding of austenitic stainless steels the following conclusions can be drawn:

1. The location of austenitic stainless steel compositions with respect to the eutectic rim in the constitutional diagram significantly affects variations of the primary solidification mode which were particularly confirmed to turn from ferrite to austenite during rapid laser welding of the austenitic stainless steels AISI 304L, 309 and 316L, while the AISI 316Ti material remains unaffected. Hot cracking associated with such solidification mode changes might be avoided by respective selection of the steel heats.
2. Such primary solidification behaviour is strongly influenced by the austenitization effect of nitrogen introduced into the melt by respective additions in the process and shielding gas, respectively.
3. As a result of nitrogen pick-up, undercooling and supersaturation, respectively, it was definitely demonstrated for the first time for rapid laser processes also a metastable ferritic crystallyzation of steels with fully austenitic behaviour might be encountered at high solidification rates. This means that during welding a solidification change can take place in both directions. Such phenomena are currently investigated further at steels with a chemical compositions located close to the eutectic rim on the primary austenite site of the constitutional diagram.
4. Geometric modelling of the solidification front with ellipsoidal segments turned out as a suitable tool to evaluate the solidification rates defining transition from primary ferritic to primary austenitic solidification as well as to scan the back front shape of the weld pool.

References

[1] W. Kurz, D. J. Fisher, Fundamentals of Solidification, 4th revised edition, Trans Tech Publications, Switzerland (1998)

[2] W. Kurz, Dendrite Growth in Welding, Mathematical Modelling of Weld Phenomena 2,H. Cerjak (ed.), The Institute of Materials, London (1995), 40–53

[3] M. Rappaz, S. A. David, J. M. Vitek, L. A. Boatner, Analysis of Soldification Microstructures in Fe-Ni-Cr Single-Crystal Welds, Metallurgical Transactions A,Vol. 21A (1990), 1767–1782

[4] H. Schobbert,V. Noack, J. Engert, J. Gebur, A. Hannemann, Zusammenhänge zwischen Erstarrungsmorphologien und Heißrissentstehung beim Laserstrahlschweißen von vornehmlich austenitischen Werkstoffen, DVS-Berichte Bd. 205, S. 18–24, Deutscher Verlag für Schweißtechnik, Düsseldorf

[5] S. Fukumoto, W. Kurz, Solidification Phase and Microstructure Selection Maps for Fe-Cr-Ni Alloys, SIJ International,Vol. 39 (1999), No. 12, 1270–1279

[6] T. Volkmann, W. Löser, D. M. Herlach, Nucleation and Phase Selection in Undercooled Fe-Cr-Ni Melts: Part II. Containerless Solidification Experiments, Metall Mater Trans A 28A (1997) 461–469

[7] T. Koseki, M.C. Flemings, Solidification of Undercooled Fe-Cr-Ni Alloys. Part II. Microstructural Evolution, Metall Mat Trans A 27A (1996) 3226–3240

25
Crystallization of the $Nd_2Fe_{14}B$ Peritectic Phase from the Undercooled Melt by Containerless Processing

Shumpei Ozawa, Mingjun Li, Suguru Sugiyama, Itaru Jimbo and Kazuhiko Kuribayashi

25.1
Introduction

The production of Nd-Fe-B permanent magnets has been significantly increased due to their excellent magnetic properties originating from the ferromagnetic $Nd_2Fe_{14}B$ intermetallic compound which has a large saturation magnetization and high anisotropy field [1, 2].

According to the Nd-Fe-B pseudo-binary phase diagram, the $Nd_2Fe_{14}B$ phase is formed *via* the peritectic reaction between liquid and pro-peritectic γ-Fe phase [3]. Therefore, the α-Fe phase transformed from the γ-Fe phase inevitably remains as a soft magnetic phase in the casting ingot, and deteriorates the hard magnetic property of the magnets [4, 5]. Thus, it is crucial to reduce the amount of the pro-peritectic iron phase in Nd-Fe-B alloy ingots.

In recent years, several studies have been conducted on solidification of the Nd-Fe-B alloys from the undercooled melt, which involved reducing the heterogeneous nucleation [6–14]. In these works, it was expected that the direct crystallization of the $Nd_2Fe_{14}B$ phase was achieved without peritectic reaction by rapid solidification from the undercooled melt. Some investigations, in fact, suggested that the $Nd_2Fe_{14}B$ phase is crystallized directly from the undercooled melt [9–11]. However, Gao *et al*. suggested that the metastable primary $Nd_2Fe_{17}B_x$ ($x \sim 1$) phase crystallizes from the undercooled melt and it decomposes into the α-Fe phase and $Nd_2Fe_{14}B$ phase during the post-solidification stage by slow cooling rate [12–14]. According to their experimental results, it can be deduced that large undercooling of the melt has little effect on diminishing the α-Fe phase. Until now, there have been only a small number of reports on the formation of the metastable phase, though many investigations have been reported involving the solidification of Nd-Fe-B alloys by rapid solidification techniques such as melt-spinning and gas atomization [15–17].

In the present study, Nd-Fe-B alloys were produced by containerless solidification processing in a 25 m drop tube. It is expected that the molten alloy droplets experience a large undercooling prior to nucleation. The relationships among the sample diameter, microstructure and magnetic properties were examined. The purpose of

the study is to investigate the phase selection from the undercooled melt of the Nd-Fe-B alloys and the resultant magnetic properties.

25.2 Experimental Procedure

Nd-Fe-B alloys with nominal compositions of $Nd_{11.8}Fe_{82.3}B_{5.9}$ ($Nd_2Fe_{14}B$) and $Nd_{14}Fe_{79}B_7$ were prepared by induction melting in an argon atmosphere. Segments of the ingots were charged in a quartz glass crucible with an orifice from 0.1 to 1.0 mm in diameter at the bottom. The drop tube was evacuated to 1×10^{-3} Pa and backfilled with He of 99.999% purity. The alloy segments were induction melted and superheated up to 1650K. The molten alloy was ejected into the drop tube through the orifice by controlling the helium pressure. The rapid solidification of the droplet in a containerless state was accomplished during its free fall. The samples accumulated at the bottom of the drop tube were all spherical grain. The resultant samples were classified into several groups according to their diameters, ranging from 2000 to 150 μm with regard to the orifice diameter and ejection gas pressure.

After the samples were polished and etched in 1% Nital, the microstructurs and the accurate diameter were examined by scanning electron microscope (SEM) equipped with an electron probe microanalyzer (EPMA) for analyzing chemical composition. The EPMA analysis was carried out in no-etched samples. A complete stoichiometric $Nd_2Fe_{14}B$ compound with the average grain size of 1.5 μm was synthesized to calibrate the accuracy of EPMA technique. The bombarded size with electron beam was about 0.8μm and the tolerance of the EPMA analysis is within 1% of its measured value. The constituent phases of the samples were identified by powdered X-ray diffraction (XRD) analysis using Cu-K_α radiation at room temperature. The magnetic properties of the samples were measured in a vibrating sample magnetometer (VSM) with a maximum applied field of 18kOe after the VSM was calibrated with a pure nickel sphere.

25.3 Results

25.3.1 $Nd_{11.8}Fe_{82.3}B_{5.9}$ ($Nd_2Fe_{14}B$) Alloy

Figure 1 shows the XRD patterns of the spherical $Nd_{11.8}Fe_{82.3}B_{5.9}$ samples with various diameters, solidified during free fall in the drop tube. Also shown is the XRD pattern of the bulk alloy, where the diffraction peaks of the α-Fe and $Nd_2Fe_{14}B$ phases can be identified. This indicates that the bulk alloy contains not only the $Nd_2Fe_{14}B$ phase but also a certain extent of α-Fe phase. In the stoichiometric $Nd_{11.8}Fe_{82.3}B_{5.9}$ alloy, it was reported that other phases such as Nd and $NdFe_4B_4$ phases may remain

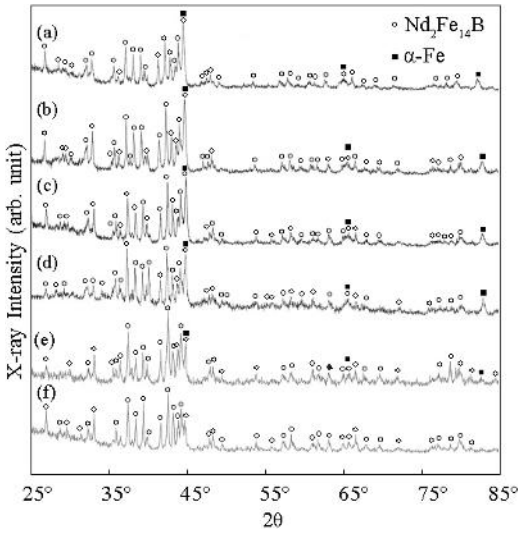

Fig. 1 XRD pattern of the (a) $Nd_{11.8}Fe_{82.3}B_{5.9}$ ($Nd_2Fe_{14}B$) alloy ingot and those of the spherical samples with diameters of (b) 2000 μm, (c) 500 μm, (d) 400, μm, (e) 350 μm, and (f) 250 μm.

[3]. However, no detectable diffraction peaks of these phases can be found in the present XRD pattern.

Although the diffraction peaks of the α-Fe phase can still be identified in the sample of 2000μm in diameter, the intensity decreased as the sample diameter decreases. This suggests that the volume fraction of the α-Fe phase decreases as the sample size becomes smaller. Consequently, the XRD pattern of the sample with 250μm in diameter shows only the diffraction peaks of the $Nd_2Fe_{14}B$ phase. This implies that the sample with 250μm in diameter consists of only $Nd_2Fe_{14}B$ phase.

Figure 2 shows the microstructures of the spherical $Nd_{11.8}Fe_{82.3}B_{5.9}$ samples and further magnified microstructures. The microstructure of the sample with 500μm in diameter (c. f. Fig. 2a) consists of dendrites embedded in matrix. EPMA study reveals that the dendrites and the matrix are the α-Fe and the $Nd_2Fe_{14}B$ phases, respectively. Even though the XRD analysis shows no other phase, the EPMA studies revealed that the Nd-rich phase remains as the intergranular phase. The volume fraction of the Nd-rich phase is smaller than the detectable limit of XRD.

In the samples with diameters of 400 μm and 350 μm (c. f. Fig. 2b, c), the microstructures consist of two regions; columnar grains with the intergranular phase and fragmented dendrites embedded in the matrix as those observed in the spherical samples with 500 μm in diameter. The region that consisted of columnar $Nd_2Fe_{14}B$ and grain boundary expands in the sample with 350 μm in diameter. The columnar grains and the intergranular phase were identified as the $Nd_2Fe_{14}B$ phase and the Nd-rich phase, respectively. If the $Nd_2Fe_{14}B$ phase is formed *via* peritectic reaction, it may surround the pro-peritectic iron phase and prevent further peritectic reaction. As the result, the pro-peritectic iron phase may remain in the $Nd_2Fe_{14}B$ phase [4, 5]. In the present experiment, however, no iron phase was observed in the columnar grains. Therefore, it can be concluded that the columnar grains must be crystallized directly from the undercooled melt. It was reported that the similar columnar grain

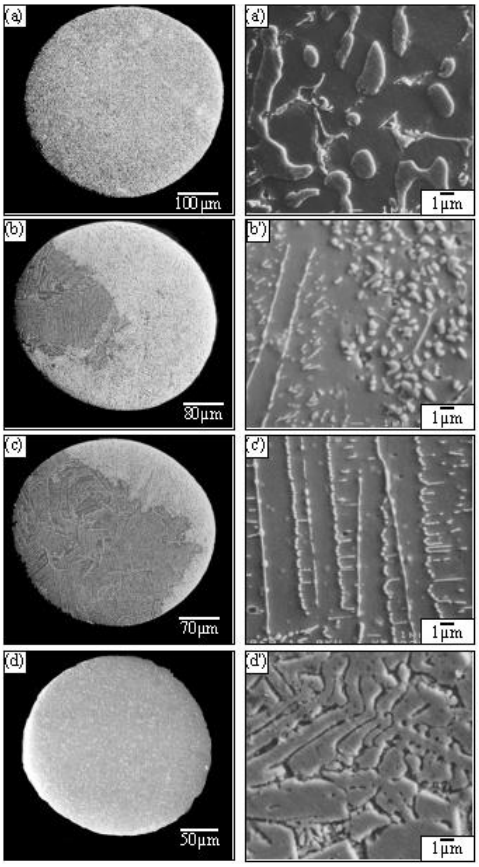

Fig. 2 SEM images of spherical $Nd_{11.8}Fe_{82.3}B_{5.9}$ samples with diameters of (a) 500 μm, (b) 400 μm, (c) 350 μm, and (d) 250 μm.

of the $Nd_2Fe_{14}B$ phase was observed in the microstructure of the Nd-Fe-B alloy solidified from the undercooled melt [12, 13]. As the sample diameter decreases, the cooling rate increases and the number of potential catalytic sites for heterogeneous nucleation is reduced [18]. Thus, the undercooling level may be enhanced as the sample diameter is reduced. Increasing of the undercooling level with decreasing the sample diameter must be responsible for the expansion of the $Nd_2Fe_{14}B$ columnar region in the microstructure of the sample with 350mm in diameter. The formation of the microstructure of two different regions can be interpreted in the following solidification path; the $Nd_2Fe_{14}B$ phase nucleates first and then grows. Due to the pronounced sluggish kinetics in the growth, the released heat may lower the interface undercooling, and thus the growth of $Nd_2Fe_{14}B$ phase is terminated. At this lower undercooling, the growth of iron phase is predominant and then followed by a peritectic reaction. This solidification mode can yield two different regions.

When the sample diameter decreases to 250 μm (c. f. Fig. 2d), the microstructure changes to dendritic grains (c. f. Fig.2d). Although the morphology is different from the $Nd_2Fe_{14}B$ columnar grains observed in the processed sample of 400 and 350 μm

in diameter, EPMA study revealed that the dendritic grains are $Nd_2Fe_{14}B$ phase. This indicates that the critical diameter for obtaining the $Nd_2Fe_{14}B$ phase without α-Fe is in the region less than 350 μm, which coincides with the value reported by Gao and Wei [7]. It is well known that dendrites are formed by continuous growth of a primary phase. Moreover, no α-Fe phase is observed in the interdendritic region. Therefore, it is expected that the direct crystallization of the $Nd_2Fe_{14}B$ phase is completely achieved in the sample with 250 μm in diameter. However, no microstructure containing α-Fe is observed in all the samples with 250 μm in diameter. The cooling rate of the sample is enhanced as the sample diameter decreases; the estimated cooling rate of the spherical sample with 250 μm in diameter is 1.3×10^4 K/s, which is high enough to be comparable with that of other rapid solidification techniques such as melt-spinning and gas atomization. Hence, the direct growth of the $Nd_2Fe_{14}B$ phase in the spherical sample with 250 μm in diameter depends not only on large undercooling but also on high cooling rate.

25.3.2
$Nd_{14}Fe_{79}B_7$ Alloy

Figure 3 shows the XRD patterns of the spherical $Nd_{14}Fe_{79}B_7$ samples, solidified during free fall together with that of the bulk alloy. The XRD pattern of the bulk alloy shows the diffraction peaks of the α-Fe and $Nd_2Fe_{14}B$ phases, suggesting that the alloy contains certain amount of the α-Fe phase. Although the diffraction peaks of the $Nd_2Fe_{14}B$ phase can still be observed in the spherical $Nd_{14}Fe_{79}B_7$ sample with 1200 μm in diameter, the intensity decreased with decreasing the diameter. Conse-

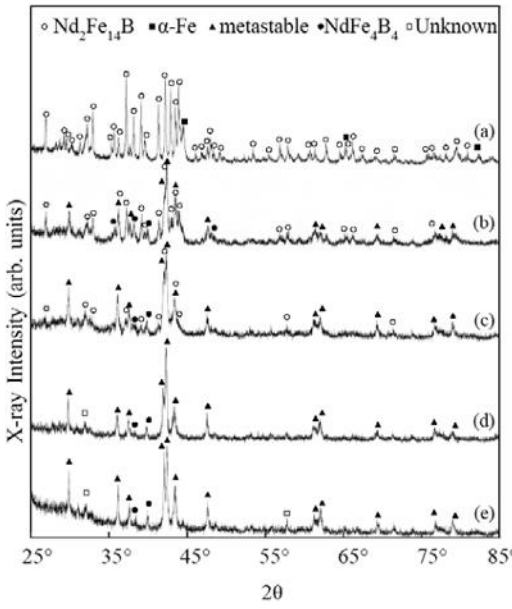

Fig. 3 XRD pattern of the (a) $Nd_{14}Fe_{79}B_7$ alloy ingot and those of the spherical samples with diameters of (b) 1200 μm, (c) 800 μm, (d) 430 μm, and (e) 350 μm.

Tab. 1 Average bulk composition of $Nd_{14}Fe_{79}B_7$ ingot and the spherical sample as determined by ICP-AES.

	Nd (at%)	*Fe (at%)*	*B (at%)*
Nominal composition	14.0	79.0	7.0
Ingot	13.4	80.2	6.3
Spherical sample	13.4	80.3	6.2

quently, the XRD patterns of the samples with diameters from 800 to 350 μm simply exhibit the diffraction peaks of both the Nd_2Fe_{17} and $NdFe_4B_4$ phases, which are similar to the XRD pattern of the metastable $Nd_2Fe_{17}B_x$ phase reported by Gao *et al.* [12, 13]. It has been reported that the trigonal binary Nd_2Fe_{17} is formed in $Nd_{15}Fe_{85-y}B_y$ alloys when the boron content is less than 6% [19]. As shown in Table 1, the averaged bulk composition of the spherical samples is almost the same as that of the bulk alloy, where the boron content is larger than 6%. Hence, it is reasonable to conclude that a phase with the composition of the Nd_2Fe_{17} phase cannot be formed in this experiment.

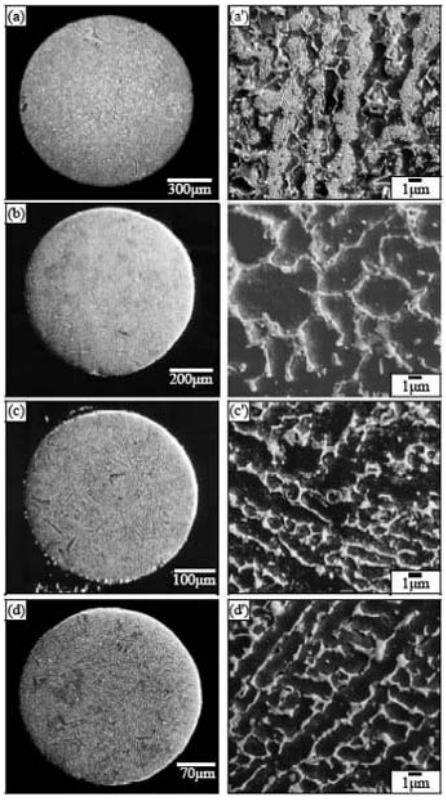

Fig. 4 SEM images of spherical $Nd_{14}Fe_{79}B_7$ alloys with diameters of (a) 1200 μm, (b) 800 μm, (c) 430 μm, and (d) 350 μm.

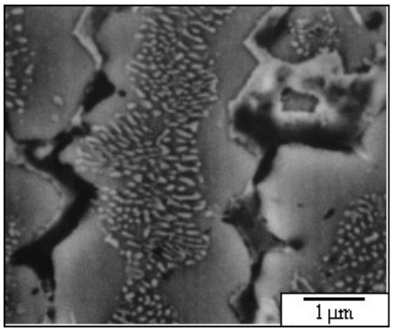

Fig. 5 Magnified backscattered electron micrograph of the decomposed lamellar in the spherical $Nd_{14}Fe_{79}B_7$ sample with 1200 μm in diameter.

Figure 4 shows the microstructures of the spherical $Nd_{14}Fe_{79}B_7$ samples. The sample with 1200μm in diameter consists of fine irregular lamellar grains of bright and dark phases embedded in the matrix of dendrites magnified in Fig. 5. The average lamellar spacing is less than 1 μm, suggesting that the lamellar grains were formed by solid-state decomposition reaction of the metastable phase during the post-solidification cooling stage. Gao *et al.* [12, 14] reported that the metastable $Nd_2Fe_{17}B_x$ phase transforms into mixture grains of the α-Fe and $Nd_2Fe_{14}B$ phases by solid-state decomposition reaction. Although the morphology of the decomposed microstructure shown in Fig. 5 is similar to the microstructure observed by Gao *et al.*, not the α-Fe phase but the Nd-rich phase is formed in our experiment.

Table 2 shows the ratio of Nd to Fe in the dendrites surrounding the decomposed grains analyzed by EPMA. The average dendrite arm spacing is 1.6μm even in the sample with diameter of 350μm that has smallest microstructure in this study. Since the average dendrite arm spacing is large enough compared with the bombarded size of 0.8μm in the EPMA analysis, the analysis is a valid method. Although the XRD analysis gives a suggestion that the spherical sample with 1200μm in diameter contains several Nd-containing phases such as the $Nd_2Fe_{14}B$, Nd_2Fe_{17}, $Nd_2Fe_{17}B_x$ and $NdFe_4B_4$ phases (c.f. Fig. 3), the ratio of Nd to Fe is close to that of the bulk alloy rather than those of the Nd-containing phases. This indicates that the matrix of dendrite is neither

Tab. 2 Quantitative analysis in dendrite of spherical $Nd_{14}Fe_{79}B_7$ alloys by EPMA, together with the ratio of Nd to Fe in Nd-containing phases.

	Ratio (at%)	
	Nd	***Fe***
dendrite in sample with a diameter of 1200 μm	14.4	85.6
dendrite in sample with a diameter of 800 μm	15.2	84.8
dendrite in sample with a diameter of 400 μm	15.2	84.8
$Nd_2Fe_{14}B$	12.5	87.5
Nd_2Fe_{17}	10.5	89.5
$Nd_2Fe_{17}Bx$	10.5	89.5
$NdFe_4B_4$	20.0	80.0
$Nd_{14}Fe_{79}B_7$ (original ingot)	15.1	84.9

$Nd_2Fe_{14}B$ nor $Nd_2Fe_{17}B_x$. Considering the results of the XRD and EPMA studies, the matrix of the dendrite in the spherical sample with 1200μm in diameter can be deduced to be a metastable phase with a similar crystal structure to that of the trigonal Nd_2Fe_{17} phase and a chemical composition close to that of the bulk alloy.

When the sample diameter is below 800 μm, the microstructures of the spherical samples consist of the dendrites and grain boundary. No decomposed lamellar grains are observed in the matrix, where the averaged ratios of Nd to Fe are almost the same as that of the sample with 1200 μm in diameter. This indicates that the spherical samples with diameter less than 800 μm mainly consist of a similar metastable phase to that of the spherical sample with 1200 μm in diameter. Particularly, the samples with diameter less than 400 μm exhibit no evidence for existence of the $Nd_2Fe_{14}B$ phase even in the XRD patterns (c. f. Fig.1).

In order to elucidate thermal stability of the metastable phase in the samples, the differential thermal analysis (DTA) of the samples, in an argon atmosphere with a heating rate of 0.5 Ks^{-1}, was carried out up to 1100 K repeatedly. It was noted that a small endothermic peak at about 590 K corresponding to the Curie temperature of the ferromagnetic $Nd_2Fe_{14}B$ phase was observed only in the sample of 1200 μm in diameter.

A small exothermic peak was observed at about 950K in the sample of 1200 μm in diameter, which can be attributed to the decomposition of the metastable phase. The exothermic peak became clear in the DTA curves of the samples with diameters of 800 and 430 μm. This means that the metastable phase becomes predominant as the sample diameter decreases. It is known that some exothermic peaks are usually observed at about 850 K in the DSC curves of the rapid solidified Nd-Fe-B alloys due to the crystallization of the $Nd_2Fe_{14}B$ phase from amorphous materials [16, 20]. However, it is clear that the exothermic peak observed in our experiment is different from that of the crystallization, because the temperature of the exothermic peak is much higher and the XRD analysis showed no evidence for existence of the amorphous phase in the samples.

In the second heating, only the endothermic peak at about 590 K was observed in all the samples. This suggests that the metastable phase transforms into the $Nd_2Fe_{14}B$ phase by heating the samples up to 1100 K.

After DTA measurement, the XRD patterns of the samples were markedly changed to the well-indexed tetragonal $Nd_2Fe_{14}B$ phase regardless of the sample diameter. This confirms that the metastable phase transforms into the stable $Nd_2Fe_{14}B$ phase by heat treatment. No detectable diffraction peaks of the metastable phase are observed in the XRD patterns.

25.4 Discussions

As mentioned above, the sample composition is strongly associated with the phase selection in the Nd-Fe-B alloys produced by a containerless solidification in the drop tube; the $Nd_2Fe_{14}B$ phase is crystallized from the melt directly in the stoichiometric $Nd_{11.8}Fe_{82.3}B_{5.9}$ alloy and the metastable phase forms in the hypo-peritectic $Nd_{14}Fe_{79}B_7$ alloys.

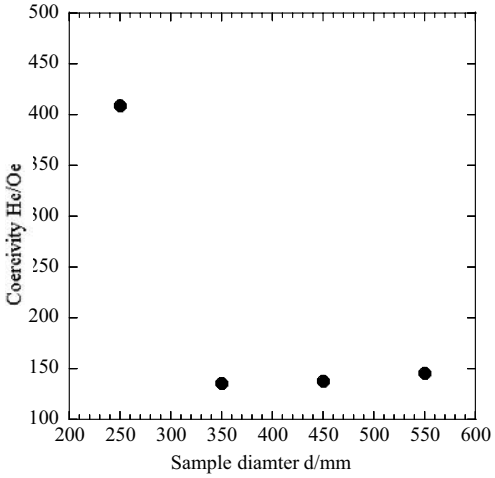

Fig. 6 Intrinsic coercivity of spherical $Nd_2Fe_{14}B$ samples as a function of sample diameter.

Since it is important to note the magnetic properties in magnetic materials, VSM measurement was carried out. Figure 6 shows the intrinsic coercivity of the spherical $Nd_{11.8}Fe_{82.3}B_{5.9}$ samples. The spherical $Nd_{11.8}Fe_{82.3}B_{5.9}$ samples with diameter lager than 350μm have low coercivity values less than 0.15 kOe. This is due to the relatively large grain size of the $Nd_2Fe_{14}B$ phase in the spherical samples [16,21]. The low coercivity is partly due to the existence of the soft magnetic α-Fe phase in the samples. On the other hand, the coercivity increases up to 0.41 kOe in the spherical sample of 250 μm in diameter. The refinement of the $Nd_2Fe_{14}B$ phase and absence of the α-Fe phase is responsible for the observed increase in coercivity.

When the magnetic properties of the new metastable phase are discussed, not only the coercivity but also the saturation magnetization and the remanence should be noted, because the coercivity is mainly dependent on the microstructure whereas the saturation magnetization and the remanence are associated with the constituent phase in the samples. Figure 7 depicts the hysteresis loops of the processed sample of $Nd_{14}Fe_{79}B_7$ and those of the sample after the DTA measurement. The hysteresis loop of the as-processed samples of 1200 μm in diameter shows the saturation magnetization of 103 emu/g, the remanence of 26.7 emu/g, and the coercivity of 1.1 kOe. These values decreased as the sample diameter was decreased; for instance, in the sample of 430 μm in diameter, the saturation magnetization, the remanence and the coercivity are 88 emu/g, 4.5 emu/g and of 0.14 kOe, respectively. These values, the saturation magnetization, the remanence, and the intrinsic coercivity, are much lower than those of the Nd-Fe-B alloy produced by rapid solidification techniques such as the melt-spinning and the gas atomization [15–17]. As mentioned earlier, the volume fraction of the metastable phase increases and that of the ferromagnetic $Nd_2Fe_{14}B$ phase reduces as the sample diameter is decreased. The reduction of the volume fraction of the $Nd_2Fe_{14}B$ phase gives rise to the lowering of the magnetic properties in the processed samples; namely, the metastable phase has low magnetic properties of the magnetization, the remanence and the coercivity.

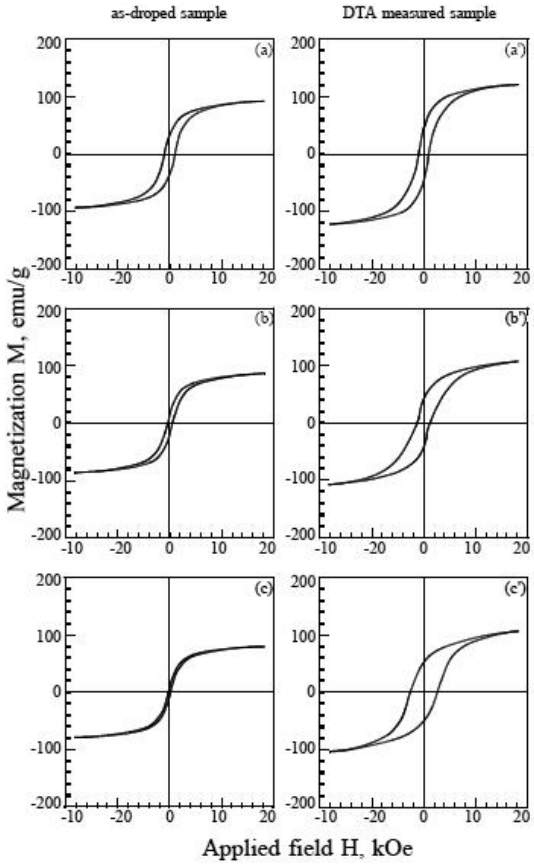

Fig. 7 Hysteresis loops of the spherical $Nd_{14}Fe_{79}B_7$ samples with diameters of (a) 1200 μm, (b) 800 μm, and (c) 430 μm. (a′), (b′), and (c′) depict the hysteresis loops of the samples after DTA measurement.

In the sample of 1200 μm in diameter, heating the sample results in the increase of the saturation magnetization, the remanence and the coercivity to 132.8 emu/g, 41 emu/g and 2.1 kOe, respectively. These values are much larger than those of the as-dropped samples. The increase in the amount of the $Nd_2Fe_{14}B$ phase by heating the sample must be closely related to this improvement of the magnetic properties. When the sample diameter is decreased to 430 μm, the coercivity increases to 2.8 kOe because of the refinement of the $Nd_2Fe_{14}B$ phase.

The above results suggest that a better understanding of the solidification behavior of Nd-Fe-B alloys from the undercooled melt advanced. Unfortunately, the Nd-Fe-B alloys produced by containerless solidification exhibit poor magnetic properties. For the improvement of the magnetic properties of Nd-Fe-B, which is the most important goal, the direct crystallization of the $Nd_2Fe_{14}B$ phase and the refinement of the grain size are required. Further improvement in the solidification conditions such as the ejection gas pressure, composition and temperature of the molten metals together with the composition modifications would lead to the enhancement of the undercooling level for the direct crystallization and refinement of the $Nd_2Fe_{14}B$ phase.

25.5 Conclusion

Nd-Fe-B alloys with the composition of $Nd_{11.8}Fe_{82.3}B_{5.9}$ and $Nd_{14}Fe_{79}B_7$ were melted and solidified by containerless solidification processing in the 25m drop tube. The relationships among the sample diameter, microstructure, and magnetic properties were investigated.

In the $Nd_2Fe_{14}B$ alloys, the direct crystallization of the $Nd_2Fe_{14}B$ phase was achieved from the undercooled melt. The microstructures of the sample with diameter of 400 μm that consisted of two regions; one is directly formed $Nd_2Fe_{14}B$ columnar grain and the other is the α-Fe dendrite in $Nd_2Fe_{14}B$ matrix. The region of the $Nd_2Fe_{14}B$ columnar grain expands as the sample diameter decreases from 400 to 350 μm. The microstructure of the sample with 250 μm in diameter consisted of only primary $Nd_2Fe_{14}B$ dendrite without any α-Fe phase in the sample.

The coercivity of the $Nd_{11.8}Fe_{82.3}B_{5.9}$ samples increases from the value less than 0.15 kOe to 0.41 kOe as the sample diameter decreases from 550 to 250 μm due to the refinement of the $Nd_2Fe_{14}B$ phase and absence of the pro-peritectic α-Fe phase.

In the $Nd_{14}Fe_{79}B_7$ alloy, on the other hand, the microstructure of the processed sample of 1200 μm in diameter consisted of the metastable phase and fine lamellar grains with the intergranular Nd-rich phases. The lamellar grain was formed by a solid-state reaction from the metastable phase. When the sample diameter is less than 800 μm, the microstructure consisted of the metastable phase and the intergranular Nd-rich phase. The chemical composition of metastable phase is near that of the bulk alloy and the crystal structure is similar to the trigonal Nd_2Fe_{17} phase. The metastable phase was changed to the stable $Nd_2Fe_{14}B$ phase by heating during the DTA measurement.

The magnetic properties of the metastable phase were poor; the saturation magnetization, the remanence and the coercivity are 86.7 emu/g, 4.5 emu/g and 0.14 kOe, respectively. Heating the sample up to 1100 K markedly improved the magnetic properties due to the increase in the amount of the $Nd_2Fe_{14}B$ phase; the saturation magnetization, the remanence and the coercivity of the sample with 1200 μm in diameter are 132.8 emu/g, 41 emu/g and 2.1 kOe, respectively. In the sample with 430 μm in diameter, the coercivity value is increased up to around 2.8 kOe.

Acknowledgements

This work was financially supported by a grant-in aid for Scientific Research from the Ministry of Education, Culture, Sports, Science and Technology. One of the authors (SO) acknowledges the Japan Society for Promotion of Science (JSPS) for offering a JSPS fellowship. Another author (ML) is grateful to the Foreign Research Fellowship Project from Institute of Space and Astronautical Science, Japan Aerospace Exploration Agency (ISAS/JAXA).

References

[1] N. C. Koon, B. N. Das, M. Rubinstein and J. Tyson, J. Appl. Phys. 1985, 57, 4091–4093.

[2] C. Abache and H. Oesterreicher, J. Appl. Phys. 1985, 57, 4112–4114.

[3] G. Schneider, E.-T. Hening, G. Petzow and H. H. Stadelmaier, Z. Metallkd. 1986, 77, 755–771.

[4] S. Ozawa, J. Yoshizawa, T. Saito and T. Motegi, Mater. Trans. JIM 2000, 41, 1121–1124.

[5] R. Hermann, I. Bächer, D. M. Matson, W. Löser, and L. Schultz, IEEE Trans. Magn. 2001, 37, 1100–1105.

[6] R. Herrmann and I. Bächer, J. Magn. Magn. Mater. 2000, 213, 82–86.

[7] J. Gao and B. Wei, J. Alloys. Comp. 1999, 285, 229–232.

[8] R. Hermann, I. Bächer, W. Löser, and L. Schultz, J. Magn. Magn. Mater. 1999, 196–197, 737–739.

[9] S. Ozawa, T. Saito, J. Yu and T. Motegi, J. Alloys. Comp. 2001, 322, 276–280.

[10] S. Ozawa, H. Sato, T. Saito and T. Motegi, J. Appl. Phys. 2002, 91, 8831–8833.

[11] T. Volkmann, J. Gao, and D. M. Herlach, Appl. Phys. Lett., 2002, 80, 1915–1917.

[12] J. Gao, T. Volkmann, and D. M. Herlach, Acta Mater. 2002, 50, 3003–3012.

[13] J. Gao, T. Volkmann, S. Roth, W. Löser, and D. M. Herlach, J. Magn. Magn. Mater. 2001, 234, 313–319.

[14] J. Gao, T. Volkmann, and D. M. Herlach, J. Alloys. Comp. 2003, 350, 344–350.

[15] J. J. Croat, J. F. Herbst, R. W. Lee and F. E. Pinkerton, J. Appl. Phys. 1984, 55, 2078–2082.

[16] S. Ozawa, T. Saito, and T. Motegi, J. Alloys. Comp. 2004,363263–270.

[17] Y. Sakaguchi, T. Harada, and T. Kuji, Mate. Sci. Eng. A. 1994, 181–182, 1232–1236.

[18] D. Turnbull and R. E. Cech, J. Appl. Phys. 1950, 21, 804–810.

[19] M. Sagawa, S. Fujimura, N. Togawa, H. Yamamoto and Y. Matsuura, J. Appl. Phys. 1984, 55, 2083–2087.

[20] G.-H. Tu, Z. Altounia, D. H. Ryan, and J. O. Ström-Olessen, J. Appl. Phys. 1988, 63, 3330–3332.

[21] J. D. Livingston, J. Appl. Phys. 1985, 57, 4137–4139.

26
Thermomagnetic Analyses of Nd-Fe-B Bulk Alloys Solidified from the Undercooled Melt

S. Reutzel, T. Volkmann, J. Gao, J. Strohmenger, D.M. Herlach

Abstract

Electromagnetic levitation experiments have been performed to investigate phase selection in undercooled Nd-Fe-B alloy melts with respect to the competitive formation of the peritectic $Nd_2Fe_{14}B_1$-phase (ϕ-phase) and the properitectic γ-Fe solid solution [1], [2]. The results demonstrate that the phase selection of Nd-Fe-B alloy melts can be changed by undercooling of the liquid phase. It is shown that primary solidification of stable γ-Fe is suppressed in favour of the direct crystallisation of the peritectic $Nd_2Fe_{14}B_1$ intermetallic compound with increasing undercooling [3]. Besides the primary ϕ-phase, another solidification pathway of the undercooled melt resulting in a metastable $Nd_2Fe_{17}B_1$-phase (χ-phase) is found in a wide range of alloy compositions. In this work thermomagnetic analyses (TMA) with a high resolution Faraday-balance allow to determine magnetic bulk properties, such as magnetisation, magnetic susceptibility and Curie-temperature of Nd-Fe-B bulk alloys solidified from the undercooled melt. These measurements are performed to analyse the dependence of their intrinsic magnetic properties on alloy composition, undercooling level and microstructure. The magnetisation of Nd-Fe-B specimens is sensitively depending on the volume fraction of the included phases, which are qualitatively evaluated from the acquired data. The detection of the metastable χ-phase or its decomposition products is thereby of special interest.

26.1
Introduction

Solidification processing of Nd-Fe-B alloys such as mould casting and rapid quenching has been widely used to produce precursor materials for commercial magnets [4]. Because the as-solidified microstructure of the precursor materials can influence the magnetic properties significantly, it is of great technical interest to study and to control the solidification behaviour of Nd-Fe-B alloy melts. The chemical compositions of commercial Nd-Fe-B alloys are in the crystallisation region of the ternary system where γ-Fe is the primary nucleating phase. Under equilibrium solidifica-

tion conditions the hard magnetic ϕ-phase ($Nd_2Fe_{14}B_1$) is formed in a peritectic reaction from the primary γ-Fe phase and the residual liquid phase [5]. Due to an incomplete peritectic transformation in industrial casting, γ-Fe phase is often preserved and transformed into soft-magnetic α-Fe phase during the continuous cooling. It is well known that undercooling of an alloy melt can drastically change the solidification behaviour. In our case the electromagnetic levitation technique was used to process Nd-Fe-B bulk alloy melts. Owing to the containerless environment, large undercooling levels can be achieved, leading to metastable solidification pathways. The peritectic ϕ-phase is a potential metastable phase with respect to the properitectic γ-Fe phase, and hence can be crystallised directly from the liquid undercooled phase [5].

First basic investigation of solidification and growth kinetics on Nd-Fe-B melts near peritectic composition were done by Hermann et al. using quenching technique [6]. In our previous work, the electromagnetic levitation processing has been applied to peritectic Nd-Fe-B alloys over a wide range of composition [1]–[3]. It has been found that primary γ-Fe phase is suppressed in favour of the ϕ-phase, which has been correlated to significant undercoolings achieved by containerless processing. In addition, the metastable χ-phase ($Nd_2Fe_{17}B_1$) which decomposes in a post-recalescence process into γ-Fe and ϕ-phase can also be formed from undercooled alloy melts. In drop tube experiments the metastable χ-phase can be sustained down to room temperature due to the elevated cooling rates and small droplet sizes and the χ-phase has been identified by energy dispersive X-ray analysis (EDX) and X-ray diffraction (XRD) [7].

26.2 Experimental

Alloys with peritectic ($Nd_{11.8}Fe_{82.3}B_{5.9}$), hyper-peritectic ($Nd_{14}Fe_{79}B_7$) and non-peritectic composition ($Nd_{22}Fe_{67}B_{11}$) were prepared by arc-melting high purity elemental materials (Nd 99.9%, Fe 99.99% and B 99.8%) under the protection of an argon atmosphere (99.999% purity). After evacuating the chamber of the electromagnetic levitation facility (details see [8]) to a vacuum pressure in the order of 10^{-6} mbar, the alloy samples of about 1 g were levitated and melted under a highly purified helium gas atmosphere (99.9999%). In order to attain a substantial undercooling each sample was overheated to a temperature of 100 to 200 K above its liquidus temperature and afterwards cooled by blowing helium gas onto its surface. After reaching a certain undercooling the sample was solidified spontaneously and usually, several recalescence events could be observed due to subsequent phase formations. The sample temperature before and during solidification was measured using a two-colour pyrometer with a relative accuracy of ± 5 K. The bulk undercooling of the sample was determined in the recorded cooling curve as the difference between the liquidus temperature of the sample and the onset temperature of the first recalescence event. The microstructure of the solidified sample was examined with a LEO1530VP scanning electron microscope (SEM) under back scattering conditions. Elemental con-

centrations of phase constituents, except for boron, were analysed using an energy dispersive X-ray analyser (EDX) on cross sections of the samples.

In order to study the intrinsic magnetic properties of the bulk samples thermomagnetic analyses were performed using a Faraday-balance, where the change of the magnetic force on the specimen is measured in absolute values [9]. In our set-up the resulting magnetic force $\vec{F}$ on a sample with magnetisation $\vec{M}$

$$\vec{F} = \mu_0 \cdot \mathrm{grad}\,(\vec{M} \cdot \vec{H}) \tag{1}$$

was reduced to one dimension in vertical direction:

$$F_Z = \mu_0 \cdot M \cdot \frac{\partial H}{\partial z} \tag{2}$$

where μ_0 is the permeability constant, M the magnetisation and $\frac{\partial H}{\partial z}$ the magnetic gradient field.

The magnetisation was calculated by measuring the change of force during constant heating or cooling with a frequency of 6–12 min^{-1} and a resolution of the balance of ± 2 µg at a maximum load of 20 g. The specimen was located in an inner ceramic crucible (Al_2O_3 or ZrO_2) placed in an outer metallic crucible (Ta or Mo) under helium atmosphere. A graphite-tube furnace of a Tammann type produces temperatures up to 1200 K. The temperature was measured 1 mm below the tantalum crucible by a thermocouple. The temperature signal was used to control the temperature of the furnace. Slow cooling and heating rates of 1–3 K/min were used in order to avoid a substantial offset between the temperature of the furnace and of the specimen at higher rates. The temperature homogeneity of the furnace at the position of the crucible was better than ± 2 K.

26.3 Results and Discussion

For peritectic $Nd_{11.8}Fe_{82.3}B_{5.9}$-alloy melts low and intermediate undercooling level are not sufficient to primarily solidify the ϕ-phase. Figure 1 shows the temperature-time profile of a levitated $Nd_{11.8}Fe_{82.3}B_{5.9}$-specimen where the primary phase formation of γ-Fe occurred at an undercooling $\Delta T = 60$ K. The subsequent phase formation of the ϕ-phase led to an increase of temperature near the peritectic temperature $T_{per}(\phi)$.

The thermomagnetic analysis (TMA) of the as-solidified $Nd_{11.8}Fe_{82.3}B_{5.9}$-sample presented in Figure 2 shows two magnetic transitions: the one of the ϕ-phase at $T_C^{\phi} = 584$ K and the one of the α-Fe phase at $T_C^{\alpha} = 1047$ K. The distinct difference between the characteristics of the magnetisation for the first heating and the subsequent cooling can be ascribed to the ongoing peritectic reaction. Due to the elevated temperatures the solid sample changes its volume fractions of phase constituents during the measurement and the α-Fe content is significantly reduced at temperatures above T > 900 K.

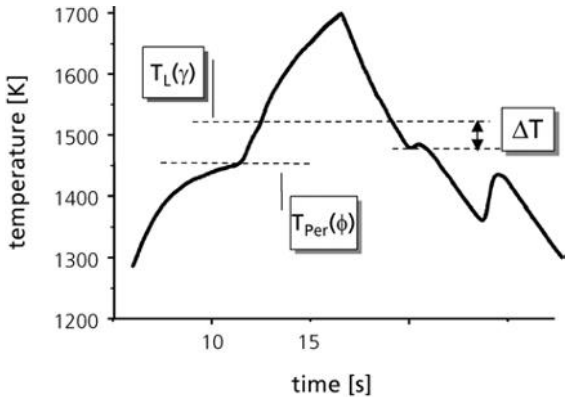

Fig. 1 Temperature-time profile of a levitated $Nd_{11.8}Fe_{82.3}B_{5.9}$-bulk alloy melt during solidification obtained by electromagnetic levitation. The liquidus temperature $T_L(\gamma)$ and the peritectic temperature $T_{Per}(\phi)$ are obtained from the pseudo-binary phase diagram according to Schneider et al. [10]. The primary nucleation set in at an undercooling $\Delta T = 60$ K.

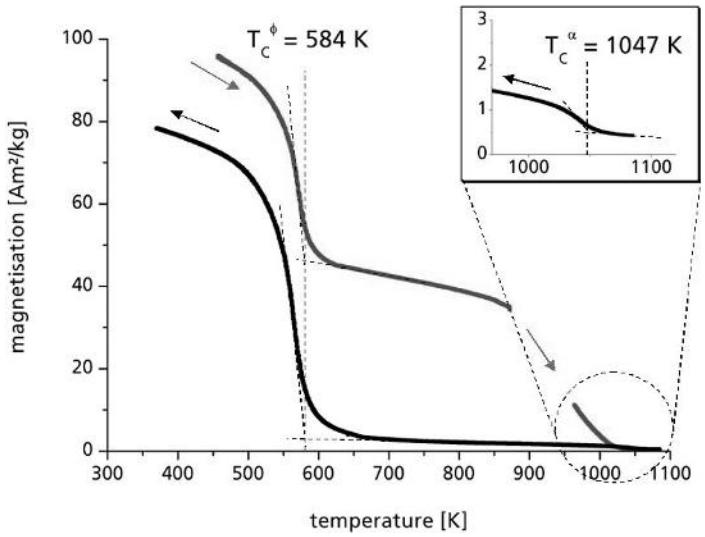

Fig. 2 TMA of a $Nd_{11.8}Fe_{82.3}B_{5.9}$-sample solidified primarily in γ-Fe at $\Delta T = 60$ K, according to Figure 1, at a homogeneous magnetic field $H_0 = 512.5$ kA/m. The heating (→) was operated by 2 K/min, the subsequent cooling (←) by –2 K/min.

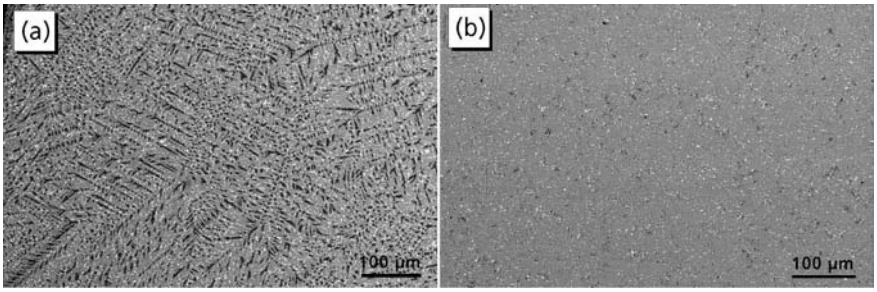

Fig. 3 Scanning electron micrographs in the backscattered mode of a levitated $Nd_{14}Fe_{79}B_7$-sample solidified primarily in γ-Fe at ΔT = 35 K (a) before and (b) after the thermomagnetic analysis. The phases are marked in the micrograph as: α-Fe (black), ϕ-phase (grey) and Nd-rich phase (white). The original α-Fe dendrites and the Nd-rich phase nearly completely dissolved by the heat treatment in a solid state transformation into the ϕ-phase as shown in micrograph (b).

The microstructure of the as-solidified samples is mainly dependent on the composition, the undercooling level and the primary nucleating phase. If a Nd-Fe-B melt of peritectic and near-peritectic concentration solidifies primarily in γ-Fe at low undercooling levels, the resulting microstructure is dominated by the α-Fe dendrites, as can be seen exemplarily on the cross section of the hyper-peritectic $Nd_{14}Fe_{79}B_7$-alloy in Figure 3 (a). However, the microstructure exhibits large grains of the ϕ-phase, if the undercooling levels is extended and the primary solidification of the ϕ-phase occurs (see Figure 5).

The thermomagnetic measurement of the $Nd_{14}Fe_{79}B_7$-sample which solidified primarily in γ-Fe, according to Figure 3(a), reveals two magnetic phase transitions: the first transition at T_C^{ϕ} = 585 K, identifying the content of the ϕ-phase and the second transition at T_C^{α} = 1046 K, identifying the content of α-Fe.

The characteristics of the magnetisation of the hyper-peritectic $Nd_{14}Fe_{79}B_7$-sample does not distinguish significantly from the one of the peritectic $Nd_{11.8}Fe_{82.3}B_{5.9}$-sample (shown in Figure 2), both primarily solidified in γ-Fe. Merely, the absolute value of the mass magnetisation is marginally decreased due to the lower volume fraction of α-Fe in the hyper-peritectic alloy sample. The cross section of the sample after the thermomagnetic analysis presented in Figure 3(b) shows that the α-Fe dendrites nearly completely dissolved by the peritectic reaction. The result of TMA shows qualitatively the decrease in the volume content of α-Fe but still evinces its residual amount (see insert in Figure 4).

At first glance, the thermomagnetic measurement of a hyper-peritectic $Nd_{14}Fe_{79}B_7$-sample which solidified primarily in ϕ-phase presented in Figure 6 reveals only one magnetic phase transition at T_C^{ϕ} = 583 K, identifying the ϕ-phase according to the cross section of the as-cast specimen in Figure 5.

However, the progression of the magnetisation at elevated temperatures shows that the sample still contains a residual amount of α-Fe which can be ascribed to the

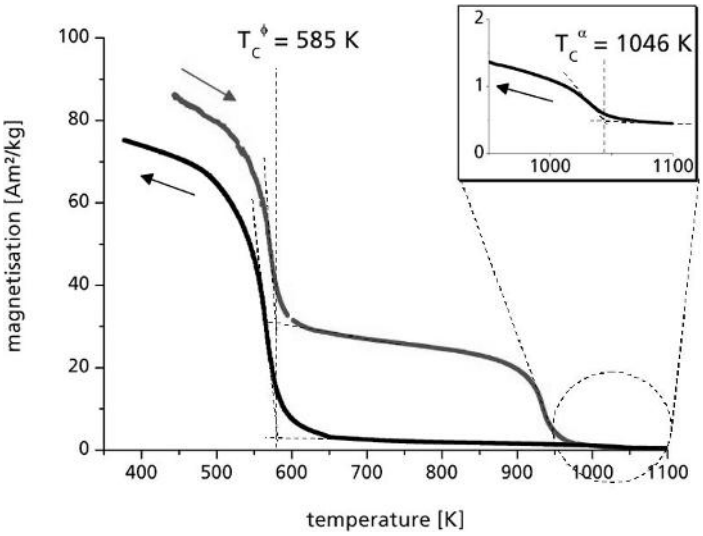

Fig. 4 TMA of a $Nd_{14}Fe_{79}B_7$-sample solidified primarily in γ-Fe at $\Delta T = 35$ K, according to Figure 3(a), at a homogeneous magnetic field $H_0 = 512.5$ kA/m. The heating ($\rightarrow$) was operated by 2 K/min, the subsequent cooling ($\leftarrow$) by –2 K/min.

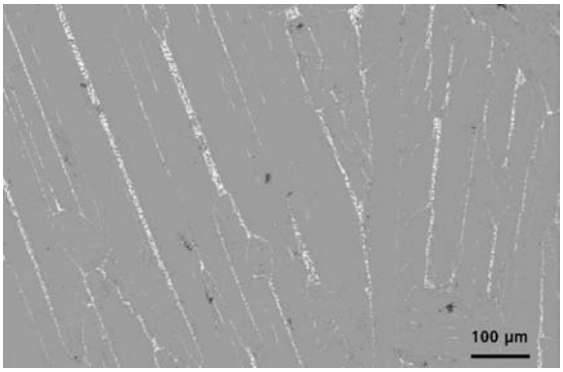

Fig. 5 Scanning electron micrograph in the backscattered mode of a levitated $Nd_{14}Fe_{79}B_7$-sample solidified primarily in ϕ-phase at $\Delta T = 60$ K. The phases are marked in the micrograph as: ϕ-phase (grey) and Nd-rich phase (white). Obviously, no γ-Fe can be detected in this cross section.

re-entrant formation of iron dendrites [7]. Due to its limited amount the α-Fe phase was not detectable in previous XRD analyses and could have been recently identified in this work because of the high sensitivity of the magnetic measurement.

At higher undercooling levels a third type of microstructure, a fine mixture consisting out of an iron-rich phase and the ϕ-phase, can be found locally as shown in

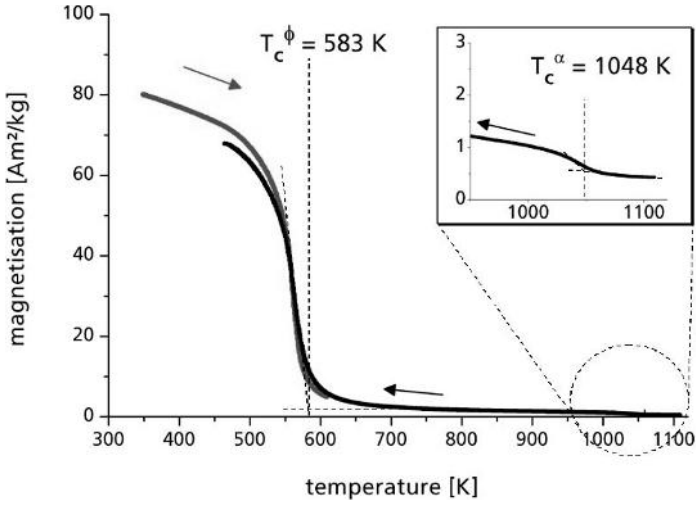

Fig. 6 TMA of a $Nd_{14}Fe_{79}B_7$-sample solidified primarily in ϕ-phase at $\Delta T = 60$ K, according to Figure 5, at a homogeneous magnetic field $H_0 = 512.5$ kA/m. The heating ($\rightarrow$) was operated by 2 K/min, the subsequent cooling ($\leftarrow$) by –2 K/min.

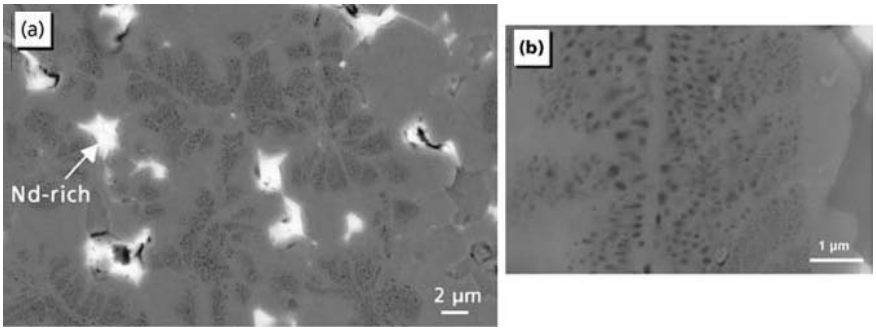

Fig. 7 Scanning electron micrographs in the backscattered mode of a levitated $Nd_{14}Fe_{79}B_7$-sample solidified primarily in a metastable phase at $\Delta T = 80$ K. The subsequently nucleating liquid is Nd-rich (white). The metastable phase decomposed into a fine mixture of an iron-rich phase (dark dots) and the ϕ-phase (grey matrix) as shown enlarged in micrograph (b).

Figure 7. It is assumed that these structures originate from a metastable phase which has been solidified primarily in the undercooled melt and decomposed during subsequent cooling. Presumably, the metastable phase is identical to the χ-phase, observed in drop tube solidified particles, with a Curie-temperature $T_C \sim 373$ K [11].

The thermomagnetic analysis of the corresponding bulk-sample presented in Figure 8 reveals that no residual amount of the primarily nucleated metastable γ-phase

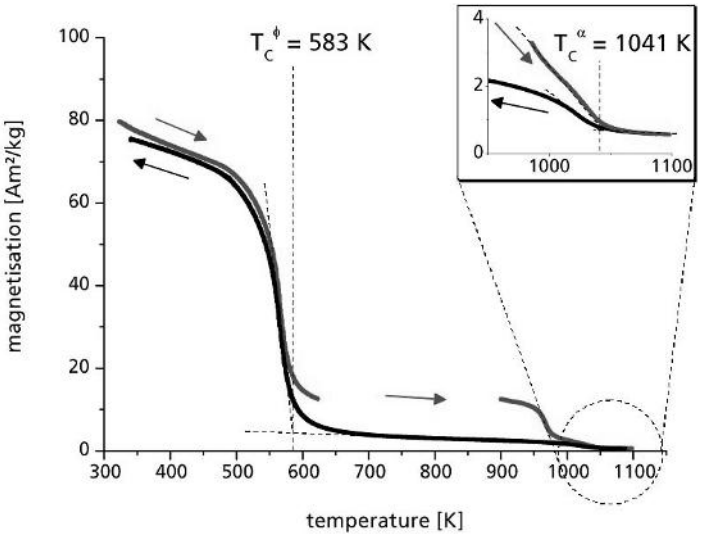

Fig. 8 TMA of a $Nd_{14}Fe_{79}B_7$-sample solidified primarily in a metastable phase at ΔT = 80 K, according to Fig. 7, at a homogeneous magnetic field H_0 = 512.5 kA/m. The heating (→) was operated by 2 K/min, the subsequent cooling (←) by –2 K/min.

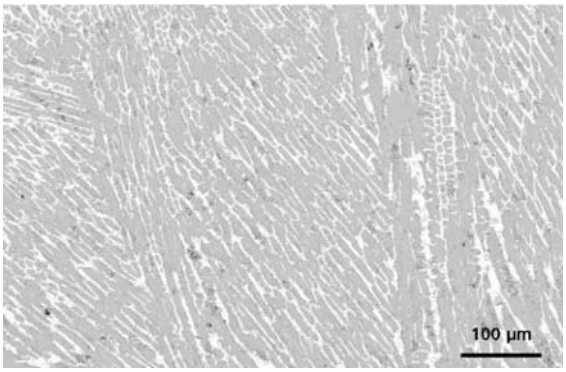

Fig. 9 Scanning electron micrograph in the backscattered mode of a levitated $Nd_{22}Fe_{67}B_{11}$-sample solidified primarily in ϕ-phase at ΔT = 87 K. The phases are marked in the micrograph as: ϕ-phase (grey) and Nd-rich phase (white). Obviously, no γ-Fe can be detected in this cross section.

can be preserved. Instead, the fraction of α-Fe is enhanced compared to that of the sample primarily solidified in ϕ-phase (see Figure 6) as reflected by the higher magnetisation above T_C^{ϕ} = 583 K. The distinct decrease of the magnetisation above 950 K while heating is again a hint for the ongoing peritectic transformation. Due to the elevated temperatures the iron phase is partially dissolving and hence, the subse-

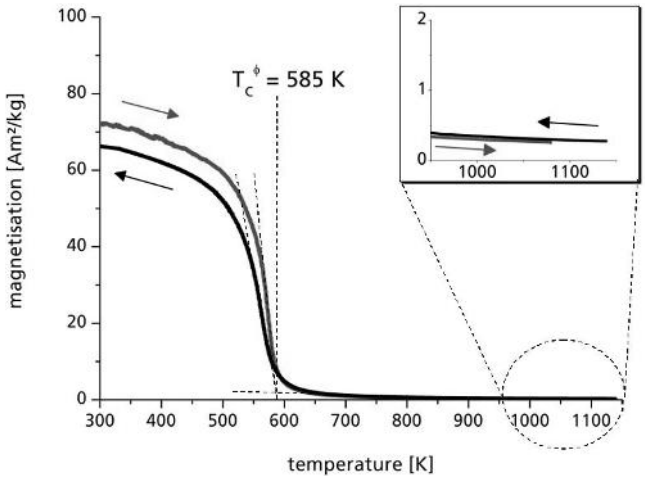

Fig. 10 TMA of a $Nd_{22}Fe_{67}B_{11}$-sample solidified primarily in ϕ-phase at $\Delta T = 87$ K, according to Figure 9, at a homogeneous magnetic field $H_0 = 512.5$ kA/m. The heating (→) was operated by 2 K/min, the subsequent cooling (←) by –2 K/min.

quent cooling reveals a lower content of α-Fe. Thus, it is concluded that the decomposed structure consists of the ϕ-phase and the α-Fe phase, which are identified by their Curie-temperatures $T_C^{\phi} = 583$ K and $T_C^{\alpha} = 1041$ K.

According to the published phase diagram of the ternary Nd-Fe-B alloy system [10], $Nd_{22}Fe_{67}B_{11}$ is in the non-peritectic region where the ϕ-phase is the equilibrium phase for primary solidification. From the thermodynamic point of view the metastable γ-phase may compete with the ϕ-phase during solidification of undercooled alloy melts if kinetic aspects are taken into account [12]. The cross section of a $Nd_{22}Fe_{67}B_{11}$ alloy solidified at an undercooling $\Delta T = 87$ K presented in Figure 9 illustrates large dendrites of primary ϕ-phase in a Nd-rich matrix.

The corresponding thermomagnetic analysis shown in Figure 10 confirms that no residual amount of α-Fe due to the decomposition of potential primary solidification of metastable χ-phase can be detected in the volume content of the specimen. The sole magnetic transition of the sample is detected at $T_C^{\phi} = 585$ K, the Curie-temperature of the ϕ-phase. For undercooling levels $\Delta T < 90$ K no solidification of the metastable χ-phase can be listed in this non-peritectic composition.

26.4 Summary

Bulk $Nd_xFe_{100-1.5x}B_{0.5x}$ alloy droplets (x = 11.8, 14, 22) undercooled and solidified using the electromagnetic levitation technique have been investigated thermomagnetically using a high resolution Faraday-balance. The phase content of the magnetic phases is detected which allows to analyse the correlation of the macroscopic magnetisation on the microstructure and hence the primary nucleating phase. No preserved metastable phase is found in the bulk alloys but the decomposition products α-Fe and ϕ-phase can be detected. Even smallest amounts of α-Fe which have not been detected by surface-sensitive EDX-analyses are verified by the bulk-sensitive TMA. In comparison to the primary solidification of γ-Fe phase (i) the samples with moderate and large undercoolings which have been primarily solidified in the ϕ-phase (ii) or the metastable χ-phase (iii) are found to contain a reduced amount of α-Fe. In case (ii), the primary solidification of the ϕ-phase, small contents of α-Fe follow presumably from multiple nucleation and in case (iii), the primary solidification of the metastable γ-phase, the amount of α-Fe results from the decomposition process. In all cases (i), (ii) and (iii) the amount of α-Fe is reduced in the thermomagnetic processing due to the slow cooling and heating rate at elevated temperatures. The suppression of primary solidification of pro-peritectic γ-Fe phase and as a consequence thereof the primary solidification of either peritectic ϕ-phase or metastable χ-phase can be verified by TMA only for hyper-peritectic alloy samples. Since the field strength of the external magnetic field $H_0 \leq 1025$ kA/m is not sufficient to reach the complete saturation of the residual ϕ-phase further quantitative analyses on the sustained samples have to be limited to the volume content of soft-magnetic α-Fe phase. In order to further reduce the amount of α-Fe in the as-solidified samples the cooling rate of the samples has to be increased to avoid the re-entrant formation of the α-Fe phase.

Acknowledgements

This work is financially supported by the German Space Agency (DLR) under contract No. 50WM9930 (S.R.) and the Deutsche Forschungsgemeinschaft under contract No. He 1601/14 (J.S.). One of the authors (J.G.) is also grateful to the Alexander von Humboldt Foundation for a long-term cooperation research fellowship. The authors wish to express their thanks to Dr. H. Bach, Dr. D. Holland-Moritz and Dr. M. Kolbe for continuous support.

References

[1] J. Gao, T. Volkmann, D. M. Herlach, IEEE Trans. Mag. 2002,Vol. 38, No. 5, 2910-2912

[2] J. Gao, T. Volkmann, D. M. Herlach, Act. Mat. 2002,Vol. 50, 3003-3012

[3] T. Volkmann, J. Gao, D. M. Herlach, Appl. Phys. Lett. 2002,Vol. 80, 1915-1917

[4] M. Seeger, H. Kronmüller, Z. Metallk. 1996,Vol. 87, 923

[5] T. Umeda, T. Okane, W. Kurz, Acta Mater. 1996,Vol. 44, 4209

[6] R. Hermann, I. Bđcher, D. Matson, W. Löser, L. Schultz, IEEE Trans. Mag. 2001,Vol. 37, No. 3, 1100

[7] J. Gao, T. Volkmann, D. M. Herlach, J. of Alloys and Comp. 2000,Vol. 308, 296

[8] D. M. Herlach, R. Willnecker, F. Gillessen in Proc. 5th Europ. Symp. on Mater. Sci. under Microgravity, Ed.: T. D. Guyenne, ESA-SP 222, European Space Agency, Noordwijk, 1984, 399

[9] S. Reutzel, D.M. Herlach, Adv. Eng. Mater. 2001,Vol. 3, No. 1-2, 65-67

[10] G. Schneider, E.-T. Henig, G. Petzow, H. H. Stadelmaier, Z. Metallkd. 1986, Vol. 77, 755

[11] J. Gao, T. Volkmann, S. Roth. W. Löser, D. M. Herlach, J. Magn. Magn. Mater. 2001,Vol. 234, 313

[12] H. W. Kerr, W. Kurz, Inter. Mater. Rev. 1996,Vol. 41, 129

27
Analysis of the Solidification Microstructure of Multi-component Gamma Titanium Aluminide Alloys

Viola Küstner, Michael Oehring, Anita Chatterjee, Helmut Clemens, Fritz Appel

27.1
Introduction

In the last decade significant progress has been achieved in the development of γ titanium aluminide alloys for high-temperature applications [1–4]. Casting of components has already been explored and developed up to successful turbine tests of low-pressure turbine blades [5, 6] as well as to the commercial use of turbo-charger wheels [4, 7]. However, cast alloys suffer in general from coarse microstructures, which limit the damage tolerance of the materials, in particular in the case of high-strength alloys. In addition, after casting, large columnar grains with a pronounced preferential crystallographic orientation in the growth direction [8, 9] are often found. According to the phase diagram [10, 11], solidification of engineering γ titanium aluminide alloys occurs via the β and/or α phase. Thus, owing to different solidification paths, both the microstructure and casting texture are highly sensitive to alloy composition in the concentration range of 45–49 at.% Al. In the present work, the microstructure formation during solidification of γ titanium aluminide alloys was investigated to determine the dependence on the alloy composition. Although quite a number of studies have been devoted to this topic [8–10, 12–16], the understanding of the manifold processes occurring on solidification and their relation to alloy composition still is not complete. A particular difficulty arises due to the fact that subsequent solid-state transformations may mask the initial solidification structure. In this context, micro-analytical investigations have been performed, as they may provide additional evidence with respect to phase constitution during solidification. The study included binary alloys, since the equilibrium constitution is only sufficiently known for the binary system. Further, the effect of alloying additions has been investigated which are interesting with respect to engineering applications. Here, in particular, Nb and B were selected, which improve the high-temperature properties [17] or act as grain-refining agents [13, 18], respectively.

27.2 Experiments

In this work the dependence on the composition of the solidification behaviour was studied on arc-melted alloy buttons. Buttons of about 32 g weight were melted in a laboratory arc-melting furnace on a water-cooled copper plate under Ar atmosphere. The investigated materials included binary alloys with an Al concentration of 42–51 at.% and some multi-component alloys on the basis of Ti-45Al and Ti-47Al (at.%) containing different additions of Nb, Mo and B. As starting materials high-purity metals and an Al-4wt.% B master alloy were used. The buttons were melted at least 5 times to ensure sufficient homogeneity. Consideration of the heat flow on solidification of the buttons suggests the cooling conditions in regions near the symmetry axis might be similar to those during casting an alloy into a metallic mould. Thus, it is believed that along the symmetry axis the ratio of the temperature gradient G to the solidification velocity R decreases continuously with increasing distance to the mould [19]. This, however, does not hold for areas close to the top of the buttons where heat losses occur due to radiation.

For microstructural and analytical investigations, slices were taken from the buttons which contained the symmetry axis. The macrostructure was made visible by etching the specimens in a solution of 5 vol. % HF + 15 vol.% HNO_3 + 80 vol.% distilled water. Specimens for scanning electron microscopy were prepared by grinding and subsequent electropolishing at –19 V and a temperature of –45 °C. The electrolyte used consisted of 600 ml methanol, 300 ml n-butanol and 60 ml perchloric acid. Scanning electron microscopy was performed exclusively in the back-scattering mode using a Zeiss DSM962 microscope. The microscope was equipped with an energy-dispersive X-ray (EDX) analysis system (Link Oxford), which was calibrated using binary and ternary alloy standards. The overall compositions of all buttons were found to match the nominal composition within a maximum deviation of 0.7 at.% in the Al concentration.

27.3 Results

After etching, longitudinal sections of some buttons showed a distinct zone (chill zone) along the bottom and in some cases also at the top of the buttons (Figure 1). Apart from this zone, the solidification microstructure changed significantly with composition. The binary alloy Ti-45Al showed a microstructure consisting of large, equiaxed grains, whereas alloys with Al contents 46 at.% clearly exhibited columnar grains which had grown in the direction of the heat extraction. Ternary alloys based on Ti-45Al and Ti-47Al containing additions of 5 at.% Nb or 2 at.% Mo showed similar macrostructures to the corresponding binary alloys.

Additions of 0.2, 0.5 and 1 at.% B to alloys of base compositions Ti-45Al-5Nb as well as 0.5 at.% B to a multi-component alloy in general resulted in microstructural refinement, as is well known from literature [13, 18]. The change in microstructure

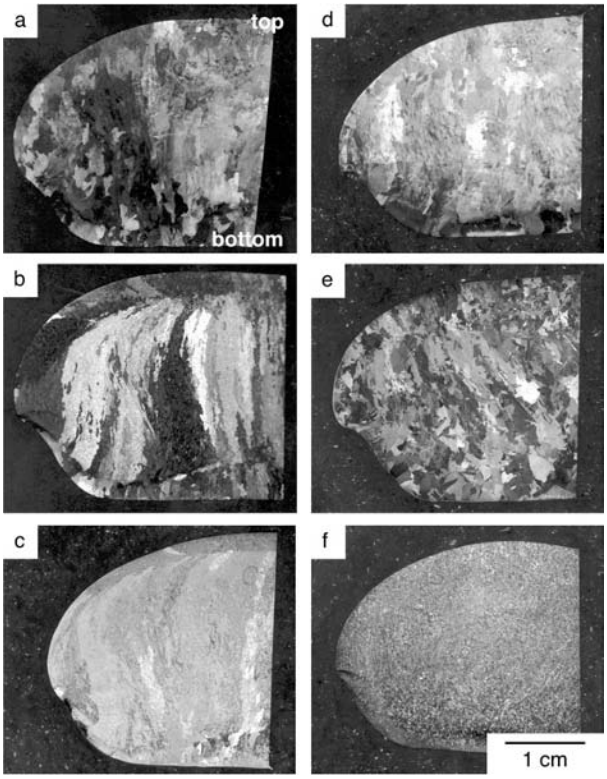

Fig. 1 Macro-photographs of etched specimens: a) Ti-45Al, b) Ti-47 Al, c) Ti-48Al, d) Ti-45Al-5Nb, e) Ti-45Al-2Mo, f) Ti-45Al-5Nb-1.0B. Top and bottom are indicated in a).

by alloying with B in particular was strongly pronounced for all B containing alloys based on Ti-45Al-5Nb. As shown in Figure 1 f., homogeneous and very fine equiaxed microstructures over the entire buttons were obtained for these alloys.

Scanning electron microscope observations have shown that the microstructure of the binary Ti-45Al alloy exhibits a morphology similar to that of lamellar near-α Ti alloys (Figure 2 b). Higher magnifications show that the plate-like constituent consists completely of α_2 and γ lamellae. This morphology is explained by the solid-state reaction path $\beta \rightarrow \alpha \rightarrow \alpha + \gamma$. In the first transformation crystallographically oriented Widmannstätten α plates are precipitated from the β phase. This leads to the segregation of Ti to ribs of remaining β phase, which transform in later stages of the process. Subsequently, γ lamellae are formed within α plates. This type of morphology was also observed in micrographs of the alloys Ti-45Al-5Nb and Ti-45Al-2Mo, in which the ribs of retained β phase are clearly marked due to the segregation of the heavy alloying elements (Figure 3 a). Similar microstructures have often been reported to occur in γ (TiAl) cast alloys [8, 14, 20]. From the microstructural observations reported here it is concluded that in agreement with the phase diagram, solidi-

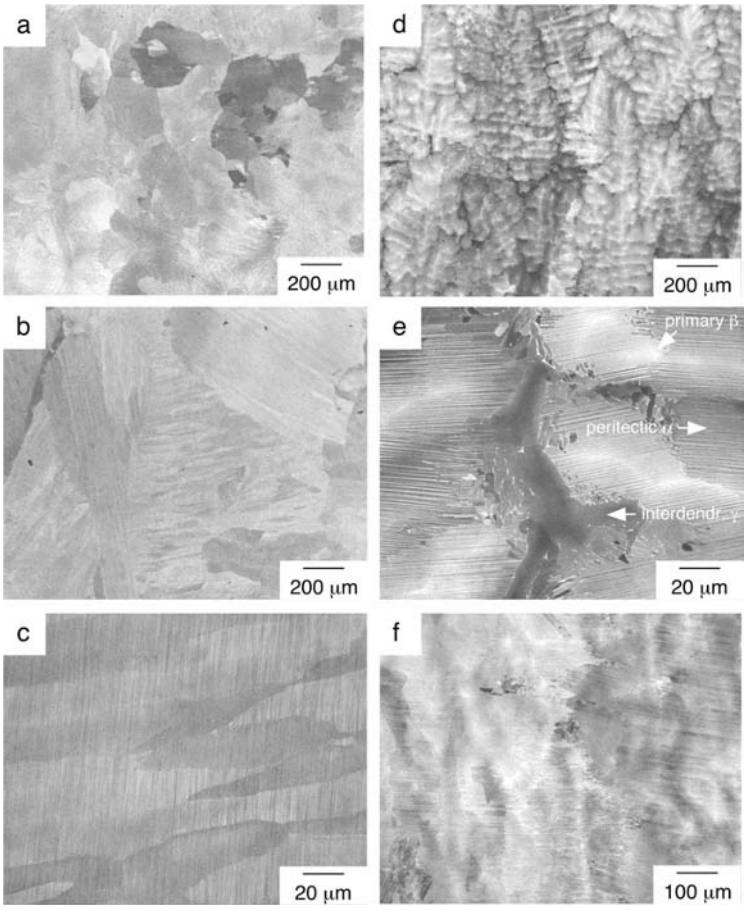

Fig. 2 Scanning electron micrographs taken in the back-scattering electron mode from arc-melted buttons: a) Ti-45Al, upper part of the button, b) Ti-45Al, lower part of the button, c) region from b) in higher magnification, d) Ti-48Al, upper part of the button, e) region from d) in higher magnification, f) Ti-48Al lower part of the button. Please note that some dendrites in d) have orthogonal side arms.

fication occurred solely via the β phase for the foregoing alloys. Further, it should be noted that for these alloys no indications of dendritic or cellular solidification were observed over the whole longitudinal sections of the buttons.

The microstructural observations were supported by microchemical analyses as depicted in Figure 4. As shown in the concentration line profile taken perpendicular to the heat flow direction near the bottom of the button (Figure 4b), small concentration fluctuations between 44 and 46 at.% Al were found in the alloy Ti-45Al. These inhomogeneities might be attributed to the $\beta \rightarrow \alpha$ transformation or to segregation on solidification. Also, in the upper half of the ingot (Figure 4a), concentration varia-

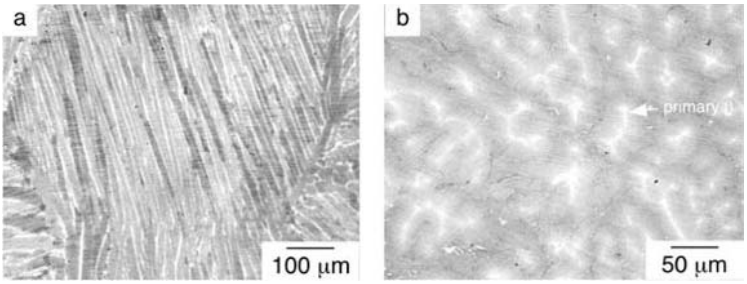

Fig. 3 Scanning electron micrographs taken in the back-scattering electron mode from arc-melted buttons: a) Ti-45Al-5Nb, b) Ti-46.5Al-3.7(Nb,Cr,Mn,Si)-0.5B. Please note the different morphology of segregation which arises in a) due to solid-state transformations and reflects the dendrite coring in b).

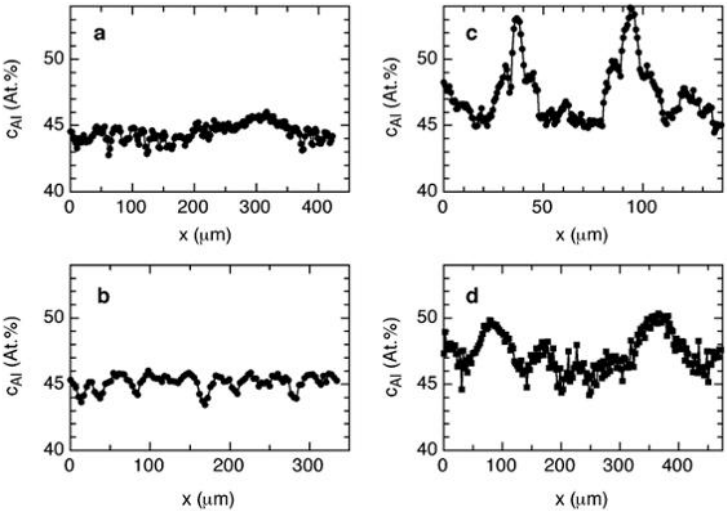

Fig. 4 Quantitative concentration line profiles as obtained by EDX analysis from arc-melted buttons. a) Ti-45Al, upper part of the button, b) Ti-45Al, lower part, c) Ti-48Al, upper part, and d) Ti-48Al, lower part of the button.

tions with a relatively small amplitude were observed. However, the wavelength was significantly increased, which might indicate segregation due to dendritic solidification. Similarly, only modest concentration variations were found for the alloys Ti-45Al-5Nb, Ti-45Al-5Nb-1B and Ti-45Al-2Mo, with the exception of the previously mentioned bands of the β phase. Thus, from the EDX investigations, it is concluded that all alloys on the base Ti-45Al solidified completely through the β phase without pronounced segregation.

Microstructural investigations on the alloys with Al contents >45 Al showed that the tendency for both columnar growth in the lower part of the buttons and for dendrite formation in the upper part increased with the Al concentration. As an example, the microstructure of Ti-48Al will be described in more detail in the following. In the lower part of the buttons a nearly lamellar microstructure was observed. The colonies were extended in the direction of heat flow (Figure 2f). In most, but not all cases the lamellae were aligned perpendicular to the temperature gradient. The dendrites occurring in the upper part of the buttons were also lamellar (Figure 2d, e) and with dendrite cores that appear light in the image indicating the enrichment of Ti. The interdendritic regions consisted of single-phase γ grains. In the lower part of the buttons, Al concentrations of 45 at.% were found in the center of columnar grains (Figure 4d). This indicates that β was the primary solidifying phase, whereas intercellular regions showed the concentration of the peritectic α phase (47–48 at.%). A line profile taken across three dendrite arms in the upper part of the button again showed the concentration of the primary β phase in the dendrite cores, that of the peritectic α phase in adjacent dendrite regions and interdentritically Al enrichments up to 54 at.% (Figure 4c). Thus, the alloy passed through both peritectic transformations of the system resulting in concentration variations of 9 at.% over relatively short distances. Similar features were also observed for the alloys Ti-46Al, Ti-47Al, Ti-47Al-5Nb, Ti-47Al-2Mo and a B containing alloy based on Ti-46.5 Al (Figure 4b). For the TiAl alloy with the highest Al concentration investigated (Ti-51Al), an Al concentration of 47–48 at.% was determined in dendrite cores and thus, α was the primary solidifying phase in agreement with the phase diagram.

27.4 Discussion

The results observed in this work showed that in the concentration range 45–47 at.% Al the microstructure changed markedly from equiaxed to columnar grains and the degree of segregation increased significantly with increasing Al content. It could be speculated that this difference arises due to the occurrence of plane front solidification for 45 at.% Al and of constitutional undercooling for Al concentrations >46 at.%, which would result in a cellular or cellular-dendritic solidification mode. However, in this case it has to be assumed that α is the primary phase for Al concentrations >46 at.% which clearly contradicts the experimental observations. Nevertheless, it seems useful to consider whether there are significant changes between the β and the α phase with respect to constitutional undercooling. Constitutional undercooling occurs if the ratio of the temperature gradient G to the solidification velocity R fulfils the following condition [21, 22]

$$G/R \leq m_L c_0 (k_0 - 1)/(k_0 D_L), \quad (1)$$

with m_L: slope of the liquidus line, c_0: alloy concentration, $k_0 = c_S/c_L$: partitioning coefficient, and D_L: diffusion coefficient in the liquid phase. In the following it is as-

sumed that β solidifies at 45 at.% Al and α at 47 at.% Al. m_L and k_0 were determined by linearly approximating the phase diagram of Ohnuma et al. [11] under the condition that the liquidus and the solidus lines intersect for 0 at.% Al. For the diffusion coefficient of the melt in both cases the value $D_L = 2.8 \cdot 10^{-9}$ m^2 s^{-1} was taken [23]. Then, for solidification of the β and the α phases critical values for G/R of $1.1 \cdot 10^{10}$ K s m^{-2} and of $8.9 \cdot 10^9$ K s m^{-2} are obtained, respectively. Since much larger variations in G/R than this small difference are expected to occur in the buttons, it has to be concluded that the investigated alloys solidify under constitutional undercooling irrespective of their Al content. Because only rarely indications for cellular or cellular-dendritic growth were found in alloys with an Al content of 45 at.%, this further means that such alloys solidify by equiaxed dendritic growth of the β phase. In the final state of solidification a β grain is formed from each equiaxed dendrite. In such alloys β dendrites grow in the stationary case with the composition of the alloy and only modest segregations occur. In contrast, in peritectic alloys solidification over the peritectic cascade leads to considerable concentration differences and steep concentration gradients at phase boundaries.

It remains to understand why peritectic alloys exhibited columnar growth and hypo-peritectic alloys did not. Generally, in alloys, except rather pure metals, columnar growth is of cellular-dendritic type [21]. If during columnar growth the temperature of the melt in front of the solid/liquid interface is above the nucleation temperature, no further nuclei can form and columnar growth will proceed. On the other hand, if nucleation is possible in this zone, new crystals are formed and an equiaxed microstructure is formed. Since the β phase is kinetically favoured over the α phase due to its stronger bias to nucleation sites in the liquid as found by Valencia et al. [16], equiaxed solidification microstructures of completely β solidifying alloys appear plausible. Johnson et al. [14] have analysed the columnar/equiaxed transition which occurs according to Hunt [24] if

$$G < 0.617\, N_0^{1/3}\, (1 - \Delta T_N^3/\Delta T_c^3)\, \Delta T_c\,, \tag{2}$$

with N_0 being the number of sites for heterogeneous nucleation, ΔT_N the undercooling for heterogeneous nucleation and $\Delta T_c \sim \sqrt{R}$ the undercooling at the solid/liquid interface. They concluded that the columnar/equiaxed transition will always occur for the β phase in an earlier stage of solidification than for the α phase, even if in both cases the same values are assumed for ΔT_N and N_0. This behaviour is caused by the smaller freezing interval of α according to the phase diagram, which, when compared to β, results in a smaller value of ΔT_c [19]. If, in addition, the undercooling ΔT_N on heterogeneous nucleation is smaller for the β than for the α phase, equiaxed growth of the β phase will occur in an even wider field of conditions. However, β is also the primary phase for peritectic alloys. For these alloys the cellular-dendritic growth as observed in the lower parts of the buttons may then be understood by the interdendritic formation of the α phase. The EDX line profiles have shown that the melt is enriched up to Al concentrations around 54 at.% Al near the peritectic α phase (Figure 4). At such Al contents the β phase cannot be formed ahead of the solid/liquid interface and thus, columnar growth is expected to occur. After the alloy

has completely solidified, the interdendritically formed α phase then can grow into the β phase due the β/α transformation. Thus, the β/α transformation will not occur via the nucleation of crystallographically oriented α plates from the parent β phase as observed for alloys which solidify completely through the β phase (see previous section). This could not only explain the transition in the solidification morphology from equiaxed to columnar growth when the Al concentration is raised from 45 to 47 at.% but also make plausible why the β/α transformation results in completely different microstructures (compare Figure 3). Further, also the texture of peritectic alloys could be understood in this way, which clearly originates from the α phase [8], although β was found to be the primary phase by EDX analysis.

27.5 Conclusions

The microstructure formation during solidification of γ titanium aluminide alloy buttons has been investigated for binary and multi-component alloys. In agreement with literature it was found that the solidification microstructure is highly dependent on the solidification path – either solidification solely via the β phase or peritectic solidification. The observed difference in morphology can be attributed to the columnar/equiaxed transition, which for the β phase seems to be favoured in comparison to the α phase due to a kinetic preference of heterogeneous nucleation and a larger freezing interval. The isotropic and texture-free solidification microstructures of alloys solidifying solely via the β phase seem in principle attractive with respect to the mechanical properties if the strong grain-refining effect due to alloying with B is used.

Acknowledgements

We are very grateful to C. Buque, S. Eggert, P. Fischer, U. Fröbel, R. Imayev, V. Imayev, U. Lorenz, J. Müllauer, and J.D.H. Paul for cooperation in research on γ titanium aluminides.

References

[1] Y-W. Kim, D.M Dimiduk, in Structural Intermetallics 1997 (Eds. M.V. Nathal, R. Darolia, C.T. Liu, P.L. Martin, D.B. Miracle, R. Wagner, M. Yamaguchi), TMS, Warrendale, PA, USA, 1997, 531–543.

[2] F. Appel, R. Wagner, Mater. Sci. Eng. R 1998, R22, 187–268.

[3] H. Clemens, H. Kestler, Adv. Eng. Mater. 2000, 2, 551–570.

[4] M. Yamaguchi, H. Inui, K. Ito, Acta mater. 2000, 48, 307–322.

[5] C.M. Austin, T.J. Kelly, in Gamma Titanium Aluminides (Eds. Y-W. Kim, R. Wagner, M. Yamaguchi), TMS, Warrendale, PA, USA, 1995, 21–32.

[6] R. Wagner, F. Appel, B. Dogan, P.J. Ennis, U. Lorenz, J. Müllauer, H.P. Nicolai, W. Quadakkers, L. Singheiser, W. Smarsly, W. Vaidya,

K. Wurzwallner, in Gamma Titanium Aluminides (Eds. Y-W. Kim, R. Wagner, M. Yamaguchi), TMS, Warrendale, PA, USA, 1995, 387–404.

[7] T. Tetsui, S. Ono, Intermetallics 1999, 7, 689–697.

[8] S. Naka, M. Thomas, C. Sanchez, T. Khan, in Structural Intermetallics 1997 (Eds. M.V. Nathal, R. Darolia, C.T. Liu, P.L. Martin, D.B. Miracle, R. Wagner, M. Yamaguchi), TMS, Warrendale, PA, USA, 1997, 313–322.

[9] M. DeGraef, N. Biery, L. Rishel, T.M. Pollock, A. Cramb, in Gamma Titanium Aluminides 1999 (Eds. Y-W. Kim, D.M. Dimiduk, M.H. Loretto), TMS, Warrendale, PA, USA, 1999, 247–254.

[10] C. McCullough, J.J. Valencia, C.G. Levi, R. Mehrabian, Acta metall. 1989, 37, 1321–1336.

[11] I. Ohnuma. Y. Fujita, H. Mitsui, K. Ishikawa, R. Kainuma, K. Ishida, Acta mater. 2000, 48, 3113–3123.

[12] M.E. Hyman, C. McCullough, J.J. Valencia, C.G. Levi, R. Mehrabian, Metall. Trans. A 1989, 20A, 1847–1859.

[13] T.T. Cheng, in Gamma Titanium Aluminides 1999 (Eds. Y-W. Kim, D.M. Dimiduk, M.H. Loretto), TMS, Warrendale, PA, USA, 1999, 389–396.

[14] D.R. Johnson, K. Chihara, H. Inui, M. Yamaguchi, Acta mater. 1998, 46, 6529–6540.

[15] H.N. Lee, D.R. Johnson, H. Inui, M.H. Oh, D.M. Wee and M. Yamaguchi, Acta mater. 2000, 48, 3221–3233.

[16] J.J. Valencia, C. McCullough, C.G. Levi, and R. Mehrabian, Acta metall. 1989, 37, 2517–2530.

[17] J.D.H. Paul, F. Appel, and R. Wagner, Acta mater. 1998, 46, 1075–1085.

[18] D.E Larsen, in Intermetallic Matrix Composites (Eds. D.L. Anton, R. McMeeking, D. Miracle, P. Martin), Mater. Res. Soc. Symp. Proc. Vol. 194, MRS, Pittsburgh, PA, USA, 1990, 285–292.

[19] W. Kurz, D.J. Fisher, Fundamentals of Solidification, Trans Tech Publications, Aedermannsdorf, Switzerland, 1984.

[20] A.K. Singh, D. Banerjee, Metall. Mater. Trans. A 1997, 28, 1735–1743.

[21] B. Chalmers, Principles of Solidification, John Wiley and Sons, New York, NY, USA, 1964.

[22] W.A. Tiller, K.A. Jackson, J.W. Rutter, B. Chalmers, Acta metall. 1953, 1, 428–437.

[23] Y. Liu, G. Yang, Y. Zhou, J. Cryst. Growth 2002, 240, 603–610.

[24] J.D. Hunt, Mater. Sci. Eng. 1984, 65, 75–83.

28
Formation of Eutectic Cells in Ternary Al-Cu-Ag Alloys

Ulrike Hecht, Victor Witusiewicz, Anne Drevermann, Stephan Rex

28.1
Introduction

In ternary alloys A-B-C coupled growth of two solid phases α(A) and β(B) in *univariant eutectic reaction* occurs with an exchange of species A and B by interlamellar diffusion, much like in binary (nonvariant) eutectic growth. Additionally a long-range solute boundary layer is established at the solid/liquid interface due to the segregation of the third component C, similar to what is known from the solid/liquid interface of a solid solution-phase growing from a binary liquid (univariant).

With this, the univariant eutectic interface can be constitutionally undercooled and morphological transitions can occur leading to eutectic cells or dendrites, as is observed in metallic [1–3], ceramic [4] and transparent organic systems [5].

The destabilization of a planar eutectic interface, the morphological transition to cells and finally the characteristics of the resulting cellular array are still far from being understood. This is especially true for 3D, meaning for bulk samples. For 2D or thin samples, the linear stability analysis performed by Plapp and Karma [6] for lamellar eutectic interfaces in the presence of a ternary impurity gives valuable insight into the dynamics of the eutectic front. According to their analysis the instability is similar to the standard Mullins-Sekerka instability for single phase solidification, but with an oscillatory character that results from specific contributions of the lamellar eutectic structure. Moreover, the interlamellar diffusion acts as a capillary force that controls the restabilization of the interface at short wavelengths.

In the present contribution we report on experimental observations related to the formation of eutectic cells and the characteristics of cellular arrays in ternary Al-Cu-Ag alloys during univariant eutectic growth in bulk samples.

28.2
Experimental Procedure

28.2.1
Sample Material

Throughout this paper we refer to unidirectionally solidified samples of ternary Al-rich alloys from the Al-Cu-Ag system. The composition of the sample materials Al-Cu 13.66 at%-Ag 10.27 at% and Al-Cu 15.52 at%-Ag 9.04 at% are located on or close to the eutectic groove that corresponds to the univariant eutectic reaction "liquid → α(Al) + Al_2Cu + liquid'", as indicated on the liquidus projection of the system Al-Cu-Ag [7] presented in figure 1. The samples were prepared by melting an appropriate mixture of Al (99.99 wt%), Cu (99.99 wt%) and Ag (99.97 wt%) under protective atmosphere (Ar) and subsequently casting the melt into a metallic mold with 6 cylindrical cavities ∅ 12 × 220 [mm].

28.2.2
Solidification Process and Sample Analysis

Unidirectional solidification of cylindrical samples (∅ 7.5 × 165 [mm]) contained in alumina tubes was performed in a vertical Bridgman-type furnace with liquid metal cooling, after having molten about 115 mm of the sample. With heater and cooler temperatures set at 1175 °C and 50 °C, respectively the solid/liquid interface was positioned in the middle of the adiabatic zone (baffle) and a temperature gradient of 27 ± 2 [K/mm] was achieved at the interface. Solidification was performed in direc-

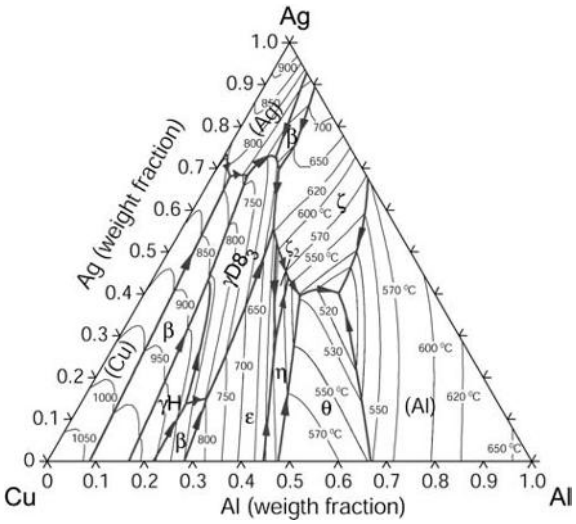

Fig. 1 Projection of the liquidus surface of the ternary system Al-Cu-Ag calculated with Thermo-Calc and the thermodynamic database [7].

tion opposite to gravity, in a thermosolutally stable configuration, on a length of 40 mm at different furnace velocities ranging from 0.05 mm/min to 0.23 mm/min followed by quenching.

All the samples were polycrystalline and showed strong grain selection within the first 15 mm of solidification, the selection resulting in an overall reduction of the number of grains from some more than 20 at the beginning of solidification to about 5 grains at quenching.

After solidification the samples were extracted from the alumina crucible and metallographically prepared for analysis in longitudinal section first and later on in cross sections close to the quenched-in solid/liquid interface. The microstructures were analyzed by means of scanning electron microscopy (SEM Gemini 1515) and image analysis (software KS400). For measuring concentration profiles and the chemical composition of the different phases we used energy dispersive X-ray analysis (EDX).

28.3 Experimental Results

All samples solidified along the univariant eutectic reaction *liquid* → α *(Al)* + *Al_2Cu* + *liquid'* exhibit coupled eutectic growth of two solid phases, α(Al) and Al_2Cu: α(Al) is a solid solution phase with large solubility for Ag and less for Cu with a cubic face centered crystal structure (cF4). Al_2Cu, the so called θ-phase with a tetragonal structure (tP12), shows very limited solubility for Ag and a narrow solubility range around the stoichiometric composition Al 66,66at%-Cu33.33at%. From figure 2, that shows the tie triangle calculated for the alloy Al-Cu 15.52 at%-Ag 9.04 at% with Thermo-Calc [8] and the thermodynamic database of the ternary system Al-Cu-Ag [7], one can read the composition of the phases in equilibrium at the solid/liquid interface for

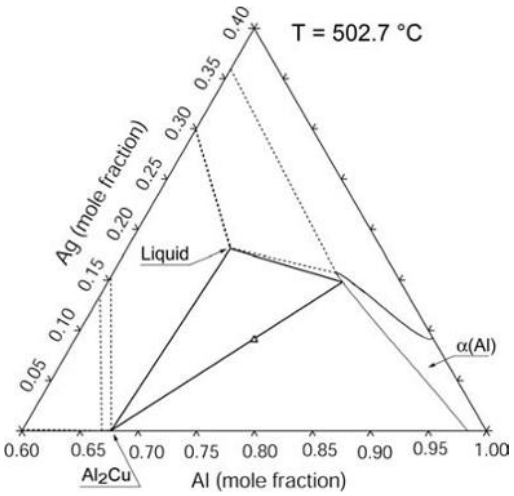

Fig. 2 Tie triangle for alloy Al-Cu 15.52 at%-Ag 9.04 at% calculated with Thermo-Calc and the database for Al-Cu-Ag [7].

the steady stategrowth rate approaching zero. For non-zero growth rates departure from thermodynamic equilibrium is due to undercooling and the correspondingly selected growth morphology.

In what follows we shortly discuss planar coupled growth and estimate the limit of stability, then proceed to describe the process of cell formation and the characteristics of cellular patterns.

28.3.1 Planar Coupled Growth

Figure 3 shows the quenched interface obtained for a sample of Al-Cu 15.52 at%-Ag 9.04 at% solidified with a furnace velocity of v = 0.085 mm/min in longitudinal section. The composition of the solid phases was measured by EDX along a line scan perpendicular to the lamellae and close to the quenched interface and is given in figure 4. From the maxima and minima of the line scan, the composition of α(Al) and Al_2Cu was determined: The α (Al) contains 4.64 at%Cu and 16.78 at%Ag and Al_2Cu contains 32at%Cu and 0.59at%Ag, these values being close to the respective edge points of the alloys tie triangle (figure 2).

The diffusion profile along the solute boundary layer ahead of interface was measured as function of the distance from the interface: For this a measuring field of 3000 µm × 20 µm with the long side parallel to the interface was displaced stepwise into the quenched liquid. The step size employed was of 20 µm. Figure 5 shows the diffusion profile of all three elements inside the boundary layer, while figure 6 shows the diffusion profile of the main element Ag fitted with an exponential function.

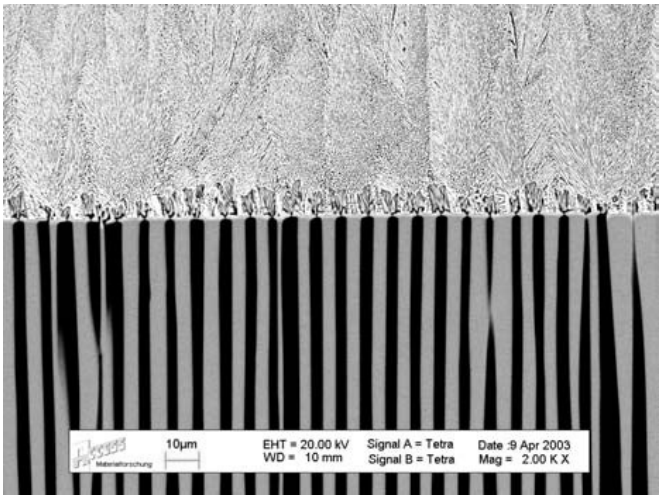

Fig. 3 Planar lamellar growth of α (Al) (light grey) and Al_2Cu (black) in the ternary alloy Al-Cu 15.52 at%-Ag 9.04 at% solidified at v = 0.85 mm/min and G = 27 ± 2 K/mm

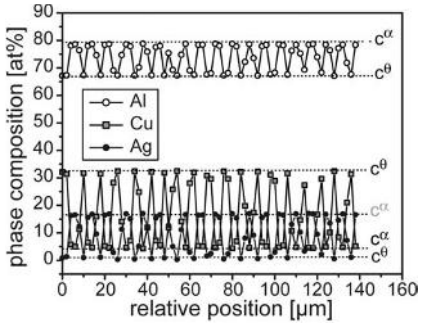

Fig. 4 Element distribution in the phases α (Al) and Al2Cu measured in a linescan perpendicular to the lamellae close to the quenched interface by energy dispersive X-ray analysis (EDX).

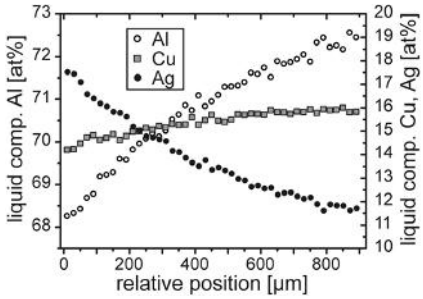

Fig. 5 Element distribution inside the solute boundary layer as function of the distance from the quenched interface.

From the parameters of the fit, and the known growth velocity, the effective diffusion coefficient of Ag can be calculated to be $0.89 \cdot 10^{-9}$ m^2/s. Moreover, from the difference between the Ag-concentration in the liquid and in the solid (weighted average) at the interface, the partition coefficient of Ag can be determined to be k_{Ag} = 0.54. Knowing from thermodynamic calulations that the slope of the eutectic groove with respect to Ag ranges at about M_{Ag} = –1.8 [K/at%] for the liquid composition at the interface, the Mullins-Sekerka criterion for the stability limit of the planar eutectic interface [9] gives a G/v-value of $16.6 \cdot 10^9$ Ks/m^2, or else for a temperature gradient G = 27 K/mm a critical velocity of 0.1 mm/min. Indeed, unidirectional solidification performed at a velocity of 0.122 mm/min shows morphological breakup and an early stage of cell formation.

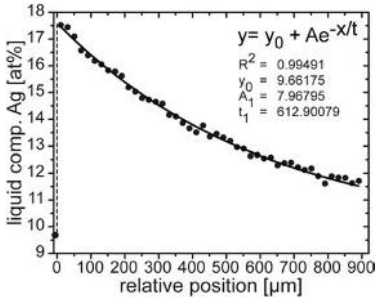

Fig. 6 Diffusion profile of Ag inside the solute boundary layer. The datapoint at (x = –1 µm, y = 9.68at%) shows the average Ag-concentration in the solid.

28.3.2
Cellular Coupled Growth: Elongated and Regular Cells

Figures 7a and 7b show the microstructure of a sample Al-Cu 13.66 at%-Ag 10.27 at% after unidirectional solidification at v = 0.122 mm/min in longitudinal and cross section. The most prominent feature, more easily observable in the cross section is

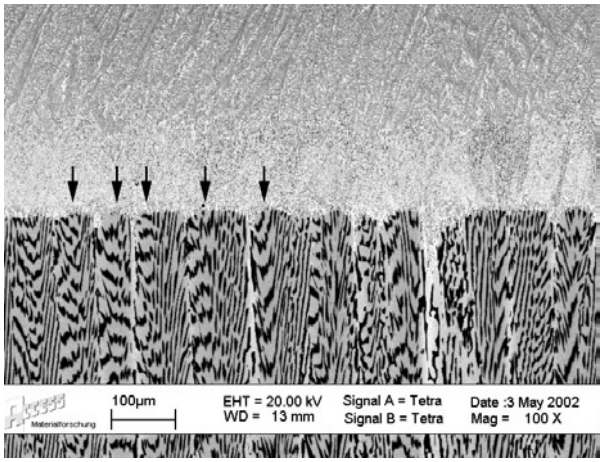

a)

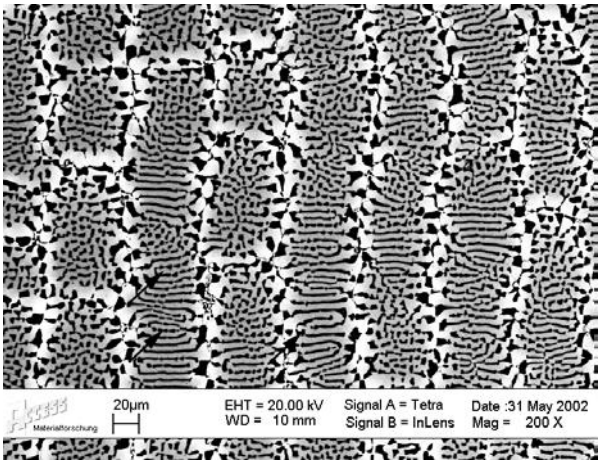

b)

Fig. 7 a) Longitudinal section through an array of elongated cells in sample Al-Cu 13.66 at%-Ag 10.27 at% solidified at v = 0,122 mm/min and G = 27 ± 2K/mm. b) Cross section through an array of elongated cells in sample Al-Cu 13.66 at%-Ag 10.27 at% solidified at v = 0,122 mm/min and G = 27 ± 2K/mm.

the elongated or ridge-like shape of the cells with walls that are perpendicular to the eutectic lamellae. The width of the cells is about one order of magnitude larger than the interlamellar spacing.

At several places inside the elongated cells, regular cells with square-like shape can be observed in various states of maturity: On the left hand side of figure 7b one elongated cell shows almost completely developed, mature regular cells. On the right hand side of figure 7b the elongated cells show regular cells in their nascent state. Obviously the eutectic structure inside the regular cells is no longer lamellar, while the elongated cells retain a lamellar arrangement, though with prominent nodul-like distorsions. To guide the eye some of these nodules are marked with black arrows in figure 7b. Here, neighboring lamellae of the θ-phase Al_2Cu (black) seem to loop up and give spiral-like or concentric structures. Such features are captured in the longitudinal section (figure 7a) as banded arrangements of α(Al) and Al_2Cu, and are marked with black arrows, likewise. Indeed, a 3D-object with a square base and long length consisting of a concentric or a spiral-like arrangement of two layers of different material, e.g. phases, will show banded structures, presuming that the sectional plane is neither parallel to the longitudinal axis nor to the edges of the object.

Figures 8a and 8b show the microstructure of a sample Al-Cu 13.66 at%-Ag 10.27 at% after unidirectional solidification at v = 0.156 mm/min in longitudinal and cross section. The sample consists of regular cells with a square shape arranged in an array of more or less square-like order. The pattern of regular eutectic cells in array was characterized according to the "minimum spanning tree", MST, a method initially proposed by [10] for assessing the order of a pattern based on the arrangement of the center points of a representative number of objects from the pattern. This method has sucessfully been applied [11,12] for the characterization of single phase cellular and dendritic patterns. The position of the centers of the individual cells needed as input for the MST construction have been determined by automatic image analysis, taking advantage of the fact that both phases α(Al) and Al_2Cu are coarse at the cell boundaries due to the curvature of the cells.

Figure 9a shows an analyzed cellular array, that includes a number of 273 cells with the identified cell centers and figure 9b gives the result of the MST-analysis performed for this array giving a normalized average edge length of $m^* = 0.9008$ and a normalized standard deviation of $\sigma^* = 0.1052$. A second array from within the same sample with a number of 279 cells gives similar results. Both arrays show (m^*, σ^*)-values that are close to the trajectory of square order patterns. With the standard deviation σ^* being non-zero, the patters show some amount of random gaussian noise. The analysis confirms the square order apparent to the eye. Inside the array, the intercellular spacings λ_c are distributed around the mean value $\lambda_c = 74$ μm. This value is one order of magnitude larger then the lamellar spacing of the planar eutectic and one order of magnitude smaller then the diffusion length of Ag. The mean characteristics of the cellular pattern are stable over large solidification lengths, a detailed presentation of this topic will be communicated elsewhere.

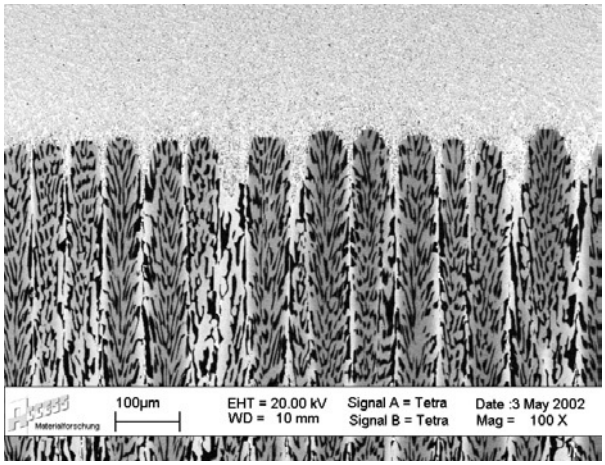

a)

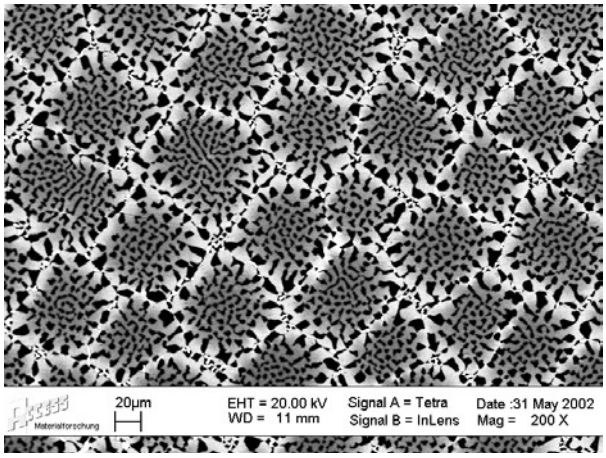

b)

Fig. 8 a) Longitudinal section through an array of regular cells in sample Al-Cu 13.66 at%-Ag 10.27 at% solidified at v = 0,156 mm/min and G = 27 ± 2K/mm. b) Cross section through an array of regular cells in sample Al-Cu 13.66 at%-Ag 10.27 at% solidified at v = 0,156 mm/min and G = 27 ± 2K/mm.

It is quite important to point out here, that regular cells develop from elongated cells as the velocity of solidification increases, but that elongated cells can persist in some grains inside a sample even if neighboring grains grow with regular cell structure. This is evidenced in figure 10a and figure 10b, showing two neighboring grains from within the sample Al-Cu 13.66 at%-Ag 10.27 at% after unidirectional solidification at v = 0.122 mm/min.

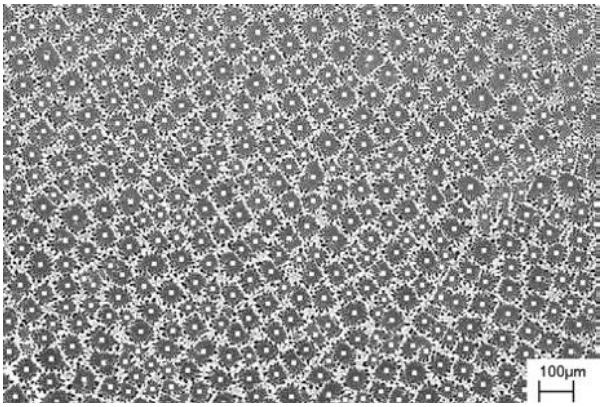

a)

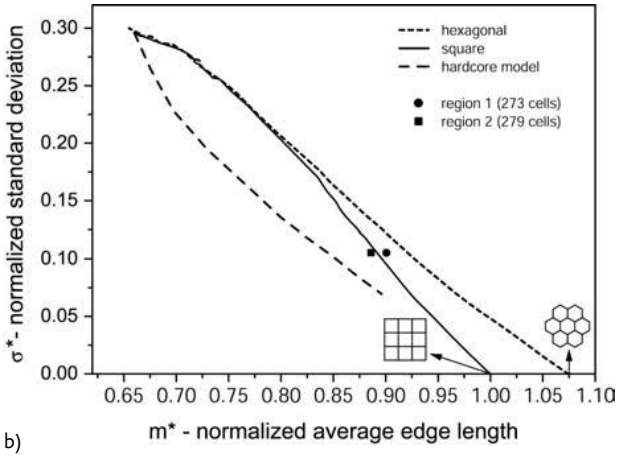

b)

Fig. 9 a) Region 1 of an array of regular cells used for determination of the order of the cellular pattern by the minimum spanning tree method in the alloy Al-Cu13.66 at%-Ag 10.27 at% solidified at v = 0,156 mm/min and G = 27 ± 2 K/mm. b) Minimum spanning tree analysis for two regions of sample Al-Cu 13.66 at%-Ag 10.27 at% solidified at v = 0,156 mm/min and G = 27 ± 2 K/mm show that the measured values are close to the trajectory of square-order patterns.

28.4 Discussion of the Process of Cell Formation

Based on the microstructural features described above that we observed and analyzed in many more then just the two samples referred to above, we propose the following three-step and 3D mechanism of cell formation to be operating for the univariant eutectic growth of α (Al) and Al_2Cu.

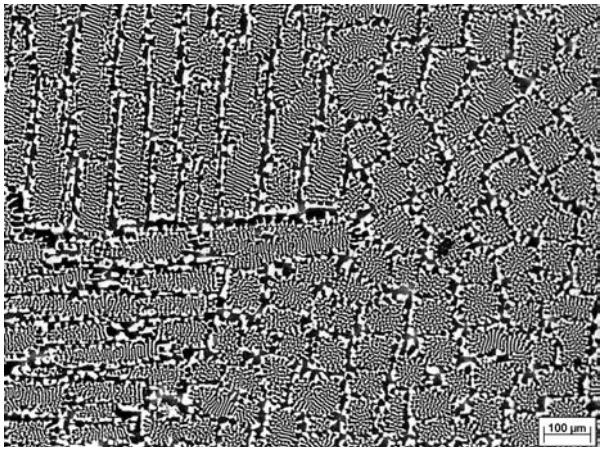

a)

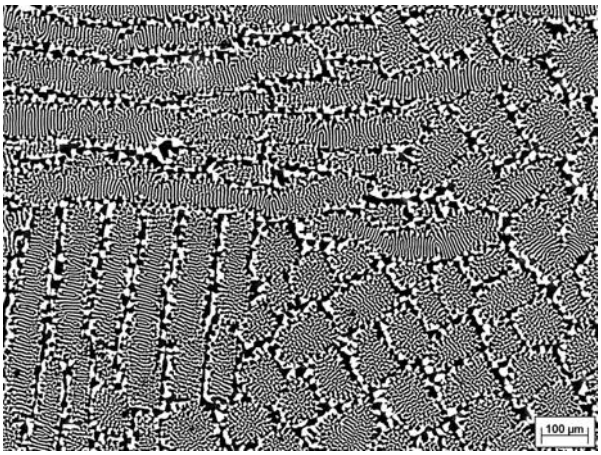

b)

Fig. 10 Grains with elongated cell structure coexisting near grains with regular cell structure inside the sample Al-Cu13.66 at%-Ag 10.27 at% solidified with v = 0,122 mm/min and G = 27 ± 2 K/mm, are shown in to different regions (a. and b.) of the cross section as shown. The images areis taken by optical microscopy, the sample being etched with an aqueous solution of 5 %HF. Here the α (Al) appears dark.

In a first step, the destabilization of the planar lamellar eutectic occurs in the plane of the lamellae like a coupled single-phase instability, leading to the formation of rather flat elongated cells with walls that are perpendicular to the lamellae. Inside these elongated cells the lamellar structure is retained.

In a second step, the lamellae inside the elongated cells form nodules with a spiral-like or concentric arrangement of the two phases, both of whom keep their

continuity as layers. These nodules are maybe slightly protruding into the liquid, such that the solid/liquid interface of the elongated cells becomes bumpy all along the cell lengths.

Finally, in a third step, regular cells can develop from the nodules, leading to a regular cell pattern. This third step is quite complex, as it is associated to a fragmentation of the lamellar structure inside the nodules, such that the intracellular eutectic pattern becomes rather rod-like. This last step may be absent in some grains.

Two questions arise:

a) Why does the first break-up of the initially planar lamellar eutectic interface occur with an instability in the plane of the lamellae, giving elongated cells oriented perpendicular to the lamellae? Several arguments can be outlined here, based on anisotropy effects, but they need further investigation: First, the anisotropy of the solid/liquid interface energy of the theta-phase needs further consideration, assuming that theta acts as the leading phase during destabilization. The effect of anisotropy of a growing single phase solid has been discussed by Morris and Winegard [13] based on experiments with binary Pb-Sb alloys. For the [110] axis of the fcc solid solution aligned in the direction of growth, elongated cells formed, while for [100] and [111] regular cells formed. A second source of anisotropy may be the eutectic coupling itself. Plapp and Karma [6] performed a linear stability analysis for a 2D lamellar eutectic in the presence of a ternary impurity and showed that the interlamellar cross diffusion acts as an effectively stabilizing surface tension in direction perpendicular to the lamellae.
b) Why do some grains exhibit more stable elongated cells then others, or else, why are regular cells not common to all grains? As explained above, the formation of regular cells is connected to a fragmentation of the lamellar structure, a process that may include oscillatory modes and that bears some similarity to the transition from lamellar to rod-like growth. In this respect the most important distiction between different grains is the structure and the energy of the hetero-interfaces between α(Al) and Al_2Cu and the crystal orientation of the two phases in growth direction.

In view of the two questions outlined above our present investigations are focused on the crystallographic aspects of coupled growth between α(Al) and Al_2Cu in univariant ternary alloys.

28.5 Summary and Outlook

In this contribution we described and discussed the coupled growth of α(Al) and Al_2Cu from ternary Al-Cu-Ag alloys in univariant eutectic reaction during unidirectional solidification with some emphasis on the process of cell formation. We proposed a phenomenological model to explain the different stages of cell formation, showing that at least for the system under consideration cell formation in bulk sam-

ples is a truly 3D process in all of it's stages, quite different from colony formation in thin (2D) samples.

More detailed investigations that focus on the effect of different types of anisotropy on the morphological transition from planar lamellar to cellular eutectic structures are presently ongoing.

Acknowledgements

We gratefully acknowledge the funding of this work by the German Space Agency DLR under grant no. FKZ 50 WM 0043 and the support by the European Space Agency ESA within the frame of the SETA-project. Thanks are due to Prof. L. Froyen and J. DeWilde from the Katholieke Universiteit Leuven, Belgium for producing the sample material and for many interesting discussions.

References

[1] C.T. Rios, S. Milenkovic, R. Caram, J. Crystal Growth 2000, 211, 466–470.

[2] G. Garmong, Met. Trans., 1971, 2, 2025–2030.

[3] M. Durand-Charre, F. Durand, J. Crystal Growth, 1972, 13/14, 747–754

[4] A. Sayir, S.C. Farmer, Acta mater., 2000, 48, 4691–4697.

[5] S. Akamatsu, and G. Faivre, Phys. Rev. E, 2000, 61, 3757–3770.

[6] M. Plapp, A. Karma, Phys. Rev. E, 1999, 60, 6865–6889.

[7] The thermodynamic database for Al-Cu-Ag was developed within this project, and will be submitted for publication to the Journal of Alloys and Compounds.

[8] Thermo-Calc is a software tool for thermodynamic calculations.

[9] D.G. McCartney, J.D. Hunt, R.M. Jordan, Met. Trans. A, 1980, 11A, 1243–1249.

[10] C. Dussert, G. Rasigni, M. Rasigni , J. Palmari, Phys. Rev. B, 1986, 34, 3528–3531.

[11] B. Kauerauf, G. Zimmermann, S.Rex, B. Billia, H. Jamgotchian, J.D. Hunt, J. Crystal Growth, 2001, 277–284.

[12] L. Sturz, G. Zimmermann, B. Kauerauf, M. Mathes, S. Rex, acceppted for publication in Met. Mat. Trans. A

[13] L.R. Morris and W.C. Winegard, J. Crystal Growth 1969, 5, 361–375.

29
Lamellar Pattern Formation during 2D-Directional Solidification of Ternary Eutectic Alloys

Markus Apel, Bernd Böttger, Victor Witusiewicz, Ulrike Hecht, Ingo Steinbach

29.1
Introduction

Regular binary eutectic alloys form lamellar growth structures during 2D directional solidification. The different growth modes and their stability have been carefully investigated by experimental and numerical means [e. g. 1–4]. This includes the understanding of oscillating structures or tilted lamellae which violate the principal symmetry in regular binary eutectics On the other hand systematic studies of lamellar growth pattern formed during solidification of ternary eutectic alloys are lacking.

The objective of this paper are 2D growth modes of invariant eutectic solidification in a ternary alloy when the liquid transforms into three distinct solid phases. The situation is depicted in fig. 1, showing the microstructure of a directionally solidified 30 μm thin foil of an In-Bi-Sn alloy [5]. The microstructure consists of a lamellar pattern in an axisymmetric arrangement with a stacking sequence ABCB, build by γ-Sn, In_2Bi and β-In. Obviously the lamellar structure does not show a simple ABC stacking sequence. Now questions arise which are possible growth structures and which are the selection principles determine a specific pattern in a three phase lamellar structure?

In this paper we present a variety of possible growth structures for a ternary eutectic alloy, calculated by applying a general multiphase and multicomponent phase field model. The phase field calculations lead to various stable lamellar growth modes with different symmetry properties. The aim is not to discuss microstructure formation for a specific alloy, but we take real thermodynamic data of Al-Cu-Ag as a model for an asymmetric ternary eutectic alloy.

29.2
Phase Field Model

We are using the general multiphase field model derived in [6,7] for the calculation of the microstructure formation during solidification. This model allows for simula-

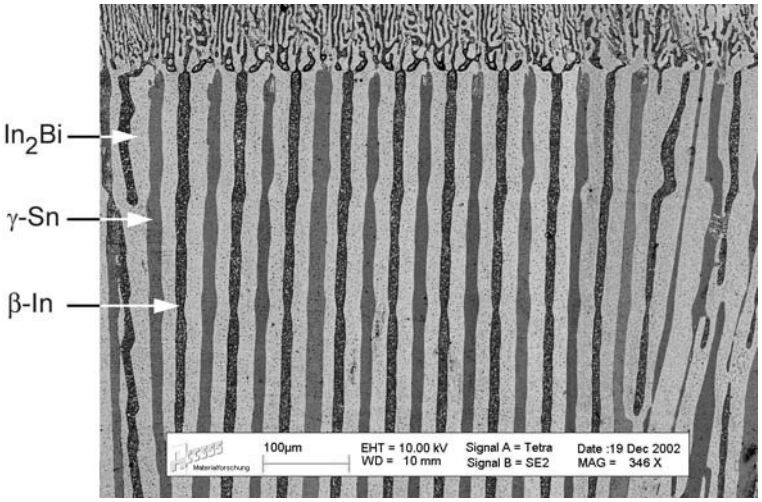

Fig. 1 Lamellar microstructure of an In-Bi-Sn alloy, (34.1 at% Bi, 50.6 at% In, 15.3 at% Sn) after directional solidification of a 30 µm thin foil. The micrograph shows the lamellar sequence in one grain at the quenched solid-liquid interface. Different lamellar structures were observed along the solidification front.

tions with multiple phases or alloy components. Consider N field variables ϕ_i, i labeling individual grains of solid and the liquid region. In the bulk of one grain i $\phi_i = 1$ holds, within an interface between grain i and j, $\phi_i < 1$, $\phi_j < 1$. In general, the constrain $\Sigma\phi_i = 1$ must be fulfilled in the whole domain. Following the approach described in [6] and using a double obstacle formulation for the potential leads to a set of phase field equations for each ϕ_i.

$$\dot{\phi}_i = \sum_{j \neq i} \mu \left\{ \sigma \left[\left(\phi_j \nabla^2 \phi_i - \phi_i \nabla^2 \phi_j \right) + \frac{\pi^2}{2\,\eta^2} \left(\phi_i - \phi_j \right) \right] + \frac{\pi}{\eta} \sqrt{\phi_i \phi_j} \Delta G_{ij} \right\}$$

We consider only the isotropic case were the interface mobility μ and boundary energy σ are constants. The parameter η is the width of the diffuse interface. The last term in the equations accounts for the thermodynamic driving force. ΔG_{ij} is the free energy difference between two interacting phases i and j. The free energy difference itself can be expressed as follows:

$$\Delta G_{ij} = \Delta S_{ij}^{tr} \cdot \Delta T = \Delta S_{ij}^{tr} \cdot \left(T - T_{ij}^{m} - \sum_k m_{ij}^k \left(c_i^k - c_{ij}^{eq,k} \right) \right)$$

The index k denotes individual components, c_i^k is the composition regarding component k in phase i, $c_{ij}^{eq,k}$ the eutectic composition regarding i/j interaction and m_{ij}^k are the liquidus slopes derived from a linearization around the eutectic point. Finally ΔS_{ij}^{tr} is the transformation entropy.

The driving-force term accounts for the coupling of the phase field equations to the composition. The composition is coupled to the phase field by an equilibrium condition in the interface using partitioning coefficients k_{ij}^k calculated from the slopes m_{ij}.

$$c_i^k = k_{ij}^k \, c_j^k$$

Here c_i^k are partial compositions in each phase fraction and the overall composition c^k is related to the partial compositions by the weighted sum

$$c^k = \sum_i \phi_i \, c_i^k$$

Solute diffusion is described by an ideal solution approximation

$$\dot{c}^k = \sum_i \nabla \cdot \left(\phi_i \, D_i^k \, \nabla c_i^k \right)$$

with the diffusion coefficients D_i^k of components k in phase i. Off diagonal diffusion terms which should occur in general for multicomponent diffusion are neglected.

29.2.1 Material Data

The phase field model sketched above has the advantage that it can be easily adapted to different alloys. As a model we use the ternary system Al-Ag-Cu for which a complete thermodynamic dataset has been assessed [8]. This alloy system shows a ternary eutectic reaction at 776.5K were the liquid decomposes into fcc-Al, hcp-Ag_2Al and the Cu rich θ-phase Al_2Cu. The eutectic composition is [Al]=69.96at%, [Ag] = 16.97at% and [Cu] = 13.07at%.

For the diffusion coefficients in the liquid we assume 10^{-5} cm^2 s^{-1} for all components. Interfacial energy σ is set to 10^{-5} J/cm^2 for each boundary. A further unknown material parameter is the kinetic coefficient μ. We derived the value for μ from a series of simulations performed with increasing mobility. The contribution of the kinetic undercooling and therefore the average undercooling of the solid-liquid interface decrease with increasing mobility. The average interface temperature converge against a fixed value which is determined by the diffusion controlled growth regime. As a convergence criteria we define in a somewhat arbitrary manner that the average interface temperature does not change by more than 5% with a further mobility increase of a factor 10. This procedure leads to a μ value of 5×10^{-4} cm^4/Js which was used for all simulations.

The interfacial widths η were set to 6 grid cells in all simulations.

29.2.2
Numerical Aspects and Simulation Procedure

The equations were solved on a finite difference grid using an explicit forward Euler scheme. Grid sizes for the simulation were between 50×400 and 160×400 cells with a cell size of 0.25 μm according to the lamellar pattern width.

All simulations were made for directional solidification conditions in a temperature gradient of 50 Kcm^{-1} with a pulling velocity of 1 μms^{-1}. As initial structures we set a predefined lamella sequence at the bottom of the calculation domain with slightly different lamellae thicknesses compared to the final values. Periodic boundary conditions were applied on east and west side. On the bottom side adiabatic boundary conditions have been used, on the top side eutectic composition was set as Dirichlet condition.

Figure 2a shows diffusion profiles in the liquid parallel to the growth direction. A short range solute pile up on the length scale of the lamella width and a long range pile up can be seen. The short range pile up gives rise to diffusion fluxes parallel to the interface. The long range pile up results from asymmetric phase fractions and compositions of the eutectic. It requires a larger calculation domain compared to domain sizes needed for the simulation of symmetric alloys. To improve computational effectiveness we use a moving calculation domain. The phase and concentration fields are shifted by one grid cell each $\Delta t = \Delta x/v$, whereas v is the pulling speed. As a result the temperature at the bottom of the domain is fixed. Furthermore far field diffusion was calculated in a 1D approximation, starting at a distance of 2.5 times the width of the simulation domain, in front of the solid-liquid interface. The 1D calculation was then performed on a grid 10 times longer than the 2D domain, which corresponds to 1 mm. We could not determine any notable effect by a further increase of the length of the 1D domain nor of an enlargement of the region of full 2D calculation. This can be understood considering the fact that the amplitude of the short range pile up decrease exponentially on a length scale in the order of the lamella thickness λ.

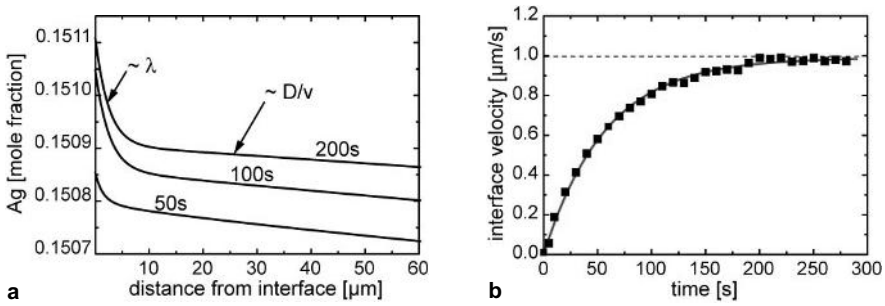

Fig. 2 a) Diffusion profiles in the liquid in growth direction for different times after start of solidification. A short range pile up on the length scale of the lamella width and a pile up ~ D/v can be seen. b) Interface velocity as a function of solidification time.

The steady state growth mode is determined by checking the solid-liquid interface position in the calculation domain. In figure 2b a plot of the interface velocity as a function of time is shown. From single phase solidification theory the transient time t can be estimated as D/v^2 which gives 1000 s, however after ~300 s of growth the interfacial undercooling and therefore the interfacial velocity reached a stable value within a range of <5%. This indicates a minor contribution of the long range pile up to the interfacial undercooling.

The term interfacial undercooling denotes in the following always the average undercooling determined in between the minimal and maximal position of the interface.

29.3
Simulation Results

29.3.1
The Basic State and Tilted Growth

The simplest stacking sequence is the ABC ordering. In the following we will call this sequence the basic state. Indeed the ABC sequence leads to stable lamella growth. Figure 3a shows such a growth structure for a periodic sequence of silver rich hcp-Ag_2Al (A), fcc-Al (B) and θ phase (C). The wave length of the structure is 15 µm which in this case corresponds to the width of the calculation domain. Each phase can be easily identified by its Ag concentration and therefore the Ag pile up in front of each phase will be different. On the other hand the Cu content in fcc-Al and hcp-Ag_2Al differs only about ~10% (compare figure 3b), therefore

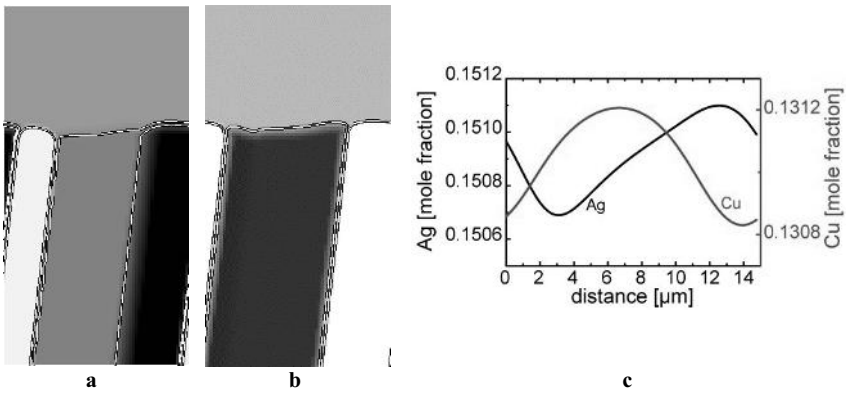

Fig. 3 Simulated growth structure with a simple ABC stacking sequence, domain width 15 µm a) Ag and b) Cu composition maps. First lamella consists of Ag_2Al (A), second one is fcc-Al (B) and the last one reflects Al_2Cu-phase (C). Iso-concentration lines are added to give a better impression of the solid-liquid interface contour. c) Diffusion profiles in the liquid parallel to the solid-liquid interface.

both phases show a similar segregation behavior regarding Cu. Hence the Cu concentration profile in the liquid parallel to the solid-liquid boundary is rather symmetric (figure 3c).

In general the basic state has no mirror symmetry along the growth direction. In our case this can be seen best in the Ag distribution. As a result of this missing symmetry the lamellae of the basic state do not grow parallel to the temperature gradient but they are slightly tilted. The growth direction is inclined to the ABC-direction, caused by a favored growth of Ag-poor θ (C) towards the Ag-consuming hcp-phase (A). We checked that the tilting switches to the opposite direction if we revert the stacking order.

This tilting is a qualitatively new behavior in contrast to the axisymmetric growth of ideal regular binary eutectics. It is a direct consequence of the asymmetric segregation behavior between neighboring lamellae. In binary eutectics tilted lamellae occur only at higher driving forces or are induced by crystal anisotropies.

According to the classical analysis for binary eutectics presented by Jackson and Hunt [1] the average interface undercooling should vary with the lamellae distance or in our case with the width of the simulation domain. The plot in figure 4a shows that the interface undercooling increases linearly with the periodic length of the basic state. According to Jackson and Hunts' solution this will imply that the undercooling is dominated by solute pile up which scales linearly with the lamellar width. Within this series of simulations we were not able to go below a domain width of 12 μm because for smaller domains the hcp-lamella is not resolved properly with the applied grid resolution. Therefore the spacing of minimum undercooling could not been deduced from these simulations.

Within the range of simulated domain sizes the tilt angle increases in a quadratic manner with increasing width. This is accompanied by a larger bulged solid-liquid interface which forces the triple junctions into increasing off-axis directions. Beyond a periodic length of 27.5 μm we do not observe stable steady state patterns anymore.

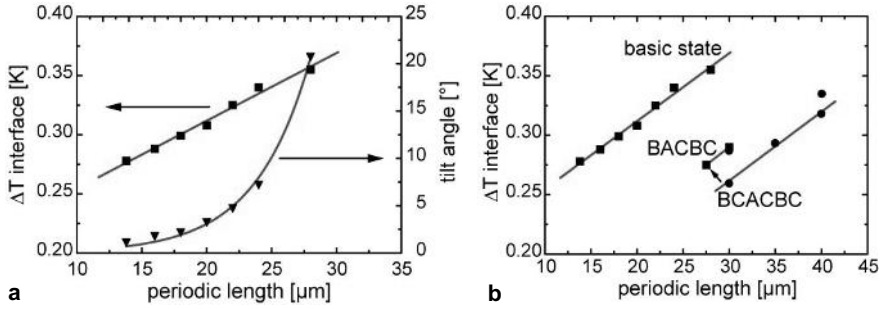

Fig. 4 a) Average interface undercooling (squares) and the lamellae tilt angle (triangles) for basic states. b) Interface undercooling for different stacking sequences. Circles denote axisymmetric, squares tilted states, respectively. The arrow indicates a transition to another branch by further decreasing the structure size.

29.3.2
Higher Order Stacking Sequences and Axisymmetric Growth

Figure 5 shows different stable lamellar structures which have a more complex stacking sequence instead of simply ABC. It turned out that not every sequence leads to a stable growth structure but decomposes by lamella termination. Nevertheless various stable growth patterns could be observed in the investigated range of domain widths. Mirror symmetric sequences lead to axisymmetric lamellar growth structures. The average interfacial undercooling lies within the same temperature range as calculated for the basic states (figure 4 b). We plotted the undercooling as a function of the periodic length of the sequence, however the average lamellae width could be taken as another characteristic length, too. As can be seen we obtain several branches for the undercooling curves. Structures with the same periodic length can have a different interfacial undercooling. By increasing the number of lamellae within a fixed domain the undercooling decreases for a ACBCBC pattern compared to ABCBC, which would be the expected behavior in the regime were solutal undercooling dominates. But changing to ACBCBCB with one more lamella will decrease interfacial undercooling, too.

29.4
Discussion and Summary

To our knowledge we investigated for the first time 2D solidification morphologies of a ternary eutectic alloy by means of phase field simulations. Several new features could be identified. First of all the stacking sequence of the lamellae is an additional

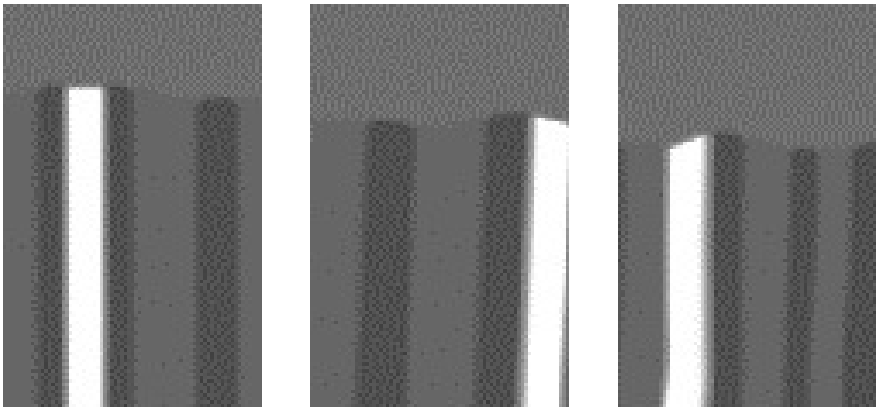

Fig. 5 Simulated growth structures (Ag composition maps) with different axissymmetric and non-axissymmetric stacking sequences, domain width 30 µm. The position of the interface reflects the different interfacial undercooling.

degree of freedom with respect to two phase solidification. This leads to a whole variety of new possible growth structures. Not only the spacing has to be adapted during growth but a selection among different patterns takes place as well. In the general case of an asymmetric phase diagram the basic growth mode with an ABC sequence is tilted with respect to the growth direction. In contrast to tilted modes in binary alloys the tilted growth is a direct consequence of the lack of mirror symmetry in the diffusion field and occurs even in crystallographic isotropic systems.

Higher order sequences can accomplish axisymmetric growth.

Further consequences of different stacking possibilities are multiple branches for the relationship of interfacial undercooling as a function of interlamellar spacing or size of the unit cell, respectively. Structures with the same periodic length can have different interfacial undercooling.

The question of maybe most practical interest is which pattern will be selected in a solidification experiment and whether the pattern selection can be controlled by process variables. One could argue that a pattern with minimal undercooling will be selected. However a minimal average interfacial undercooling itself does not explain the selection alone. This can be deduced from the observed transition from a BCACBC to a BACBC sequence with decreasing domain size from 30 μm to 27.5 μm. In this case lamella termination occurs, one C lamella vanishes, but the interfacial undercooling increase by this reorganization. This suggests that the selection is controlled rather by interaction between neighboring lamellae and not by global minimization. The sequence shown in figure 1 would then be stabilized by the exchange of Bi atoms between neighboring lamella. A further aspect in the pattern formation process is nucleation. In our simulation we always start with a predefined sequence and in case of termination the new neighboring relationship is already defined. Only by nucleation of new lamellae a free choice of sequences becomes possible.

To gain more insight into the selection rules between different 2D lamellae sequences will be the subject of further work. However, technical solidification processes always deal with bulk samples instead of quasi-2D foils. The invariant point for ternary alloys is a 4-phase equilibrium. Such a quadruple junction can not be represented in 2D directional solidification. Because the quadruple junction will have the lowest constitutional undercooling a lamellar 3D structure seems to be unlikely. Indeed in directional solidified Al-Ag-Cu samples and also in first 3D simulations fibrous like microstructures were found [9]. Nevertheless 2D experiments offer the opportunity to study very carefully pattern selection mechanism in multiphase alloys and enable a quantitative comparison with simulated microstructures on today's available computers.

Acknowledgement

We gratefully acknowledge the DLR (Deutsches Zentrum für Luft- und Raumfahrt) and the DFG (Deutsche Forschungsgemeinschaft) who support this work under grant No. 50WM0043 and SSP 1120, respectively.

References

[1] A. Jackson, D.J. Hunt, TMS AIME 236 (1966) p. 1129.

[2] M. Ginibre, S. Akamatsu, G. Faivre, Phys. Rev. E 56 (1997), p. 780.

[3] A. Karma, A. Sarkissian, Met. and Mat. Transactions A 27A (1996), p. 635.

[4] K. Kassner, C. Misbah, R. Baumann, Phys. Rev. E51 (1995), p. 2751.

[5] I.A. Galdos, V. Vitusevych, U. Hecht, M. Apel, unpublished results.

[6] I. Steinbach, F. Pezzolla, B. Nestler, M. Seesselberg, R. Prieler, G.J. Schmitz, J.L.L. Rezende, Physica D 94 (1996), p. 135.

[7] J. Tiaden, B. Nestler, H.J. Diepers, I. Steinbach, Physica D 115 (1998), p. 73.

[8] V. Witusiewicz, U. Hecht, S.Rex, to be published.

[9] M. Apel, B. Böttger, I. Steinbach, Modelling of Casting, Welding and Advanced Solidification Processes X, Ed. D. M. Stefanescu, J. Warren, M. Jolly, M. Krane, TMS Publication 2003.

30
Simulation of Stray Grain Formation in Investment Cast Turbine Blades

X. L. Yang, H. B. Dong, W. Wang and P. D. Lee

Abstract

The alloying content of nickel-based superalloys for the production of single crystal turbine blades is continually increasing, with a concomitant decrease in the castability of these alloys. The prevention of defect formation in modern turbine blades is becoming increasingly challenging. One of the major defects is stray grain, which can severely reduce the performance of single crystal turbine blades. In this study a combined cellular automata-finite difference model was applied to simulate dendritic growth in the platform region of turbine blades and to study the influence of withdrawal velocity and thermal gradient on the formation of stray grains.

The effects of tip undercooling, growth rate and inclination angle of isotherms on the formation and growth of stray grains are examined. The simulation results show that areas at the outermost end of platform provide favourable locations for stray grain formation, and that either increasing withdrawal velocity or inclination angle of isotherms favours the formation of stray grains.

30.1
Introduction

Continued advancement in the development of single crystal turbine blades relies on achieving better control of investment casting process. As alloy content and turbine blade geometry for modern engines become more complex, process requirements become more stringent and production yield emerges as a limiting factor.

One of the major problems encountered during directional solidification and single crystal growth is the formation of stray grains. Stray grains are heterogeneously nucleated in random orientations and hence can form high angle boundaries (HABs), which act as favourable locations for crack initiation, causing in-service failure [1]. During directional solidification and single crystal growth of turbine blades, nickel-based superalloys solidify dendritically and the dendrites grow in a preferential direction. Because of the complexity of the second and third generation single crystal superalloys, controlling the orientation is more difficult due to differ-

ent interaction distances of solute field in the presence of refractory elements (e.g. Rhenium) which have a low diffusivity in liquid.

Several experimental and analytical studies have been carried out on the formation of stray grains in investment cast turbine blades. The effects of various casting conditions such as different thermal fields [2, 3], and the remelting of dendrite fragments on the formation of stray grains have been experimentally investigated by prior authors [4]. It has been found that stray grains grow from undesirable nuclei at specific locations in turbine blades, such as the platform ends [1, 3].

Recently coupled cellular automaton with finite element (CA-FE) models have been applied to simulate grain structures in investment cast turbine blades [5–7]. The advantages of the CA-FE models are that the individual grains are identified, and their shapes and sizes can be illustrated graphically during solidification. However, the CA-FE model is based on the assumption that the envelope of the growing grains can be approximated as idealised primary dendrite tips, allowing the analytical solution of KGT to be applied [8]. Using the KGT model to relate thermal undercooling to the restriction in grain growth allows only the thermal field to be solved, not the solute field. Therefore it cannot be used to simulate the solute interaction at the growth front and hence the constitutional undercooling, which is critical to determine the nucleation of stray grains.

In this study, a combined cellular automata-finite difference (CA-FD) model is applied to simulate the dendritic growth and stray grain formation. This is an extension of the cellular automata technique to include solute diffusion through combination with a finite difference solver. Spittle [9] first used a CA-FD model to simulate the solidification structure with the stepped front motion technique. Lee *et al.* [10] and Nastac *et al.* [11] coupled a more accurate front tracking technique with solid fraction evolution in each growing cell, and their models allow the resolution of not only the grain envelopes but also the detailed dendritic structures. The model in this study is based on Lee and co-worker's [10, 12] approach, and the crystallographic anisotropy of cubic metals is accounted for by modified decentred square growth algorithm [13].

In this paper, the model is briefly described first. Then the predicted tip undercooling over different isothermal fields and varying withdrawal velocities is reported. Finally, the influence of temperature fields and withdrawal velocities on the formation of stray grains is discussed.

30.2
Model Description

The model combines a description of grain growth by cellular automaton (CA) with a computation of solute diffusion by finite difference (FD). Both the CA and FD components of the model use the same square grid and time step. Details of the model have been published previously [12, 13], therefore only the key assumptions and extension are detailed below.

The model starts with all cells in a liquid state, from which they may transform to a partly solid (growing) state by either nucleation or growth from a neighbouring

cell. In a growing cell, solute is partitioned between the solid and liquid phases. The change in solute concentration affects the degree of local undercooling and therefore affects the nucleation and growth processes.

Nucleation is determined stochastically, representing its essentially random nature. The probability that a nucleus forms in a particular cell is determined by the degree of undercooling in that cell. It is assumed that a population of potential nucleation sites exists within the domain such that each site may initiate nucleation if exposed to liquid with a critical undercooling. The relationship between the nucleation probability and the nucleation undercooling was implemented using a Gaussian law, in which the probability of nucleation depends upon a normal distribution function as suggested by Rappaz [14].

Once nucleated, the growth of dendrites is governed by the diffusion of solute. Assuming that equilibrium occurs at the solid/liquid interface, the partitioning of solute in the growing cell is determined by phase diagram. The solid fraction change in a growing cell is controlled by the diffusion of solute between cells and the variation of the solute within that cell. When the change in the solid fraction is obtained, the growth of solid is governed by a modified decentred square growth algorithm to account for the effect of crystallographic anisotropy [13].

The model was validated by comparing the predicted results with experimental observed dendritic structures in the platform region. The comparison showed a good correlation with the experimental observation. It was concluded that the model correctly predicts the microstructure of dendritic growth in the platform corner of turbine blades. Detailed description of the model validation is given in reference [15].

30.3 Simulation Parameters

Prior experimental results reveal that the platform ends are favourable locations for stray grain formation in turbine blades, simulations have therefore been carried out in platform region. A schematic diagram is shown in Figure 1. The size of the do-

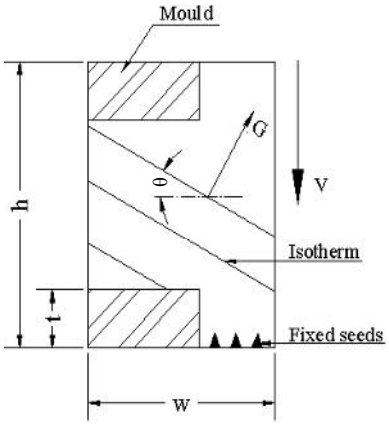

Fig. 1 Schematic diagram of the simulation domain. V: withdrawal direction; G: temperature gradient; θ: angle between isotherms and horizontal direction. h = 5 mm; t = 1mm, w = 3.5mm.

Tab. 1. Key values used in the simulation

Parameter	*Variable*	*Value*
Liquidus temperature	T_L	1609 K
Solidus temperature	T_S	1533 K
Liquidus slope	m	–10.9 K/wt%
Partition coefficient	k	0.48
Diffusion coefficient in liquid	D_L	3.0×10^{-9} m^2/s
Diffusion coefficient in solid	D_S	3.0×10^{-12} m^2/s
Initial concentration	C_0	4.85 wt%
Cell size	Δx	5 μm
Time step	Δt	1 ms

main is 3.5 mm by 5.0 mm giving a total number of 700 by 1000 cells in the domain. The time step for computing the diffusion of solute and the growth of solid was 1 ms. A zero flux boundary condition was applied to the mould. The thermal field was imposed to the domain by applying a function to represent the temperature profile in the platform region in turbine blades during casting.

A binary approximation of a nickel-based superalloy was used in these simulations. Since the alloy composition is very complex, an element with a low diffusion coefficient D_L, a high content, and a small partitioning coefficient k was considered. Key values used in these simulations are given in Table 1.

30.4 Results and Discussion

Simulations were performed for a range of withdrawal velocities and isothermal conditions to simulate the investment casting conditions. The isotherms were moving upwards at withdrawal velocities, V, ranging from 100 to 300 μm/s, and the angle of the isotherms relative to the horizontal, θ, ranging from 0° to $\pm 20^\circ$.

30.4.1 Effect of Withdrawal Velocity and Isothermal Conditions on Undercooling

The nucleation of stray grains is dominated by the tip undercooling ahead of the growth front, which is affected by withdrawal velocity and isotherms. The influences of withdrawal velocity and thermal condition upon the undercooling are investigated in this section.

Figure 2a shows the effect of withdrawal velocity upon undercooling. Undercooling at the left hand bottom corner in the domain, where it is at its highest, is plotted against velocity. The undercooling changes from 24.8 K to 35.1 K as velocity varies from 100 μm/s to 300 μm/s. This is because an increase in growth velocity increases solute concentration ahead of the dendrite tip. It can be predicted that under the

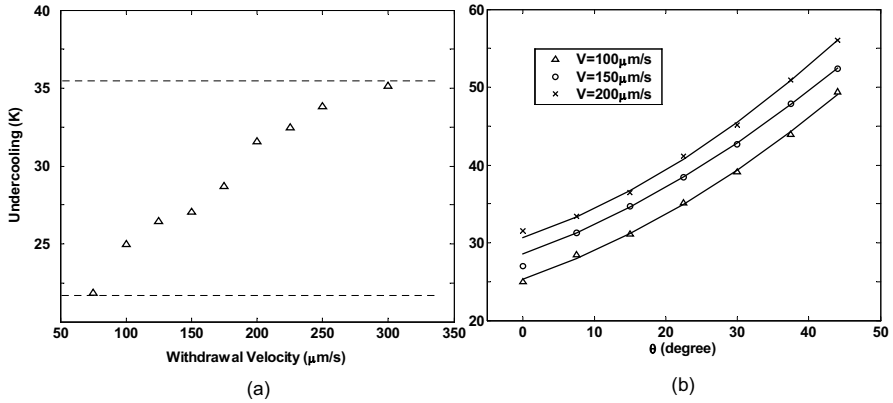

Fig. 2 (a). Relationship between withdrawal velocity and undercooling. Dotted lines show the range of undercooling as withdrawal velocity changes from 100 to 300 μm/s with horizontal isothermals. (b). Relationship between isotherm inclination angle and undercooling at the left-hand bottom corner of the domain.

same isothermal condition the higher the velocity, the higher the undercooling so that the probability for nucleation of stray grains is increased.

Undercooling was also examined as a function of isothermal inclination angle θ. The relationship is plotted in Figure 2b, where θ changes from 0° to 45° at different velocities (100, 150 and 200 μm/s). At a constant velocity, undercooling increases with the angle: for example, at a velocity of 100 μm/s, the undercooling is 24.9K at 0°, increasing to 49.4 K at 45°. This confirms that the undercooling at the outer corner increases with the inclined isothermal angle and that, as shown by Napolitano [3], the outer region of the platform is more likely to have concave isotherms than the inner region in a clustered casting, thus more favourable conditions for the formation of stray grains occur in the outside corner of the platform.

As discussed above, an increase of velocity from 100 to 300 μm/s leads to an increase in the undercooling of about 11 K (see Figure 2a) whilst varying θ from 0° to 45° increases undercooling by 25 K (see Figure 2b). Both the velocity and the isotherm angle affect the undercooling at the corner, but the influence of inclination angle is more significant. Therefore an increase in velocity can be used to increase the productivity, if a furnace can be designed to maintain lower isothermal angle.

30.4.2 Dendritic Growth and Stray Grain Formation

In this study, dendritic growth was modelled including random nucleation in the platform to simulate the stray grain formation. When undercooling ahead of the growth front reaches a critical value, nucleation occurs, and, stray grains form. Figure 3 shows the predicted dendritic structure and undercooling under horizontal isotherms moving upwards at 150 μm/s. As approximated from thermal analysis mea-

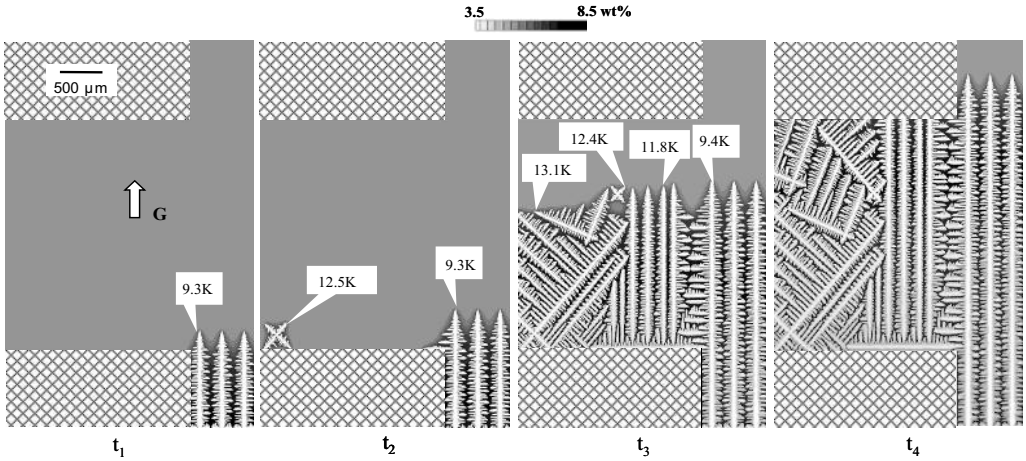

Fig. 3 Predicted dendritic structures and undercooling at different timesteps. Horizontal isotherms moving at a constant velocity of 150 µm/s. t_1 = 13s, t_2 = 15s, t_3 = 26s, t_4 = 35s.

surements [16], an undercooling of 15 K was adopted as the critical undercooling for heterogeneous nucleation. At 13s (t_1 in Figure 3), columnar dendrites grow from the bottom with one direction fully aligned with the vertical temperature gradient; no nuclei appear because the undercooling is below the threshold in the bulk liquid.

At 15s (t_2), one nucleus formed at the far corner and started to grow because its undercooling exceeded the threshold. Meanwhile, the columnar dendrite formed a secondary arm along the horizontal surface of the mould wall. Undercooling of the secondary dendrite arm had a higher level (12.5 K) than the primary dendrite tips (9.3 K), therefore, the secondary dendrites grew faster.

At 26s (t_3), several stray grains formed near the left side of the domain. Competitive growth between the stray grains and original columnar dendrites can be observed. As indicated in the plot, tip undercooling of stray grain was higher than that of original dendrites, therefore, their growth fronts caught up almost to the same level as well-aligned dendrites.

At 35s (t_4), misorientated grains occupied the left corner of the domain. Further propagation of stray grains was blocked by the original columnar dendrites. A grain boundary can be observed due to the random orientation of stray grains.

In summary, dendritic growth and the undercooling ahead of the growth fronts in the presence of random nucleation was simulated. The high undercooling in the outermost end of the platform region is both favourable to stray grain nucleation and competitive growth once formed.

30.4.3
Effect of Withdrawal Velocity on Stray Grain Formation

In this investigation, a series of simulations were performed to study the impact of withdrawal velocity on random nucleation. Figure 4 shows the predicted dendritic structures in the platform region of a turbine blade under withdrawal velocities ranging from 100 to 300 μm/s.

As shown in Figure 4, dendrite arm spacing decreases with increasing velocity, which is in agreement with the experimental observation. Only one stray grain formed at a velocity of 100 μm/s whilst four formed at 150 μm/s and seven at

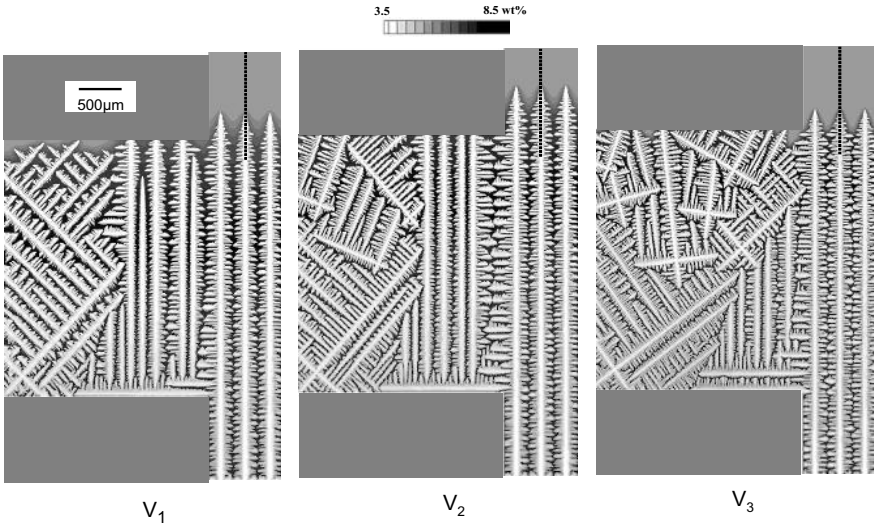

Fig. 4 Predicted dendritic structures with horizontal isotherms moving at different velocities: V_1 = 100 μm/s, V_2 = 150 μm/s, V_3 = 300 μm/s.

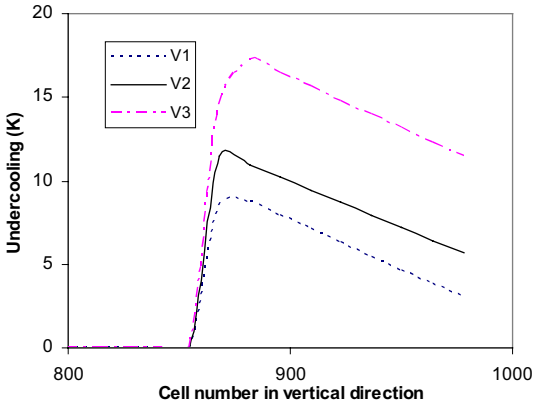

Fig. 5 Predicted tip undercooling along primary dendrite tips under horizontal isotherms moving at different velocities: V_1 = 100 μm/s, V_2 = 150 μm/s, V_3 = 300 μm/s.

300 μm/s. This can be explained from Figure 2a, where, at low velocity, the tip undercooling is low, delaying the formation of stray grains; at high velocity, the tip undercooling increases so that the potential sites for nucleation also increase. Predicted tip undercooling along primary dendrite tips (marked as dashed line in Figure 4) under different velocities is plotted in Figure 5. The tip undercooling increased from 8.6 K at 100 μm/s to 17.2 K at 300 μm/s.

It concludes that an increase in withdrawal velocities increases the potential for stray grain formation in the platform region of turbine blades.

30.4.4
Effect of Inclination Angle of Isotherms on Stray Grain Formation

The influence of the inclination angle of isotherms on stray grain formation is discussed in this section. As observed experimentally, the formation of stray grains is related to the curvature of the isotherm while it is passing through the enlarged cross section of the blades [3]. This condition is exacerbated when blades are cast in a cluster. As an approximation, the isotherms were set to be +20° with respect to the horizontal to simulate the outward side of the blade in a cluster, and –20° to simulate the inside. The predicted microstructures are shown in Figure 6 for three angles (θ = 20°, 0° and +20°) at a withdrawal velocity of 150 μm/s.

Figure 6 illustrates that the area occupied by stray grains varies with isotherm angle: (i) with isotherms at –20°, grains are relatively small showing that growth is restricted by the original columnar dendrites and the mould wall; (ii) for isotherms

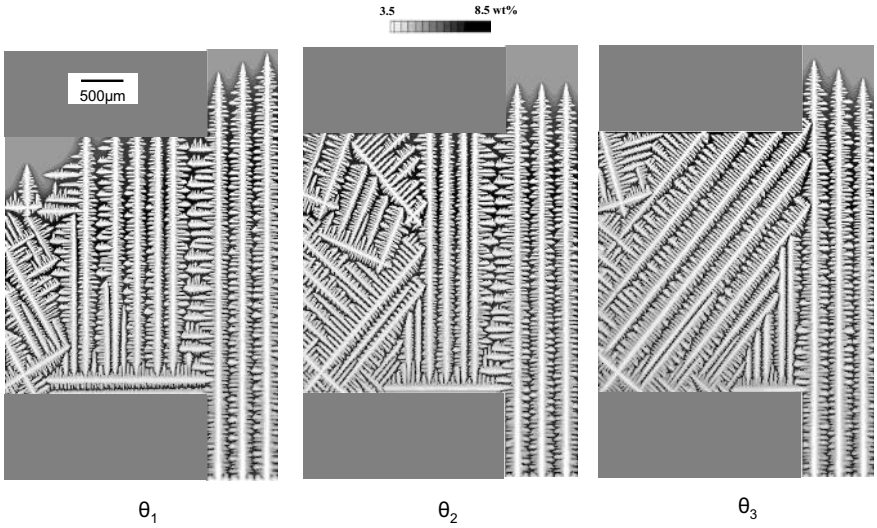

Fig. 6 Predicted dendritic structures under different isotherm angles moving at a constant velocity of 150 μm/s. $\theta_1 = -20°$, $\theta_2 = 0°$, $\theta_3 = +20°$.

of +20°, the size of the stray grains are relatively large; (iii) the area occupied by stray grains under horizontal isotherms is between the above two levels.

As discussed in section 3.2, at a constant withdrawal velocity the undercooling increases continuously with the angle. At –20° (inner side of platform), the undercooling in the corner is small while at +20° (outer side of platform) it is high. Under a higher undercoolings, the stray grain grows faster and the size of stray grain is accordingly larger.

30.5 Conclusions

The formation of stray grains in investment cast turbine blades was simulated using a combined cellular automaton-finite difference model. The simulated results show that areas at the outmost end of platform provide favourable locations for stray grain formation, and that either increasing the withdrawal velocity or the inclination angle of isotherms favours the nucleation and growth of stray grains. Change of inclination angle of isotherms increases undercooling more significantly than change of velocity.

Acknowledgements

The authors would like to thank the EPSRC (Grant no.GR/R78992) for financial support. The provision of materials, software and information from the industrial collaborators (Rolls-Royce plc, Cannon Muskegon and UES software Inc) are also gratefully acknowledged.

References

[1] De Bussac, A., Gandin, Ch -A., *Mater. Sci. Eng. A,* 1997, **237**, 35.

[2] D'Souza, N., Ardakani, M. G., McLean, M., Sholock, B. A., *Metal. Mater. Trans. A,* 2000, **31A**, 2877.

[3] Napolitano, R. E., Schaefer, R. J., *J. Mater. Sci.*, 2000, **35**, 1641.

[4] Gu, G. P., Beckermann, C., Giamei, A. F., *Metal. Mater. Trans. A,* 1997, **28A**, 1533.

[5] Boettinger, W. J., Coriell, S. R., Greer, A. L., Karma, A., Kurz, W., Rappaz, M., Trivedi, R., *Acta Mater.,* 2000, **48**, 43.

[6] Gandin, C.-A., Rappaz, M., Desbiolles, J.-L., E. A. Loria, Ed., Proceedings of the International Symposium on Superalloys 718, 625, 706 and Various Derivatives (The Minerals, Metals & Materials Society, 1997), 121.

[7] Rappaz, M., Gandin, Ch.-A., Desbiolles, J.-L., Thevoz, Ph., *Metal. Mater. Trans. A,* 1996, **27A**, 695.

[8] Kurz, W., Giovanola, B., Trivedi, R., *Acta Metall.,* 1986, **34**, 823.

[9] Spittle, J. A., Brown, S. G. R., *J. Mater. Sci.,* 1995, **30**, 3938.

[10] Lee, P. D., Atwood, R. C., Dashwood, R. J., Nagaumi, H., *Mater. sci.Eng. A,* 2002, **328**, 213.

[11] Nastac, L., *Acta Mater.,* 1999, **47**, 4253.

[12] Lee, P. D., See, D., Atwood, R. C., Proceedings of the Cutting Edge of Com-

puter Simulation of Solidification and Casting, Osaka, Japan (1999), 97.

[13] Wang, W., Lee, P. D., McLean, M., *Acta Mater.*, 2003, **51**, 2971.

[14] Rappaz, M., Gandin, C.-A., *Acta Mater,* 1993, **41**, 345.

[15] Yang, X. L., Dong, H. B., Wang, W., Lee, P. D., *Mater Sci. Eng. A*, **submitted**.

[16] Dong, H. B., Yang, X.L., Wang, W., Lee, P. D., Proceedings of Liquid Metal Processing and Casting, Nancy, France (2003), 39.

31
Laser Cladding Applications to Combinatorial Materials Science

R. Vilar, P. Carvalho, R. Colaço

Abstract

Combinatorial methods initially applied in pharmacological research are being increasingly used in the development of inorganic materials and polymers. These methods require the creation of large libraries of materials with compositions varying in wide ranges, which are scanned for the desired properties using fast micro or ultramicro characterisation techniques. This approach is particularly adequate for the systematic scrutiny of complex systems, aiming to find unsuspected materials with outstanding properties for particular applications, but its application to metallic and composite materials for mechanical applications has been restrained by the difficulty in preparing suitable libraries, because the presently available preparation methods do not allow a dependable assessment of microstructure-dependent properties. Previous work showed that laser cladding with computer controlled variable powder feed rate is an extremely powerful technique for rapid alloy composition scanning (rapid alloy prototyping). In the present paper, this technique will be briefly described and its application to combinatorial materials science illustrated.

31.1
Introduction

Nowadays, materials development is mostly incremental, in the sense that materials used for a certain application evolve in order to adapt to the shifting requirements of that application or materials created for a certain application are considered for a different application and progressively modified to satisfy the new requirements. This is because the empirical development of completely new materials usually requires the synthesis and analysis of extremely large numbers of discrete composition samples once-at-a-time, making the process so prohibitively costly and time consuming, that radical innovations are often inhibited.

Recently, combinatorial methods, initially employed in the pharmacological research [1], have been applied to new materials discovery with considerable success. Combinatorial methods require the creation of large libraries of materials with com-

positions varying in wide ranges, which are scanned for the desired properties using fast characterisation techniques. They are being increasingly used for the systematic scrutiny of complex systems, aiming to find unsuspected materials with outstanding properties for particular applications, as well as in fundamental investigations of structure-properties-processing relationships and alloying behaviour and are particularly well suited to ternary or higher-order materials. Typical applications have included the search for new luminescent metal-oxide materials for phosphor screens [2–4], catalyst research [5], hard coatings development [6, 7], and phase diagram investigations [8–10]. However, the application of combinatorial methods to the search of metallic and composite materials for many applications has been restrained, because the small amounts of material existing in libraries prepared using presently available synthesis methods (in general thin film deposition techniques [4–8, 11, 12]) and the microstructure of the materials in these libraries do not allow a dependable assessment of microstructure-dependent properties, such as tensile strength, ductility, hardness, toughness and wear and corrosion resistance. This requires that samples with physical dimensions much larger than some microstructure characteristic length (typically the grain size), i. e. at least in the millimetre range, are prepared using techniques as similar as possible to the final material production processes. Also, the screening methods required for these materials vary widely depending upon the targeted application, and it is frequently difficult to find micro-scale tests that represent adequately complex properties such as wear resistance. Despite these difficulties, several successful examples of application of combinatorial methods to metallic materials appeared recently in the literature. Cohen-Adad et al. [13] demonstrated the use of a zone melting technique for phase diagram determination and property and structure mapping in Al-Co alloys. More recently, by using multiple diffusion couples, EPMA and nanoindentation, Zhao [9, 10] rapidly mapped the mechanical properties in several Ni-based systems. These results demonstrate the potential of combinatorial methods to uncover innovative metallic alloys, but the development of synthetic and screening strategies that can quickly scan a wide range of metallic materials for a particular application remains a major challenge in combinatorial materials science.

Previous work showed that laser cladding with computer controlled variable powder feed rate is an extremely powerful technique for rapid alloy composition scanning (rapid alloy prototyping) [14, 15]. This method offers a unique possibility for the rapid and exhaustive preparation of a whole range of alloys with varying composition, which can be thoroughly analysed by using suitable micro-scale testing procedures. The first application of laser cladding with variable powder feed rate was reported by Monson *et al.* [16]. However, the systematic application of automated variable powder feed rate cladding to rapid alloy prototyping was first described by Carvalho *et al.* [14, 15] and Sexton *et al.* [17]. The process is very versatile in the materials that can be deposited and it is particularly well suited to manufacture metal-matrix composites with varying reinforcement particles content, a possibility that does not exist with thin film deposition techniques. Due to the high solidification rates achieved, the resulting microstructures are fine and frequently contain non-equilibrium phases and supersaturated solid solutions, leading to interesting and potentially useful properties [18]. Since the microstructure and properties of the materials

produced result from rapid solidification, this method can be advantageously used to develop new materials for example for coating applications, powder metallurgy and laser freeform manufacturing. In the present paper, the application of this technique to the combinatorial design of a metal-matrix composite and to alloying behaviour studies in multicomponent systems will be illustrated.

31.2
Laser Assisted Synthetic Methods

The proposed method for combinatorial material synthesis, called rapid alloy prototyping in previous publications [14, 15], is derived from laser cladding by powder injection. In this process (Fig. 1) powder of the clad material is delivered, by means of a carrier gas, to the melt pool generated on a substrate by a high power laser beam. The laser beam, which is scanned perpendicularly to the substrate, in a continuous motion, melts the incoming powder and a thin layer of the substrate. Once laser irradiation stops, rapid cooling occurs due to heat transfer to the bulk of the substrate and solidification starts at the bottom of the melt pool. The solidification front progresses rapidly towards the surface, at a speed that depends on the laser beam scanning speed and the depth and shape of the melt pool. By properly controlling the processing parameters, clad tracks can be produced with minimum contamination of the coating material by the substrate.

In rapid alloy prototyping several synchronised feeders under computer control are used to feed individual components of a multicomponent powder mixture with mass flow rates varying in real time, as powders are incorporated in the clad. As a result, the chemical composition along an individual track can be changed following a pre-set variation. If the number of powders that can be independently delivered is sufficient, elemental powders can be used to form any alloy system, but premixed powders can also be used. For example, if one of the hoppers of a two-hopper powder feeder contains the x element powder and the other a mixture of y and z powders, for instance 70y-30z, a x/70y-30z track will be produced by inversely varying the pow-

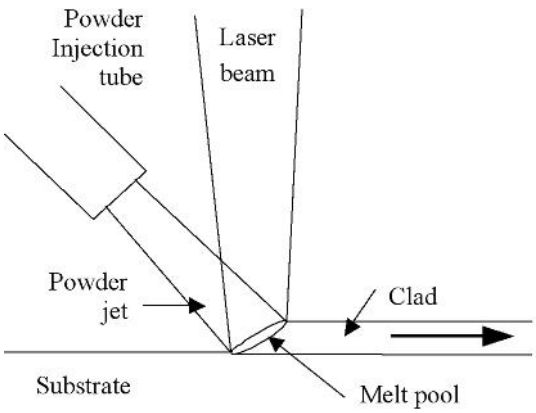

Fig. 1 Schematic representation of powder injection laser cladding.

der flow rate from the two hoppers. To create a metal-matrix composite library, one of the hoppers may contain a mixture that will form the matrix, while the other will contain the reinforcement particles powder. The process is extremely accurate both in what concerns material delivery and energy delivery, so reproducible microstructure and composition variations along the tracks are obtained. A detailed description of the method has been presented elsewhere [15, 19].

31.3 Examples of Application

31.3.1 Structure and Properties of Ni-Al-Co Alloys

Variable powder feed rate laser cladding was used to study the influence of Co on the microstructure and properties of Co-Ni-Al alloys [14, 15]. Corrosion tests were performed using specially developed micro-scale corrosion tests. The variable composition tracks were produced from mixtures of pure metal powders, using a two-hopper powder feeder. During preparation of the tracks, one of the hoppers contained Co and the other a mixture of Ni and Al powders, and the flow rate of each was made to vary inversely. Dilution was avoided in order to limit contamination of the alloys by the substrate material. To test the corrosion behaviour of selected alloys, miniaturised potentiodynamic polarisation tests were performed *in-situ*. The tracks were first embedded in epoxy resin and their top abraded to expose a flat surface. Cylindrical acrylic cells were attached to the surface and filled with the testing solution. A platinum wire immersed in the solution was used as counter electrode and a saturated calomel electrode, connected to the cell by a salt bridge, was used as the reference electrode.

The variation of composition in Co/Ni-5Al tracks, presented in Fig. 2, is typical of the results obtained. A systematic and constant deviation from the nominal compositions is

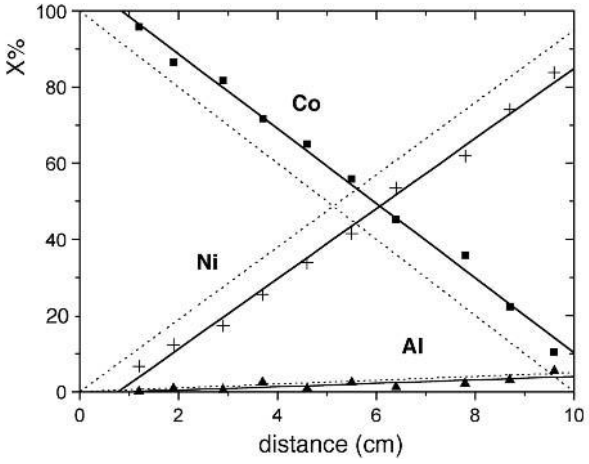

Fig. 2 Variation of chemical composition in a Co/Ni-5Al track, ■ Co, + Ni, σ Al. (.....) Expected variation.

observed, caused by the time lag in the powder feed line. This can be avoided if the time spent between the suction bores and injection into the melt pool is reduced or compensated. Chemical composition along the depth is very homogeneous and contamination by the substrate is negligible if the cladding parameters are properly selected.

The hardness variation measured along a Co/Ni-5Al track and typical microstructures are shown in Fig. 3a. The higher hardness values found in the 100 to 70 at. %

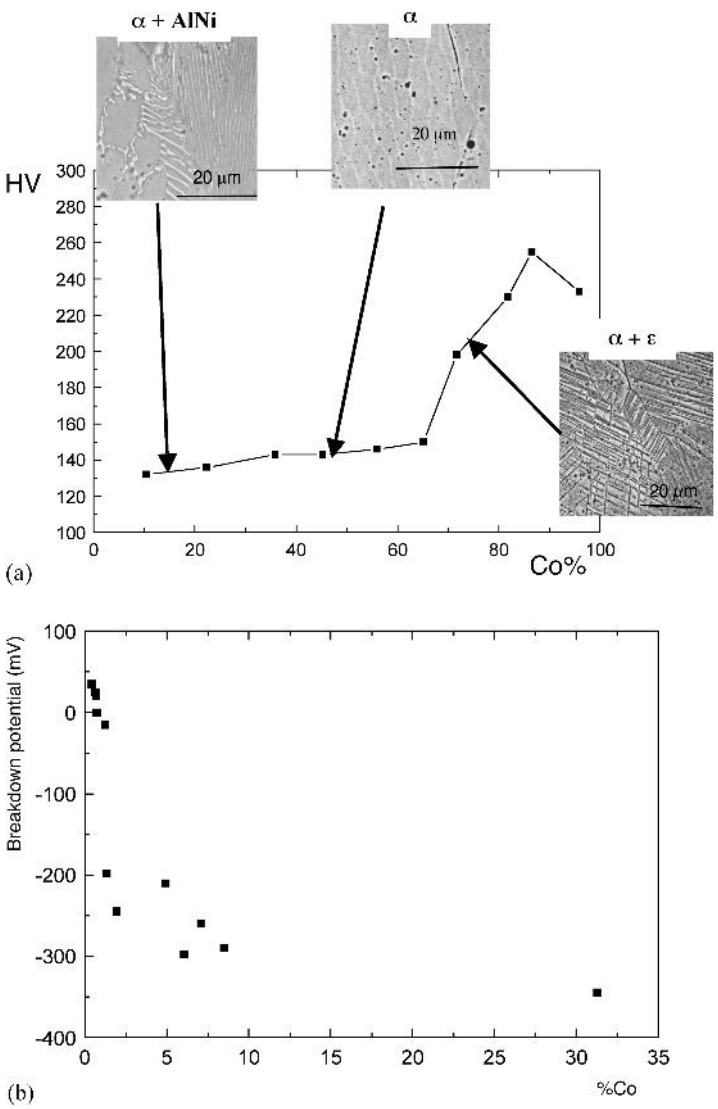

Fig. 3 Effect of composition on (a) microstructure and microhardness in a Co/Ni-5Al track, and (b) breakdown potential of Co-Ni-Al alloys (dark phase ε′, bright phase α matrix).

Co range are a consequence of the martensitic transformation of the face-centred cubic α solid solution to ε′ hexagonal close packed martensite. Al does not seem to have much influence on the alloys' hardness. For the composition range studied and Al content below 6 at. %, increasing the Co content and reducing the Ni content tends to shift the breakdown potential (E_b) to lower values, indicating an increasing susceptibility to localised pitting corrosion. The Al content does not seem to have any noticeable influence on resistance to pitting attack. If the breakdown potential of the different alloys is represented as a function of the Co/Ni atomic ratio (Fig. 3 b), two different types of behaviour are observed: alloys with Co/Ni < 1 have E_b between 35 and 0 mV vs. SCE whereas alloys with higher atomic ratios present breakdown potentials from –198 to –345 mV vs. SCE. The corrosion pits are homogeneously distributed, i. e., no preferential attack on either the α phase or the ε′ phase occurs. In consequence, the existence of ε′ martensite is not responsible for the drastic change in the pitting resistance of the alloys. On the contrary, their behaviour depends essentially on the Co/Ni atomic ratio and, therefore, on the composition and properties of the passivation films formed. In the particular alloys studied, the pitting corrosion resistance changes considerably when the Co content exceeds around 54 at. %.

31.3.2
Metal-matrix-composites for Wear-resistant Coatings

Variable powder feed rate laser cladding was also applied for developing metallic matrix composite materials for laser-assisted rapid tooling and coating applications, as a replacement for tool steels. Tool steels are designed with a tough and relatively hard matrix reinforced with a dispersion of hard particles that minimise indentation and scratching by abrasive particles. Since laser surface treatment leads to the dissolution of primary carbide particles and to the formation of large proportions of retained austenite [20, 21], the wear resistance of tool steels after laser treatment may not be as good as expected [19]. Metal–matrix composites are much better suited to rapid tooling by laser freeform manufacturing than tool steels, because their properties can be exactly tailored to requirements [22]. To create a metallic matrix composite material, mixtures of powders of the matrix components together with particles of the reinforcement materials are used. The processing parameters are controlled so that only limited dissolution of the reinforcement particles occurs, while all the components of the matrix should be thoroughly melted and mixed together by convection. The process allows easy tailoring for specific properties, by selecting the matrix and reinforcement particles within an extremely vast range of suitable materials. Cost, microstructure-properties considerations and compatibility with existing tool steels lead to choose a matrix based on the Fe-Cr-C system for the present application. The properties of the matrix are determined by the martensite substructure, selected through composition control: the acicular (or plate) morphology leads to high hardness and low toughness while the lath-type structures are softer and tougher. The properties of the matrix are also affected by the proportion of retained austenite, which, for a given composition, depends on the laser processing parameters [21]. Since abrasion resistance is a major requirement for the envisaged application, the

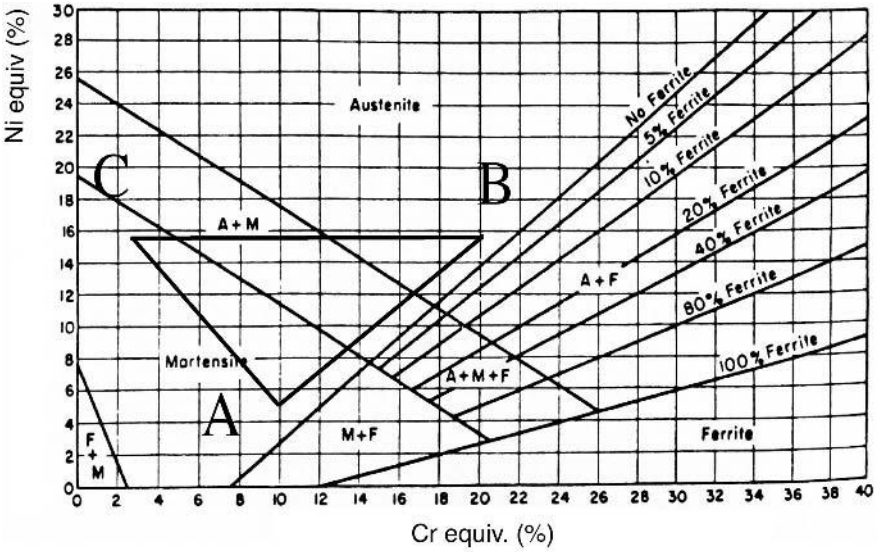

Fig. 4 Composition of matrix alloys, plotted on Schaeffler's diagram. (A: Fe-0.17C-10Cr; B: Fe-0.50C-20Cr; C: Fe-0.50C-3.25Cr).

reinforcement particles must be harder than plastic fillers such as silica and their solubility in the melt must be low, to avoid particle dissolution. NbC was, thus, selected as reinforcement material.

The composition of the matrix was first optimised for maximum wear resistance. In order to obtain a wide variety of representative microstructures, materials with compositions varying along AB, BC and CA lines on the Schaefler diagram (Fig. 4) were prepared. They were screened for their abrasion resistance by carrying out micro-scale wear tests. Alloys A and C were fully martensitic, but martensite in alloy A presented a lath-type morphology, typical of a low-carbon steel, while martensite in alloy C presented a plate morphology, typical of a high-carbon steel. Alloy B was not fully austenitic as expected from Schaeffler diagram, because austenite partially transformed into martensite during cooling. Alloys with intermediate compositions presented microstructures consisting in mixtures of these basic constituents. The highest wear resistance was obtained for the alloy Fe-0.3C-15Cr, consisting of lath type martensite, which was selected for the matrix. Its hardness is moderate (430HV) as compared to alloys B and C (700 and 810HV, respectively). The influence of reinforcement particles on hardness and wear resistance is shown in Figs. 5 a and b, respectively. The hardness is constant for volume fractions of NbC17 wt.% and increases almost linearly with NbC content for higher proportion of this phase. The wear coefficients (k) for abrasive and dry sliding wear present minima (maximum wear resistance) for 10 and 20 wt.% NbC respectively.

The existence of minima is explained by the antagonistic influences of hardness and toughness on the wear resistance. On one side, increasing the NbC content increases the hardness of the material, which is beneficial for its resistance to indenta-

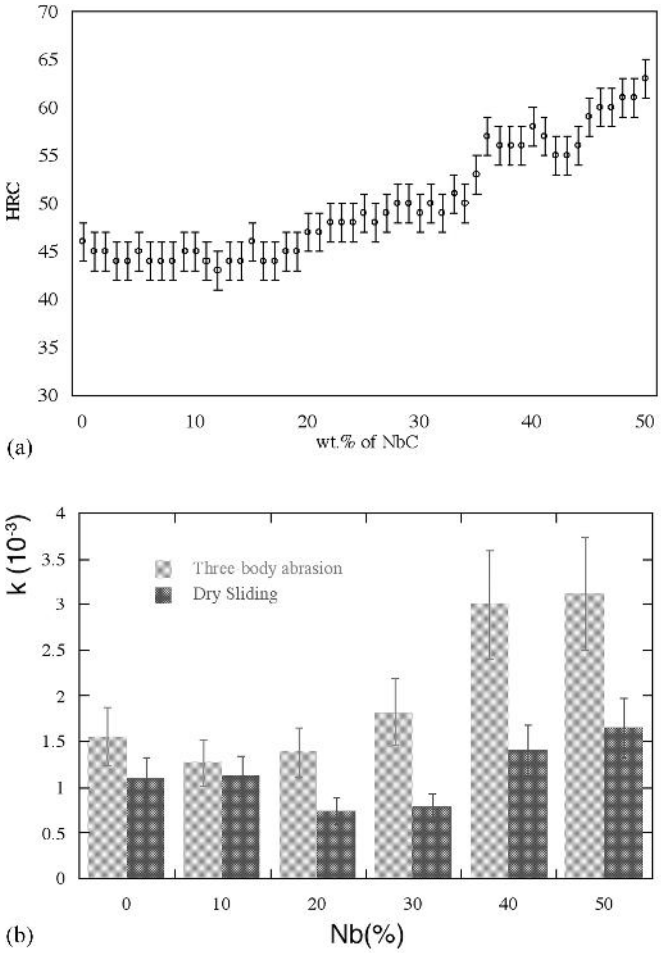

Fig. 5 Effect of NbC content on hardness (a) and wear resistance (b).

tion and load bearing capability and, hence, to the wear resistance. On the other side, the fracture toughness decreases as hardness increases, leading to increasing tendency to wear loss by brittle fracture. The Fe-Cr-C-NbC composites present considerably better abrasive wear resistance than stellite and a dry sliding wear resistance only slightly lower than that of stellite, therefore their wear resistance for rapid tooling application, where abrasive and adhesive wear coexist, should be similar or better than the wear resistance of stellite, with the additional advantages of presenting lower cost, better compatibility with tool steels and absence of cobalt in their constitution.

31.4 Conclusions

The results presented clearly demonstrate that variable powder feed rate laser cladding can be used as a tool for the combinatorial design of materials for laser free-form manufacturing. By applying this technique, libraries of metallic alloys and metal-matrix composites with compositions varying in wide ranges can be synthesised with promptness and flexibility. The microstructure and properties of the materials in the libraries represent adequately those of materials produced by laser-assisted rapid solidification processing, so this method can be advantageously used to develop new metallic alloys and metallic-matrix composite materials for many applications.

References

[1] B. B. Lin, Journal of Food and Drug Analysis 1995, 3, 233–241.

[2] X. D. Sun, K. A. Wang, Y. Yoo, W. G. W. Freedman, C. Gao, X. D. Xiang and P. G. Schultz, Advanced Materials 1997, 9, 1046–1047.

[3] T. X. Sun, Biotechnology and Bioengineering 1999, 61, 193–201.

[4] C. M. Chen, H. C. Pan, D. Z. Zhu, J. Hu and M. Q. Li, Materials Science and Engineering B-Solid State Materials for Advanced Technology 2000, 72, 113–116.

[5] W. C. Choi, J. D. Kim and S. I. Woo, Catalysis Today 2002, 74, 235–240.

[6] R. Cremer and D. Neuschutz, Surface & Coatings Technology 2001, 146, 229–236.

[7] R. Cremer, K. Reichert and D. Neuschutz, Surface and Coatings Technology 2001, 142, 642–648.

[8] H. M. Christen, S. D. Silliman and K. S. Harshavardhan, Review of Scientific Instruments 2001, 72, 2673–2678.

[9] J. Zhao, Advanced Engineering Materials 2001, 3, 143–147.

[10] J. C. Zhao, Journal of Materials Research 2001, 16, 1565–1578.

[11] H. Koinuma, M. Kawasaki, T. Itoh, A. Ohtomo, M. Murakami, Z. W. Jin and Y. Matsumoto, Physica C 2000, 335, 245–250.

[12] I. Takeuchi, R. B. van Dover and H. Koinuma, MRS Bulletin 2002, 27, 301–308.

[13] M. T. Cohen-Adad, M. Gharbi, C. Goutaudier and R. Cohen-Adad, Journal of Alloys and Compounds 1999, 289, 185–196.

[14] P. A. Carvalho, N. Braz, R. Vilar, A. A. Pontinha and M. G. S. Ferreira in LAMP'92 – International Conference on Laser Advanced Materials Processing – Science and Applications (Ed.: A. Matsunawa and S. Katayama), High Temperature Society of Japan, Nagaoka, Japan, 1992, 825–830.

[15] P. A. Carvalho, N. Braz, M. M. Pontinha, M. G. S. Ferreira, W. M. Steen, R. Vilar and K. G. Watkins, Surface and Coatings Technology 1995, 72, 62–70.

[16] P. J. E. Monson, W. M. Steen and D. R. F. West in LAMP '87 – Laser Advanced Materials Processing – Science and Applications, Osaka, Japan, 1987, 377–382.

[17] C. L. Sexton, W. M. Steen, K. G. Watkins, M. G. S. Ferreira, R. M. Vilar and P. Carvalho in AMPT'93 – International Conference on Advances in Materials & Processing Technologies (Ed.: N. S. J. Hashmi), University College Dublin, 1993, 1215–1224.

[18] R. Vilar in Lasers in Materials (Ed.: R. P. Agarwala), Trans Tech Publications Ltd., 1999, 229–252.

[19] R. Colaço, C. Pina and R. Vilar, Scripta Materialia 1999, 41, 715–721.

[20] R. Vilar, R. Colaço and A. Almeida in Laser Processing: Surface Treatment

and Thin Film Deposition (Ed.: J. Mazumder, O. Conde, W. B. Steen and R. Vilar), Kluwer Academic Publishers, Dordrecht, 1996, 453–478.

[21] R. Colaço and R. Vilar, Journal of Materials Science Letters 1998, 17, 563–567.

[22] R. Colaço and R. Vilar, Journal of Laser Applications 2003, 15, 267–272.

32
Control of Morphological Features in Micropatterned Ultrathin Films

E. Meyer, H.-G. Braun

Abstract

Crystallization in ultrathin films obeys diffusion controlled growth processes (DLA) which result in branched growth morphologies. For the first time different morphological features related to diffusion limited aggregation could be created *on request* by controlled initiation of crystallization processes in ultrathin polymer films (polyethylene oxide). Prerequisite for the controlled initiation is the generation of amorphous- with respect to crystallization-metastable films which can be realized by film formation on *micrometer-sized* isles surrounded from non-wetting barriers. Inside of this isolated amorphous microareas heterogeneous nucleation can be initiated by contact with an AFM-tip. Morphological features of the DLA- structures such as tip-radius, branch widths and correlation lengths are varied in dependence of the growth kinetic which is influenced by temperature, surface properties or other parameters. In addition influences of limited material reservoirs in confined areas on film morphology are discussed.

32.1
Introduction

Nature offers a wide range of examples with highly branched morphological features. Typical dimensions of the branches may range from the atomic (1) to the macroscopic scale. The branching structure generally originates from non-equilibrium growth processes which may appear during crystal growth – such as electrocrystallization (2) – as well as during bacteria colony growth (3). Theoretically the processes are commonly described as *diffusion limited aggregation* (*DLA*) (16). Recent studies demonstrated the presence of highly branched structures also for the crystallization of polymers in ultrathin films of homopolymers (4,5) and in blends (6,7). A theoretical approach that takes into account the peculiarities of macromolecular crystallization has recently been published by Reiter and Sommer (8,9,10). Whereas previous work focused on the crystallization of polymers on homogeneous surfaces our studies deal with crystallization processes of ultrathin films in constrained microstructures (15). The microstructured films are prepared by controlled dewetting of

polymer solutions on chemical heterogeneous surfaces (11,12,15). Surface heterogenization can be achieved by microcontact printing (13) or by electron beam lithography of self-assembled monolayers (14) of appropriate organic molecules. In our experiments a gold surface is hydrophilized by chemisorption of an organic molecule which contains a polar group (–COOH) introducing hydrophilicity and a sulphur end-group binding to the gold surface. Irradiation with an electron beam changes the molecular structure causing a change from hydrophilic to hydrophobic properties. Dip-coating of patterned surfaces in chloroformeous PEO solution causes dewetting of the hydrophilic polymer polyethylene oxide (PEO) from the hydrophobic areas (15) leading to microstructured films.

32.2 Experimental

Plasma cleaned (Harrick Plasma Cleaner) silicon substrates were coated with a 3 nm Chromium layer as adhesion promoter and with a 50 nm gold layer. The gold surface is hydrophilized by adsorption (30 minutes) of 11-Mercaptoundecanoic acid (11-MAU) dissolved in ethanol (10^{-3} molar). Hydrophobization of the 11-MAU treated surface within predefined micropatterns is achieved by electron beam lithography with a critical dose of 1000 $\mu As/cm^2$. The E-beam lithography is carried out in a Zeiss Gemini DSM 982 low voltage scanning electron microscope equipped with a Raith Quantum Plus lithography system.

Film formation on the microstructured substrates is done by dip-coating in chloroformeous PEO-solutions (~0.15 % by weight, M_w = 10000) with a lift-off velocity of the substrate of 2 mm/sec.

Crystallization at various temperatures was initiated on a peltier heating stage under light microscopic observation (ZEISS Axiotech). The light microscope is equipped with an AFM head (Ultraobjective SIS®). The films were investigated by AFM or by SEM at low voltages (1 kV) in order to obtain high contrast within the ultrathin films.

32.3 Results and Discussion

Ultrathin film formation on *micro*heterogeneous substrates allows to generate metastable amorphous areas which are created on micrometer-sized isles surrounded from non-wettable barriers (Figure1). The existence of these long time stable amorphous domains is a prerequisite for study of crystallisation processes under controlled thermal and geometrical conditions.

Immediately after dip coating the films are amorphous all over the surface. In presence of heterogenous nuclei crystallization process is initiated and the growth of highly branched lamellae structures of PEO proceeds (A in Figure 1). But inside the isolated film fragments the probability to find a nucleus is rather low and therefore

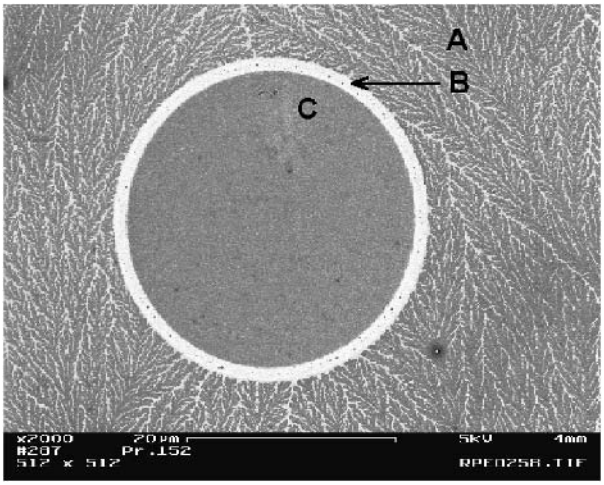

Fig. 1 Amorphous PEO-isle (C) separated by a non wettable hydrophobic barrier (B) in a crystallized film (A).

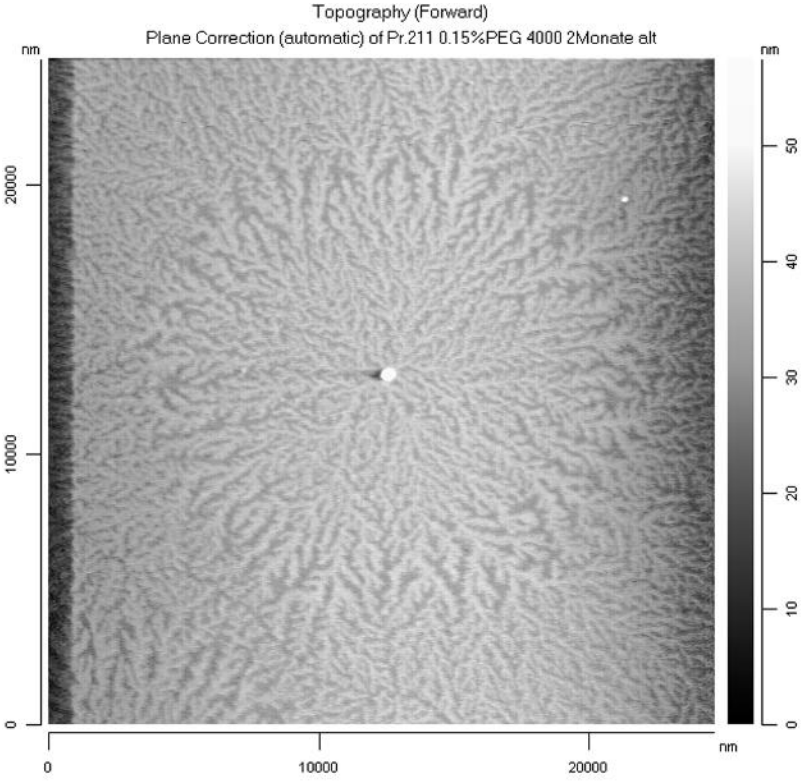

Fig. 2 Crystallized PEO-layer grown from a spherical nucleus.

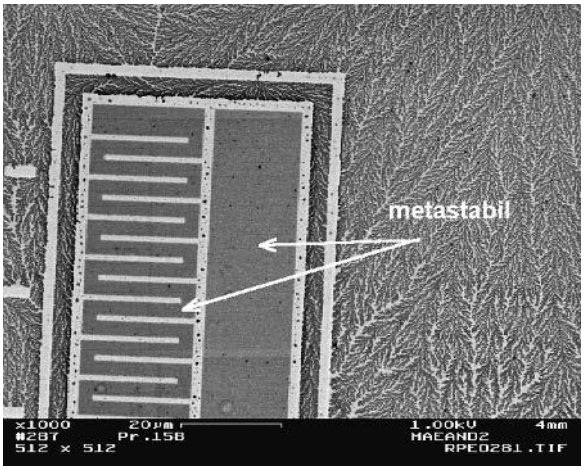

Fig. 3 Metastable PEO-film on micrometer-sized area.

the domains on micrometer-sized isles (C in Figure 1) which are separated by non-wettable barriers (B in Figure 1) remain amorphous.

More sophisticated geometries of amorphous areas are realizable by electron beam lithography of previously chemisorbed MUA (Figure 3). Complicated traces as guidelines for following crystallization processes can be generate by appropriate choice of the geometry of hydrophobic barriers.

Crystallization of amorphous films may start by nucleation from surface scratches, from rims resulting from a dewetting process or from small particles as demonstrated in Figure 2 (heterogeneous nucleation). *Controlled nucleation* can be initiated by contact with an AFM-tip at predefined times and locations (Figure 4). For the first

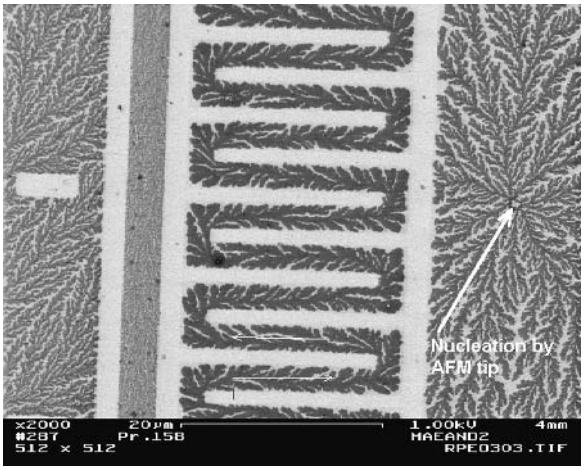

Fig. 4 Controlled nucleation by AFM-tip

time diffusion limited growth processes of branched PEO lamellae could be observed within prearranged 2d-confinements. As demonstrated in Figure 4 the initial growth of branched lamellae is radial around the nucleation side. Reaching the 2d-channel a single branch is guided by the channel geometry.

Initiation of crystallization processes on request allows to control the film morphology. Morphological features of DLA or DBM growth patterns are characterized by the tip-radius, the correlation length and the correlation width (16) of branched structures (Figure 5).

In order to understand the molecular setup of the PEO-structures that occur during the diffusion controlled growth processes in ultrathin polymer films relevant molecular parameters are considered in scheme 1.

The initial thickness of the amorphous PEO layer is about 3 nm. The typical thickness of the branched lamellae is measured to 8 nm as for example demonstrated in Figure 5. Within the crystallographic PEO-unit cell seven ethylene oxide monomer segments are arranged in a 7_2-helix (17) with a c-lattice spacing of 1.948 nm. A single branched lamellae of 8 nm thickness should contain 4 units cells with a polymer chain orientation perpendicular to the surface. The crystallization in the ultrathin PEO film is accompanied by a thickness increase whereby a depletion zone is created in front of the growing lamellae. The width of the depletion zone varies with crystallization conditions and geometrical confinements and has to be overcome by

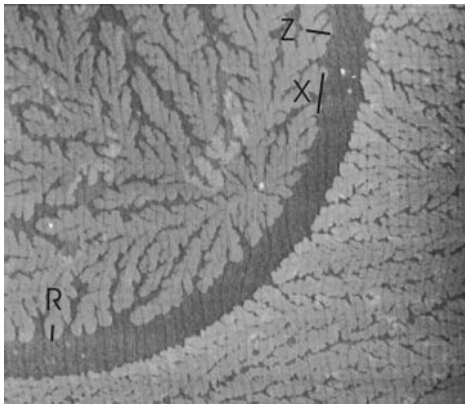

Fig. 5 Characteristic features of branched morphological structures
R tip radius
Z correlation length perpendicular to stem
X correlation width parallel to stem

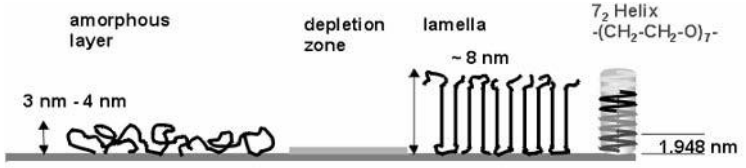

Scheme 1 Basic structural units involved in the crystallization process. Crystalline lamellae are composed of typically 4 unit cells in which PEO segments are arranged in a 7_2 helical conformation of 1.948 nm basic length (17).

the polymer chains diffusing from the amorphous layer to the crystallizing lamellae. Crystallization in ultrathin PEO-films can also result in stacked lamellae structures which will be shown later.

One of the key parameter to influence the morphological features is to control the nucleation temperature at which the diffusional growth process is initiated and at which the branched lamellae grow.

Figure 6 shows a serious of images in which the crystallization is carried out at varying crystallization temperatures inside circular motifs. The equilibrium melting temperature of the PEO is 56 °C. The heterogeneous nucleation was initiated approximately at the center of each circle. The growth history can easily be reconstructed from the direction of the branches which are oriented towards the lamellae growth front. In Figure 6 B it is easy to follow the growth pass from the center through the small gaps and then symmetrical growing to both sides of the gap. The morphologies

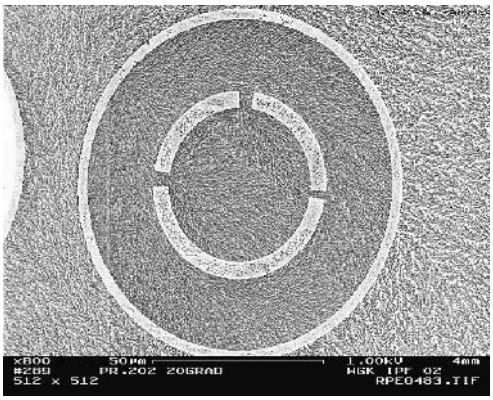

A Nucleation and growth temperature: 20 °C

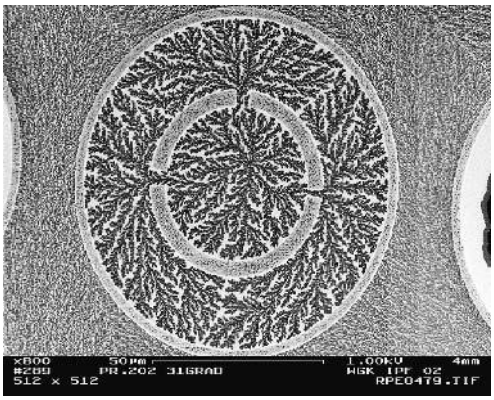

B Nucleation and growth temperature: 31 °C

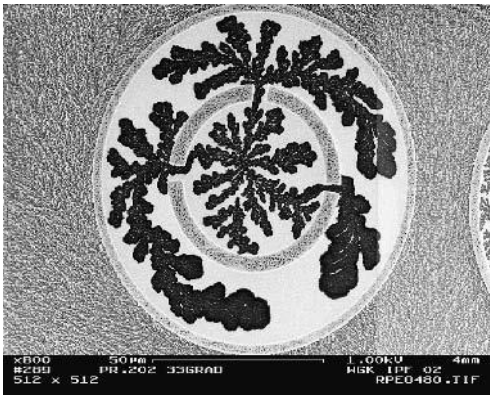

C Nucleation and growth temperature: 33 °C

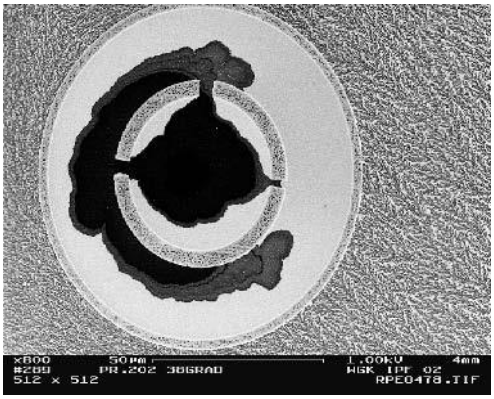

D Nucleation and growth temperature: 38 °C

Fig. 6 Control of morphological features in confined ultrathin PEO-films crystallized at different temperatures

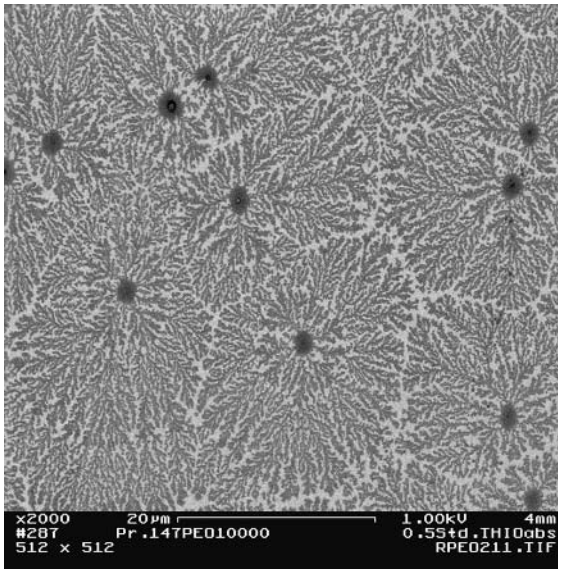

Fig. 7 "Spherolitic" growth of PEO branched lamellae initiated from different nucleation sites.

show a texture similiar to that in spherolites. Branches which grow from different directions towards each other are separated by a gap which originates from the depletion zones. Figure 7 demonstrates much more pronounced gaps for "spherolitic" growth in an ultrathin homogeneous film with a radial growth around a large number of nucleation sites. Higher crystallization temperature and consequently decreasing temperature gap between the actual sample temperature (nucleation- and crystal growth temperature) and the equilibrium melting temperature causes branch growth with larger tip-radius, increasing correlation length and an overall coarser structure (Figure 6 A–D). The coarser branch structure results from *reorganisation processes* of polymer chain segments. As a consequence of higher segment mobility at higher temperatures the strong curved tips increase their radius of curvature and reduce the interfacial energy leading to a more favorable thermodynamic state. In ultrathin polymer films not only the branch morphology is changed but also the lamellae thickness can be increased during the reorganisation processes.

At high nucleation temperatures crystallization may even result in multilamellae structures which nearly lost their branching completely (Figure 6 D, Figure 8).

Diffusion controlled growth processes are not only determined by temperature but, additionally, if the growth happens in constrained areas (in our experiment in isolated rings) the structure formation is influenced by geometry of pattern.

In confined areas the concentration gradient which is the driving force for the structure formation remains not constant during the isothermal growth process. Due to the limited material reservoir the depletion zone ahead the propagating solidification front is continuous increased (Schema 1) which causes a decrease of the tip growth velocity respectively a decrease of number of molecules/time attaching the growth front. Analogous to the temperature effect tip radii are increased, less

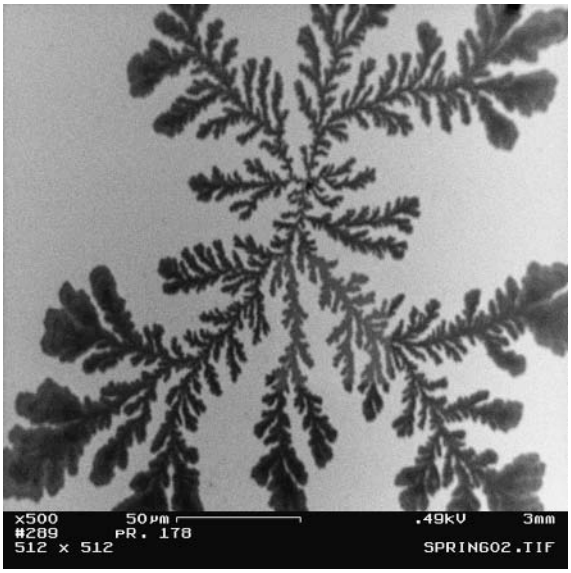

Fig. 8 Increase of tip-radii and multilamellae at the end of the dendrite due to changing of diffusion conditions during isothermal crystallization at limited material supply.

folded and thicker lamella crystals of the macromolecular stems and finally multilamella stacks are formed. Figure 6C clearly shows the changing of morphological features due to the constrained geometry. Near the nucleation centre (initiation by AFM-tip) the branches are finer than in areas far from the initiation point.

32.4 Perspectives

The structural organization of PEO-units at surfaces is of great importance for the biocompatibilisation of man-mad materials. PEO is well known to reject proteins from a surface and therefore to influence cellular growth processes in the spaces in between the PEO-branches. From this perspective it becomes obvious that the understanding of and control over morphological features of PEO on surfaces is a goal for the development of biocompatible surfaces.

Crystallization in ultrathin PEO-layers is a molecular self-organization process in which a network of highly branched lamellae structures are formed. The PEO lamellae networks with defined and controllable submicrometer-sized features (branch width, distance) may be an approach to gain control over cell adhesion and cell growth processes on surfaces. The detailed knowledge of the structure formation on surfaces in dependence of pattern geometry and the temperatures at which crystallization is initiated allows a morphological surface engineering of PEO lamellae networks. The lamellae PEO-networks can be permanently fixed to the underlying surface by electron-beam irradiation using PEO-layers as electron-beam resist (Figure 9). As a result the irradiated areas are insoluble in water.

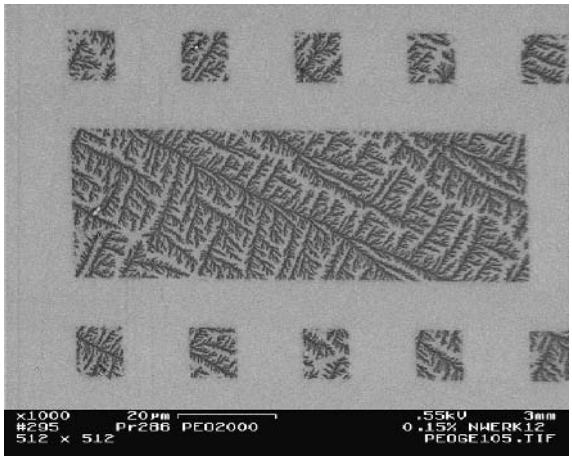

Fig. 9 Ultrathin Polyethylene oxide film which has been crystallized on a homogeneous (unstructured) surface and afterwards structured and irreversible attached to the surface by electron beam lithography.

Beside the control of morphological features of the network (distances or branch widths etc. for growth guide lines on nm-scale) the electron beam lithography can be also used for structuring of homogenous PEO-films in order to influence cellular growth processes on the scale of several micrometers.

Acknowledgement

We gratefully acknowledge financial support of the "Deutsche Forschungsgemeinschaft" within the priority program "Wetting and structure formation at interfaces".

References

[1] Z. Zhang, G. Lagally, Science 1997, 276, 377–383
[2] M. Castro, R. Cuerno, A. Sanchez, F. Domiguez-Adame, Phys. Rev. E, 2000,61,161
[3] I. Golding, Y. Kozlovsky, I. Cohen, E. Ben-Jacob, Physica A, 1998, 260, 510–554
[4] G. Reiter, J.-U. Sommer, Phys. Rev. Lett., 1998, 80, 3771–3774
[5] M. Wang, H.-G. Braun, E. Meyer, Macromol. Rapid Commun. 2002, 23, 853–858
[6] M. Wang, H.-G. Braun, E. Meyer, Polymer 2003, 44, 5015–5021
[7] M. Wang, H.-G. Braun, E. Meyer, accept. for publication in Macromolecules
[8] G. Reiter, J.-U. Sommer, J. Chem. Phys., 2000,112, 4376–4383
[9] J.-U. Sommer, G. Reiter, J.Chem. Phys., 2000, 4384–4393
[10] J.U. Sommer, G. Reiter in Polymer Crystallization LNP 606 (Eds.:J.U. Sommer, G.Reiter), Springer, Heidelberg, 2003, Chapter 9
[11] H.-G. Braun, E. Meyer, Thin Solid Films, 1999, 345,222–228
[12] E. Meyer, H.-G. Braun, Macromol. Mater. Eng., 2000, 276/277, 44–50
[13] Y. Xia, G.M.Whitesides, Angew. Chemie Int. Ed., 1998, 37, 550–575
[14] C.K. Harnett, K.M. Satyalaksmi, H.G. Craighead, Langmuir, 2001, 17, 178–182

[15] H.-G. Braun, E. Meyer, M. Wang, in Polymer Crystallization LNP 606 (Eds.: J.U. Sommer, G.Reiter), Springer, Heidelberg, 2003, Chapter 13

[16] P. Meakin, Fractals, scaling and growth far from equilibrium,Cambridge University Press, 1998

[17] Y. Takahashi, H. Tadokoro, Macromolecules, 1973, 6, 672- 675

Author Index

Apel, Markus *271*
Appel, Fritz *250*
Assadi, Hamid *17*
Bührig-Polaczek, A. *204*
Bilgram, J. H. *1, 166*
Böllinghaus, Th. *213*
Böttger, Bernd *271*
Braun, H.-G. *300*
Brener, Efim *9*
Bunzel, P. *157*
Carvalho, P. *290*
Chatterjee, Anita *250*
Clemens, Helmut *250*
Cochrane, Robert F. *175*
Colaço, R. *290*
Dong, H. B. *280*
Dragnevski, Kalin *175*
Drevermann, Anne *259*
Eckert, S. *194*
Emmerich, Heike *27*
Filip, O. *185*
Funke, O. *52*
Galenko, P. K. *52*
Gandin, Ch.-A. *70*
Gao, J. *239*
Gerbeth, G. *185*
Greer, A. Lindsay *137*
Gröbner, Joachim *95*
Guo, Z. *82*
Gutheim, Frank *9*
Hecht, Ulrike *259, 271*
Henein, H. *70*
Heringer, R. *70*
Herlach, D. M. *52, 148, 239*
Hermann, R. *185*
Holland-Moritz, D. *128, 148*
Hoyer, Walter *110*
Hu, Z. Q. *44*
Jimbo, Itaru *227*
Jurgk, Matthias *27*
Kaban, Ivan *110*
Küstner, Viola *250*
Krajewski, Witold K. *137*
Kuribayashi, Kazuhiko *227*
Lee, P. D. *280*
Lesoult, G. *70*
Li, Mingjun *227*
Liu, R. P. *148*
Ludwig, A. *34, 204*
Merkwitz, Markus *110*
Meyer, E. *300*
Michel, U. *194*
Müller-Krumbhaar, Heiner *9*
Miodownik, A. P. *82*
Mirkovic, Djordjé *95*
Mullis, Andrew M. *175*
Nestler, Britta *61*
Oehring, Michael *250*
Ozawa, Shumpei *227*
Panofen, C. *148*
Phanikumar, G. *52*
Pütter, Christoph *9*
Priede, J. *185*
Quested, Thomas E. *137*
Ratke, L. *34, 44, 119*
Reutzel, S. *239*

Rex, Stephan *259*
Rösner, H. *157*
Ryder, Peter L. *103*
Saunders, H. *82*
Schillé, J-Ph. *82*
Schmid-Fetzer, Rainer *95*
Schobbert, H. *213*
Shatrov, V. *185*
Singer, H. M. *1, 166*
Siquieri, Ricardo *27*
Spaepen, Frans *128*
Steinbach, Ingo *271*
Strohmenger, J. *239*
Sugiyama, Suguru *227*
Tscheuschner, D. *119*
Vilar, R. *290*
Volkmann, T. *148, 239*
Wang, W. *280*
Warncke, Nils *103*
Weissmüller, J. *157*
Wilde, G. *157*
Willers, B. *194*
Witusiewicz, Victor *259, 271*
Wolczynski, Waldemar *137*
Wolf, M. *213*
Wu, M. *34, 204*
Yang, X. L. *280*
Zhao, J. Z. *44*
Zouhar, G. *194*

Subject Index

binary alloy nano particles 157
binary alloys 27
cast turbine blades 280
combinatorial materials science 290
complex structures 1
containerless processing 227
dendritic solidification 27, 52
DSC experiments 95
elastic interaction 9
electrostatic levitator 103
eutectic cells 259
Fe-Cr-Ni system 213
fluid convection 194
globular equiaxed solidification 204
heterogeneous nucleation 137
hydrodynamics 185
hypermonotectic alloys 34
immiscible alloys 44
lamellar pattern formation 271
laser cladding 290
laser welding 213
liquid silicon 148
liquid-liquid interfacial tension 110
magnetic effects 128
microstructure evolution 185
multi-component alloys 82
multiple grain structures 17
Nd-Fe-B alloys 185
Nd-Fe-B bulk alloys 239
$Nd_2Fe_{14}B$ peritectic phase 227
numerical studies 1
optical determination 119
oscillating drop method 103
PbSn alloys 194
phase separation process 34
phase-field model 17
phase-field modeling 52, 61
primary dendritic structures 175
scaling relations 27
solidification curves 95
solidification microstructure 250
solidification modeling 82
solidification of droplets 70
solid-on-solid model 9
stray grain formation 280
surface tension 103
ternary Al-Cu-Ag alloys 259
ternary alloys 61
ternary eutectic alloys 271
thermal roughening 9
thermomagnetic analyses 239
titanium aluminide alloys 250
two-phase equilibrium 157
ultrathin films 300
undercooled Co-Pd melts 128
undercooled melts 103, 175
xenon dendrites 166
Zn-Al alloy 137
Zn-Ti-based master alloy 137